UNIVERSIDADE DE SÃO PAULO
INSTITUTO DE GEOCIÊNCIAS

Strontium isotope stratigraphy and trace-metal geochemistry of the Ediacaran Cambrian Bambuí Group, São Francisco Basin

CRISTHIAN CAMILO GUACANEME MORA

Tese apresentada ao programa de Pós-graduação em Geociências – Geoquímica e Geotectônica para obtenção do título de Doutor em Ciências

Área de Concentração: Geotectônica

Orientadora: Profª. Drª. Marly Babinski

SÃO PAULO

2021

Serviço de Biblioteca e Documentação do IGc/USP

Ficha catalográfica gerada automaticamente com dados fornecidos pelo(a) autor(a)
via programa desenvolvido pela Seção Técnica de Informática do ICMC/USP

Bibliotecários responsáveis pela estrutura de catalogação da publicação:
Sonia Regina Yole Guerra - CRB-8/4208 | Anderson de Santana - CRB-8/6658

Guacaneme Mora, Cristhian Camilo

Strontium isotope stratigraphy and trace-metal geochemistry of the Ediacaran-Cambrian Bambuí Group, São Francisco Basin / Cristhian Guacaneme Mora; orientadora Marly Babinski. -- São Paulo, 2021.

210 p.

Tese (Doutorado - Programa de Pós-Graduação em Geoquímica e Geotectônica) -- Instituto de Geociências, Universidade de São Paulo, 2021.

1. Ediacarano-Cambriano. 2. Grupo Bambuí. 3. Isótopos de estrôncio. 4. Metais traço. 5. Gondwana. I. Babinski, Marly, orient. II. Título.

UNIVERSIDADE DE SÃO PAULO
INSTITUTO DE GEOCIÊNCIAS

Strontium isotope stratigraphy and trace-metal geochemistry of the Ediacaran Cambrian Bambuí Group, São Francisco Basin

CRISTHIAN CAMILO GUACANEME MORA

Orientadora: Profª. Drª. Marly Babinski

Tese de Doutorado

Nº 638

COMISSÃO JULGADORA

Drª. Marly Babinski

Drª. Milene Figueiredo

Dr. Claudio Gaucher

Dr. Farid Chemale Junior

Dr. Fabrício de Andrade Caxito

SÃO PAULO

2021

Agradecimentos

O desenvolvimento deste trabalho foi possível graças ao apoio de muitas pessoas e instituições. Primeiramente, eu tenho que agradecer à minha orientadora, a professora Marly Babinski do IGc-USP, porque ela sempre acreditou em mim e me deu essa grande oportunidade de vida. Sou infinitamente grato!

Agradeço ao professor Ricardo Trindade do IAG-USP pela oportunidade de trabalhar junto a um excelente grupo de pesquisa e o vínculo com o Projeto Temático FAPESP ¨ O Sistema Terra e a evolucão da vida durante o Neoproterozoico¨.

Aos professores do IGc-USP que me deram aula, Setembrino Petri, Umberto Giuseppe Cordani, Benjamim Bley de Brito Neves, Wilson Teixeira, Adriana Alves e o resto dos professores do IGc, muito obrigado! Foi um privilégio.

Aos colegas Gustavo Macedo de Paula-Santos e Sergio Caetano-Filho, eles são os capitães deste avião da quimiostrati, excelentes investigadores e admiráveis como pessoas, muito obrigado pelos conhecimentos aportados durante todos estes anos e por muitas e interessantes discussões. Valeu demais!

Aos meus amigos e colegas do grupo da quimioestratigrafia, Carolina Bedoya Rueda, Juan Camilo Gomez Gutierrez, Paula Luiza Fraga Ferreira, Marilia Peloso, Sara dos Santos Souza, valeu pela amizade e pela ajuda incondicional.

Aos professores Juliana Leme, Matheus Kuchenbecker e Humberto Reis, e aos pesquisadores Jhon Afonso e Kamilla Amorim, muito obrigado pelos aportes, e pelas discussões e sugestões durante o desenvolvimento deste trabalho.

A todo o pessoal professional e técnico do Instituto de Geociências da USP, especialmente à Luciana Nogueira do LabPetro-USP, Alyne Barros da Silva do Laboratório de Isótopos Estáveis, Liliane Aparecida Petronilho, Kei Sato, Artur Takashi Onoe e Vasco A. Pereira dos Loios do Centro de Pesquisas Geocronologias (CPGeo), muito obrigado pelo suporte.

A Coordenação de Aperfeiçoamento de Pessoal de Nível Superior (CAPES) pela bolsa de estudo de doutorado garantida durante quatro anos, muito agradecido!

A minha família na Colômbia, meus pais, Jairo Luis Guacaneme Sanchez, que sempre me ilumina com sua luz, e Ciralba Mora, cujo amor vai além de qualquer fronteira. Aos meus irmãos Jhon Jairo e Cesar, e às minhas irmãs Carolina e Claudia, muito obrigado pela paciencia e pelo apoio incondicional durante todos esses anos. Aos meus sobrinhos Alejandro, Simón e Luis, e minhas sobrinhas Camila, Catalina, Juanita e Sarita, também aos meus cunhados y cunhadas, e à família toda pela união e suporte.

Aos meus amigos colombianos e colegas Valentina Espinel, Sebastian Echeverry, Sebastian Hernandez, Ana Maria Patiño, Veronica Ramirez, Melissa Martinez, Maria Isabel Giraldo, Andrés Salazar e Mauricio Parra.

Aos meus amigos colombianos que moram no Brasil, Luz K. Polo, Juliana Guzmán e Cristian Usma.

Aos meus amigos brasileiros do IGc-USP Victor Maure, Cleber Peralta, Renato Henrique-Pinto, Thomas Akabane e Mariza Silva e muitos mais, valeu pela amizade!

Aos meus amigos de Stereo Roca, Astrid Siachoque, Renato Silva de Oliveira, Jonathan Barré, Ginneth Pulido, Vitor e Ivan, sempre com saudades de tocar a musica colombo-brasileira!

A minha amiga e companheira Conchita Pinzón, pelo apoio e o seu amor.

Finalmente a todos aqueles que de alguma forma me ajudaram a realizar este trabalho, muito obrigado!

“Se você esconder sua ignorância, ninguém lhe baterá

e você nunca irá aprender” – Fahrenheit 451

Ray Bradbury

Resumo

A evolução geológica da bacia intracratônica do São Francisco no interior do megacontinente Gondwana é marcada por períodos de conexão e isolamento do oceano global no final do Ediacarano e início do Cambriano. Este trabalho fornece novas informações sobre a evolução estratigráfica da bacia com base na geoquímica detalhada de metais traços (Cd, Cu, Co, Cr, Mo, Ni, U, V e Zn) e na quimioestratigrafia de isótopos de Sr nas rochas carbonáticas da parte basal do Grupo Bambuí, que potencialmente registram mudanças paleoambientais importantes no contexto de uma bacia de ante-país. Na sequência regressiva basal de 2ª ordem, os dados normalizados de metais traços mostram um aumento progressivo do fator de enriquecimento em relação ao PAAS (Post Archean Australian Shale), acompanhado de um grande aumento nas razões Sr/Ca (de 0,001 até 0,004) e uma diminuição nas razões $^{87}Sr/^{86}Sr$ de 0,7086 para 0,7076. Essas mudanças precedem uma grande excursão positiva de $\delta^{13}C$ (até +16‰) tipicamente encontrada na parte intermediária do Grupo Bambuí, que compreende as formações Sete Lagoas superior e Lagoa do Jacaré. O enriquecimento em metais traços ao longo dessa sequência sugere evolução química das águas profundas com longos tempos de residência e cujas condições redox mudam progressivamente de subóxico-anóxico para anóxico-euxínico. As variações das razões $^{87}Sr/^{86}Sr$ indicam que a bacia evoluiu de uma via marítima conectada para um mar restrito, produto de mudanças paleogeográficas induzidas pela evolução dos sistemas orogênicos marginais neoproterozoicos, e mudanças no equilíbrio entre a produção de carbonatos e acomodação associadas à subsidência flexural, alterando o fluxo de estrôncio e as composições isotópicas da água do mar epicontinental. Em condições de restrição marinha, as características bioquímicas da massa de água profunda do mar Bambuí se tornaram extremadamente sulfídicas, sem renovação de águas oxigenadas, com a escassez de metais traços transportados pela ressurgência, e com a limitação da fixação de micronutrientes. Isto teria limitado a biodisponibilidade de nitrogênio, gerando um desafio para a colonização dos primeiros metazoários bentônicos nos mares epicontinentais do Gondwana na transição Ediacarano-Cambriano.

Palavras-chave: Grupo Bambuí, Metais traços, Isótopos de Sr, Gondwana Ocidental

Abstract

The geological evolution of the intracratonic São Francisco basin in the interior of Gondwana megacontinent is marked by periods of connection and isolation from the global ocean at the end of the Ediacaran and the beginning of the Cambrian. This work provides new aspects on the stratigraphic evolution of the basin based on the detailed trace-metal geochemistry (Cd, Cu, Co, Cr, Mo, Ni, U, V and Zn) and on the Sr-isotope chemostratigraphy of carbonate rocks from the basal Bambuí Group, which potentially record important paleoenvironmental changes in the context of a foreland basin. In the basal 2nd-order regressive sequence, the normalized trace metal data show a progressive increase in the enrichment factor relative to PAAS (Post-Archean Australian Shale), accompanied by a large increase in Sr/Ca ratios (from 0.001 to 0.004) and a decrease in $^{87}Sr/^{86}Sr$ from 0.7086 to 0.7076. These changes precede a large positive $\delta^{13}C$ excursion (up to +16‰) typically found in the middle part of the Bambuí Group, comprised the upper Sete Lagoas and Lagoa do Jacaré formations. The enrichment patterns of trace-metal along this sequence suggests chemical evolution of bottom waters with long residence times and whose redox conditions progressively change from suboxic-anoxic to anoxic-euxinic. Variations in the $^{87}Sr/^{86}Sr$ ratios indicate that the basin evolved from a seaway connected to the global ocean to a restricted sea, resulted by paleogeographic changes induced by the evolution of marginal Neorproterozic orogenic systems, and changes in the balance between carbonate production and accommodation associated with flexural subsidence, altering the strontium flux and the isotopic compositions of epicontinental seawater. Under conditions of marine restriction, the biochemical characteristics of the deep watermass of the Bambuí sea became extremely sulphidic, with no renewal of oxygenated water, with a scarcity of trace metals transported by upwelling, and with limited fixation of micronutrients. This would have limited nitrogen bioavailability, triggering a challenge for the colonization of the first benthic metazoans in the epicontinental seas of Gondwana in the Ediacaran-Cambrian transition.

Key words: Bambuí Group, Trace metals, Sr isotopes, West Gondwana

Summary

Figure List

Figure 1. (A) Location map of the São Francisco Basin in east-central Brazil. **(B)** Location of the study areas represented by white circles on the basin. **(C)** Bouguer anomaly map of the São Francisco Basin (modified from Reis et al., 2017a).

Figure 2. (A) geological map of the São Francisco Craton in east-central Brazil. **(B)** paleogeographic reconstruction of the late Neoproterozoic West Gondwana. (modified from Caetano–Filho et al., 2019).

Figure 3. Lithostratigraphic chart of the 1st–order sequence Bambuí Group and chemostratigraphic evolution in the São Francisco Basin (Modified from Caetano–Filho et al., 2019). Maximum depositional ages obtained by U–Pb geochronology in detrital zircon grains are represented by yellow stars (Macaúbas Gr. – Castro et al., 2020; upper Sete Lagoas Formation – Paula–Santos et al., 2015). Depositional ages obtained by U–Pb geochronology in zircons from tuff layer are represented by the red star (upper Serra da Saudade Formation – Moreira et al., 2020); *Cloudina* sp. occurrence in the lower Sete Lagoas Fm. is from Warren et al. (2014) and *Treptichnus Pedum* record in the Três Marias Fm. is from Sanchez et al. (2021).

Figure 4. Stratigraphic–chemostratigraphic correlations for the basal Bambuí Group between the southern and northern domains of the São Francisco Basin (Sete Lagoas and Januária highs, respectively). TST: Transgressive System Tract; MFS: Maximum Flooding Surface; EHST: Early Highstand System Tract; LHST: Late Highstand System Tract; SB1: Sequence Boundary. Lithostratigraphic units: SL – Sete Lagoas Formation; SSH – Serra de Santa Helena Formation; LJ – Lagoa do Jacaré Formation (extracted from Caetano–Filho et al., 2019).

Figure 5. Sketch illustrating the integrated tectonic model for the Bambuí basin and the adjoining orogens during the West Gondwana amalgamation (Extracted from Kuchenbecker et al. 2020).

Figure 6. Reservoirs of strontium and cycles of inputs and output relative to seawater. Continental sources (in general) are radiogenic and oceanic sources are non-radiogenic. Changes in the relative inputs from those two major groups of sources are influenced by oceanic spreading rates, extent of continental exposure, uplift and erosion, and many other factors (Extracted from Elderfield, 1986).

Figure 7. Secular ^{87}Sr seawater average trend line (black dashed line) and natural fluctuation band (solid lines) of 1 Ma intervals of measurements for the Phanerozoic Eon based only on biogenic calcite and aragonite material (Extracted from Zaky et al. 2019).

Figure 8. Secular $^{87}Sr/^{87}Sr$ evolution curve (black dashed line) and natural fluctuation band (solid lines) of 1 Ma intervals of measurements for the pre-Ordovician and Neoproterozoic seawater (extracted from Zaky et al. 2019).

Figure 9. Schematic behavior of Ni, Cu, Mo, U and V as a function of the redox status of the depositional environment (extracted from Tribovillard et al. 2004).

Figure 10. Diagram showing relationships of Mo and U authigenic enrichment to **(A)** benthic redox variation, **(B)** Mn-oxyhydroxide particulate shuttle, and **(C)** evolving aqueous chemistry. In **A**, the zone of aerobic respiration is shown in blue, the (generally narrow) field of anoxic–nonsulfidic conditions (zones of Fe(III), Mn(IV) and nitrate reduction in orange, and the zone of sulfate reduction in gray. In **B**, MnOOH and Mn^{+2} represent the downward flux of particulate Mn-oxyhydroxides and the upward flux of aqueous reduced Mn, respectively; Mo represents the flux of adsorbed molybdate to the sediment (left panel) and its recycling within the water column (right panel); FC and SC represent fluctuating and stable chemocline depths, respectively. In **C**, the x-axis scale relates to aqueous Mo and U vertical concentration profiles and ranges from zero to the

seawater (SW) value. In **A–C**, size of arrows shows relative magnitudes of authigenic Mo and U fluxes to the sediment. SWI = sediment/water interface (Extracted from Algeo and Tribovillard, 2009).

Figure 11. (A) Januária section showing transgresive-regressive 2nd-order cycles and facies code (modified from Caetano-Filho et al., 2019). **(B)** local geological map of the São Francisco Basin at the Januária region with location of stratigrafic sections which compose the Januária section; BAR: Barreiro, CM: Conego Marinho, JL: Januária-Lontra. **(C)** W-E cross-section (A-A´) perpendicular to the direction of the São Francisco river (modified from Iglesias-Martínez, 2007).

Figure 12. (A) Santa Maria da Vitória section showing transgresive-regressive 2nd-order cycles and facies code (modified from Caetano-Filho et al., 2019). **(B)** local geological map of the São Francisco Basin at the Santa Maria da Vitória region with location of stratigrafic sections which compose the SMV section; COR: Correntina, ALD: Aldeia, BA: Bahia, PIT: Pedreira dos Irmaos Teixeira, PT: Pedreira Terracon, CL: Caldeirao. **(C)** W-E cross-section (A-A´) perpendicular to the direction of the Formoso river (modified from Miranda, 2003).

Figure 13. (A) polished slab of dolomitic limestone with intense recrystallization (Rec) and euhedral pyrite (Epy). **(B–C)** photomicrographs of dolomitic limestone showing disseminated pyrite (Epy) within the crystalline dolomite matrix, syntaxial overgrowth of calcite (Sov) and euhedral dolomitic rhoms (Dol). **(D)** polished slab of calcimudstone showing detail of aragonite pseudomorph crystal fans (Arag). **(E–F)** photomicrographs of calcimudstone showing silica cement (Sic) associated to stylolites (Sty); organic films (Of) and sparry calcite cement (Scc). **(G)** polished slab of peloidal bindstone with stylolite (Sty). **(H–I)** photomicrographs of peloidal bindstone showing organic films (Of) and sparry calcite cement (Scc). **(J)** polished slab of peloidal bindstone with microbial lamination (Mla). **(K–L)** photomicrographs of peloidal bindstone showing microbial lamination (Mla) and sparry calcite cement (Scc). CPL: Cross-polarized light; PPL Plane-polarized light). Sample code at the upper right corner.

Figure 14. (A) polished slab of peloidal calcimudstone with clay laminae (Clay) and stylolite (Sty). **(B–C)** photomicrographs of laminated peloidal calcimudstone showing sparry calcite cement (Scc) and some fractures (Frac). **(D)** polished slab of peloidal bindstone with clay laminae (Clay). **(E–F)** photomicrographs of peloidal bindstone showing stylolites (Sty) and radiating silica micronodules (Sin). **(G)** polished slab of laminated peloidal calcimudstone. **(H–I)** photomicrographs of peloidal calcimudstone showing dissolution followed by later blocky calcite cement (Bcc) and late diagenetic calcite veins (Ve). **(J)** polished slab of peloidal calcimudstone with spherical silica nodules (Sin). **(K–L)** photomicrographs of peloidal calcimudstone displaying stylolites (Sty), sparry calcite cement (Scc) and a spherical radiating silica micronodule (Sin). CPL: Cross-polarized light; PPL Plane-polarized light. Sample code at the upper right corner.

Figure 15. (A–C) photomicrographs of laminated peloidal calcimudstones showing sparry calcite cement (Scc), replacement of intraclast by calcite (Rep), stylolites (Sty), and late diagenetic calcite vein (Ve). (**D–I)** photomicrographs of intraclastic rudstone showing detailed micritic clast (Clast) cutted by calcite vein (Ve), replacement (Rep) of detrital grain (Det) by calcite, recrystallization (Rec) and syntaxial overgrowth of calcite (Sov), euhedral dolomite rhoms (Dol) and dispersed opaque grains (Op). **(J–L)** photomicrographs of intraclastic dolograinstone showing detrital grains (Det), dissolution (Diss) and precipitation of phreatic calcite cement (Pcc), recrystalization (Rec) and euhedral dolomite (Dol). CPL: Cross-polarized light; PPL: Plane-polarized light). Sample code at the upper right corner.

Figure 16. (A–C) photomicrographs of siltstones and mudstones composed mainly of detrital quartz (Qz), feldspar (Fk), micas (Mi), and oxidized cement (Oxc). **(D–F)** photomicrographs of peloidal calcimudstone showing preserved horizontal lamination (Hl), dispersed opaque grains (Op), dissolution and precipitation of phreatic calcite cement (Pcc). **(G–L)** photomicrographs of intraclastic rudstone showing diagenetic calcite vein (Ve1) cutted by late diagenetic calcite veinlets (Ve2) and fractures (Frac), syntaxial overgrowth of calcite (Sov), replacement of detrital grains by calcite (Rep) and lesser

stylolites (Sty). CPL: Cross-polarized light; PPL Plane-polarized light). Sample code at the upper right corner.

Figure 17. (A) polished slab of dolomitic limestone with stylolites (Sty), calcite veinlets (Ve1) and late diagenetic calcite veinlets (Ve2). **(B–C)** photomicrographs of dolomitic limestone showing silica cement (Sil), dispersed opaque grains (Op) and fractures (Frac). **(D–F)** polished slab of calcimudstone showing two levels of aragonite pseudomorph crystal fans (Arag). **(G–I)** photomicrographs of calcimudstone showing detail of aragonite pseudomorph crystal fans (Arag), stylolites (Sty) and calcite vein (Ve). **(J)** polished slab of reddish laminated peloidal bindstone **(K–L)** photomicrographs of laminated peloidal bindstone with fracture (Frac). CPL: Cross-polarized light; PPL Plane-polarized light). Sample code at the upper right corner.

Figure 18. (A–C) polished slabs of peloidal bindstone with clay laminae (Clay), euhedral pyrite (Epy), stylolite (Sty) and calcite veinlets (Ve). **(D–F)** photomicrographs of peloidal bindstones showing flame structure (FS) and late diagenetic calcite vein (Ve), microbial lamination (Mla), stylolites (Sty) and recrystallization (Rec). **(G–H)** polished slab of dark-grey laminated peloidal calcimudstone with stylolites (Sty). **(I–L)** photomicrographs of laminated peloidal calcimudstone displaying recrystallization (Rec), stylolites (Sty) and fractures (Frac). CPL: Cross-polarized light; PPL Plane-polarized light). Sample code at the upper right corner.

Figure 19. (A–B) polished slabs of dark-grey laminated peloidal calcimudstone with clay laminae (Clay), framboidal pyrite (Fpy), oxided sulfides (Ox), spherical micronodules of silica (Sil) associated with stylolites (Sty), late diagenetic calcite veinlet (Ve). **(C)** photomicrograph of laminated peloidal calcimudstones showing spherical radiating micronodules of silica (Sil) associated with stylolites (Sty) (**D–F)** polished slabs of intraclastic rudstone showing clasts (Clast) cutted by stylolite (Sty). **(G)** polished slab of intraclastic dolograinstone with recrystallization (Rec). **(H–I)** photomicrographs of intraclastic dolograinstone showing dissolution (Diss) followed by precipitation of rhombic dolomite cement (Rdc), replacement of intraclastic detrital grain (Det) by calcite, crystals

of euhedral dolomite (Dol). **(J–L)** photomicrographs of intraclastic grainstone showing silica cement (Sil), recrystallization (Rec), carbonate intraclasts (clast) and blocky calcite cement (Bcc). CPL: Cross-polarized light; PPL Plane-polarized light). Sample code at the upper right corner.

Figure 20. Paragenesis of main diagenetic events and relative importance on carbonates of the Bambuí Group at the Januária High.

Figure 21. (A) Geological map of the São Francisco Basin (east-central Brazil) with location of stratigraphic sections. (modified from Caetano-Filho et al., 2019) **(B)** Paleogeographic reconstruction of the late Neoproterozoic West Gondwana (modified from Alkmim et al. 2006).

Figure 22. Lithostratigraphic chart of the 1st-order Bambuí Sequence and chemostratigraphic evolution in the São Francisco Basin (modified from Caetano-Filho et al. 2019). *Cloudina* sp. index fossil defines a late Ediacaran age (lower Sete Lagoas Formation – Warren et al., 2014). Maximum depositional ages are represented by the yellow stars (Macaúbas Group – Babinski et al. 2012; upper Sete Lagoas Formation – Paula-Santos et al. 2015), depositional age of volcaniclastic layer is represented by the red star (upper Serra da Saudade Formation - Moreira et al. 2020). Chemostratigraphic Intervals (CI) from Paula-Santos et al., (2017).

Figure 23. Arcos section − integrated sequence stratigraphy and chemostratigraphy of $\delta^{13}C$ and Sr/Ca presented by Caetano-Filho et al., (2019), and new $^{87}Sr/^{86}Sr$ ratios. TST – Transgressive System Tract; MFS – Maximum Flooding Surface; EHST – Early Highstand System Tract; LHST – Late Highstand System Tract; SB1 – Sequence Boundary. Red dots represent $^{87}Sr/^{86}Sr$ ratios presented previously by Kuchenbecker et al., (2016a).

Figure 24. Januária section − integrated sequence stratigraphy and chemostratigraphy of $\delta^{13}C$ values and Sr/Ca presented by Caetano-Filho et al., (2019), and new $^{87}Sr/^{86}Sr$ ratios.

TST – Transgressive System Tract; MFS – Maximum Flooding Surface; EHST – Early Highstand System Tract; LHST – Late Highstand System Tract; SB1 – Sequence Boundary.

Figure 25. Santa Maria da Vitória section − integrated sequence stratigraphy and chemostratigraphy of $\delta^{13}C$ values and Sr/Ca presented by Caetano-Filho et al., (2019), and new $^{87}Sr/^{86}Sr$ ratios. TST – Transgressive System Tract; MFS – Maximum Flooding Surface; EHST – Early Highstand System Tract; LHST – Late Highstand System Tract; SB1 – Sequence Boundary.

Figure 26. Cross-plot diagrams of $^{87}Sr/^{86}Sr$ ratios *vs*. geochemical ratios of Rb/Sr, Fe/Sr, Mn/Sr, Mg/Ca and Sr contents for the systems tracts (TST, EHST, LHST and 2^{nd}-S) of the basal Bambuí Sequence. Primary $^{87}Sr/^{86}Sr$ ratios are inside the grey square.

Figure 27. Stratigraphic–chemostratigraphic correlations for the basal Bambuí Sequence between Arcos, Januária and Santa Maria da Vitória sections. $\delta^{13}C$ and Sr/Ca data presented by Caetano-Filho et al., (2019). TST: Transgressive System Tract; MFS: Maximum Flooding Surface; EHST: Early Highstand System Tract; LHST: Late Highstand System Tract; SB1: Sequence Boundary.

Figure 28. Sketch illustrating the Bambuí basin and the adjoining orogens at ca. 550 Ma (modified from Kuchenbecker et al., 2020). EHST: connected basin with high relative sea-level associated to overall subsidence; LHST: restricted basin with low relative sea-level associated to flexural subsidence and uplift of marginal orogens.

Figure 29. (**A**) Geologic map of the São Francisco craton in east Brazil and locations of the stratigraphic sections in the São Francisco basin (**B**) paleogeographic reconstruction of the late Neoproterozoic West Gondwana (modified from Alkmim et al., 2006).

Figure 30. Lithostratigraphic chart of the Bambuí 1st-order sequence and chemostratigraphic evolution (modified from Caetano-Filho et al. 2019). Index fossil of *Cloudina* sp. defines a late Ediacaran age (lower Sete Lagoas Formation; Warren et al., 2014). Maximum depositional age is represented by the yellow star (upper Sete Lagoas Formation – Paula-Santos et al., 2015), depositional age of volcaniclastic layer is represented by the red star (upper Serra da Saudade Formation; Moreira et al., 2020). Index ichnofossil *Treptichnus Pedum* in the Tres Marias Formation define the Ediacaran-Cambrian transition within the Bambuí Group (Sanchez et al., 2021). Chemostratigraphic Intervals (CI) are from Paula-Santos et al. (2017).

Figure 31. Januária section showing integrated sequence and chemostratigraphy of $\delta^{13}C$ values and Sr/Ca presented by Caetano-Filho et al. (2019), and TOC values from Caetano-Filho et al. (2021), Mo/TOC ratios, Al contents and enrichment factors of trace-metal (modified from Caetano-Filho et al. 2019). Red dotted lines represent EF = 1. TST – Transgressive System Tract; MFS – Maximum Flooding Surface; EHST – Early Highstand System Tract; LHST – Late Highstand System Tract; SB1 – Sequence Boundary; 2nd-S – Upper Second Order Sequence.

Figure 32. Arcos section showing integrated sequence and chemostratigraphy of $\delta^{13}C$ values and Sr/Ca presented by Caetano-Filho et al. (2019), and TOC values from Caetano-Filho et al. (2021), Mo/TOC ratios, Al contents and enrichment factors of trace-metal (modified from Caetano-Filho et al. 2019). Red dotted lines represent EF = 1. TST – Transgressive System Tract; MFS – Maximum Flooding Surface; EHST – Early Highstand System Tract; LHST – Late Highstand System Tract; SB1 – Sequence Boundary; 2nd-S – Upper Second Order Sequence.

Figure 33. Well 1 section showing integrated sequence and chemostratigraphy of $\delta^{13}C$ values and Sr/Ca presented by Caetano-Filho et al. (2019), and TOC values from

Caetano-Filho et al. (2021), Mo/TOC ratios, Al contents and enrichment factors of trace-metal (modified from Caetano-Filho et al. 2019). Red dotted lines represent EF = 1. TST – Transgressive System Tract; MFS – Maximum Flooding Surface; EHST – Early Highstand System Tract; LHST – Late Highstand System Tract; SB1 – Sequence Boundary; 2^{nd}-S – Upper Second Order Sequence.

Figure 34. Cross-plot diagrams of trace metals contents *vs*. Al concentrations of samples from the Arcos, Well 1, and Januária sections. PAAS values from Taylor and McLennan (1985) are plotted for comparison. Red dotted line indicates a cut-off value of [Al] < 5% for less or not affected rock samples by detrital contamination.

Figure 35. Trace-metals patterns of the basal Bambuí 2^{nd}-order sequence. (**A**) Mo-EF versus U-EF. The diagonal lines represent the aqueous Mo/U ratio of the present-day seawater (SW) that ranges between ~7.5 and 7.9 (1×SW), and fractions thereof (0.3×SW and 0.1×SW as proposed by Algeo and Tribovillard (2009). (**B**) Mo versus TOC contents. (**C**) Cd/Mo ratios versus TOC content. TST – Transgressive System Tract; MFS – Maximum Flooding Surface; EHST – Early Highstand System Tract; LHST – Late Highstand System Tract; SB1 – Sequence Boundary; 2^{nd}-S – Upper Second Order Sequence.

Figure 36. Models of influences on trace-metal accumulation in different stages of the basal Bambuí 2^{nd}-order sequence in a context of a silled basin. (**A**) suboxic-anoxic basin dominated by benthic redox controls, connected with open ocean and deepwater renewal by upwelling and continuous resupply of trace metals; (**B**) anoxic basin with weak restricted circulation dominated by Mn-particulate shuttles, (**C**) anoxic-euxinic basin with limited resupply of trace metals dominated by hydrographic control and (**D**) anoxic basin with weak restricted circulation dominated by Mn-particulate shuttles.

Table List

1 CHAPTER 1 – INTRODUCTION

The marine sedimentary rocks of the Bambuí Group cover a large part of the São Francisco Craton and record a foreland basin cycle in the interior of West Gondwana. This sedimentary unit is the most widespread in the São Francisco Basin in east Brazil, and has been the target of many stratigraphic studies by geologist for more than half a century since the last seven decades. Moreover, the recent discoveries and deepening of sedimentological, geochemical and geochronological research on the Bambuí Group have allowed a significant advance in understanding the tectonic and geologic evolution of marine environments during the late Neoproterozoic and early Paleozoic (i. e., Warren et al., 2014; Reis and Suss, 2016, Reis et al., 2017; Paula-Santos et al., 2015, 2017, 2018, 2020; Kuchenbecker et al., 2016, 2020; Perrella et al., 2017; Uhlein et al., 2019; Hippertt et al., 2019, Caetano-Filho et al., 2019, 2020; Cui et al., 2020).

The Bambuí Group is defined as an unconformity-bounded 1st-order sequence, which encompasses four retrogradational-progradational 2nd-order sequences (e.g. Martins and Lemos, 2007; Reis and Suss, 2016; Uhlein et al., 2019; Caetano-Filho et al., 2019). The focus of this work is the two basal 2nd-order sequences, which comprise the Carrancas, Sete Lagoas, Serra de Santa Helena and Lagoa do Jacaré formations, integrating with the previous contributions by Caetano-Filho et al. (2019) that present a basin-scale sequence stratigraphy framework coupled to $\delta^{13}C$ and Sr/Ca chemostratigraphy, and associated with marine connection and restriction stages of the São Francisco Basin described by Paula-Santos et al. (2017). The upper 2nd-order sequences, represented by Serra de Saudade (including the Jaiba Member) and Três Marias formations, were not studied in this work; however, recent studies on these units provide important data that updates the geological knowledge of the Bambuí Group (i.e, Moreira et al., 2020, Sanchez et al., 2020, Uhlein et al., 2021).

At the base, the Sete Lagoas Formation is the most studied stratigraphic unit of the Bambuí Group, composed of limestones which have typical structures of cap carbonates (aragonite pseudomorphs and negative $\delta^{13}C$ values, and locally, thin and pale cap dolostones), overlying glacigenic rocks of the Jequitaí and Carrancas formations, this

place the Bambuí Group as a possible record of a wide glaciation that occurred during the late Neoproterozoic, as proposed in several hypotheses, (e.g., Snowball Earth, Kirschvinck, 1992; Hoffman et al., 1998; Hoffman and Schrag, 2002). Some authors based on Pb-Pb dating (i.e., Babinski et al., 2007), and C and Ca isotope chemoestratigraphy (Vieira et al., 2007a and Silva-Tamayo, 2010; respectively) interpreted the Sete Lagoas cap carbonate as post-Sturtian, whereas Caxito et al. (2012, 2018) and Alvarenga et al. (2014), using Pb isotopes, Sr-chemostratigraphy, and distintive cap dolostone with decreasing-upwards $\delta^{13}C$, interpreted it as a post-Marinoan succession. Based on U–Pb ages of detrital zircon grains, Rodrigues (2008) and Pimentel et al. (2011) report a maximum depositional age of 610 Ma for the upper portion of the Sete Lagoas Formation.

However, Warren et al. (2014) and Perrella et al. (2017) described the *Cloudina* fossil index at the middle part of the Sete Lagoas Formation, above the cap carbonate, indicating an age for deposition between 550 and 542 Ma (i.e, Grotzinger et al., 2000) for this interval, and revealing a late Ediacaran age for the basal sequence of the Bambuí Group. Moreover, the presence of detrital zircons with ages of c. 550 Ma (e.g. Paula-Santos et al., 2015; Kuchenbecker et al., 2020) in the Sete Lagoas Formation converge towards a late Ediacaran-early Cambrian age for the deposition of the Bambuí Group. This is reinforced by U-Pb dating of zircons from a tuff layer within Serra da Saudade Formation, which yields an age of 520 ±5 Ma (Moreira et al., 2020), and the recent discovery of icnofossils of the *Treptichnus Pedum* in the Três Marias Formation confirm this interpretation (Sanchez et al., 2020). These new data placed the Bambuí Group in a different context from the Neoproterozoic glaciations, just at the Ediacaran-Cambrian transition. However, fossil record remains poor and the depositional age needs to be better constrained.

In terms of paleogeographic reconstruction, part of the Bambuí foreland basin system has evolved within a restrict environment with intermittent periods of marine connection with contemporary seas at the late Ediacaran and early Cambrian (Paula-Santos et al., 2017; Kuchenbecker et al., 2020; Uhlein et al., 2019; Hippertt et al., 2019; Caetano-Filho et al., 2019, 2020), which may have allowed the occurrence of

cosmopolitan organisms (e.g., *Cloudina* sp.) in a epicontinental seaway (Warren et al., 2014; Perrella et al., 2017). Moreover, confinement of the São Francisco Basin in the inner areas of West Gondwana due the uplift of marginal Neoproterozoic orogenic belts, trigger the basin marine isolation and major paleoenvironmental changes of seawater (Paula-Santos et al., 2017, 2018; Uhlein et al., 2019; Hippertt et al., 2019; Caetano-Filho et al. 2019, 2020). The Bambuí Group rocks present isotope and geochemical signatures that deviate from the Ediacaran-Cambrian ocean reservoir, such as variable low radiogenic $^{87}Sr/^{86}Sr$ ratios, high Sr contents, extremely positive $\delta^{13}C$ values and atypical REY seawater signatures, interpreted as deposition in restricted anoxic marine conditions and inefficient seawater circulation (Paula-Santos et al., 2017, 2018; Uhlein et al., 2019; Hippertt et al., 2019; Caetano-Filho et al., 2019). High Sr contents in carbonates suggest an increase in alkalinity of seawater during the late Ediacaran and early Cambrian, possibly driven the appearance of the first biomineralizing organisms (Paula-Santos et al., 2020).

A plate tectonic scenario in the inner part of West Gondwana with high continental weathering rates has been proposed to explain the ocurrences of intervals with low radiogenic $^{87}Sr/^{86}Sr$ ratios and high Sr concentrations in the Bambuí paleomarine system, in combination with sea-level changes that might lead to high continental Sr input and low radiogenic discharge (Paula-Santos et al., 2017). Such results imply that Sr isotopes in ancient epicontinental basins are sensitive to past changes in continental weathering, runoff and mountain erosion, and sea level changes, and thus can potentially be used to infer local paleogeographic evolution and past changes in hydrological budgets. However, the marine restriction scenario has important implications for the use of strontium isotope stratigraphy on the Bambuí Group, making unfeasible a global stratigraphic correlation (Paula-Santos et al., 2017).

Moreover, sedimentation of the Bambuí Group in the interior of the West Gondwana may have represented a significant source of massive inputs of methane to the atmosphere, potentially affecting both global carbon cycle and climate (Caetano-Filho et al., 2021). This peculiar sedimentary basin presents an interesting window to the study of ancient isolated marine environments in contrast to open marine settings (i.e., Hippertt

et al., 2019), and to understanding of the Ediacaran and Cambrian marine environments linked to major continental and oceanic reconfigurations, orogenic processes, strong climatic oscillations and a profound ecological transition in marine ecosystems (i. e., Kaufman and Knoll, 1995; Knoll et al., 2004, 2006; Canfield et al., 2007; Hoffman et al., 1998; Hoffman and Schrag, 2002; Campbell and Squire., 2010, Young et al., 2013).

This work provides new aspects on the isotope and chemical evolution of the sedimentary rocks from the basal Bambuí Group based on petrographic studies and high resolution strontium isotope stratigraphy and trace-metal geochemistry that potentially can record such paleoenvironmental changes in West Gondwana. Identifying the controls on Sr isotope composition and trace metals enrichment patterns can be essential to understanding the biochemical characteristics of this epicontinental basin at the late Ediacaran and early Cambrian, and understanding how they may have affected the radiation of life in this time interval. The aim of this thesis is to understand the characteristics of the redox paleoenvironment conditions and meaning of Sr isotopes in the context of a foreland basin in West Gondwana. This occurrs through the analysis of previously chemostratigraphic data and the acquisition of new results, associated with petrographic analysis on the understanding of the diagenetic history of carbonates from the basal Bambuí Group.

1.1 Objectives

Uncertainties related to the paleogeographic and sedimentary evolution of the Bambuí Group, together with the Ediacaran-Cambrian tectonic and climatic events recorded in the São Francisco basin, east Brazil, can be better explored through the systematic study of the strontium isotope stratigraphy and trace metal geochemistry. This study addresses the isotopic and chemical evolution and the history of main diagenetic events recorded in the basal sedimentary rocks of the Bambuí Group.

Main objective

- The main goal of this research is to define the stratigraphic variation of the strontium isotope composition and trace-metal enrichment patterns of sedimentary rocks from the basal Bambuí Group to investigate major paleoenvironmental changes recorded in the São Francisco Basin and to track the chemical evolution of epicontinental seawater during the Ediacaran–Cambrian transition in West Gondwana.

Specific objectives

- Explore the main diagenetic processes and paragenesis of the Bambuí Group based on detailed petrography of carbonates.
- Apply high resolution strontium isotope stratigraphy at the basal 2nd-order sequence, and use it as a regional stratigraphic correlation tool and interpret the meaning of the isotopic and geochemical record taking into account the foreland basin context and episodes of connection and restriction in relation to the ocean reservoir.
- Determine paleoenvironmental conditions of seawater, redox state evolution, productivity/preservation of organic matter and the degree of hydrographic restriction in the marine basin through detailed trace metal geochemistry.

1.2 Dissertation outline

Data and results obtained during this investigation are presented in three chapters (chapters 4 to 6). Before presenting these chapters, geological context and fundamentals are presented in chapter 2 and 3, respectively. Chapter 4 presents a detailed petrographic study and diagenetic history on the basal Bambuí Group, integrated with stratigraphic framework and sedimentary facies in two stratigrahic sections at the Januária High.

Chapter 5 presents the manuscrpt entitled “Tectonically-induced strontium isotope changes in ancient restricted seas: The case of the Ediacaran-Cambrian Bambuí foreland basin system, east Brazil” published in *Gondwana Research*. This chapter presents a basin-scale high-resolution Sr isotope stratigraphy for the basal Bambuí Group, regarding on the spatial and temporal variations of the $^{87}Sr/^{86}Sr$ ratios and exploring the controls over the Sr isotope system in intracontinental marine environments. Anomalies in the strontium isotope record are recorded in the basal sequences and suggest that tectonics might have played an important role on seawater chemistry at the Neoproterozoic-Paleozoic transition.

Chapther 6 presents the manuscript entitle “Paleoenvironmental redox evolution of a late Ediacaran–early Cambrian restricted sea: Insights from trace–metal enrichment patterns of carbonates of the basal Bambuí Group, east Brazil” currently being prepared for submission in peer-rewiewed scientific journals. This chapther presents an integrated study of trace-metal geochemistry and stratigraphy of the basal Bambuí Group, and provides evidence for the chemical evolution of basinal deep-waters, whose conditions changed progressively from suboxic-anoxic to anoxic-euxinic. Finally, Chapther 7 summarises results and main discussions developed through chapters 4 to 6, integrating the main conclussions of the research and sugestions of future works.

2 CHAPTER 2 – GEOLOGICAL CONTEXT

The study area of this work corresponds to the São Francisco Basin which occupies a large NS–trending portion of central-east Brazil (Fig. 1A), comprises between 200 and 350 km wide and 800 km long, and covers an area of approximately 300,000 Km^2 across the states of Minas Gerais, Bahia, Goiás and Tocantins (Fig. 1B). This basin presents three major structural domains defined by gravimetric and seismic data: i) the Sete Lagoas and ii) Januária highs, which represent basement expositions at the southern and northern portions, respectively; and iii) the Pirapora Aulacogen in central part of the basin, which exhibits sedimentary record thickness of several kilometers and a typical steer-head geometry (Fig. 1C). Four local study areas on the São Francisco Basin were selected for this work based on previous research, corresponding to Arcos and Pompeú (Well 1) areas on the Sete Lagoas High, and Januária and Santa Maria da Vitória areas on the Januária High (Fig. 1B).

Arcos and Well 1 sections correspond to two drill cores on the Sete Lagoas High, previously studied by Kuchenbecker et al. (2016a) and Reis and Suss (2016), respectively; which provides core samples for isotope and geochemical analyses. On the other hand, Januária and Santa Maria da Vitória sections are composed sections, described and sampled in a fieldwork campaign carried out between January 30th and February 12th in 2017 at Januária and Santa Maria da Vitoria regions (north of Minas Gerais and south of Bahia states, respectively). These sections were constructed and analyzed based on sequence stratigraphy method, $\delta^{13}C$ profiles, and available geological maps by Caetano-Filho et al. (2019).

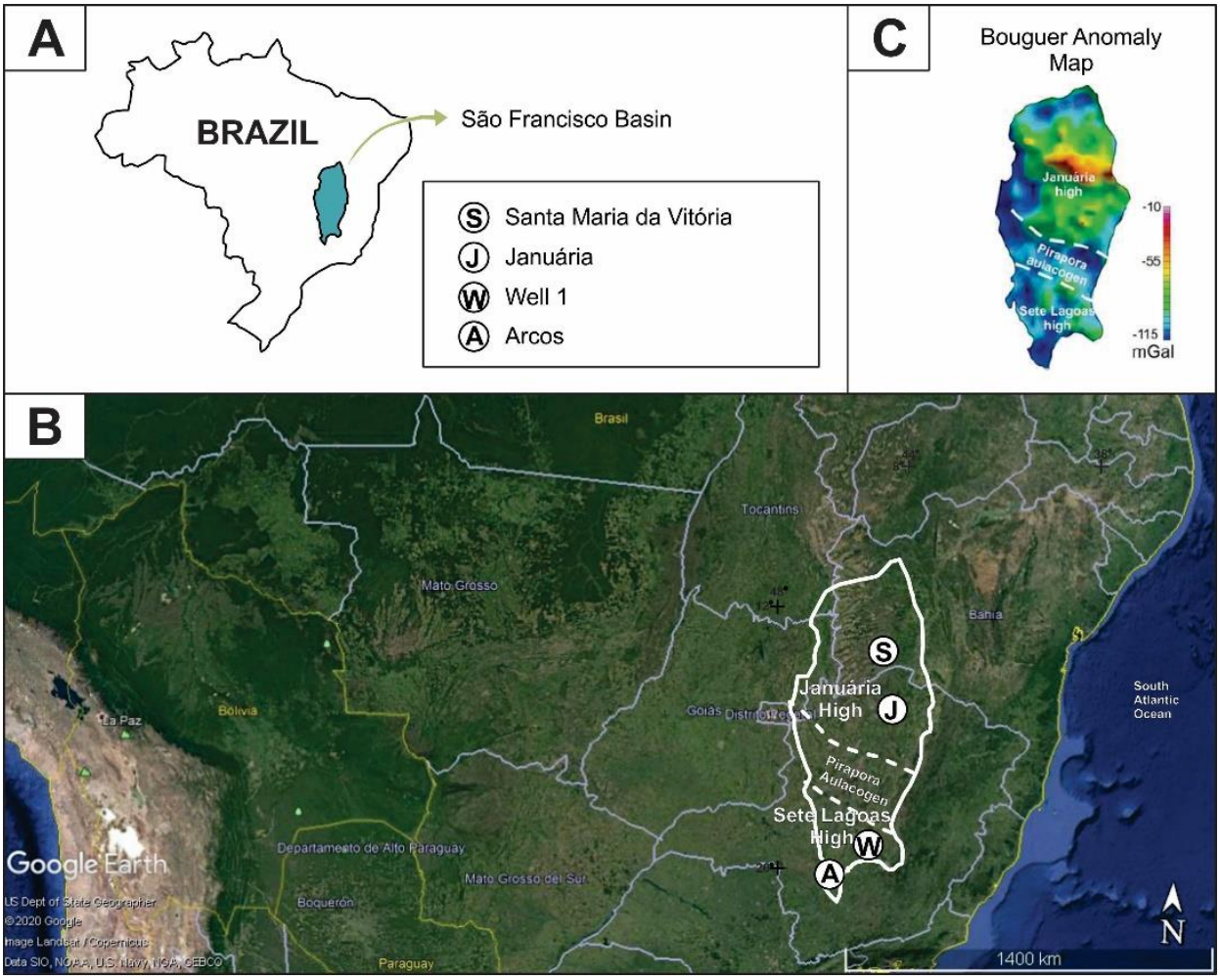

Figure 1. (A) Location map of the São Francisco Basin in east-central Brazil. **(B)** Location of the study areas represented by white circles on the basin. **(C)** Bouguer anomaly map of the São Francisco Basin (modified from Reis et al., 2017a).

2.1 The São Francisco Craton in West Gondwana

The Precambrian nucleus of the South America consists essentially of Archean and Paleoproterozoic cratons with additions of Meso- and Neoproterozoic juvenile orogenic belts (Fig. 2). The Amazon craton together with the São Francisco, Paranapanema and Rio de la Plata cratons correspond to the internal portions of the plates involved in the assembly of West Gondwana at the Neoproterozoic in the Pan–African/Brasiliano orogeny, encompassing the margin of major plates and intervening accretionary material

(Chemale et al., 1993; Alkmim et al., 1996; Brito Neves et al., 1999; Almeida et al., 2000; Teixeira et al., 2000; Alkmim et al., 2001; Alkmim and Martins-Neto, 2012).

The São Francisco Craton forms a coherent NS-trending block in the eastern portion of Brazil (Fig. 2A), and it consists of an Archean nucleus and two amalgamated Paleoproterozoic segments related to rift, passive and foreland basins associated to the Rhyacian orogeny (Alkmim and Marshak, 1998; Teixeira et al., 2000). These assemblages include Archean TTG-complexes (migmatites and gneisses), granitic plutons, greenstone belt successions, and metasedimentary rocks (Teixeira et al., 2000).

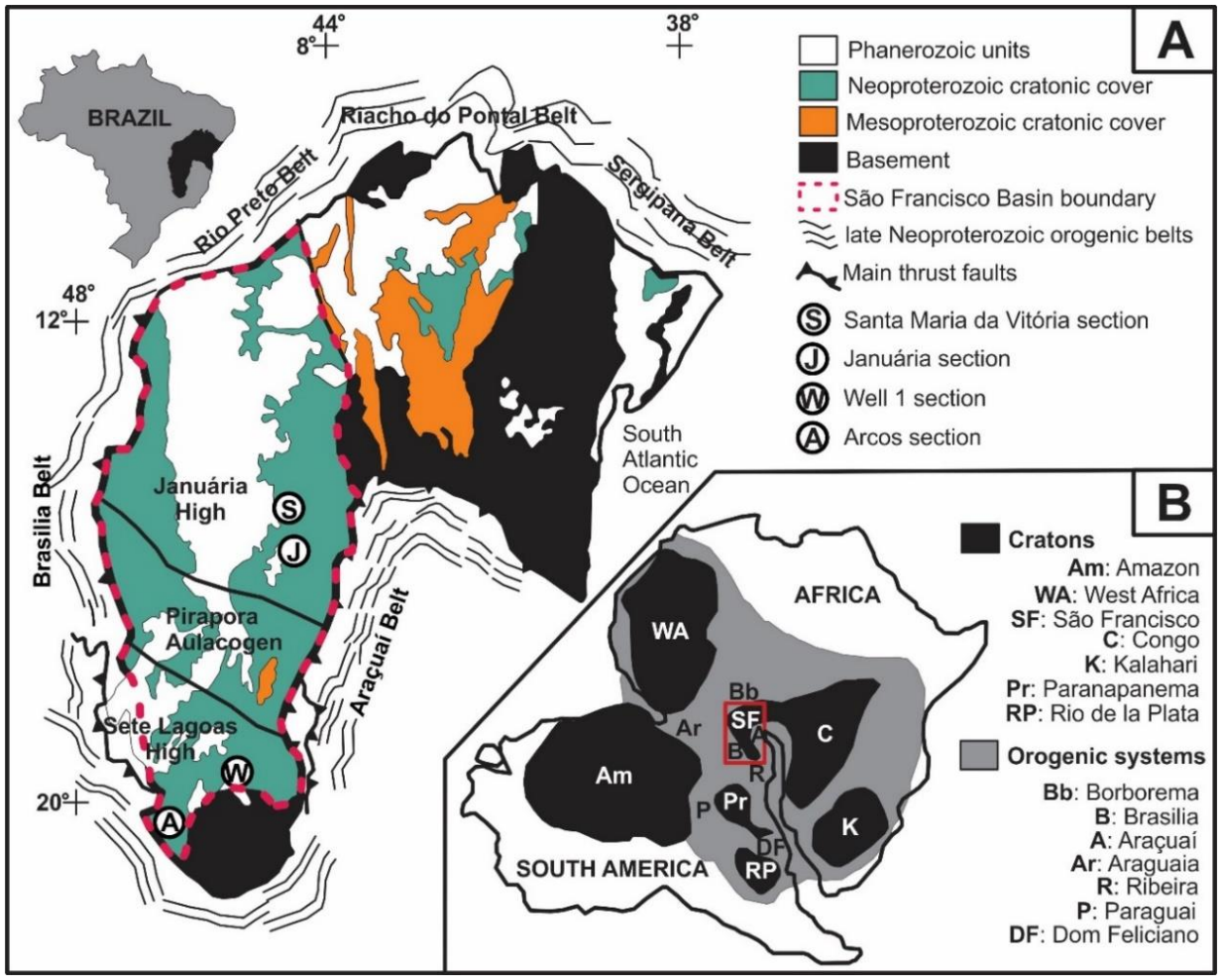

Figure 2. (A) geological map of the São Francisco Craton in east-central Brazil. **(B)** paleogeographic reconstruction of the late Neoproterozoic West Gondwana (Modified from Caetano–Filho et al., 2019).

The sedimentary units that cover the São Francisco Craton occur in two tectonic domains, the São Francisco Basin and the Paramirim Aulacogen, recording plate reorganizations and climatic oscillations that affected the craton and its margins from the late Paleoproterozoic to the Cretaceous (Martins-Neto et al., 2009; Alkmim and Martins-Neto, 2012; Reis et al., 2016). The Brasiliano orogenic systems that surround the São Francisco Craton are the Brasília at west, Araçuaí at the east, and Rio Preto, Riacho do Pontal and Sergipano belts at the northern part (Fig. 2A). These Neoproterozoic orogenic belts present thrust faults and folds with differentiated tectonic characteristics at the cratonic margins (Alkmim et al., 1996; Alkmim and Martins-Neto, 2001; Coelho et al., 2008).

The African counterpart of the São Francisco Craton (the Congo Craton) stretches over a wide area in the eastern part of central Africa (Fig. 2B). The basement consists of a large Archaean-Paleoproterozoic nucleus delimited by the Neoproterozoic Pan-African orogenic belts (Alkmim and Martins-Neto, 2012). The São Francisco-Congo cratons and several fragments derived from Rodinia began to converge at the end of the Cryogenian and their reassembly resulted in the formation of the supercontinent Gondwana during the late Ediacaran. In this process, plate margins were diacronically converted into fold-thrust belts by the Pan-African/Brasiliano orogenic event, affecting the interior of the São Francisco Craton, which behaved as a foreland marine basin, thus receiving mixed carbonate-siliciclastic sediments of the Bambuí Group (Alkmim et al., 1996; Alkmim and Marshak, 1998; Alkmim and Martins-Neto, 2012; Reis and Suss, 2016; Reis et al., 2016). Stratigraphic correlation between the Neoproterozoic sequences on West Gondwana cratons, as well as on the marginal orogenic belts are essential in the understanding of the tectonic scenario of the Bambuí Group and its depositional paleoenvironment.

2.2 The São Francisco Basin

Three first-order sequences compose the tectono-sedimentary record of the São Francisco Basin, correlated with neighboring orogens: i) The Mesoproterozoic to Early Neoproterozoic Paranoá-Upper Espinhaço sequence; ii) the Neoproterozoic Macaúbas

sequence; and iii) the Ediacaran-Cambrian Bambuí sequence (Martins-Neto 2009; Reis and Suss, 2016; Reis et al., 2016 – Fig. 3). These successions are locally deformed and uncomfortably overlain by discontinuous Phanerozoic strata (Reis et al., 2016).

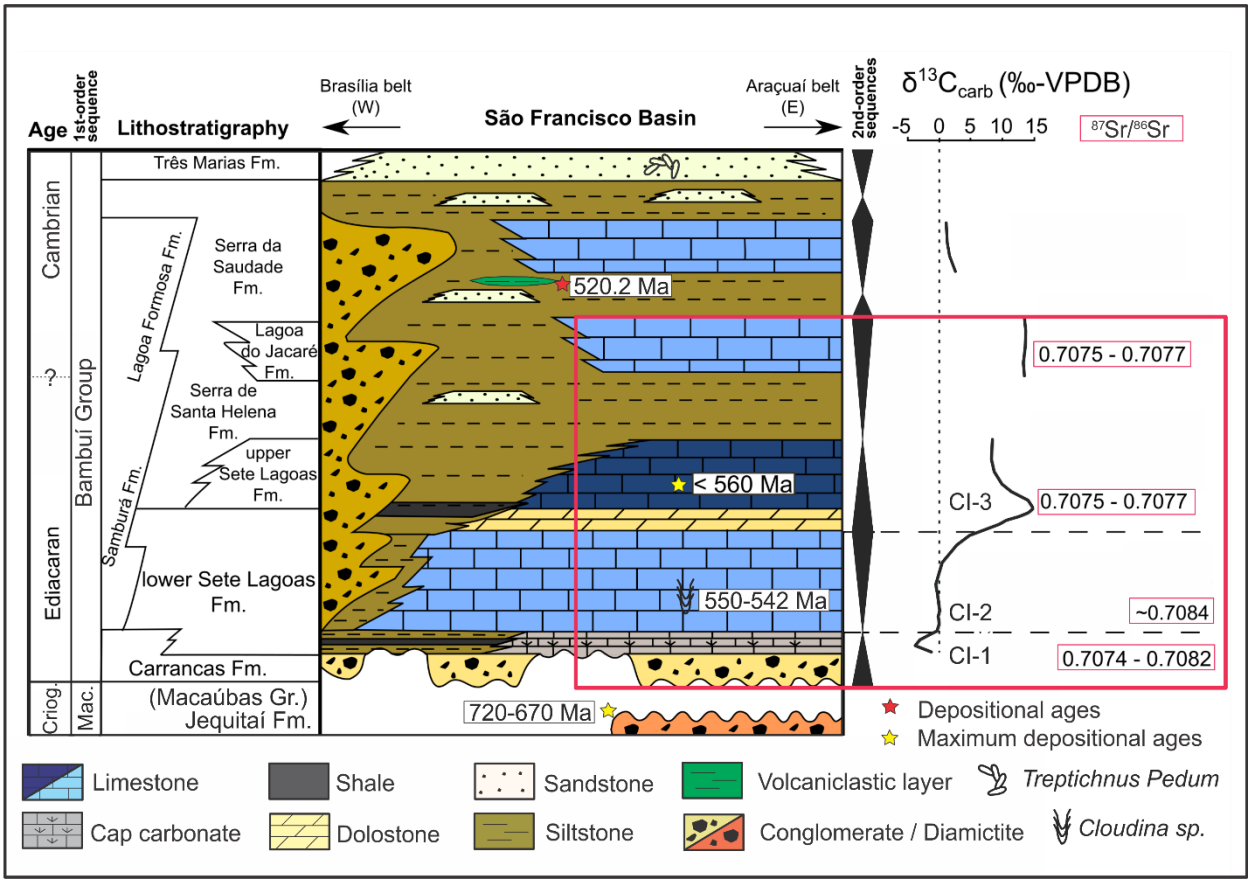

Figure 3. Lithostratigraphic chart of the 1st–order sequence Bambuí Group and chemostratigraphic evolution in the São Francisco Basin (Modified from Caetano–Filho et al., 2019). Maximum depositional ages obtained by U–Pb geochronology in detrital zircon grains are represented by yellow stars (Macaúbas Gr. – Castro et al., 2020; upper Sete Lagoas Formation – Paula–Santos et al., 2015). Depositional ages obtained by U–Pb geochronology in zircons from tuff layer are represented by the red star (upper Serra da Saudade Formation – Moreira et al., 2020); *Cloudina* sp. occurrence in the lower Sete Lagoas Fm. is from Warren et al. (2014) and *Treptichnus Pedum* record in the Três Marias Fm. is from Sanchez et al. (2021).

The Mesoproterozoic to Early Neoproterozoic Paranoá-Upper Espinhaço sequence represents a rift-sag basin-fill succession, which is laterally associated with deposits of a rift-passive margin basin, developed along the western boundary of the São Francisco Craton, composed of a siliciclastic-dominated package that grades upward into marine to transitional pelites, sandstones and carbonates; exposed in relatively small

areas of the basin (Chemale et al. 2012; Guadagnin and Chemale, 2015; Reis et al., 2016). The correlatives of the Paranoá–Upper Espinhaço sequence in the Brasília metamorphic belt are the marine packages of the Paranoá and Canastra groups, which consist of passive margin fine to coarse-grained siliciclastics, organic matter-rich shales, and carbonates with cyanobacteria mats and columnar stromatolites (Dardenne, 1978, 1981, 2000; Martins-Neto, 2009, Reis et al., 2016). Provenance studies carried out on these rocks indicated a sedimentary supply mainly derived from the cratonic area, with important Archean and Paleoproterozoic sources (Valeriano et al., 2004a, b; Pimentel et al., 2001; Rodrigues et al., 2012). The available U–Pb ages on detrital zircons younger than ca. 1.3 Ga extracted from Paranoá–Upper Espinhaço sequence in the São Francisco Basin indicate a time span between ca 1.3 and 0.9 Ga for its deposition (Chemale et al. 2012; Lopes, 2012; Alvarenga et al., 2012; Kuchenbecker et al., 2014, 2015; Reis et al., 2014, 2016).

The Neoproterozoic Macaúbas Sequence records rift to passive margin sedimentary successions during the rupture of the supercontinent Rodinia, comprising transitional to shallow marine deposits associated to magmatic events about 850 Ma, documented along the central–western portion of the São Francisco Basin and eastern Araçuaí Belt (Almeida et al., 1976; Almeida, 1977; Dardenne, 1978; Uhlein et al., 1999; Pedrosa-Soares et al., 2008, 2011; Silva et al., 2008; Danderfer et al., 2009; Martins-Neto et al., 2009, Alkmim and Martins-Neto, 2012; Reis and Suss, 2016; Reis et al., 2016).

The record of glacial sedimentation in the precursor basin of the Araçuaí Belt is represented by the Macaúbas Group, which includes pre–glacial, glaciogenic and post–glacial sucessions (Pedrosa-Soares et al., 2011). The Serra do Catuni Formation (glaciogenic unit of the Macaúbas Group) seems to be a proximal glacio–marine equivalent of the Jequitaí glacio–terrestial deposits, exposed along the rims of regional–scale anticlines in the eastern portion of São Francisco Basin (Isotta et al., 1969; Viveiros and Walde, 1976; Uhlein et al., 1999). The Jequitaí Formation comprises around 300 m–thick strata of massive polimyctic diamictites, matrix–supported conglomerates, massive sandstones, fine rhythms and subordinated pelites deposited inside the São Francisco Craton in a glacial marine–continental environment, corresponding to

ice–proximal till, alluvial–fan, lacustrine and proglacial fluvial deposits (Dardenne, 1978; Rocha-Campos et al., 1981; Uhlein et al., 1999, 2004; Karfunkel and Hoppe, 1988; Hercos, 2008; Martins-Neto and Hercos, 2002). The Jequitaí Formation is traditionally interpreted as the intracratonic condensed section of rift–passive margin successions accumulated along the margins of the São Francisco plate (e.g. Uhlein et al., 2004), probably during a global–scale glacial event in the Cryogenian Period (Babinski et al., 2007, 2012). A maximum depositional age of 880 Ma have been proposed based on the youngest detrital zircon found in the Jequitaí diamictites (Rodrigues, 2008). Moreover, U–Pb ages between 720 Ma and 670 Ma, and negative Lu-Hf signatures from detrital zircon grains of the Chapada Acauã Formation (a distal glaciomarine unit of the Macaúbas Group) indicate sediment sources from the Early Cryogenian anorogenic magmatic rocks found in Araçuaí–West Congo Orogen and adjacent Congo–São Francisco Craton, and suggest correlation with the Sturtian global glaciation (Fig. 3 – Castro et al., 2020).

The Macaúbas Sequence can be correlative to the Vazante Group (Alkmim and Martins-Neto, 2012), which is exposed close to the western boundary of the basin and comprises a ca. 5 km–thick succession dominated by marine carbonates and fine–grained siliciclastics, locally interbedded with conglomerates sandstones, diamictites and phosphorite deposits (Dardenne, 2000; Azmy et al., 2008; Martins-Neto, 2009; Reis et al., 2016). The Vazante Group is interpreted as a passive margin basin–fill succession, later converted into an active margin setting (Dardenne 2000; Pimentel et al., 2011); fed mainly by Archean and Paleoproterozoic cratonic sources (Pimentel et al., 2011; Rodrigues et al., 2012).

In the Araçuaí belt, the Macaúbas 1st–order sequence is represented by the glacial to post–glacial metasedimentary successions of the Macaúbas Group (Karfunkel and Hoppe, 1988; Uhlein et al., 1999; Martins-Neto, et al. 2001; Martins-Neto and Hercos, 2002; Martins-Neto 2009; Pedrosa-Soares et al., 2007, 2011; Babinski et al., 2012; Castro et al., 2019, 2020). In this tectonic domain, the Macaúbas Sequence is composed of sandstones, diamictites, carbonates, basic volcanic rocks, iron formations and metamorphosed green shale to amphibolite facies, representing pre–rift, rift, transitional and passive margin phases of the tectonic evolution of a Red Sea–type basin (Uhlein et

al., 1999; Martins-Neto et al., 2001; Pedrosa-Soares et al., 2001, 2008, 2011; Alkmim and Martins-Neto, 2012). These successions record a Cryogenian–Ediacaran rift–passive margin basin developed in the São Francisco–Congo paleocontinent, and the closure of this confined basin during the Brasiliano/Pan–African event led to the development of Araçuaí–West Congo orogen around 570 Ma (Pedrosa–Soares et al., 2001; Alkmim et al., 2006; Castro et al. 2019).

The Macaúbas sequence is correlative of the rift–related successions of the Santo Onofre Group in the western Paramirim Aulacogen (Schobbenhaus, 1996; Danderfer et al., 2009) and the diamictite–bearing Canabravinha Formation exposed in the Rio Preto belt along the northern margin of the craton (Schobbenhaus, 1996; Caxito et al., 2014; Reis et al., 2016). According to U–Pb data of the youngest detrital zircons from the Chapada Acauã Formation of the Macaúbas Group, the maximum depositional age is defined at ca. 667 Ma (Castro et al., 2020). The entire Macaúbas Group must be older than the regional metamorphism dated at ~580 Ma (Pedrosa-Soares et al., 2001; Silva et al., 2006).

2.3 The Ediacaran–Cambrian Bambuí Group

Covering the largest area of the São Francisco Basin, the Bambuí 1st–order sequence (i.e., the Bambuí Group – Fig. 3) comprises a package of carbonates, pelites, sandstones and subordinated conglomerates (Alkmim and Martins-Neto, 2001, 2012; Martins-Neto et al., 2001; Martins-Neto, 2005, 2009; Alkmim et al., 2011; Reis and Suss, 2016; Reis et al., 2016, Uhlein et al., 2017). The sequence is interpreted as the record of an Ediacaran foreland marine basin generated in the São Francisco Craton in response to lithospheric overburden caused by the uplift of the Neoproterozoic orogenic belts (Barbosa et al., 1970; Chang et al., 1988; Alkmim and Martins-Neto, 2001; Alkmim et al., 2011; Reis and Suss, 2016), especially the thrust and crustal pressure of Brasília orogen along the west part of the craton (Fig. 2), as product of arc–continent and continent–continent collision between 800 and 550 Ma (Pimentel et al., 1999). On seismic

sections, the Bambuí sequence displays a typical wedge–shaped geometry, whose thickness varies from ~800 m on the east (near the flexural border), to ca. 3000 m in the presumed foredeep area (depocenter) on the west (Fig. 2 – Reis and Suss, 2016; Reis et al., 2016). Remarkably, the seismic sections also reveal a slight thickening of the lower Bambuí sequence over preexisting large–scale structures (Pirapora Aulacogen), a fact that suggests reactivation of older fabric elements induced by the orogenic overburden along the craton margins (Reis et al., 2016).

The classic lithostratigraphy of the Bambuí Group involves basal diamictites covered by carbonate and siliciclastic rocks (Costa and Branco, 1961; Almeida, 1976; Dardenne, 1978). In this work is considered the Carrancas Formation as the basal sedimentary unit of the Bambuí Group (Vieira et al., 2007; Kuchenbecker et al., 2013, 2016; Reis et al., 2016; Caetano-Filho et al., 2019). The Carrancas Formation comprises diamictites, sandstones, rhythmites, shales and dolostones, sometimes reported in a gradational contact with carbonates of the Sete Lagoas Formation (Reis and Suss, 2016; Kuchenbecker et al., 2016a), and possibly related to glacial environments (Romano, 2007; Rocha-Campos et al., 2011; Kuchenbecker et al., 2013; 2016a; Reis and Suss, 2016; Uhlein et al., 2016). Several stratigraphic units overlie the Carrancas Formation and comprises from base to top: dolostones and limestones with interbedded pelites of the Sete Lagoas Formation; mudstones and siltstones with subordinated limestones of the Serra de Santa Helena Formation; oolitic limestones, siltstones, and marlstones of the Lagoa do Jacaré Formation; siltstones, shales, and limestones of the Serra da Saudade Formation; and sandstones and siltstones of the Três Marias Formation (Fig. 3).

At the eastern border of the São Francisco Basin, other stratigraphic units of limited spatial distribution are recognized in the Bambuí Group. These units correspond to the Jaíba and Gorutuba formations, studied by Chiavegatto et al. (2003) and Uhlein et al. 2020, and Kuchenbecker et al. (2016b), respectively. On the other side, the Samburá and Lagoa Formosa formations on the western portion of the basin, comprise conglomerates and siliciclastic rocks, associated to delta and submarine fan deposits sourced mainly from the orogenic building of the Brasília belt (Castro and Dardenne, 2000; Dardenne, 2003; Baptista, 2004; Fragoso, 2011; Uhlein et al., 2011, 2017), recording foredeep

sedimentation in the western border of the Bambuí foreland system (Fig. 2 – Martins-Neto, 2009; Alkmim et al., 2011; Reis et al., 2017; Uhlein et al., 2017).

2.4 Chemostratigraphy and sequence stratigraphy of the Bambuí Group

In last decades, many works of chemostratigraphy studies have been carried out to investigate the sedimentary evolution of the Bambuí Group and define marine paleoenvironmental conditions in West Gondwana (Iyer et al., 1995; Kawashita, 1998; Misi and Veizer, 1998; Santos et al., 2000, 2004; Misi et al., 2007; Vieira et al., 2007; Babinski et al., 2007; Caxito et al., 2012, 2018; Alvarenga et al., 2014; Warren et al., 2014; Paula-Santos et al., 2015, 2017; Kuchenbecker et al., 2016a; Guacaneme et al., 2017; Perrella et al., 2017; Okubo et al., 2018; Uhlein et al., 2019; Hippertt et al., 2019; Caetano-Filho et al., 2019, 2021). Paleogeographic conditions such as oceanic connection and restriction of the Bambuí Group were interpreted in three different isotope ($\delta^{13}C$–$^{87}Sr/^{86}Sr$) evolution stages defined as Chemostratigraphic Intervals (Fig. 3 – Paula-Santos et al., 2017). Moreover, progresses on sequence stratigraphy coupled to chemostratigraphy were recently made on the basal Bambuí Group in order to correlate the Sete Lagoas and Januária basements highs (Fig. 3 – Caetano-Filho et al., 2019). Based on the recognition of system tracts and stratigraphic surfaces (maximum flooding surface – MFS and sequence boundary – SB1), and high resolution $\delta^{13}C$ data and Sr/Ca ratios, Caetano-Filho et al. (2019) established similar transgressive–regressive stratigraphic patterns in a 2nd–order basin–scale correlation, provided new insights of major paleoenvironmental changes in the basal Bambuí sequence (i.e., Vieira et al., 2007; Kuchenbecker et al., 2016a; Reis and Suss, 2016).

The initial transgression (transgressive system tract – TST) is represented by basal diamictites and lodgment tillites of the Carrancas Formation sometimes grading to impure limestones and dolostones of the lower Sete Lagoas Formation, displaying a retrogradational pattern until the MFS (Vieira et al., 2007; Kuchenbecker et al., 2013, 2016; Reis et al., 2016; Perrella et al., 2017; Caetano-Filho et al., 2019). This interval corresponds to the CI–1 of Paula-Santos et al. (2017), recording a rapid increase of the $^{87}Sr/^{86}Sr$ ratios from 0.7074 to 0.7082 (i. e., Babinski et al., 2007). The TST presents

seafloor precipitates (aragonite pseudomorphs) and negative to positive $\delta^{13}C$ excursion from –5 to 0‰ (Santos et al., 2000; Babinski et al., 2007; Vieira et al., 2007, 2015; Caxito et al., 2012, 2018; Alvarenga et al., 2014; Paula-Santos et al., 2015, 2017), which are typical features of Neoproterozoic cap carbonates (Hoffman et al., 1998; Hoffman and Schrag, 2002). Sr contents for the transgressive stage are low (< 500 ppm), reflected in low average Sr/Ca ratio of 0.001 (Caetano-Filho et al., 2019; Fig. 4).

The highstand system tract (HST) initiates after the MFS, marking a change in the stacking pattern from a retrogradational to a progradational setting within the middle part of Sete Lagoas Formation (Reis and Suss, 2016; Caetano-Filho et al., 2019). This stage matches the onset of the CI–2 that shows $\delta^{13}C$ values around 0‰ and $^{87}Sr/^{86}Sr$ ratios of 0.7080–0.7084 (Paula-Santos et al., 2017 – Fig. 3). At the CI–2, oceanic connection was suggested considering strontium isotope homogenization process with the contemporary seawater, and the record of the index fossil *Cloudina* sp. (Warren et al. 2014; Perrella et al. 2017) support a connected seaway in the interior of West Gondwana at the late e Ediacaran (Paula-Santos et al., 2017). An important geochemical change in the Sr contents and Sr/Ca ratios within the HST (Fig. 4) allows the subdivision into early highstand systems tract (EHST) and late highstand systems tract (LHST).

The EHST is represented by dark–gray calcimudstones to bindstones with very low terrigenous contents, display a slight positive $\delta^{13}C$ excursion between 0 and +1‰ right after the MFS, and an increase in the Sr contents, but no more than 1000 ppm. Average Sr/Ca ratios remains similar to the TST around 0.001. This stratigraphic interval marks the stabilization of the marine carbonate ramp in the Bambuí sequence, with predominance of carbonate sedimentation after the initial mixed carbonate–siliciclastic sequence of the transgressive stage (Fig. 4).

The LHST is the final stage of progradational stacking pattern, representing the carbonate ramp climax throughout the basin, and display chemostratigraphic features related to major paleoenvironmental changes in the basal Bambuí Group (Caetano-Filho et al., 2019). The $\delta^{13}C$ values remains a plateau between 0 and +1‰, however, a remarkable increase in Sr content and Sr/Ca ratios show high values between 1000 and 3500 ppm, and an average ratio of 0.004, respectively. Such increase is not followed by a change in the carbonate facies through regressive stages, neither by any major increase

in carbonate content (Caetano-Filho et al., 2019). This stage is correlated to the *Cloudina* fossil interval, characterized by very pure carbonates dominated by dark–grey bindstones and peloidal calcimudstones with hummocky cross–stratification to wave ripples in the middle–upper part of Sete Lagoas Formation. Thicker carbonate breccia layers are frequent towards the top of the LHST in Januária High, whereas intraclastic to oolitic grainstones ends the sequence at Sete Lagoas High (Fig. 4 – Caetano-Filho et al., 2019).

An erosional unconformity with dolomitic layers and local subaerial exposures is associated with the sequence boundary, showing a major increase in $\delta^{13}C$ values up to +16‰ (i. e., Iyer et al., 1995), and persisting positive throughout the next transgressive–regressive 2nd–order sequence (Reis and Suss, 2016, Caetano-Filho et al., 2019). This interval characterizes the CI–3 of Paula-Santos et al. (2017), represented by the upper portion of the Sete Lagoas Formation and most of the Serra de Santa Helena and the Lagoa do Jacaré formations (Fig. 4), comprising shales, siltstones and sandstones with interbedded dark pure laminated limestones and oolitic limestones (Santos et al., 2000; Martins and Lemos, 2007; Vieira et al., 2007; Caxito et al., 2012; Alvarenga et al., 2014; Paula-Santos et al., 2015, 2017; Reis et al., 2017; Caetano-Filho et al., 2019). The $^{87}Sr/^{86}Sr$ ratios recorded in the CI–3 are 0.7074–0.7076 (Caxito et al., 2012; Alvarenga et al., 2014; Paula-Santos et al., 2015, 2017) and deviate from $^{87}Sr/^{86}Sr$ ratios around 0.7084 expected for the late Ediacaran and early Cambrian (Melezhik et al., 2001; Halverson et al., 2010; Kuznetsov et al., 2013, Zaky et al., 2019). Therefore, the second 2nd–order sequence and the CI–3 records the marine isolation stage of the foreland Bambuí basin, possible caused by mountain uplift at its margins, prevented seawater circulation and effective watermass connection with others epicontinental seas and open oceanic environments (Paula-Santos et al., 2017; Uhlein et al., 2019; Hippertt et al., 2019; Caetano-Filho et al., 2019).

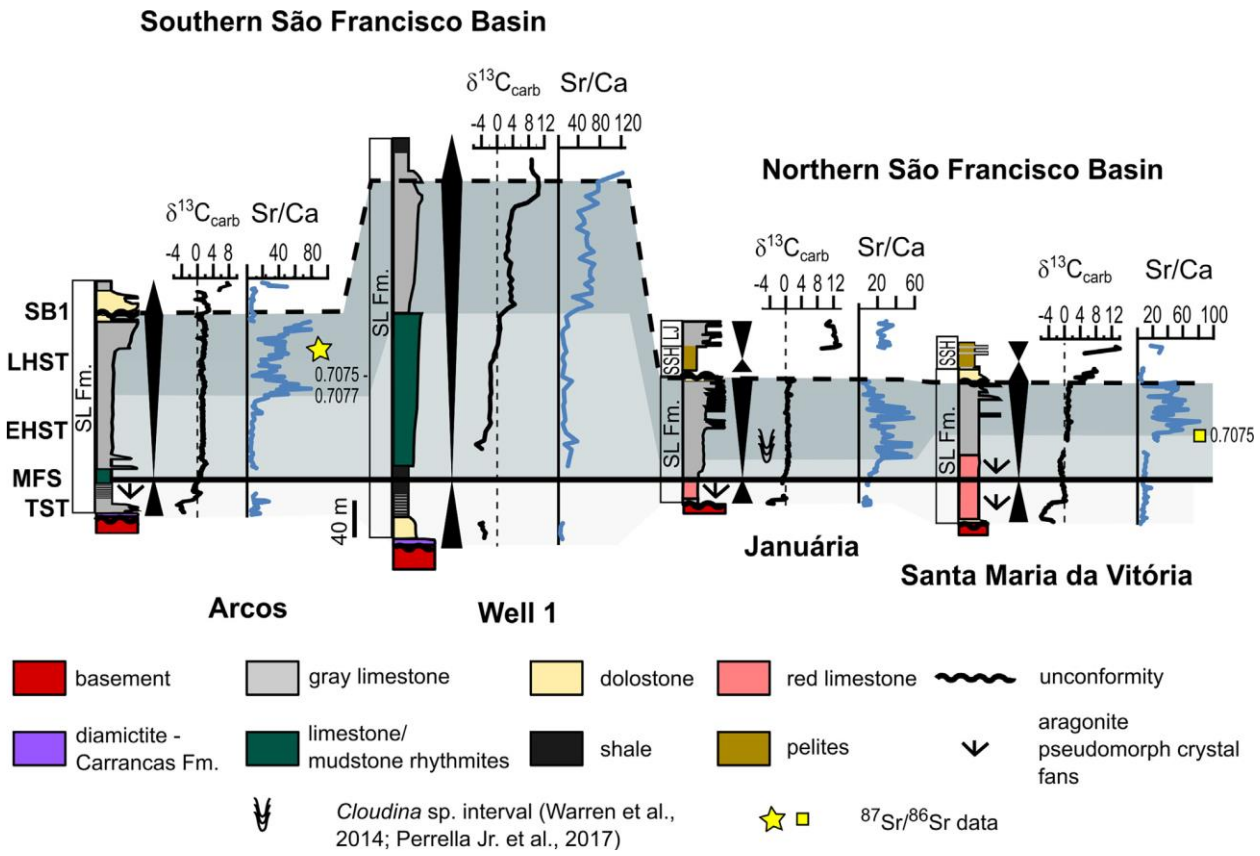

Figure 4. Stratigraphic–chemostratigraphic correlations for the basal Bambuí Group between the southern and northern domains of the São Francisco Basin (Sete Lagoas and Januária highs, respectively). TST: Transgressive System Tract; MFS: Maximum Flooding Surface; EHST: Early Highstand System Tract; LHST: Late Highstand System Tract; SB1: Sequence Boundary. Lithostratigraphic units: SL – Sete Lagoas Formation; SSH – Serra de Santa Helena Formation; LJ – Lagoa do Jacaré Formation (extracted from Caetano-Filho et al., 2019).

2.5 Depositional age and sedimentary provenance of the Bambuí Group

The depositional age of the Bambuí Group is controversial. Cryogenian (~740 Ma), early Ediacaran (~630 Ma), late Ediacaran (~550 Ma) and early Cambrian (520 Ma) ages have been suggested for different stratigraphic levels and based on different geochronological, lithostratigraphic and/or biostratigraphic methods (Babinski et al., 2007, 2018; Vieira et al., 2007; Caxito et al., 2012, 2018; Warren et al., 2014; Paula-Santos et al., 2015; Kuchenbecker et al., 2020; Moreira et al., 2020, Sanchez et al., 2020).

A Pb–Pb isochron age of 740 ± 22 Ma was reported by Babinski et al. (2007) in the basal Sete Lagoas cap carbonate at the southern São Francisco Basin, interpreted as the depositional age of these rocks and positioned them as post–Sturtian in the context of Neoproterozoic global glaciations. On the other hand, detrital zircon U–Pb ages obtained from Bambuí Group rocks point to a maximum depositional age of ~610 Ma for most of the sequence (Rodrigues, 2008; Pimentel et al., 2011). But, the recent discover of *Cloudina* sp. fossil remnants in the middle Sete Lagoas Formation at the Januária region indicates an Ediacaran age of 553 – 542 Ma (Grotzinger et al., 2000; Warren et al., 2014, Perrella et al., 2017). In addition, Paula–Santos et al. (2015) reported an U–Pb age of 560 Ma in the younger detrital zircon population, interpreted as maximum depositional age of the upper Sete Lagoas Formation (Fig. 3), supported by detrital LA-ICP-MS U–Pb ages of 537 ± 4 Ma and 506 ± 6 Ma in pelite sediments from the lower and upper Sete Lagoas Formation, respectively.

Recent U–Pb SHRIMP detrital zircon ages reveal that the Bambuí Group could be younger than previously thought and the deposition may have occurred during early Cambrian times for most of its stratigraphy including part of the basal Sete Lagoas Formation (Babinski et al., 2018). Moreira et al. (2020) report concordant prismatic zircon grains that cluster in a well constrained age of 520.2 ± 5.3 Ma, interpreted as the age of a tuff layer, and by extent, the depositional age of the upper Serra da Saudade Formation (Fig. 3 – middle to upper Bambuí sequence). Moreover, the recent discovery of icnofossils of the *Treptichnus Pedum* in the Três Marias Formation at the top of the Bambuí Group confirm this interpretation (Sanchez et al., 2020). The continuous sedimentary record throughout the basal sequence (Kuchenbecker et al., 2016a; Reis et al., 2016; Caetano-Filho et al., 2019), and recent geochronological U-Pb data of both detrital and volcanic zircons suggest the entire Bambuí sequence may be younger than ca. 550 Ma, recording a late Ediacaran-early Cambrian basin-cycle (Kuchenbecker et al., 2020; Moreira et al., 2020).

Nevertheless, some authors based on lithostratigraphy and isotope data (e.g., Caxito et al., 2012, 2018; Uhlein et al., 2016; 2017; 2019) suggest that the Sete Lagoas Formation represents a cap carbonate sequence of early Ediacaran age deposited after

the Marinoan glaciation and claim the possibility of an unconformity or depositional hiatus between the lower and upper sequences of the Sete Lagoas Formation, with a deposition gap of tens of million years. This is supported by a Pb–Pb whole rock isochron of 608 ± 19 Ma determined on carbonates that provides additional data for deposition during the early Ediacaran (Caxito et al., 2018). In spite of the poor age constraints of the carbonate–siliciclastic rocks from the Bambuí sequence, there is no field evidence supporting such stratigraphic gap (Paula–Santos et al., 2015, 2017; Reis and Suss, 2016, Caetano–Filho et al., 2019).

U–Pb ages for detrital zircons of the Bambuí Group range from the Archean to the early Cambrian (Pimentel et al., 2012; Kuchenbecker et al., 2014, 2020; Paula-Santos et al., 2015, 2018; Reis et al., 2016; Babinski et al., 2018). Provenance studies and facies distribution indicate that the two main source areas are the Archean-Proterozoic rocks represented by the basement and older basin–fill units, and the Neoproterozoic orogenic belts, but the current data is insufficient to distinguish between the contribution from sources in the Brasília and Araçuaí belts (i. e., Paula-Santos et al., 2018; Reis et al., 2016), and The Rio Preto and Riacho do Pontal Belts (i. e., Caxito et al. 2017). Also, the orogenic source is suggested by the spatial distribution and provenance of the Samburá and Lagoa Formosa rudites, as well as consistent eastward paleocurrent indicators measured in the uppermost Três Marias sandstones (Chiavegatto, 1992; Castro and Dardenne, 2000; Uhlein, 2014, Uhlein et al., 2017). The expressive occurrence of shallow carbonate facies in the central and eastern portions of the basin (Nobre-Lopes, 1995, 2002; Vieira et al., 2007; Iglesias and Uhlein, 2009), associated with pro–gradational seismic patterns outward from the large Januária and Sete Lagoas basement highs suggest that the cratonic basement strongly contributed with sediments during the deposition of the Bambuí sequence (Reis et al., 2016).

Paula-Santos and Babinski (2018) present geochronology data for the siliciclastic rocks in the southern sector of the São Francisco Basin, reporting an abrupt change in the Sm–Nd data in the oligomitic conglomerates from the Carrancas Formation, and the finer facies of the Moema Laminite. However, no further significant changes in the Sm–Nd data were reported farther upwards in the Bambuí Group, showing a lack of reorganization

in the source areas throughout the deposition of the basin. These data are used as another argument to dismiss an unconformity within the Bambuí Group.

Recently, Kuchenbecker et al. (2020) present new U–Pb and Lu–Hf isotopic analyses on detrital zircon grains extracted from the rocks of the Bambuí Group and Salinas Formation, together with a thorough data compilation from the literature. The two units present similar provenance patterns, sharing the major detrital zircon age peaks (550–650 Ma, 950–1050 Ma, 1750–2000 Ma, 2600–2800 Ma) and maximum depositional age in c. 550 Ma. The variation in detrital zircon age patterns and εHf(t) values from different units within the Bambuí Group provided additional clues of provenance changes occurred during the evolution of the basin.

Kuchenbecker et al. (2020) propose that in both Brasília belt and Araçuaí orogen sides, the early foredeep deposits of the Bambuí basin should have been incorporated to the orogenic domains, which could explain the apparent lack of deposits recording the climax of the Brasília belt uplift (c. 630 Ma) within the cratonic area. These authors consider that both Salinas Formation and Ibía Group could represent remnants of these early foreland deposits related to the uplift of Brasília belt and Araçuaí orogen, respectively, incorporated to the orogenic wedges due to the advance of the deformational fronts. This suggests that the Bambuí Group is the remaining record of an advanced stage of the foreland system, when subsidence was already influenced by the two evolving orogens (Fig. 5). Altogether, the analyses of the stratigraphic, structural and geochronological data converge towards an integrated tectonic model for the interaction between the Bambuí basin and the surrounding orogens during West Gondwana amalgamation.

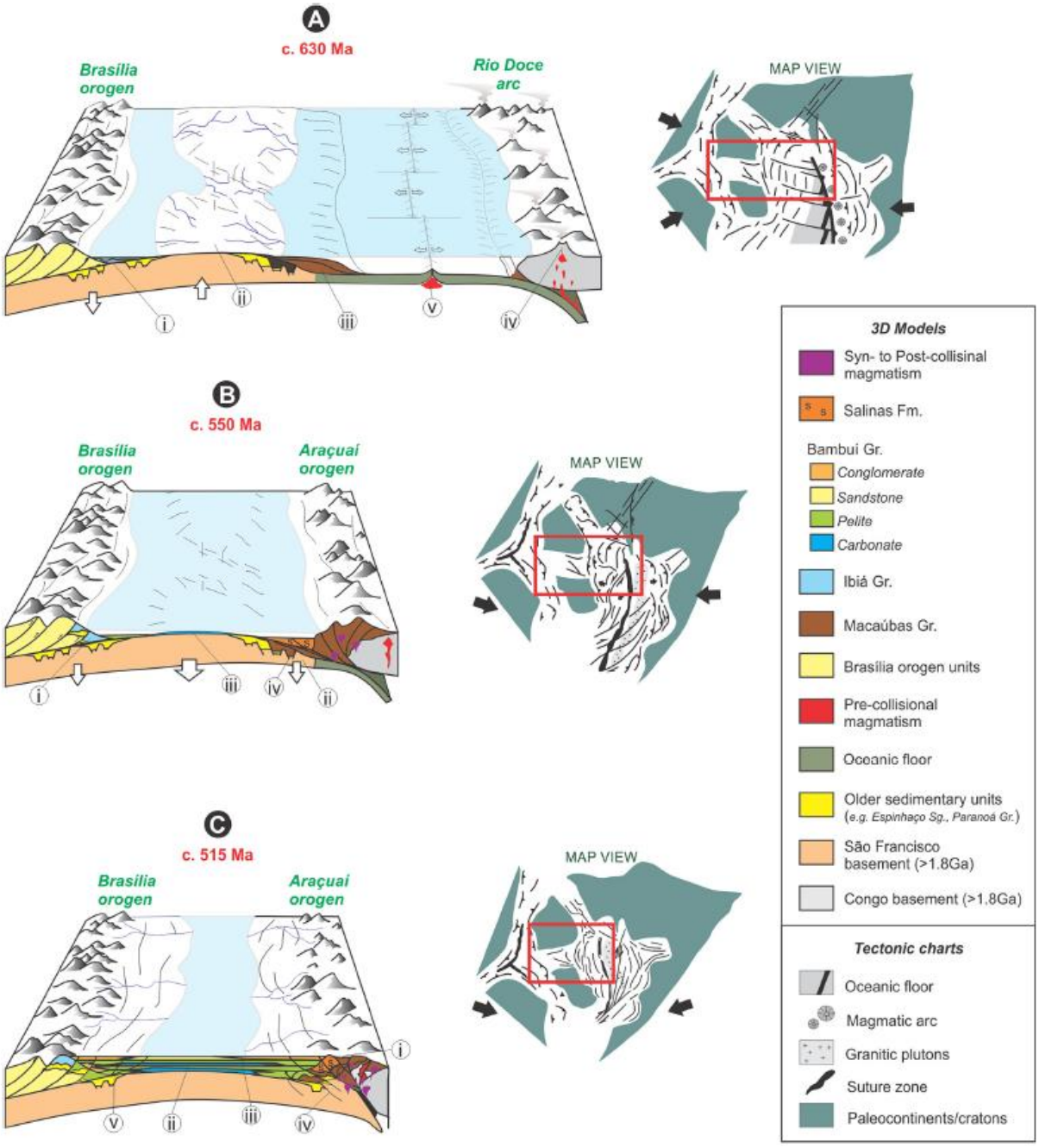

Figure 5. Sketch illustrating the integrated tectonic model for the Bambuí basin and the adjoining orogens during the West Gondwana amalgamation (Extracted from Kuchenbecker et al., 2020).

2.6 Paleoenvironmental conditions of deposition of the Bambuí Group

In recent geochemical studies of rare earth elements concentrations (REY) developed in carbonates at the southern portion of the São Francisco Basin, Paula-Santos et al. (2018) reported geochemical patterns matching C and Sr isotope variations that subdivide the Bambuí Group in three chemostratigraphic intervals. According to these authors, the CI–1 exhibits flat REY shale normalized distributions that record a high freshwater input in the basin after a glacial period. CI–2 shows subsequent marine transgression that diminished the continental influence and initiated the development of La, Gd, and Y positive anomalies in the carbonates. CI–3 records "seawater" like REY pattern, which strangely, correspond to the closure of the São Francisco Basin. Rather than open marine conditions, the CI–3 records a decrease in the silicate chemical weathering of sources located on the marginal belts of the São Francisco Craton due to higher denudation rates and a change in the dissolved influx towards carbonate rocks. The resultant high concentration of carbonate ions in the restricted sea induced a REY fractionation process similarly to that of the modern ocean. Also, Paula-Santos et al. (2018) reported constant positive Ce/Ce$*$ values throughout the basal Bambuí Group suggesting anoxic early diagenetic conditions, inefficient circulation and stratified water column, which could have worked as a barrier for life diversification in the basin at the Ediacaran–Cambrian limit.

In contrast, Caxito et al. (2018) reported geochemical and isotope data of carbonates from the basal Sete Lagoas Formation at the central portion of the São Francisco basin, including multiproxy geochemical and isotope stratigraphy. These authors put forward a model for the deposition of the Sete Lagoas cap carbonate which starts in the glacial aftermath and subsequent sea level rise, with important mixing of glacial meltwaters in anoxic bottom waters.

Recently, Fe speciation data, Ce anomalies and enrichments of redox sensitive elements (RSE) reported by Hippertt et al. (2019) suggest that the lower sedimentary units of the Bambuí Group were likely deposited in an open marine scenario featuring high productivity in shallow environments with euxinic incursions in predominant

anoxic/ferruginous bottom waters. Nevertheless, the upper Bambuí Group sedimentary units display a marine evolution in a restricted scenario, where anoxic ferruginous conditions probably reached surface waters. These authors claim that the lack of oceanic connection prevented the resupply of marine sulfate, redox-sensitive elements (RSE), bionutrients and ultimately dissolved O_2 which may have decreased biological activity and probably hindered biological evolution, preventing the rise of a typical modern–like Cambrian ecosystem.

Other lookout based on rare earth elements plus yttrium (REE+Y) patterns of the basal sequence of the Bambuí Group, suggest that high alkalinity of seawater during Late Ediacaran may have driven the appearance of the first biomineralizing organisms (Paula-Santos et al., 2020). These authors report a REY change from the EHST to LHST in the basal sequence marking an important paleoenvironmental overturn in the basin, with increasing alkalinity in seawater driving REY fractionation and LREY depletion. Restriction of the basin in the inner areas of West Gondwana due to the uplift of adjacent orogenic belts probably changed the weathering style of source areas to more congruent, thus delivering a higher ionic influx to a restricted setting, increasing alkalinity during LHST at the regressive stage. Moreover, *Cloudina sp*. fossils were reported in this interval of the basal Bambuí sequence and in other West Gondwana basins (Paula-Santos et al., 2020). To understand the geochemical conditions and major paleoenvironmental changes recorded in the Bambuí Group, other proxies such as trace metals geochemistry can be applied and compared with REE+Y patterns, Fe speciation data and Ce anomalies reported in carbonates of this unit. This could improve the knowledge about the redox evolution, alkalinity and major paleoenvironmental changes recorded in this peculiar epicontinental basin at the late Ediacaran and early Cambrian.

3 CHAPTER 3 – FUNDAMENTALS

3.1 Strontium isotope stratigraphy

Strontium isotope stratigraphy rests on the assumption that the modern oceans are homogeneous with respect to the $^{87}Sr/^{86}Sr$ ratios because the residence time of Sr in this reservoir (~10^6 years) is far longer than the mixing time (~10^3 years), so they are thoroughly mixed on short time scales, allowing isotopic homogenization (Elderfield 1986; Veizer 1989; Krabbenhoft et al., 2010; McArthur et al., 2012). In long-term secular changes, interactions between major reservoirs of radiogenic and non-radiogenic strontium and the geochemical cycles control the first-order variations of the $^{87}Sr/^{86}Sr$ ratios in seawater through geologic time (Fig. 6 – Elderfield 1986). The $^{87}Sr/^{86}Sr$ ratios of Sr dissolved in the oceans evolved in a known way, which allow their use to indirectly date and to correlate marine sedimentary successions worldwide (Veizer et al., 1999; Melezhik et al., 2001; Halverson et al., 2007, 2010; Krabbenhoft et al., 2010; McArthur et al., 2012, 2016; Kuznetsov et al., 2013). Moreover, definition of changes of the marine $^{87}Sr/^{86}Sr$ ratio is of great importance not only for correlating marine sedimentary rocks at both regional and global scales, but also for understanding the tectonic processes of the past and their impacts on marine ecosystems, habitats, biological diversity, and geochemical cycles (DePaolo and Ingram, 1985; Palmer and Elderfield, 1985; Chaudhuri and Clauer, 1986; Zaky et al., 2019).

Zaky et al. (2019) adopted a temporal resolution of 1 Myr for the Sr residence time in seawater for reconstruction of the $^{87}Sr/^{86}Sr$ seawater composition curves and with mixing times ranging from 10000 to 1000 years, the world's ocean is assumed homogenous with respect to $^{87}Sr/^{86}Sr$. However, some authors argue that the present–day mass balance of strontium in seawater is not at steady state (i. e., Allegre et al., 2010; Vance et al., 2009; Pearce et al., 2015; Peucker-Ehrenbrink and Fiske, 2019). Significant differences in the stable Sr isotope composition ($^{88}Sr/^{86}Sr$) between sources and sinks of

strontium in seawater support this interpretation (Krabbenhoft et al., 2010; Pearce et al., 2015).

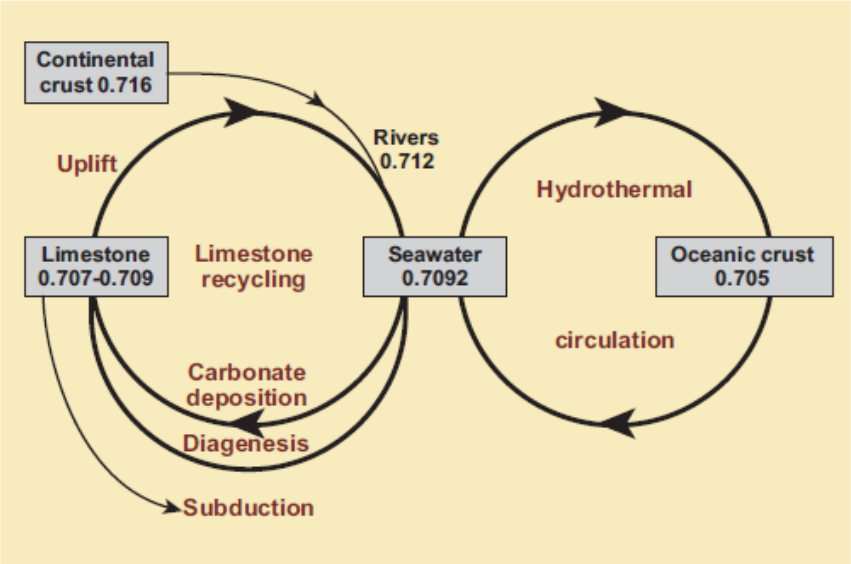

Figure 6. Reservoirs of strontium and cycles of inputs and output relative to seawater. Continental sources (in general) are radiogenic and oceanic sources are non-radiogenic. Changes in the relative inputs from those two major groups of sources are influenced by oceanic spreading rates, extent of continental exposure, uplift and erosion (Extracted from Elderfield, 1986).

In modern epicontinental basins, variations in climate and sea level changes can influence the $^{87}Sr/^{86}Sr$ record, and continental water inputs can locally modify the $^{87}Sr/^{86}Sr$ ratios of coastal waters (i. e., Ingram and Sloan, 1992; Huang et al., 2011; Beck et al., 2013; Schildgen et al., 2014; Peucker-Ehrenbrink and Fiske, 2019). On longer time scales, low $^{87}Sr/^{86}Sr$ ratios in Miocene marine basins such as the Mediterranean, adjacent to the uplifting Alps and Apennines mountains, are attributed to a high influx of Sr from non-radiogenic $^{87}Sr/^{86}Sr$ (Mesozoic) carbonates in the hinterland coupled with restricted exchange of water with the global oceans (Schildgen et al., 2014). Moreover, some argues that temporal variations in $^{87}Sr/^{86}Sr$ ratios of seawater are not primarily caused by variations in the balance between radiogenic continental and unradiogenic submarine hydrothermal sources of Sr to the oceans. Rather, $^{87}Sr/^{86}Sr$ temporal variations primarily reflect the changing composition of continental runoff that is determined by the changing

spatial distributions and age of the exoreic continental bedrock, climate and drainage patterns through geologic time (i. e., Peucker-Ehrenbrink and Fiske, 2019).

Sr isotopes also provide valuable information about the predominant tectonic regimes and their evolution in time (Shields, 2007). High $^{87}Sr/^{86}Sr$ ratios are usually interpreted as reflecting periods of enhanced orogenic processes, and low ratios characterize periods of continental breakup and enhanced hydrothermal activity (Jacobsen and Kaufman, 1999; Melezhik et al., 2001; Shields, 2007). This is well observed during the break–up of the supercontinent Rodinia (between 900–850 Ma) recording low radiogenic $^{87}Sr/^{86}Sr$ ratios, and became more radiogenic at the end of the Neoproterozoic and early Cambrian when several orogenic events occurred (as a product of weathering and erosion of continental rocks to the oceans associated with the Pan–African orogeny), showing that $^{87}Sr/^{86}Sr$ ratios also record important events resulting from the Earth's internal dynamics. It is also noticeable a small drop of these ratios during the glacial events (Fig. 8) that have isolated the ocean through a thick layer of ice, preventing the arrival of more radiogenic Sr from the continents (Kirschvink, 1992; Hoffman et al., 1998; Halverson et al., 2010; Zaky et al., 2019).

Modern investigations prove the capability of some chemically/biochemically precipitated marine archives (e.g., brachiopods, mollusks, corals, foraminifera, and evaporites) to inherit the $^{87}Sr/^{86}Sr$ signature of seawater at the time of their formation (DePaolo and Ingram 1985; Brand et al., 2003; Ando et al. 2009; Kuznetsov et al. 2012; Zaky et al., 2019). In contrast, some other archival minerals such as phosphate suffer a certain degree of alteration during early and (or) late burial that overprints their original elemental and isotopic compositions, and raises their radiogenic ^{87}Sr content (e. g., Trueman et al., 2002; Bright et al., 2009; Zaky et al., 2019).

Secular trends have been published tracking the evolution of marine $^{87}Sr/^{86}Sr$ ratios during the Phanerozoic (e.g., Burke et al., 1982; Veizer et al., 1999; McArthur et al., 2012; Zaky et al., 2019). Refinement of these trends is achieved by excluding results of archives that (*i*) lack modern representatives such as conodonts, (*ii*) are unable to retain their original compositions to the present day because of syn– or post–depositional alteration like biogenic phosphate, and (*iii*) lack sufficient stratigraphic resolution (Zaky et al., 2019).

These authors aim to apply the natural variation in Sr isotopes observed in modern marine biogenic carbonates (±0.000054) to the fossil record. Thus, the modified Phanerozoic trend relies only on the biogenic carbonate archives of either calcite or aragonite that were evaluated thoroughly for the preservation of the original structure, mineralogy, and chemistry (Fig. 7).

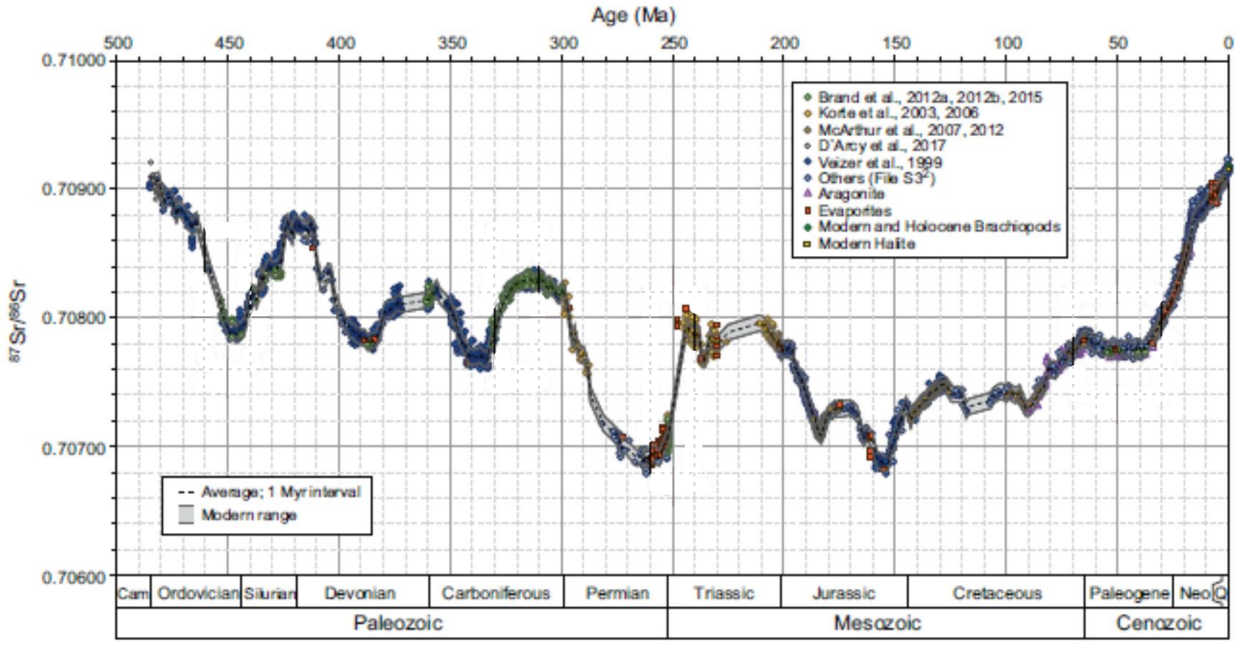

Figure 7. Secular $^{87}Sr/^{86}Sr$ seawater average trend line (black dashed line) and natural fluctuation band (solid lines) of 1 Ma intervals of measurements for the Phanerozoic Eon based only on biogenic calcite and aragonite material (Modified from Zaky et al., 2019).

In contrast to the Phanerozoic curve, the Neoproterozoic $^{87}Sr/^{86}Sr$ seawater curve and trend is poorly constrained in the literature. It is composed either of sporadic data points or a discontinuous curve (Halverson et al., 2007; McArthur et al. 2012). Zaky et al. (2019) reconstructed the secular trend for the Neoproterozoic Era using the Shields and Veizer (2002) data and the Halverson et al. (2007) one as guidelines (Fig. 8). The amount of work published in the last seven to eight years is sufficient to aid in the reconstruction of an enhanced Neoproterozoic seawater–Sr isotope curve (Zaky et al., 2019 and references therein). Similar to the Paleozoic, the proposed average trend line for the Neoproterozoic is constructed by grouping archival material of whole rock carbonate and evaporites into 1 Ma intervals (e.g., Frimmel and Jiang 2001; Kah et al., 2001; Mazumdar

and Strauss 2006; Halverson et al., 2009). Generally, the average trend line displays an increasing curve from 0.7062 during the late Tonian to 0.7092 by the early Ordovician punctuated by excursions (Fig. 8).

Despite some efforts to compile Sr–isotope data to determine the secular $^{87}Sr/^{86}Sr$ variation curve for the entire Proterozoic or just for the Neoproterozoic (e.g., Jacobsen and Kaufman, 1999; Melezhik et al., 2001; Halverson et al., 2007, 2010, Zaky et al., 2019) the use of strontium isotopes in chemostratigraphy is limited by the lack of accurate ages for the carbonates and the diversity of analytical procedures adopted to obtain the isotope data. These problems plus spatial and temporal isotopic variations, identification of restrict marine environments, and post–depositional alteration of carbonates, make difficult the elaboration of strontium evolution curves; and the comparison of strontium isotope data obtained without the necessary analytical care, in particular, it cannot be used with confidence for indirect dating (Melezhik et al., 2001; 2009). Even so, the main observation of these evolution curves is that $^{87}Sr/^{86}Sr$ ratios increase progressively from 0.7050 to 0.7095 throughout the entire Neoproterozoic (i.e., Melezhik et al., 2001; Halverson et al., 2010; Kuznetsov et al., 2013; Zaky et al., 2019). In the Tonian, the $^{87}Sr/^{86}Sr$ ratios vary between 0.7050 and 0.7070, in the Cryogenian gradually rise from 0.7060 to 0.7075 with some records of low radiogenic ratios, during the Ediacaran these values vary from 0.7075 to 0.7090, and then became as high as 0.7095 in the Cambrian ocean (Fig. 8).

Such $^{87}Sr/^{86}Sr$ evolution curves are not yet well calibrated and, while being effective correlation tool of carbonate successions and good markers of tectonic events, the $^{87}Sr/^{86}Sr$ ratios must be correctly positioned in geological time by means of geochronology and biostratigraphy. In this way, the Sr isotope chemistry becomes very reliable in the establishment of relative time and global correlations during Neoproterozoic (Melezhik et al., 2001). Moreover, it is observed that the evolution of the $^{87}Sr/^{86}Sr$ ratios is less fluctuant than $\delta^{13}C$ values, which makes it a more efficient instrument in the temporal positioning of stratigraphic sections (Halverson et al., 2010). Thus, well calibrated Sr isotope evolution curves must be developed, and might be used to indirectly date Neoproterozoic marine sequences (Melezhik et al., 2001).

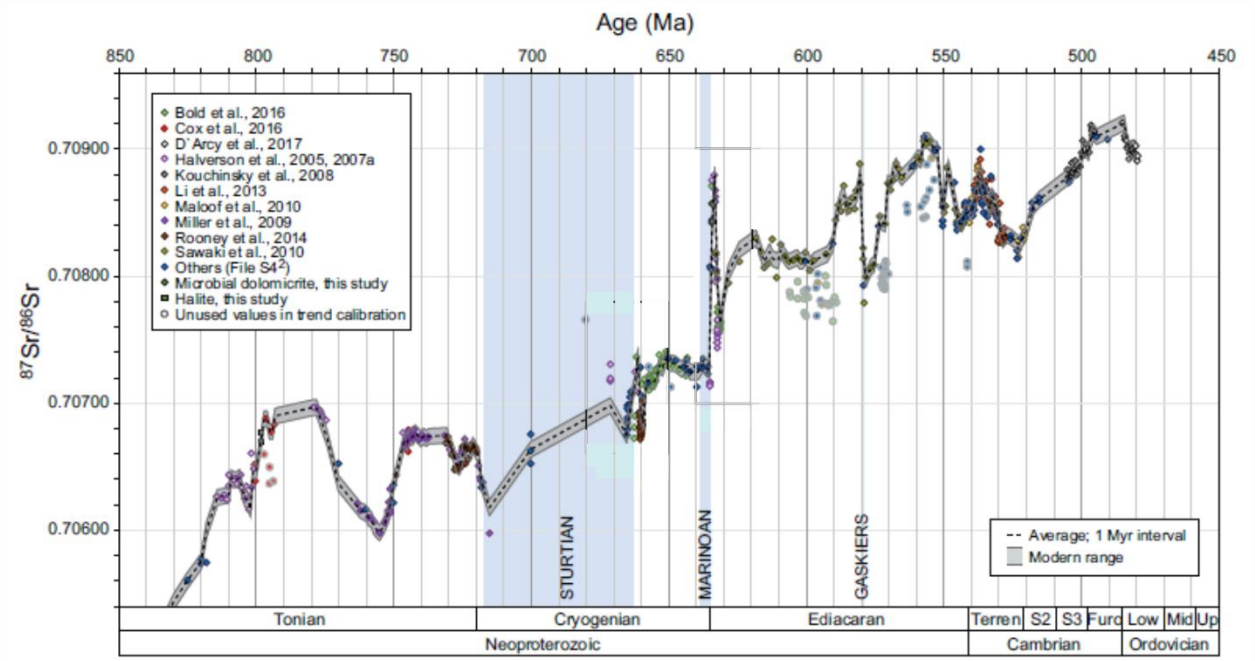

Figure 8. Secular $^{87}Sr/^{87}Sr$ evolution curve (black dashed line) and natural fluctuation band (solid lines) of 1 Ma intervals of measurements for the pre-Ordovician and Neoproterozoic seawater (Modified from Zaky et al., 2019).

Several authors have investigated the impact of subterranean groundwater discharge (SGD) in the marine strontium isotope budget (i.e. Basu et al., 2001; Dowling et al., 2003; Rahaman and Singh, 2012; Beck et al., 2013, Chakabarty et al., 2018). The strontium flux from SGD to the ocean is a major component (13 to 31%) of the marine Sr isotope budget and is proposed that global average SGD $^{87}Sr/^{86}Sr$ ratios vary from 0.7083 to 0.7094 (Beck et al., 2013). However, there is some controversy regarding if groundwater sources are less or more radiogenic relative to the $^{87}Sr/^{86}Sr$ seawater composition, which is influenced by both carbonate and silicate weathering, with a negative or positive effect on the SGD $^{87}Sr/^{86}Sr$ ratios. Recently, measurements of water samples collected from the Bay of Bengal show radiogenic $^{87}Sr/^{86}Sr$ ratios, high Sr and Ca concentrations, and high salinity in samples collected dominantly from 100–120 m depth, which can be explained by the contribution of saline groundwater from the Bengal Basin, providing direct evidence of the SGD–Sr flux to the Bay of Bengal (Chakabarty et al., 2018). In a similar way, the Ediacaran marine basins might have also been subject to local isotopic exchange processes of seawater with SGD, incorporating external strontium (Guacaneme et al., 2017).

Assessing the $^{87}Sr/^{86}Sr$ variations in ancient seawater and its evolution through time requires measuring the strontium composition of pristine marine archives that inherit a marine signature (Brand and Veizer, 1980, 1981; Kaufman and Knoll, 1995; Brand, 2004; Brand et al., 2010; McArthur et al., 2010; Zaky et al., 2019). This precondition has been subject to intensive work in last decades aimed to evaluate the diagenetic state, alteration and contamination of ancient marine carbonates and thus their preservation (Veizer et al., 1983; Banner and Hanson, 1990; Asmeron et al., 1991; Derry et al., 1992; Kaufman et al., 1991, 1993; Kuznetsov et al., 1997; Semikhatov et al., 1997; Jacobsen and Kaufman, 1999; Melezhik et al., 2001; Folling and Frimmel, 2002; Halverson et al., 2007, 2010; Frimmel, 2010; Kuznetsov et al., 2013; Paula-Santos et al., 2015, 2017; Caxito et al. 2018; Zaky et al., 2019).

Several studies suggest that sequential leaching of carbonates and simultaneous analysis of Sr isotopes and trace elements may help select the sequentially leached fraction of sample with the "closest" to a primary Sr isotope marine value (i. e., Banner et al., 1988; Bailey et al., 2000; Li et al., 2011; Liu et al., 2013, Paula-Santos et al., 2017; Bellefroid et al., 2018). These studies may help in renovate whole rock analyses especially when it comes to applying strontium isotope stratigraphy and reconstructing deep–time seawater Sr–isotope curves that lack biogenic archives (McArthur et al., 2010; Zaky et al., 2019). Actually, the degree of post–depositional and diagenetic alteration can be assessed by rigorous screening of geochemical proxies and petrographic means, including cathodoluminescence and Scanning Electron Microscopy (SEM) of marine carbonates (i. e., Brand and Veizer, 1980; Kaufman and Knoll, 1995).

The trace element (Mn, Fe, Mg and Sr) contents and stable isotope ($\delta^{13}C$ and $\delta^{18}O$) compositions and distribution within the calcite lattice of carbonates are governed primarily by their original mineralogy, seawater composition, partition coefficients, and the fluid/rock ratio of the diagenetic system (Brand and Veizer 1980, 1981; Hood and Wallace, 2018; Zaky et al., 2019). During post–depositional rock/fluid interaction, such as meteoric–water diagenesis, marine Ca and Sr are removed from the carbonate lattice and incorporate more Mn and Fe and light stable isotope ^{16}O, as well as more radiogenic $^{87}Sr/^{86}Sr$ ratios (Brand and Veizer 1980, 1981; Veizer et al., 1983; Drever, 1988; Banner and Hanson, 1990; James and Choquette, 1983; Denison et al., 1994; Jones et al., 1994;

Gorokhov et al., 1995; Chaudhuri and Clauer, 1993; Melezhik et al., 2001; Brand, 2004; Halverson et al., 2007; Derry, 2010). In contrast, carbon isotopes may be preserved in what is deemed to be an "original" composition, however, CO_2–charged marine pore water or meteoric water might increase or decrease it during diagenesis (Brand and Veizer, 1981; Walter et al., 1993; Patterson and Walter, 1994; Hover et al., 2001; Hu and Burdige, 2007; Schrag et al., 2013).

Based on these observations, $^{87}Sr/^{86}Sr$ *vs*. Mn/Sr and Fe/Sr diagrams, as well as $^{87}Sr/^{86}Sr$ *vs*. [Sr] can be used to monitor diagenetic alteration (i. e., Paula-Santos et al., 2017). Also, Mg/Ca ratios can be used to track both sedimentary and early diagenetic dolomitization processes on carbonates (Ahm et al., 2018; Higgins et al., 2018; Hood and Wallace, 2018; Wei et al., 2019). Moreover, some works attempted to define "cut-off" values for these ratios in order to determine the reliability of a given isotope dataset (i. e., Asmeron et al., 1991; Derry et al., 1992; Kaufman et al., 1993; Kaufman and Knoll, 1995; Kuznetsov et al., 1997; Jacobsen and Kaufman, 1999; Folling and Frimmel et al., 2002; Halverson et al. 2007; Kuznetsov et al., 2013). However, such works used a limited number of samples, usually from a single stratigraphic unit or from sedimentary units that share similar geological histories. This means that these "cut-offs" may not be suitable for every ancient carbonate succession (Paula-Santos et al., 2017; Zaky et al., 2019). Thus, instead of fixed numerical values for the preservation "cut-off" point, it could be suggested that these values should be dynamic, based on the geochemical database each basin and specific geological context (Zaky et al., 2019).

3.2 Trace metals geochemistry

Trace metals are frequently used to infer seawater paleoredox state, indicate paleoproductivity and reconstruct ancient depositional conditions of marine sediments and rocks due to these elements show variations in the oxidation state and solubility as a function of the redox state of the depositional environment (Lyons et al., 2003; Riboulleau et al., 2003; Algeo and Maynard, 2004; Brumsack, 2006; McManus et al., 2006;

Tribovillard et al., 2006; Algeo and Tribovillard, 2009; Algeo et al., 2012; Algeo and Rowe, 2012; Sansjofre et al., 2014; Sweere et al., 2016).

Redox–sensitive elements (RSE) such as uranium, vanadium and molybdenum tend to be more soluble under oxidizing conditions and less soluble under reducing conditions, resulting in authigenic enrichments in oxygen-depleted sedimentary facies, making useful elements as paleoredox proxies. The combined use of U, V and Mo enrichments allow distinguish oxic from anoxic–euxinic environments (Fig. 9). These elements tend to be much more enriched in anoxic–euxinic environments and to exhibit weaker co–variation with TOC than in suboxic environments (Brumsack, 2006; Tribovillard et al., 2006; Algeo et al., 2012).

Some redox–sensitive elements are delivered to the sediment mainly in association with organic matter (i.e. Ni, Cu, Zn) and they may be retained within the sediment in association with pyrite, after organic matter decay in reducing sediment. This particularity confers to Ni and Cu a good value as proxies for organic carbon sinking flux (frequently referred to as productivity). Concentrations of organic matter (OM) in sediments and sedimentary rocks record only a fraction of the total biological productivity in surface waters of the ocean. This material is delivered to the sediment–water interface following additional degradation during passage through the water column (Tribovillard et al., 2006; Algeo and Rowe, 2012).

Although Zn, Pb, Cu, Ca, Ni and V accumulation in sediments depends on redox conditions, their geochemical cycles are also highly influenced by biological activity, detrital input or hydrothermal activity, complicating their use in redox environment reconstructions (Tribovillard et al., 2006). Several of these elements are important components of enzymes (e.g., Cu, Zn and V) and can be concentrated in modern phytoplankton. In some cases, enrichment of these elements can result from an increase in organic matter accumulation (Sansjofre et al., 2014).

Trace metals accumulated in oxic sediments by oxy–hydroxides will be released in the porewater only if redox conditions in the sediment reach the manganous and ferruginous zones where oxy–hydroxides are reduced (Canfield and Thamdrup, 2009). Whether trace metals have been released in the pore water by organic matter mineralization or by oxy–hydroxides reductive dissolution, if the porewater redox

conditions reach the sulfidic zone, some elements, such as Zn and Pb, will be precipitated and trapped into the sediment as sulphides (Tribovillard et al., 2006).

Trace metals are present in seawater either in soluble form or adsorbed onto particles, and the removal from the water column to the sediments results from both biochemical processes that comprise the uptake of trace metals as micronutrients for phytoplankton, and chemical or abiotic processes that are relatively limited in oxic environments, but in suboxic environments, some enrichment may occur through diffusion of dissolved trace elements from the water column across the sediment–water interface or through remobilization along redox gradients (Brumsack, 2006).

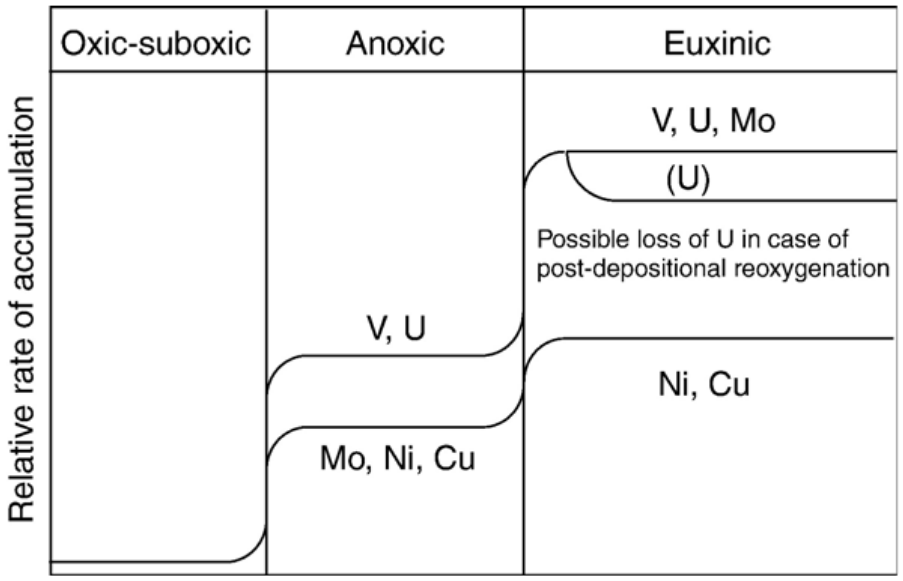

Figure 9. Schematic behavior of Ni, Cu, Mo, U and V as a function of the redox status of the depositional environment (Extracted from Tribovillard et al., 2004).

Abiotic processes are particularly efficient under reducing conditions, including adsorption of metallic ions onto organic or mineral substrates, formation of organometallic complexes, precipitation of Fe–sulfides and insoluble hydroxides. This variety of processes results in trace metal enrichments that reflect the specific conditions prevailing by the time of deposition and early diagenesis (Brumsack, 2006; Tribovillard et al., 2006; 2009).

Redox conditions in marine environments track the relative distributions of oxidizing agents across depositional and diagenetic gradients and biogeochemical processes that

control these distributions. Paleoredox conditions typically means determining whether conditions were oxidizing or reducing (Tribovillard et al., 2006).

Anoxic conditions are sulfidic (also called euxinic when H_2S occurs within the water column, usually related to restricted or semi–enclosed basins) and non-sulfidic (without H_2S in the water column). Hydrogen sulfide is a catabolic byproduct of sulfate–reducing bacteria. Suboxic settings are characterized by extremely low oxygen concentrations in the water column, where H_2S is limited to pore waters below the sediment–water interface. In oxic conditions, aerobic organisms can use dissolved O_2 from the overlying and interstitial waters for their metabolism (OM degradation). As dissolved oxygen becomes depleted, OM decomposition continues via organisms using secondary oxidant sources in order of consumption: nitrate, manganese oxides and iron oxides, oxyhydroxides, and sulfate. Ultimately, in the early diagenesis sequence when all free oxidants are exhausted, methanogenic bacteria begin to break down organic matter via an oxidative–reductive disproportionation of carbon (Tribovillard et al., 2006, 2009).

At the sediment–water interface or within sediments, oxygen–limited conditions and ultimately anoxia may develop when the oxygen demand exceeds the supply. In the water column, anoxia may develop in stagnant or confined water masses where insufficient circulation prevents O_2 renewal, or in places where intense OM degradation consumes O_2 faster than it is replenished, even in open–marine conditions (Tribovillard et al., 2006, 2009; Algeo et al., 2012; Algeo and Rowe, 2012).

U and Mo are trace metals of particular interest because they share chemical properties: i) these elements are present in low concentrations in the continental crust (~2.7 ppm U and ~3.7 ppm Mo), ii) they are mainly derived from oxidative weathering and subsequent riverine input, iii) they are not concentrated in marine phytoplankton, iv) they have residence times of ~450 ky (U) and ~780 ky (Mo), that ensures steady state equilibrium and uniform concentration in the modern ocean and v) they are conservative under oxic conditions and trapped into the sediment under anoxic conditions (McLennan, 1989; Brumsack, 1986; Chaillou et al., 2002; Sansjofre et al., 2014). As a consequence, sediment enrichments in U and Mo are generally related to anoxic and/or euxinic environments, where these elements can be easily scavenged or diffusively trapped

across the sediment–water interface from the oceanic reservoir into the sediment (Sansjofre et al., 2014).

Although U and Mo share many properties in seawater, the process by which each are incorporated into anoxic sediments are different (Algeo and Maynard, 2004; Algeo and Tribovillard, 2009). In modern settings, part of dissolved U (VI) diffuses into the sediment. When it reaches the ferruginous redoxcline (where Fe^{3+} reduces to Fe^{2+}), the U (VI) is reduced to U (IV) and fixed into the sediment by adsorption or precipitation. Accumulation is partly mediated by bacterial sulfate reduction, leading authigenic U enrichments in marine sediments with free H_2S. Also, re-oxidation process can either erase a primary U signal or result in vertical migration (Sansjofre et al., 2014).

Reduction of Mn–oxyhydroxides liberates adsorbed Mo to pore waters through the formation of thiomolybdate (MoO_4^{2-}) which is fixed in Fe–sulfide and/or organic matter molecules and subsequent Mo enrichment in the shallow burial environment. Since thiomolybdate requires free H_2S to form, Mo accumulation in the sediment requires more reducing conditions than U accumulation, and occurs dominantly under euxinic conditions (Zheng et al., 2000; Tribovillard et al., 2004, 2012).

The Mo/TOC ratio in euxinic settings is a good proxy for assessing the global dissolved–Mo content of the ocean (Algeo and Lyons, 2006; Algeo and Rowe, 2012). In present–day oceans, where euxinic conditions are rare, Mo is dominantly delivered to the ocean by riverine inputs and accumulates conservatively. The present oceanic Mo concentration is 105 nmol/kg, which makes it one of the most abundant trace metals in the ocean. When euxinia occurs only locally, Mo sequestration is not limited by Mo availability (because Mo is available from the remaind of the oxic ocean), leading to high Mo/TOC values (Algeo and Rowe, 2012).

Applications of trace–metal geochemistry on the analysis of paleoceanographic systems have been developed recently (Algeo and Lyons 2006; Algeo and Rowe, 2012). Trace–metal/TOC ratios can provide insights into the degree of water–mass restriction and estimates of deepwater renewal times. In such systems, secular changes in sediment trace–metal ratios may provide evidence of the chemical evolution of basinal deep–waters in response to differential rates of trace–metal removal to the sediment. The degree of

deepwater restriction in silled basins is generally controlled by eustatic elevations, with higher (lower) sea levels resulting in lesser (greater) watermass restriction.

Algeo and Rowe (2012) suggest that caution must be exercised in evaluating trace–metal patterns in paleomarine systems. Analyses based on trace–metal/TOC relationships can be undertaken only on systems that had anoxic deep–waters, due to the influence of redox variation on trace–metal accumulation patterns can outweighs that of hydrographic factors in some paleomarine systems (i.e., restricted anoxic marine systems).

A method for estimating watermass restriction from sediment trace–metal concentrations was proposed by Algeo and Lyons (2006). The method is based on the observation that the amount of Mo taken up by sediments in anoxic marine systems depends on both the aqueous concentration of Mo (i.e., source–ion availability) and the concentration of sedimentary organic matter (i.e., host–phase availability) as showed in equation 1:

$$[Mo] = [TOC]_s * [Mo]_{aq} \quad \text{or} \quad [Mo] / [TOC]_s = [Mo]_{aq} \quad \text{(Eq. 1)}$$

Where TOC is total organic carbon, and the subscripts “s” and “aq” denote sediment and aqueous concentrations, respectively. This equation indicates that the ratio of Mo to TOC in the sediment should be proportional to the concentration of aqueous Mo in the deep watermass. Where $[Mo]_{aq}$ concentrations are high due to relatively unrestricted conditions and strong deepwater renewal, $[Mo/TOC]_s$ ratios will be high. Conversely, where $[Mo]_{aq}$ concentrations are low due to strongly restricted conditions and limited deepwater renewal, $[Mo/TOC]_s$ ratios will be low. Normalization of $[Mo]_s$ to organic carbon is necessary because of the role that organic matter has as a substrate for Mo uptake by the sediment, allowing comparison of levels of sediment Mo enrichment among marine systems containing variable amounts of organic matter (Algeo and Lyons, 2006; Algeo and Rowe, 2012).

Deepwater residence times, estimated on the basis of Mo/TOC ratios, ranged from decades to hundreds of years in different basins and varied somewhat through time within

individual basins in response to eustatic and tectonic forcing (Algeo et al., 2007; Algeo and Tribovillard, 2009).

Trace–metals concentrations are used for paleoenvironmental work emphasizing fine–grained siliciclastic sediments and sedimentary rocks relatively rich in OM, such as gray and black shales, however, an assessment of whether they are relatively enriched or depleted is necessary. The degree of enrichment or depletion of a trace element in a sample is evaluated relative to its concentration in a reference that is commonly the average crustal rocks or average shale. The classic standard of comparison is average shale (i. e., PAAS – Taylor and McLennan, 1985).

Sediments and sedimentary rocks may have variable proportions of mineral phases, often of biogenic origin, that dilute the trace–element abundance of a sample. The most common biogenic diluents are calcium carbonate and opal. Thus, to be able to compare trace–element proportions in samples with variable carbonate and opal contents, it is customary to normalize trace–element concentrations to aluminum content (e.g. Tribovillard et al., 2006). For most sedimentary deposits, aluminum can be considered as an indicator of the aluminosilicate fraction of the sediments, with very little ability to move during diagenesis (Brumsack, 1989). To make results of the normalization procedure easier to interpret, it is common to use enrichment factors (EF) by equation 2:

$$EF_{element}\ X = (X / Al_{sample}) / (X / Al_{PAAS}) \quad \text{(eq. 2)}$$

If EF > 1, then the element X is enriched and, if EF < 1, X it is depleted relative to average shale. Although Al normalization is an easy way to normalize geochemical data for comparisons among different units, this method also has some complications. Trace–metal concentrations may acquire spurious correlations when normalized, and that normalization can also increase, decrease, change the sign of or even blur the correlations between unmodified variables (Van der Weijden, 2002; Tribovillard et al., 2006). In addition, there are also distinct instances when Al should not be used for normalization (Murray and Leinen, 1996). This could be the case for marine sediments with a detrital fraction lower than 3–5% and a relative excess of aluminum compared to other detrital elemental proxies such as titanium (Kryc et al., 2003; Tribovillard et al., 2006).

Van der Weijden (2002) also showed that the comparison to average shale values may raise some complications. Firstly, the composition of the commonly used standard shale and, consequently, the reference values of normalized elements are not necessarily representative of the local/regional sediments in the study area. This fact may complicate the comparison of the chemical composition of geological formations that are geographically and/or stratigraphically somewhat atypical. Secondly, reference shales may also include a diagenetic component, leading to systematic underestimation of EF for certain trace elements.

One approach to minimizing normalization biases is to focus on stratigraphic variation in EF or Al–normalized elemental concentrations rather than on absolute values provided that the coefficient of variation of Al is not too large, which is the case with studies involving high–resolution sampling of stratigraphic sequences. Al normalization of elemental concentrations is a useful procedure for examining the degree of enrichment of an element in sediments and sedimentary rocks but it cannot be relied on alone to identify and quantify contributions by sediment components other than the detrital fraction (Van der Weijden, 2002; Tribovillard et al., 2006).

Sansjofre et al. (2014) reported low contents of trace metals (U, Mo, Zn, Pb, Cd, Cu, Ni, V) and Al concentrations, pyrite abundance and total organic carbon (TOC) in the Early Ediacaran Araras Group, Brazil. Significant stratigraphic variations were identified, with successive enrichments of Pb–Zn, U, and U–Mo in the thin marl levels containing the highest amount of organic carbon and pyrite. Sansjofre et al. (2014) interpret these data as record of the progressive evolution of sediment pore-waters from oxic to more reducing conditions, driven by an increase in sedimentary organic matter accumulation. In the same way, trace metals geochemistry applied on carbonates from the Bambuí Group may improve the knowledge of the redox state of epicontinental seawater and track major paleoenvironmental changes in the Sao Francisco Basin.

Differences in the authigenic Mo–U covariation patterns of modern low-oxygen marine systems (for example, the tropical eastern Pacific, the Cariaco Basin and the Black Sea) suggest that multiple factors may be influencing uptake of authigenic trace metals by the sediment (Algeo and Tribovillard, 2009). These controls are mainly: (1) benthic redox conditions, including both the mean redox state and the degree of redox variability, (2)

operation of particulate shuttles that could accelerate removal of trace metals to the sediment, and (3) changes in the chemistry of the overlying water column, especially its aqueous Mo/U ratio (Fig. 10).

Benthic redox conditions are generally recognized as a dominant influence on the accumulation of authigenic trace metals in the sediment. For example, in the tropical eastern Pacific system examined by Algeo and Tribovillard (2009), it comprises unrestricted marine sites in which benthic redox conditions range from well oxygenated to strongly oxygen depleted (i. e., anoxic and intermittently sulfidic). The relationship of redox conditions to authigenic Mo–U enrichment in this system is fairly unambiguous due to oxic facies exhibit little or no enrichment, while suboxic facies exhibit modest enrichment with authigenic Mo/U ratios distinctly lower than the seawater ratio, and anoxic facies exhibit strong enrichment accompanied by progressively higher authigenic Mo/U ratios as total authigenic concentrations increase. This pattern is consistent with well-understood controls on trace-metal uptake by sediments in open marine or continent-margin upwelling systems. Under suboxic conditions, authigenic U is taken up preferentially over authigenic Mo because U(VI) is reduced at the Fe(II)–Fe(III) redox boundary, prior to the onset of sulfate reduction, which controls the authigenic accumulation of Mo (Fig. 10A).

Another controls on authigenic Mo–U accumulation must be invoked to explain features of the datasets from weak restricted basins, such as the Cariaco and Orca basins and the Black Sea. The strong relative enrichment of authigenic Mo relative to authigenic U in the Cariaco and Orca basins is probably due to operation of a “particulate shuttle” linked to Mn–Fe redox cycling within the water column (Algeo and Tribovillard, 2009). The effectiveness of a particulate shuttle in promoting authigenic accumulation of Mo may be enhanced by strong variation in water-column redox conditions at short to intermediate timescales (Fig. 10B).

An additional factor may influence authigenic Mo–U enrichment patterns in the Black Sea: evolution of the watermass chemistry (Fig. 10C). Unlike both the eastern tropical Pacific and the Cariaco Basin, in which aqueous Mo/U molar ratios are generally close to that of seawater (~7.5–7.9), aqueous Mo/U ratios in the Black Sea decrease from 4.6–4.9 in the surface watermass rapidly downward below the chemocline to a minimum of ~0.3 (Algeo and Tribovillard, 2009 and references therein).

Thus, substantially less dissolved Mo is available for uptake by sediments in slope and basinal areas of the Black Sea than at sites bathed in seawater of “normal” chemistry. Algeo and Lyons (2006) demonstrate that the signal of the evolved chemistry of Black Sea deepwaters can be recorded by sediment Mo/TOC ratios. This signal may also be apparent in a Mo–U enrichment factor cross-plot, which shows a distinct trend toward lower authigenic Mo/U ratios with increasing total authigenic enrichment (Algeo and Tribovillard, 2009). The relationship of this trend to the seawater molar ratio line (1×SW) is unambiguously different from that for open-marine systems and at odds with expectations of enhanced authigenic accumulation of Mo in sulfidic restricted basins. The most likely explanation for this pattern is that sites exhibiting lower authigenic Mo/U ratios accumulated under the influence of the Mo–depleted deep watermass (Mo/U molar ratio ~0.3–0.5), and sites yielding higher authigenic Mo/U ratios were exposed to the relatively Mo-enriched surface watermass (Algeo and Tribovillard, 2009).

Figure 10. Diagram showing relationships of Mo and U authigenic enrichment to **(A)** benthic redox variation, **(B)** Mn-oxyhydroxide particulate shuttle, and **(C)** evolving aqueous chemistry. In A, the zone of aerobic respiration is shown in blue, the (generally narrow) field of anoxic–nonsulfidic conditions (zones of Fe(III), Mn(IV) and nitrate reduction in orange, and the zone of sulfate reduction in gray. In B, MnOOH and Mn^{+2} represent the downward flux of particulate Mn-oxyhydroxides and the upward flux of aqueous reduced Mn, respectively; Mo represents the flux of adsorbed molybdate to the sediment (left panel) and its recycling within the water column (right panel); FC and SC represent fluctuating and stable chemocline depths, respectively. In C, the x-axis scale relates to aqueous Mo and U vertical concentration profiles and ranges from zero to the seawater (SW) value. In A–C, size of arrows shows relative magnitudes of authigenic Mo and U fluxes to the sediment. SWI = sediment/water interface (Extracted from Algeo and Tribovillard, 2009).

The figure 10 is in the next page.

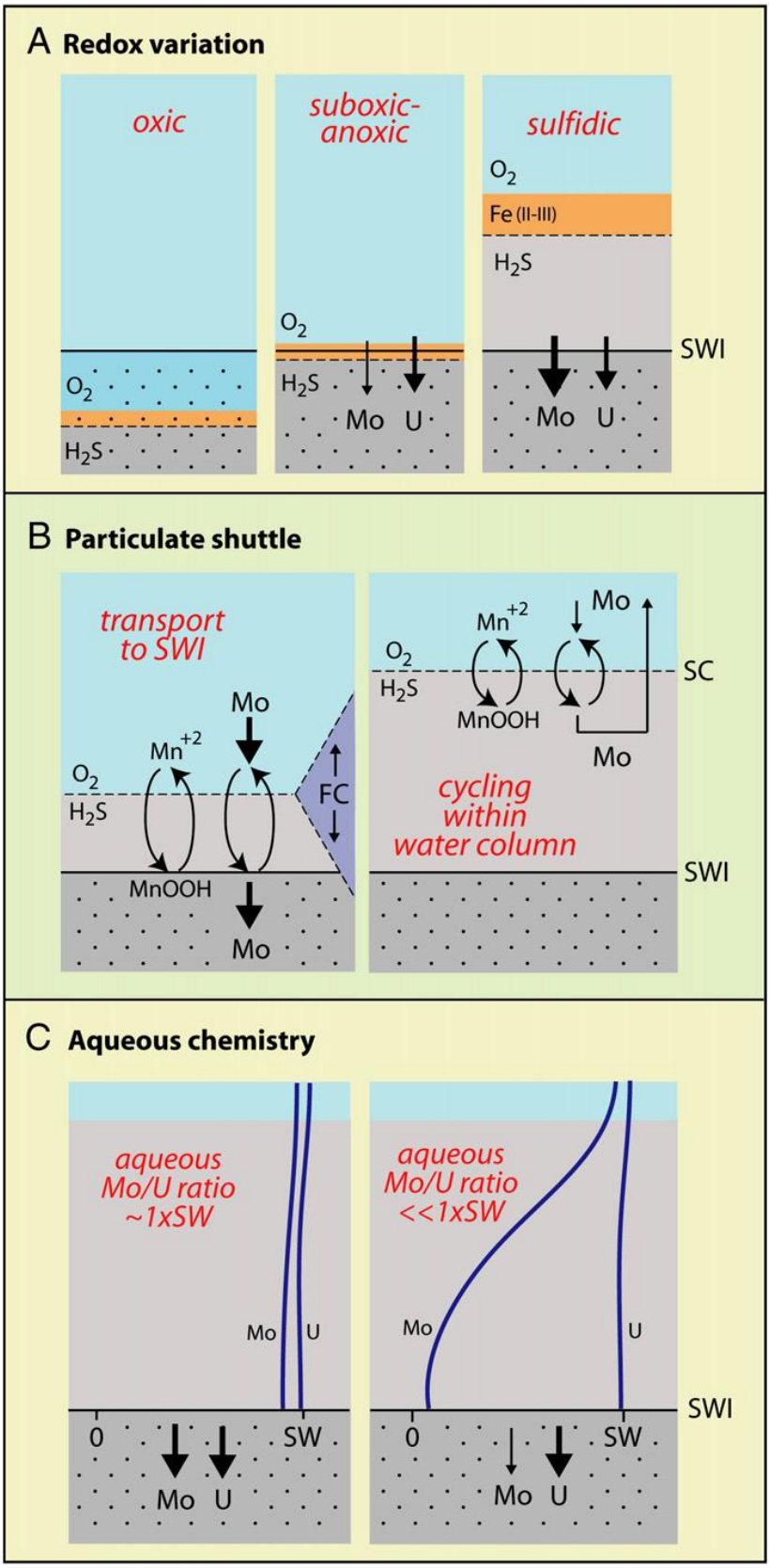
A Redox variation
oxic
suboxic-anoxic
sulfidic
O2
Fe (II-III)
H2S
SWI
Mo
U
B Particulate shuttle
transport to SWI
Mn+2
FC
MnOOH
SC
cycling within water column
C Aqueous chemistry
aqueous Mo/U ratio ~1xSW
aqueous Mo/U ratio <<1xSW
0
SW

4 CHAPTER 4 – CARBONATE PETROGRAPHY AND DIAGENETIC HISTORY OF THE BASAL BAMBUÍ GROUP AT THE JANUÁRIA HIGH

4.1 Introduction

The marine sedimentary record of the Bambuí Group in east Brazil in one of the most studied stratigraphic units that span the Ediacaran/Cambrian transition in West Gondwana. Sedimentary facies of these rocks at the Januária High comprises mixed carbonate-siliciclastic successions and record dominantly subaqueous sedimentary processes operating within a carbonate platform (i. e., Caxito et al. 2018; Caetano-Filho et al., 2019). Despite that these marine carbonates are intra-basin in nature, they are very complex to describe in petrography due to the variety of constituents, diagenetic changes and the underestimation of the complexity of biological controls on their formation. Moreover, carbonate petrography of samples from the Bambuí Group can be very difficult at the time of distinguish the true micritic matrix from microbial or inorganic in-situ microcrystalline precipitates. Here is presented a detailed petrographic study and a diagenetic history of the sedimentary rocks from the basal Bambuí Group at the Januária High, aiming to understand the sedimentary and diagenetic evolution of marine carbonates deposited in intracontinental marine environments.

4.2 Carbonate diagenesis

The diagenesis emcompasses any physical or chemical changes in sediments or sedimentary rocks that occur after deposition, excluding processes involving high enough temperatures and pressures to be called metamorphism. Carbonate diagenesis involves many different processes and products, and takes place in near-surface marine and meteoric environments, down into the deep-burial environment (i. e, Tucker, 2001; Scholle and Ulmer-Scholle, 2003). In the marine environment, diagenesis takes place on and just below the sea-floor in both shallow and deep water, and in the intertidal-supratidal zone. Meteoric diagenesis can affect a sediment soon after it is deposited if there is shoreline

progradation or a slight sea-level fall, or it may operate much later when a limestone is uplifted after burial. It is most important in occluding and generating porosity in the sediment. The burial environment, begins at a depth below the sediment surface of tens to hundreds of meters, that is, below the zone affected by surface processes, down to several kilometers where metamorphic dehydration reactions and wholesale recrystallization take over (Scholle and Ulmer-Scholle, 2003). Several diagenetic processes can be distinguished in carbonates, such as authigenesis, cementation, microbial micritization, neomorphism (replacement and recrystallization), dissolution, compaction (physical and chemical) and dolomitization (Tucker, 2001; Scholle and Ulmer-Scholle, 2003). A brief description of each diagenetic process in made below.

Authigenesis comprises the in-situ formation of minerals in a diagenetic environment which are controlled by pressure, temperature and time, availability of ions and stability of minerals (pH), and redox potential (Eh).

Cementation is the major diagenetic process producing a solid limestone from a loose sediment and taking place principally where there is a significant throughput of pore-fluid saturated with respect to the cement phase. The mineralogy of the cements depends on water chemistry, particularly pCO_2 and the Mg/Ca ratio, and carbonate supply rate.

Neomorphism is used to describe replacement and recrystallization processes where there may have been a change of mineralogy. Examples include the coarsening of crystal sizes in a lime mud/micrite (aggrading neomorphism) and the replacement of aragonite shells and cements by calcite (calcitization).

Dissolution is the result of the passage of pore-fluids undersaturated with respect to the carbonate phase present. This is a major process in near-surface, meteoric diagenetic environments, and may lead to the formation of karst, but it can also take place on the sea-floor and during deep burial. The secondary porosity created by carbonate dissolution can be important in some hydrocarbon reservoirs.

Compaction takes place during burial, resulting in a closer packing of grains, their fracture and eventual dissolution where in contact. Chemical compaction leads to stylolites and dissolution seams, when burial exceeds many hundreds of meters of overburden.

Dolomitization is a major alteration process for many limestones and the dolomite, may be precipitated in near-surface and burial environments. There are undefined number of models for dolomitization, but the matter is still one of great debate.

4.3 Geological background

4.3.1 Studied sections

Two stratigraphic sections of the basal Bambuí Group were studied at the Januária basement high, in the northern São Francisco Basin, corresponding to the Januária and Santa Maria da Vitória sections (Figs. 11 and 12). Detailed sedimentary facies and facies associations description of the basal Bambuí Group, as well as stratigraphic and chemostratigraphic correlation of the Januária and Santa Maria da Vitória sections is provided by Caetano-Filho et al. (2019).

The Januária section is a 140 m-thick composite section recording mixed sedimentary strata of the Sete Lagoas, Serra de Santa Helena and Lagoa do Jacaré formations overlying the basement at the northern Minas Gerais state (Fig. 11). The basal transgressive system tract (TST) display pinkish to reddish limestones with microbial lamination and aragonite pseudomorphs at the first 5 m-height. An interval of reddish to light gray peloidal bindstones with more frequent pelite laminations and lacking sedimentary structures marks the MFS (Fig. 11). Upward section, EHST comprise peloidal limestones with microbial laminations, hummocky cross-stratification and wavy bedding. Peloidal limestones with intercalated terrigenous clay laminations and an increase in the Sr/Ca ratios marks the onset of the LHST (Fig. 11 – Caetano-Filho et al., 2019). In this interval, peloidal limestones changes upward section to intraclastic calcarenite layers and intraclastic carbonate breccia beds that ends with a intraclastic doloarenite that marks the

SB1 (Fig. 11). The second 2nd-order sequence is represented by mudstones and siltstones with horizontal planar laminations of the Serra de Santa Helena Formation and intraclastic oolitic limestones of the Lagoa do Jacaré Formation (Caetano-Filho et al., 2019).

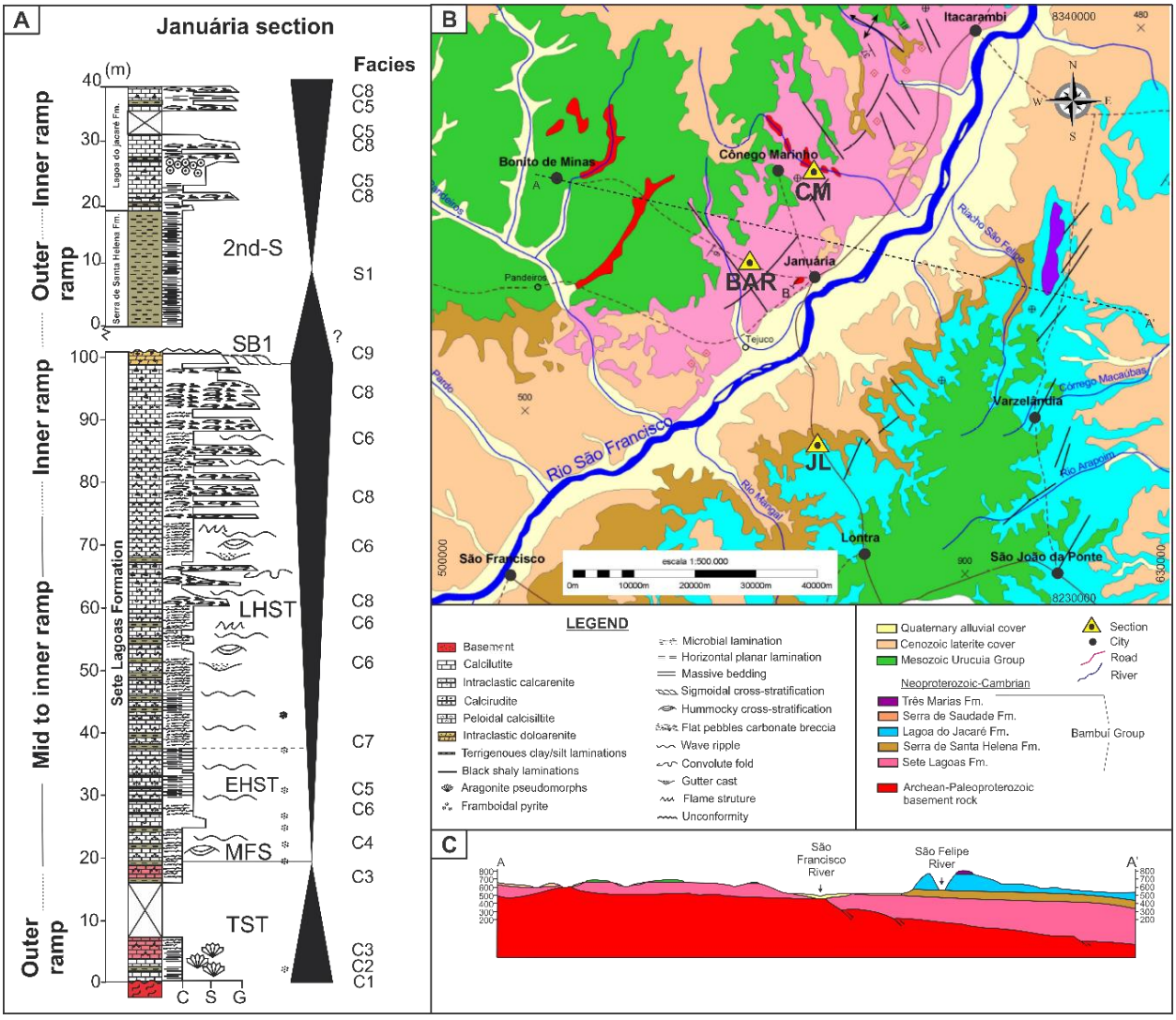

Figure 11. (A) Januária section showing transgresive-regressive 2nd-order cycles and facies code (modified from Caetano-Filho et al., 2019). **(B)** local geological map of the São Francisco Basin at the Januária region with location of stratigrafic sections which compose the Januária section; BAR: Barreiro, CM: Conego Marinho, JL: Januária-Lontra. **(C)** W-E cross-section (A-A´) perpendicular to the direction of the São Francisco river (modified from Iglesias-Martínez, 2007).

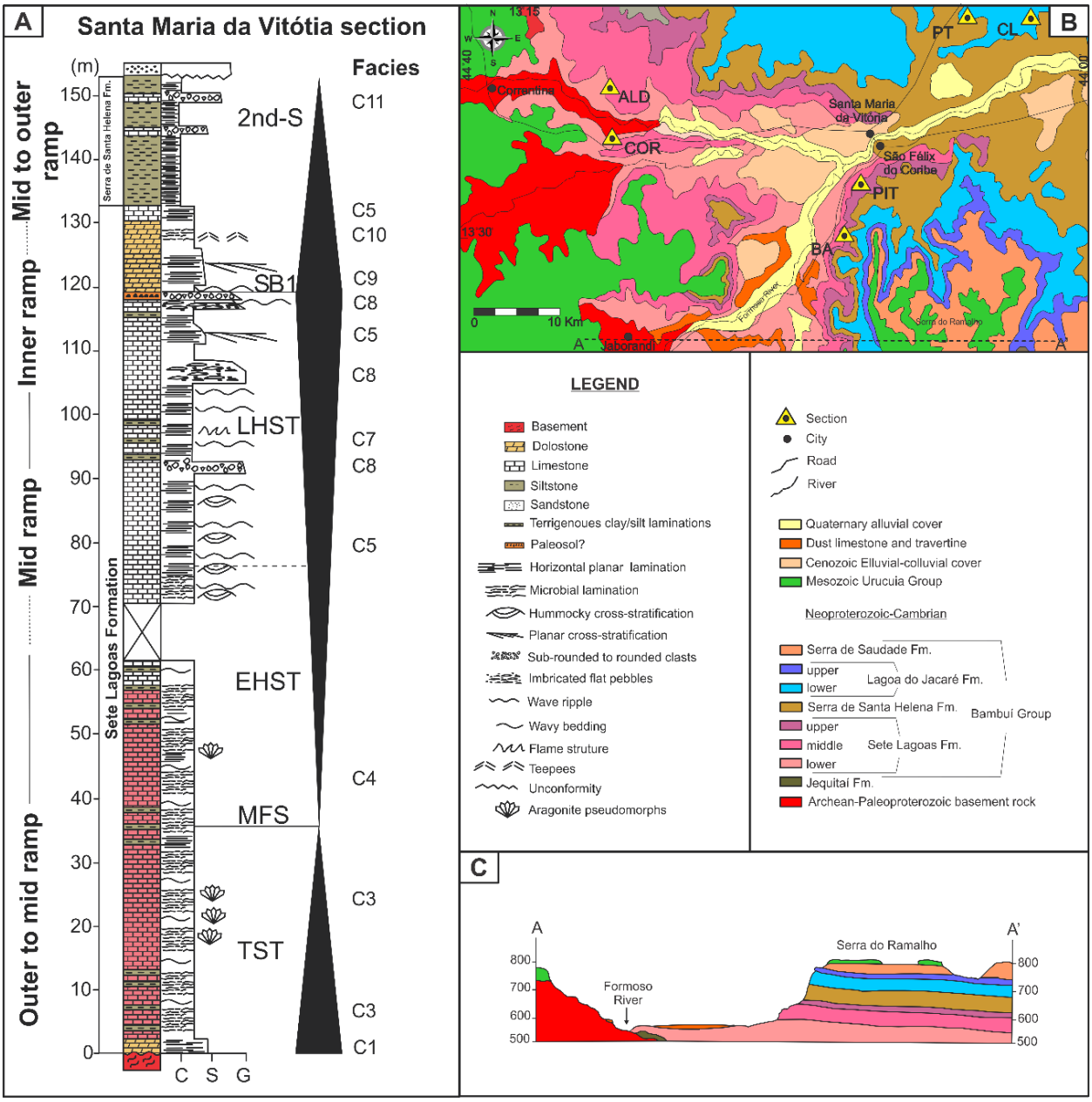

Figure 12. (A) Santa Maria da Vitória section showing transgresive-regressive 2nd-order cycles and facies code (modified from Caetano-Filho et al., 2019). **(B)** local geological map of the São Francisco Basin at the Santa Maria da Vitória region with location of stratigrafic sections which compose the SMV section; COR: Correntina, ALD: Aldeia, BA: Bahia, PIT: Pedreira dos Irmaos Teixeira, PT: Pedreira Terracon, CL: Caldeirao. **(C)** W-E cross-section (A-A´) perpendicular to the direction of the Formoso river (modified from Miranda, 2003).

The Santa Maria da Vitória section (SMV) is a composite section that comprises around 150 m-thick of carbonate-siliciclastic sedimentary record of the Sete Lagoas, Serra de Santa Helena and Lagoa do Jacaré formations overlying the basement craton at the

southern Bahia state (Fig. 12 – Caetano-Filho et al. 2019). In this section, the initial transgression (TST) over the craton is represented by 3 m-thick strata of white dolostones, overlying by a thick succession of pinkish limestones with microbial lamination and sporadic occurrences of aragonite pseudomorphs. Interbedded shale layers occur within the microbial limestones and marks the maximum flooding surface between the TST and EHST at the 20 m-height (Fig. 12).

Upward section, microbial pinkish limestones grade to gray limestones with hummocky cross-stratification and wavy bedding and some interbedded carbonate breccia layers, accompanied by an increase in the Sr/Ca ratios within the gray limestone interval, defining the late high stand system tract (LHST) (Fig. 12 – Caetano-Filho et al., 2019). The record of a paleosol layer covering gray limestones marks the sequence boundary (SB1), and the onset of the second 2nd-order sequence (2nd-S) is defined by dolostones strata with microbial lamination and tepee-like structures of the upper most Sete Lagoas Formation, in transition to siltstones and interbedded oolitic limestone of the Serra de Santa Helena Formation (Fig. 12 – Caetano-Filho et al., 2019).

4.3.2 Sedimentary facies of the Bambuí Group at the Januária High

Twelve sedimentary facies were described by Caetano-Filho et al. (2019) in the northern Januária High, they comprise mixed carbonate-siliciclastic successions, and records dominantly subaqueous sedimentary processes operating within a carbonate platform. In the basal 2nd-order sequence (i.e., Carrancas and Sete Lagoas formations), these successions represent outer to inner carbonate ramp associations (Tucker and Wright, 1990; Flügel, 2004), supported by a similar ramp geometry previously identified through seismic data and the overall facies characteristics (e. g., Martins and Lemos, 2007; Zalán and Romeiro-Silva, 2007; Vieira et al., 2007b; Reis and Suss, 2016; Perrella et al., 2017). This succession grades upward into the siliciclastic-dominated and carbonate-dominated deposits of the Serra de Santa Helena and Lagoa do Jacaré formations, respectively, in the overlying 2nd-order sequence from the Bambuí Sequence

(Caetano-Filho et al., 2019). Facies associations from the Januária and Santa Maria da Vitória sections (Figs. 1 and 2, respectively) are described below.

Facies C1, C2, C3, and S1 comprises outer to mid ramp facies associations. Facies C1, C2, and C3 correspond to the base of the lower Sete Lagoas Formation and the initial marine transgression over the forebulge domain, while siltstones and mudstones from facies S1 are fine-grained terrigenous siliciclastic sedimentation associated with the Serra de Santa Helena Formation, marking the drowning of the carbonate ramp (Caetano-Filho et al., 2019). At the basal contact with the basement, carbonates of the Sete Lagoas Formation are intensively recrystallized (facies C1), as a thin ~1 m massive white crystalline limestone layer in the Januária section and a 3 m-thick dolomitic limestone layer in the base of Santa Maria da Vitória section (Figs. 11 and 12, respectively).

Light grey calcimudstones from facies C2 are composed of micritic matrix and frequent seafloor cements of aragonite pseudomorphs crystal fans up to 1 cm, and reddish laminated bindstones from facies C3 also present aragonite pseudomorphs, as smaller crystals disposed in irregular crusts (< 0.5 cm). It is having been interpreted that horizontal planar-parallel lamination from facies C2 and S1 points to suspension/particle settling, whereas irregular and discontinuous lamination from facies C3 suggests a microbial-related precipitation (Caetano-Filho et al., 2019). The lack of oscillatory-related sedimentary structures and the presence of well-preserved seafloor cement in facies C2 and C3 suggest deposition below the storm wave base level (Vieira et al., 2015; Okubo et al., 2018; Caetano-Filho et al., 2019). Occasional occurrences of wave rippled cross bedding in facies C3 suggest a rebound of the wave base level to the mid ramp domain, between storm and fair-weather wave base levels (Caetano-Filho et al., 2019).

Facies C4, C5, C6, and C7 comprises mid to inner ramp facies association (Caetano-Filho et al., 2019). Pinkish to light grey bindstones from facies C4 occur at the base to the middle portion of the Sete Lagoas Formation, it presents peloidal matrix (20–30 μm) and frequent terrigenous mud laminae. Framboidal pyrite is abundant and suggests anoxic sulfidic early diagenesis environment (e.g. Wilkin and Barnes, 1997; Caetano-Filho et al., 2019). Local occurrences of thin layers (1–2 cm) of intraclastic packstones within facies C4 mark changes in the base level in the inner ramp domain. The microbial lamination of facies C4 is marked by sets of wave rippled cross bedding

and hummocky cross-stratification, indicating deposition between storm wave and fair weather wave base levels.

Topwards, the mid ramp domain is dominated by dark grey bindstones from facies C6, and associated dark gray calcimudstones from facies C5 with variable amount of terrigenous mud laminae from facies C7. Bindstones from facies C6 exhibit peloidal matrix and irregular lamination, resembling crusts with abundant organic films. These organic features display honeycomb-like structures and can be associated with microbial extracellular polymeric substances (Caetano-Filho et al., 2019). All these facies display sets of wavy bedding and hummocky cross-stratification, including tempestite cycles, representing the mid ramp domain between the storm wave and fair weather wave base levels. Local occurrences of wave ripples mark a transition to the inner ramp domain, above fair-weather wave base (e.g. Tucker and Wright, 1990; Caetano-Filho et al., 2019).

Facies C8, C9, C10, and C11 comprise inner ramp facies association of environments with high-energy shallow waters. These facies occur at the top of the basal Sete Lagoas Formation and the overlying Serra de Santa Helena and Lagoa do Jacaré formations. Intraclastic rudstones occur as carbonate breccias of facies C8 and are remarkable stratigraphic levels defining sequence boundaries at Januária High domain (e.g. Iglesias-Martínez, 2007; Perrella et al., 2017; Caetano-Filho et al., 2019), occurring in the Januária and Santa Maria da Vitória sections (Figs. 11 and 12, respectively). These breccias are composed of intraformational limestones fragments, as flat pebbles to cobbles (2 to 10 cm) and subrounded pebbles (0.5 to 2 cm). The clasts are poorly sorted and support the fabrics, with a close packing. They occur as massive layers from 0.5 to 2 m, which thicken upward in the basal sequence. Occasionally fining-upward pattern and frequent imbricated flat pebbles occur at the base of the layers. Some levels also resemble reworked teepee structures. Due to high compaction, contacts between carbonate breccia layers and underlying facies are sharp planar surfaces, often associated with stylolites (Caetano-Filho et al., 2019). Considering the abundance of flat pebbles, the oligomictic (intraclastic) character and the association with wave ripple facies, these carbonate breccias were attributed to the inner ramp domain in a shallow marine environment, probably related to variations in the base level and consequent exposure, locally re-

worked by tidal currents and storm-driven events (Flügel, 2004; Perrella et al., 2017; Caetano-Filho et al., 2019).

Dolomitization is observed at the top of Sete Lagoas Formation in the Januária High (Caetano-Filho et al., 2019). In Januária section, intraclastic dolograinstones from facies C9 occur at the top of section (Fig. 11) and are composed of subangular intraclasts, with dissolution features, as vugular to moldic porosity, and also display sets of planar to trough cross-stratification associated with intertidal environment. In the Santa Maria da Vitória section, a thicker dolomite interval of ~10 m-thick was described (Fig. 12), with a variety of shallow water facies, including subaerial exposure features in a supratidal domain. Also, a possible paleosol layer was described at the base of this interval and marks a sharp discontinuity in the $\delta^{13}C$ profile (Caetano-Filho et al. 2019). The overlying dolomitic interval starts with deposition of intertidal dolomites with sets of planar cross-stratification from facies C9, followed by laminated to domical dolomitic stromatolites from facies C10, and it is interpreted in terms of a shallow to subaerial condition related to the sequence boundary. Caetano-Filho et al. (2019) suggest a dolomitization model of a meteoric-marine mixing zone (e.g., Flügel, 2004), considering the dolomitization of intertidal facies during early diagenesis in the shallower areas of the carbonate ramp, which is not restricted to supratidal facies and is associated with dissolution features. Nevertheless, despite the absence of evaporitic minerals, usual high $\delta^{18}O$ values in this dolomite interval (Caetano-Filho et al., 2019) suggest more evaporitic conditions in these shallow environments. Finally, oolitic to intraclastic grainstones represent the inner ramp domain and correspond to grainstones shoals from facies C11. In Januária section, this facies composes a 17 m-thick interval associated with calcimudstones and collapse breccias, in shallow water domain (Fig. 11). In Santa Maria da Vitória section, this facies occurs as oolitic grainstone lenses within pelites from facies S1 of the Serra de Santa Helena Formation, indicating episodic changes from deeper siliciclastic-dominated settings and shallow water carbonate systems (Fig. 12).

4.4 Petrographic analyses

Sixty-five carbonate samples distributed along the two studied sections were selected for petrographic analyses, based on previously bulk rock samples analyzed for Sr and Ca using X-ray fluorescence, as well as stratigraphic-chemostratigraphic framework and sedimentology (Caetano-Filho et al., 2019). These petrographic analyses were carried out to help in the selection of the more preserved areas in polished rock slabs to obtain carbonate powder. The petrographic thin sections were analyzed using a polarizing microscope (Carl Zeiss - model Axioplan 1), with polarized light features, dolly with variable precision (ideal for counting). It has the software LAS - Leica Application Suite with module for image analysis, and Leica MC170HD camera. Carbonate rock classifications are commonly used in facies analyses based on textural and compositional criteria (Flügel, 2010). The classifications proposed by Dunham (1962) and Folk (1962) have proved most practical, and modifications suggested by Embry and Klovan (1971) and Wright (1992) are helpful. Carbonate facies of the Bambuí Group were described in these sections by Caetano-Filho et al. (2019), and their classification is adopted in this work. Also, a useful part of petrographic studies is the determination of the sequencing of diagenetic events relative to each other (paragenesis) and to external marker events in the sedimentary evolution of the Bambuí Group.

4.5 Results

4.5.1 Januária section

White to beige dolomitic limestone from facies C1 presents intense recrystallization, vugs filled with sparry calcite, and disseminated oxidized sulfide minerals. In thin sections, syngenetic euhedral pyrite grains of 40–100 µm in diameter are observed within the crystalline dolomite matrix, generally being opaque to nearly opaque grains (Figs. 13A-B). A crystal with strong development of twinning in calcite displays syntaxial overgrowth, and replacement calcite shows medium- to coarse crystalline euhedral rhombs (Fig. 13C).

Light grey calcimudstone from facies C2 display micritic matrix and irregular laminations with abundant aragonite pseudomorph crystal fans up to 1000 μm long (Fig. 13D). Thin sections from this facies show silica cementation associated to pressure-dissolution structures (stylolites) and insoluble material (organic films). Sparry calcite cementation also occurs in this facies but in lesser proportion relative to silica cementation (Figs. 13E-F). Reddish laminated bindstone from facies C3 presents some stylolites and disseminated oxides within the matrix (Fig. 13G). Petrographic photos show carbonate matrix composed of peloidal grains of 20–30 μm, irregular laminations of organic films and sparry calcite cementation, which is distinguished from the peloidal matrix by being clearer, as well as by having a thicker crystalline size (Figs. 13H-I).

Pinkish to light grey limestone from facies C4 presents microbial lamination well observed in both polished slabs and thin sections, presenting frequent intercalations of brown to green argillaceous laminae and nodular fabrics developed by differential mechanical compaction (Fig. 13J). This facies show a carbonate matrix of fine peloidal grains of 20–30 μm in diameter, and sparite forms crystals generally larger than 30 μm in diameter, which can reach up to 1 mm (Figs. 13K-L). Also, abundant framboidal pyrite and oxides are also reported.

Dark grey calcimudstone from facies C5 presents clay laminae, stylolites and dissolution seams (Fig. 14A). Thin sections display preserverd horizontal planar-lamination within the peloidal matrix of sediments (20–30 μm in diameter), and some areas with sparry calcite cementation and fracturing (Figs. 14B-C). Dark-grey laminated peloidal bindstone from facies C6 presents irregular lamination and thin clay layers (Fig. 14D). In petrography, this facies show stylolites and radiating silica micronodules within a carbonate matrix of peloidal grains of 20–60 μm in diameter (Figs. 14E-F). Nodular fabrics are developed by different compaction between carbonates and insoluble laminations.

Argillaceous dark grey laminated calcimudstone from facies C7 display well-preserved horizontal planar-lamination and silica micro-nodules (Figs. 14G and 14J). Thin sections show fine-grained carbonates with peloidal matrix (20–60 μm), dissolution followed by later blocky calcite cementation and late diagenetic calcite veins limiting argillaceous layers (Figs. 14H-I). Pressure-dissolution structures as stylolites, sparry calcite cementation and spherical radiating silica micro-nodules are observed in this facies

(Figs. 14K-L and 15A-C). Also, replacement of intraclast by calcite is documented (Fig. 15B).

Intraclastic rudstone from facies C8 presents limestone fragments of imbricated flat pebbles to cobbles of 2–10 cm long and subangular to subrounded peebles of 0.5–2 cm (Figs. 15D-G). Photomicrographs of this facies show micritic intraclasts cut by diagenetic calcite vein, partial replacement by calcite (Rep) of detrital extraclast (Det) of 500–600 µm in diameter, recrystallization of the carbonate matrix (Rec), syntaxial overgrowth of calcite (Sov), replacement of dolomite and some dispersed euhedral opaque grains (Figs. 15H-I). Intraclastic dolograinstone from facies C9 also show detrital grains, and dissolution features such as vugular porosity, followed by precipitation of phreatic calcite cement, recrystalization and replacement dolomite (Figs. 15J-L).

Laminated to massive siltstones and mudstones from facies S1 at the upper 2nd-order sequence are composed mainly of detrital monocrystalline quartz grains, followed in abundance by potassium feldspars, mica grains, and subordinated oxidized cement (Figs. 16A-C). Dark-grey laminated peloidal calcimudstone from facies C5 at this interval display a peloidal matrix (20–30 µm) with preserved horizontal lamination, some dispersed opaque grains, and dissolution followed by precipitation of phreatic calcite cement (Figs. 16D-F). Thin sections of intraclastic rudstone from facies C8 at this interval show diagenetic calcite veins cut by late diagenetic calcite veinlets and followed by fractuting; syntaxial overgrowth of calcite, replacement of detrital grains by calcite, and subordinated stylolites are also documented (Figs. 16G-L).

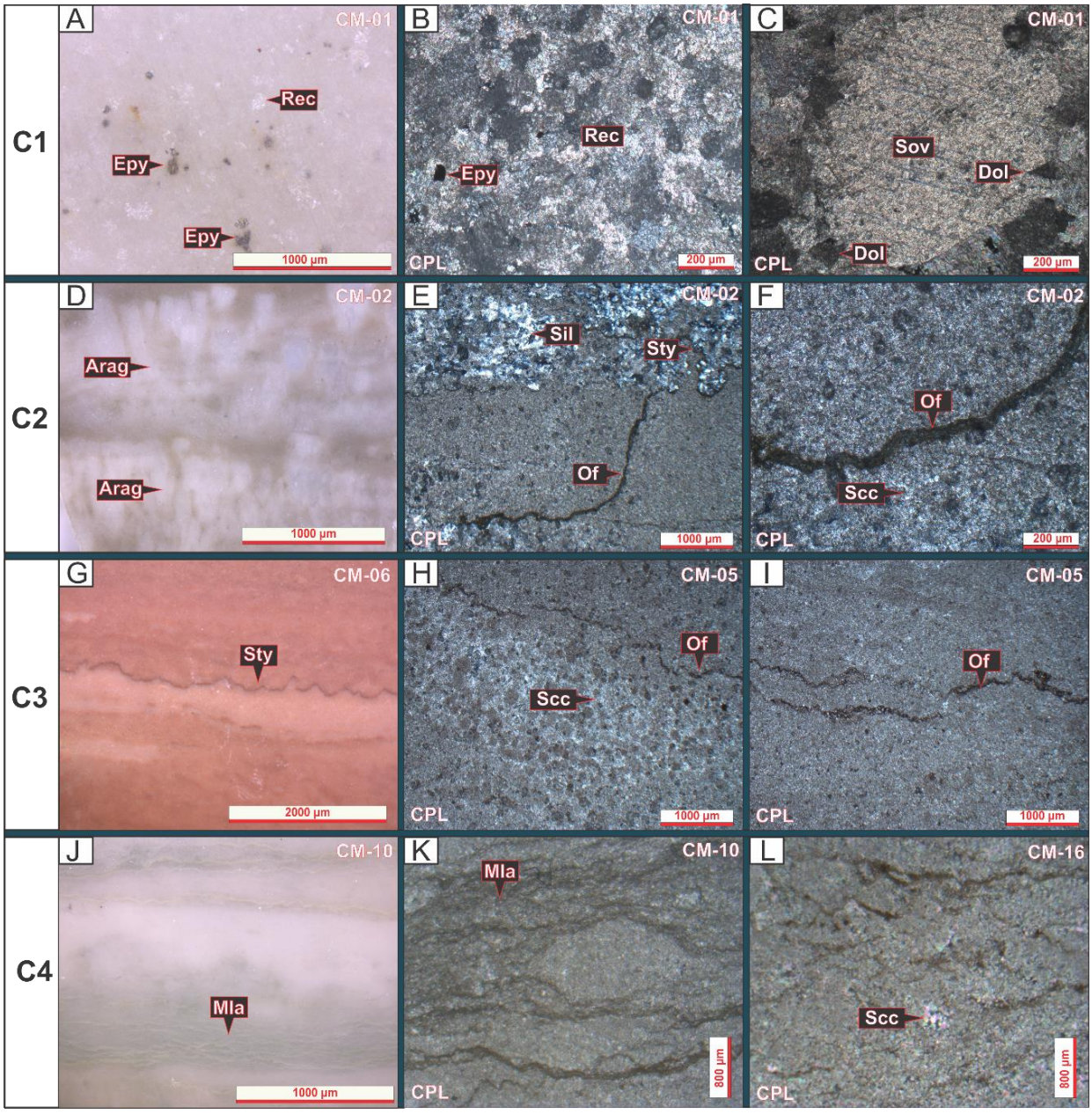

Figure 13. **(A)** polished slab of dolomitic limestone with intense recrystallization (Rec) and euhedral pyrite (Epy). **(B–C)** photomicrographs of dolomitic limestone showing disseminated pyrite (Epy) within the crystalline dolomite matrix, syntaxial overgrowth of calcite (Sov) and euhedral dolomitic rhoms (Dol). **(D)** polished slab of calcimudstone showing detail of aragonite pseudomorph crystal fans (Arag). **(E–F)** photomicrographs of calcimudstone showing silica cement (Sic) associated to stylotiles (Sty); organic films (Of) and sparry calcite cement (Scc). **(G)** polished slab of peloidal bindstone with stylolite (Sty). **(H–I)** photomicrographs of peloidal bindstone showing organic films (Of) and sparry calcite cement (Scc). **(J)** polished slab of peloidal bindstone with microbial lamination (Mla). **(K–L)** photomicrographs of peloidal bindstone showing microbial lamination (Mla) and sparry calcite cement (Scc). CPL: Cross-polarized light; PPL Plane-polarized light). Sample code at the upper right corner.

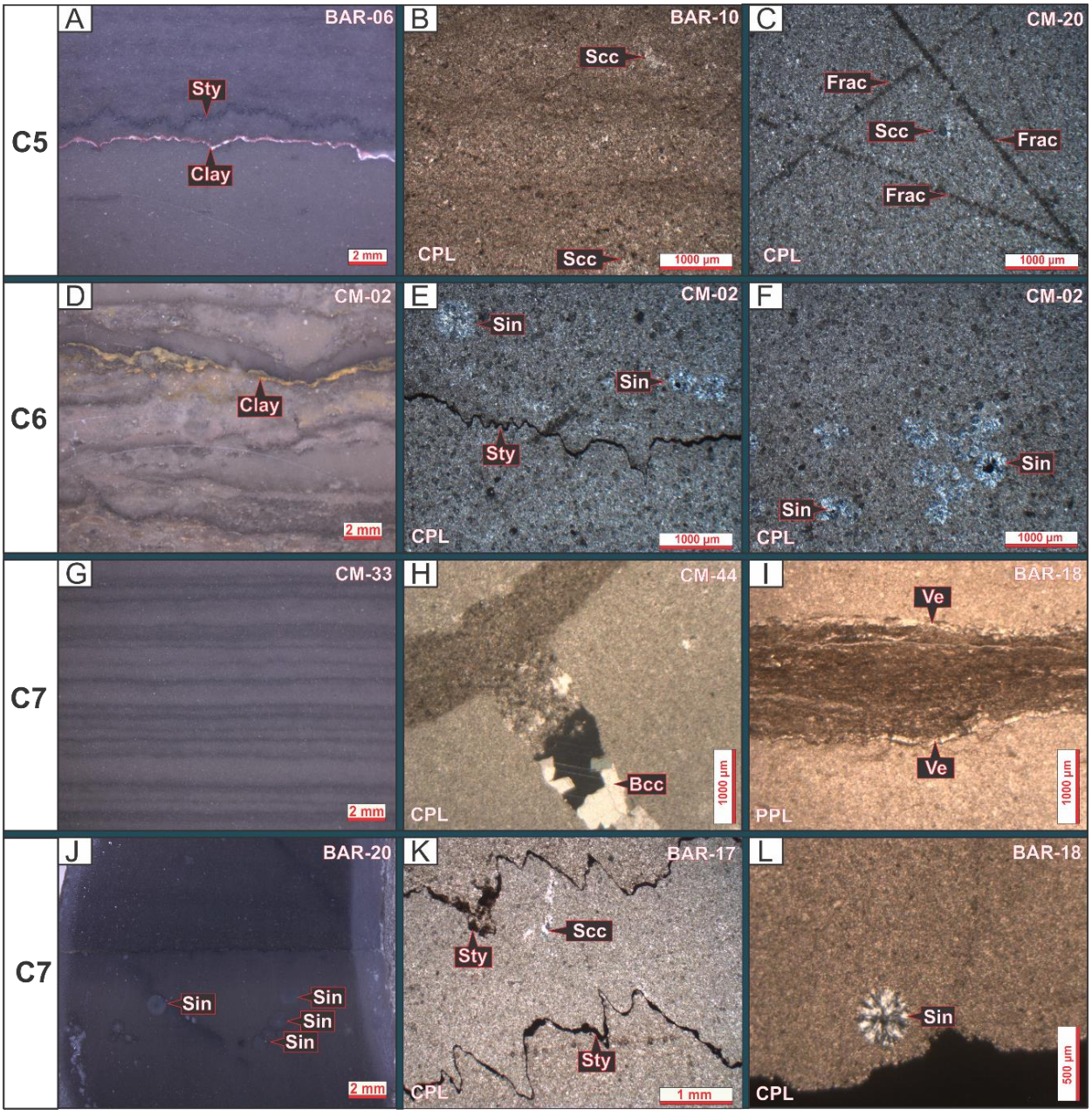

Figure 14. **(A)** polished slab of peloidal calcimudstone with clay laminae (Clay) and stylolite (Sty). **(B–C)** photomicrographs of laminated peloidal calcimudstone showing sparry calcite cement (Scc) and some fractures (Frac). **(D)** polished slab of peloidal bindstone with clay laminae (Clay). **(E–F)** photomicrographs of peloidal bindstone showing stylotiles (Sty) and radiating silica micronodules (Sin). **(G)** polished slab of laminated peloidal calcimudstone. **(H–I)** photomicrographs of peloidal calcimudstone showing dissolution followed by later blocky calcite cement (Bcc) and late diagenetic calcite veins (Ve). **(J)** polished slab of peloidal calcimudstone with spherical silica nodules (Sin). **(K–L)** photomicrographs of peloidal calcimudstone displaying stylolites (Sty), sparry calcite cement (Scc) and a spherical radiating silica micronodule (Sin). CPL: Cross-polarized light; PPL Plane-polarized light. Sample code at the upper right corner.

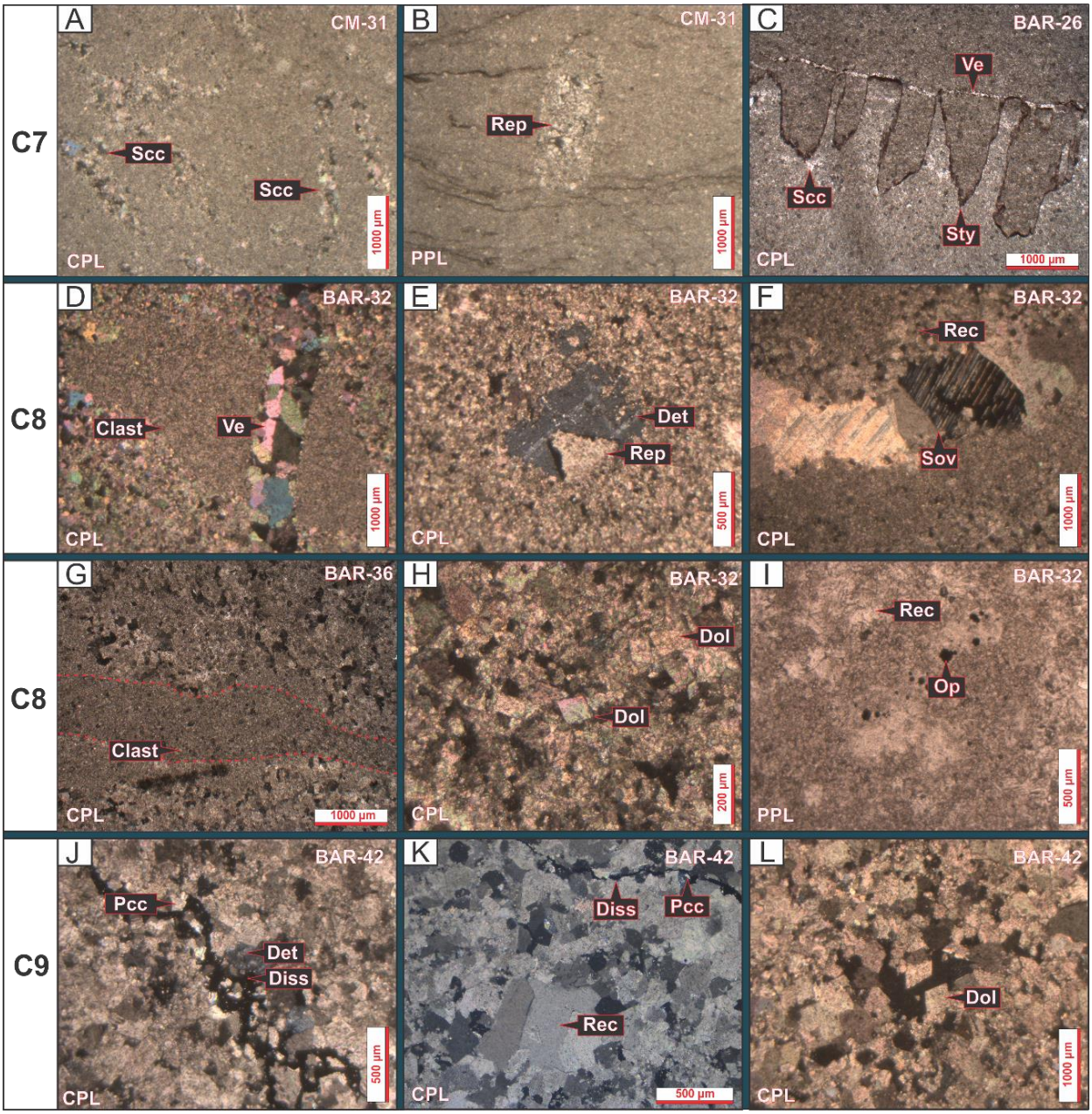

Figure 15. **(A–C)** photomicrographs of laminated peloidal calcimudstones showing sparry calcite cement (Scc), replacement of intraclast by calcite (Rep), stylotites (Sty), and late diagenetic calcite vein (Ve). (**D–I)** photomicrographs of intraclastic rudstone showing detailed micritic clast (Clast) cutted by calcite vein (Ve), replacement (Rep) of detrital grain (Det) by calcite, recrystallization (Rec) and syntaxial overgrowth of calcite (Sov), euhedral dolomite rhoms (Dol) and dispersed opaque grains (Op). **(J–L)** photomicrographs of intraclastic dolograinstone showing detrital grains (Det), dissolution (Diss) and precipitation of phreatic calcite cement (Pcc), recrystalization (Rec) and euhedral dolomite (Dol). CPL: Cross-polarized light; PPL: Plane-polarized light). Sample code at the upper right corner.

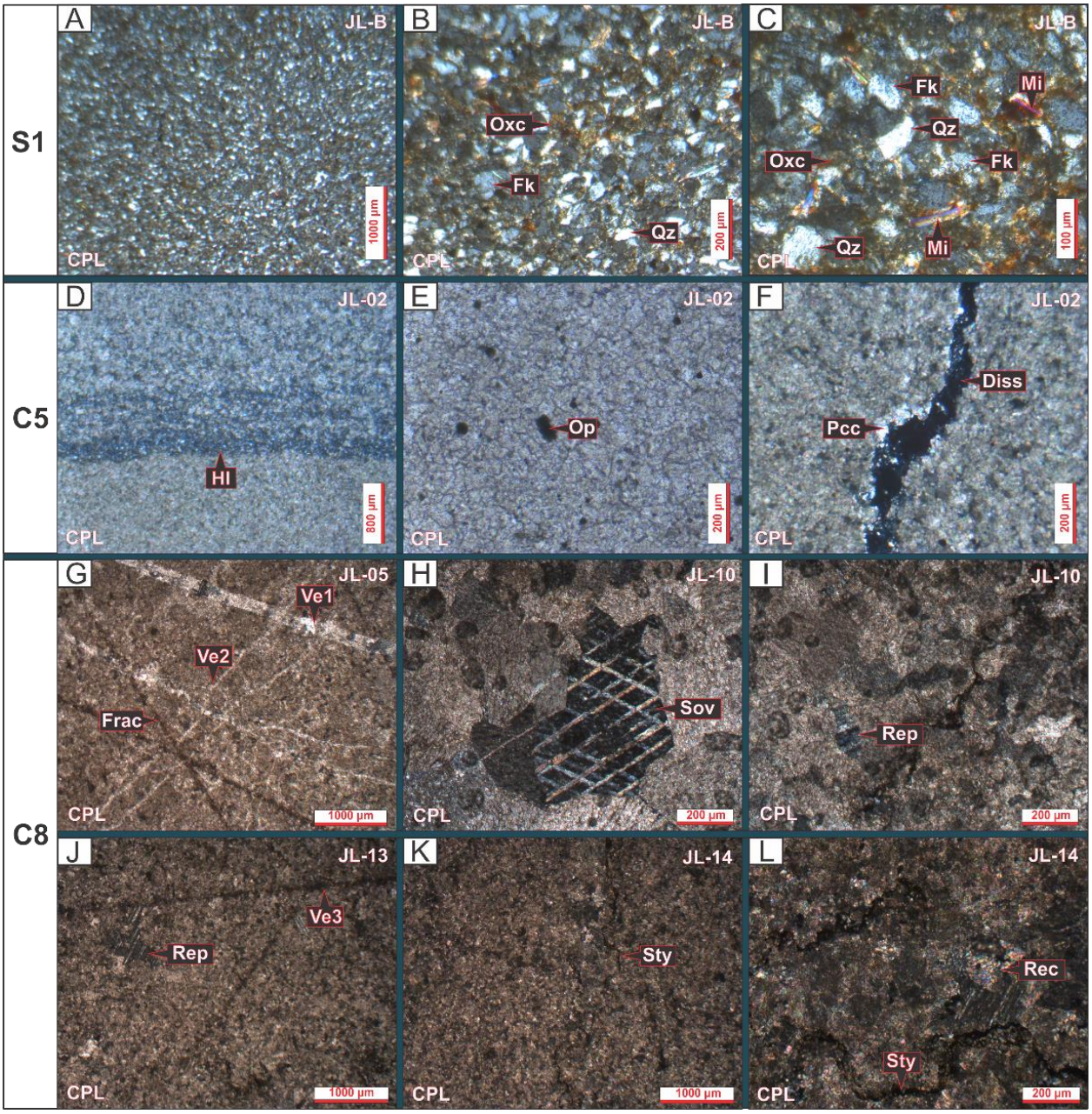

Figure 16. **(A–C)** photomicrographs of siltstones and mudstones composed mainly of detrital quartz (Qz), feldspar (Fk), micas (Mi), and oxidized cement (Oxc). **(D–F)** photomicrographs of peloidal calcimudstone showing preserved horizontal lamination (Hl), dispersed opaque grains (Op), dissolution and precipitation of phreatic calcite cement (Pcc). **(G–L)** photomicrographs of intraclastic rudstone showing diagenetic calcite vein (Ve1) cutted by late diagenetic calcite veinlets (Ve2) and fractures (Frac), syntaxial overgrowth of calcite (Sov), replacement of detrital grains by calcite (Rep) and lesser stylolites (Sty). CPL: Cross-polarized light; PPL Plane-polarized light). Sample code at the upper right corner.

4.5.2 Santa Maria da Vitória section

White to beige dolomitic limestone from facies C1 at the SMV section is less recrystalized than the basal dolomitic facies from Januária section, however, presents intense fracturing and several stages of veinlets and stylolites (Fig. 17A). In thin section, this facies display silica cementation, disseminated opaque grains within a micro-crystalline dolomite matrix, and some fractures (Figs. 17B-C). Light grey to reddish calcimudstone from facies C2 display several levels abundant aragonite pseudomorph crystal fans up to 2000 µm (Figs. 17D-G). Thin sections from this facies show pressure-dissolution structures (stylolites) and calcite vein (Figs. 17H-I). Reddish bindstone from facies C3 presents a carbonate matrix composed of peloidal grains of 20–30 µm with preserved horizontal planar lamination well observed in both polished slabs and thin sections, and some fractures (Figs. 17J-L).

Pinkish to light grey limestone from facies C4 in this section displays clay layers (Fig. 18A), syngenetic euhedral cubic pyrite up to 200 µm long, stylolites and late diagenetic veinless (Figs. 18B-C). In thin sections, this facies show a carbonate matrix of fine peloidal grains of 20–30 µm in diameter, and presents frequent intercalations of brown to green argillaceous laminae, irregular microbial lamination, pressure-dissolution structures and recrystallization (Figs. 18D-F). Dark grey calcimudstone from facies C5 at the SMV section presents abundant stylolites and dissolution seams (Figs. 18G-H). In petrography, this facies show stylolites and sparry calcite cementation within a carbonate matrix of peloidal grains of 20–30 µm, and some areas with recrystallization and fracturing (Figs. 18I-L).

Argillaceous dark grey laminated calcimudstone from facies C7 at the SMV section displays abundant silica nodules associated with stylolites; also exhibits red clays, framboidal pyrite and some late diagenetic vein (Figs. 19A-B). Thin sections show the detailed association between silica cementation (spherical radiating silica micro-nodules) and pressure-dissolution structures (stylolites), within a peloidal matrix composed by grains of 20–60 µm in diameter ((Fig. 19C). Intraclastic rudstone from facies C8 display dark-gray limestone fragments of imbricated flat pebbles to cobbles of 2–10 cm long and subangular to subrounded peebles of 0.5–2 cm (Figs. 19D-F).

White to beige intraclastic dolograinstone from facies C9 at the SMV section presents partial recrystallization and diagenetic calcite veins (Fig. 19G). In petrography,

this facies exhibit puntual dissolution followed by precipitation of rhombic dolomite cement, partial replacement of extraclastic detrital grain by calcite and replacement by euhedral dolomite (Figs. 19H-I). Oolitic to intraclastic grainstones from facies C11 presents moderately-sorted fine to coarse grains with open packing and early cementation (blocky calcite cement). Photomicrographs of intraclastic grainstones show silica cementation and partial recrystallization (Fig. 19J-L).

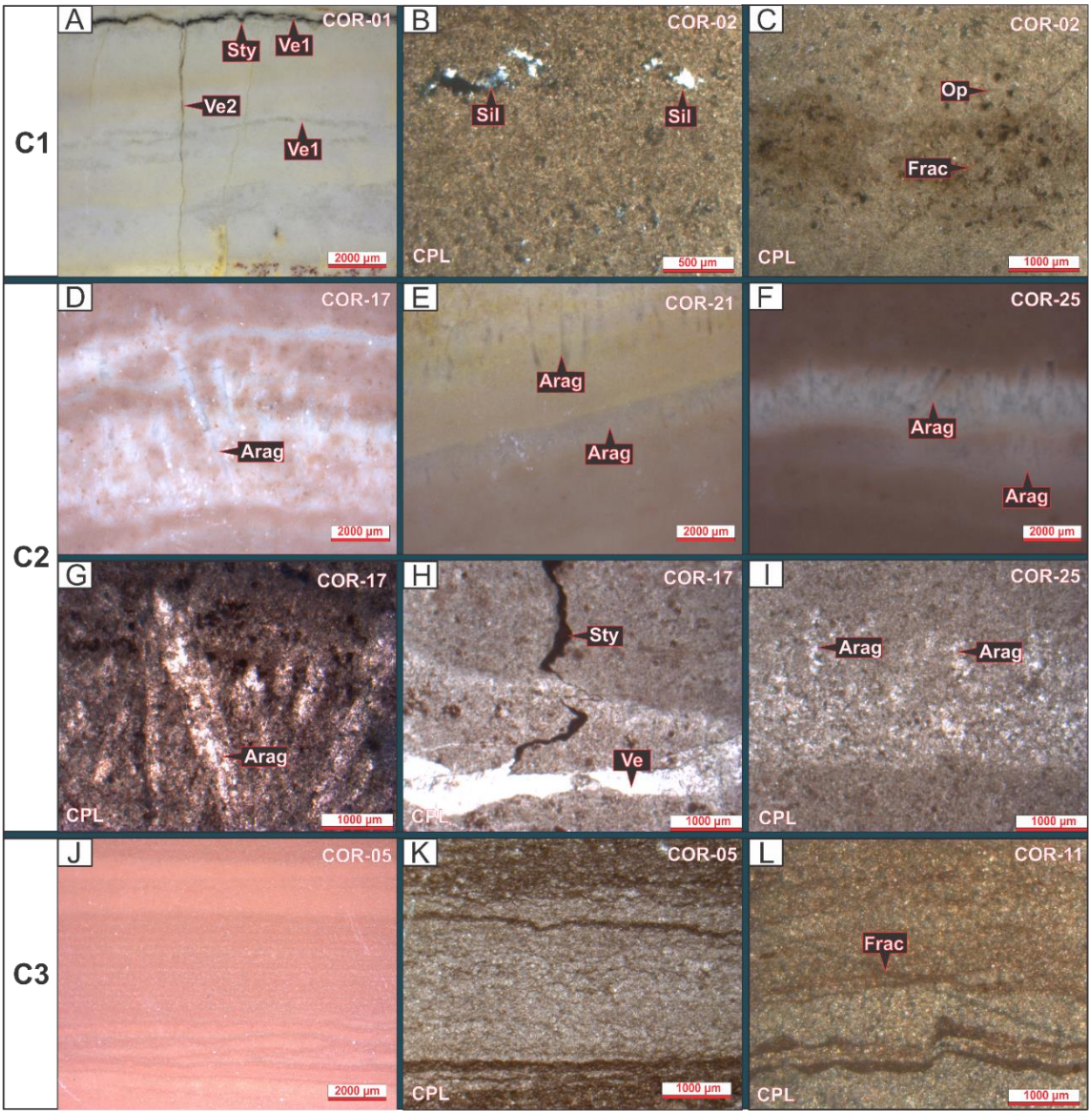

Figure 17. **(A)** polished slab of dolomitic limestone with stylolites (Sty), calcite veinlets (Ve1) and late diagenetic calcite veinlets (Ve2). **(B–C)** photomicrographs of dolomitic limestone showing silica cement (Sil), dispersed opaque grains (Op) and fractures (Frac). **(D–F)** polished slab of calcimudstone showing two levels of aragonite pseudomorph crystal fans (Arag). **(G–I)** photomicrographs of calcimudstone showing detail of aragonite pseudomorph crystal fans (Arag), stylolites (Sty) and calcite vein (Ve). **(J)** polished slab of reddish laminated peloidal bindstone **(K–L)** photomicrographs of laminated peloidal bindstone with fracture (Frac). CPL: Cross-polarized light; PPL Plane-polarized light). Sample code at the upper right corner.

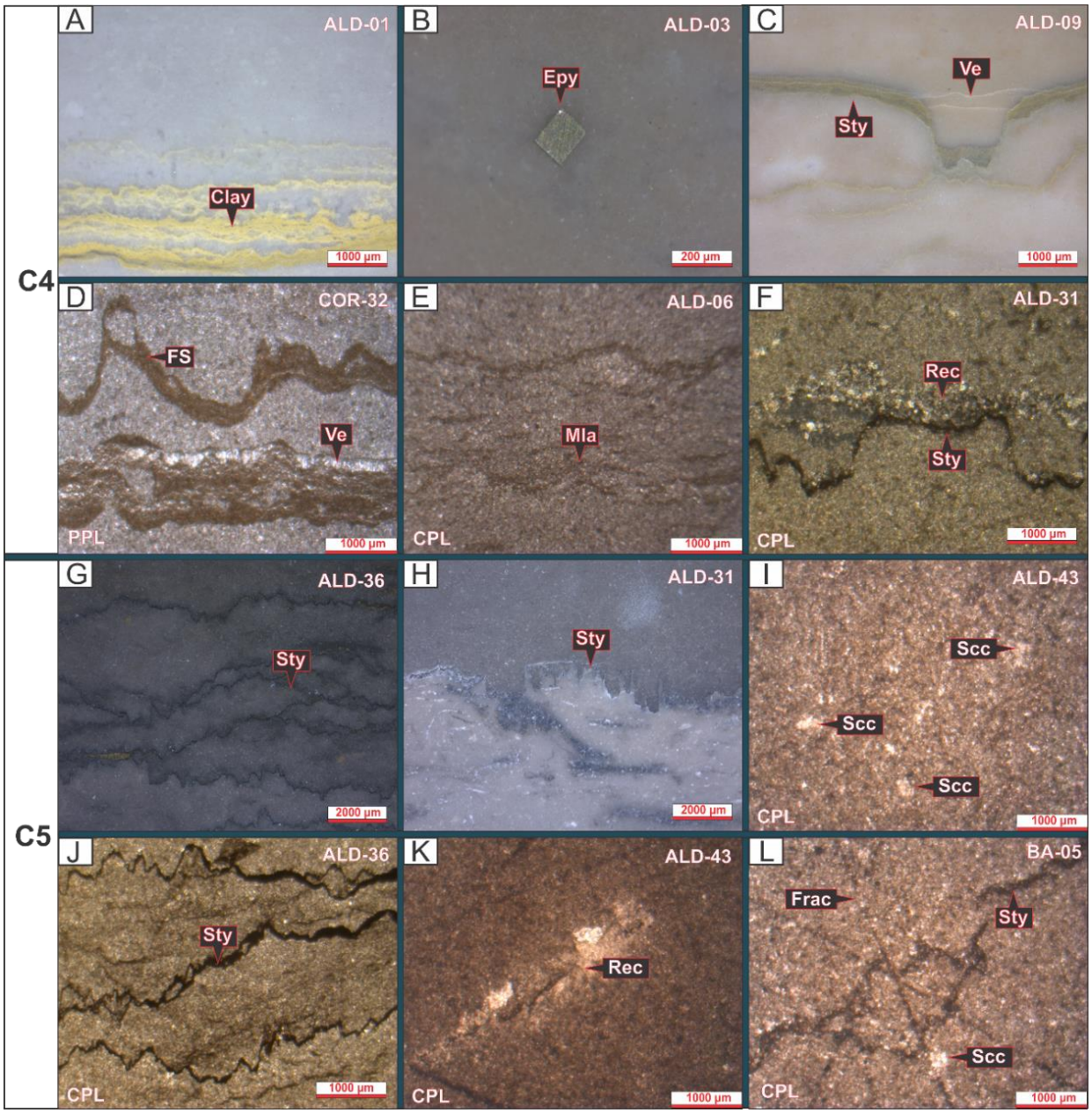

Figure 18. **(A–C)** polished slabs of peloidal bindstone with clay laminae (Clay), euhedral pyrite (Epy), stylolite (Sty) and calcite veinlets (Ve). **(D–F)** photomicrographs of peloidal bindstones showing flame structure (FS) and late diagenetic calcite vein (Ve), microbial lamination (Mla), stylolites (Sty) and

recrystallization (Rec). **(G–H)** polished slab of dark-grey laminated peloidal calcimudstone with stylolites (Sty). **(I–L)** photomicrographs of laminated peloidal calcimudstone displaying recrystallization (Rec), stylolites (Sty) and fractures (Frac). CPL: Cross-polarized light; PPL Plane-polarized light). Sample code at the upper right corner.

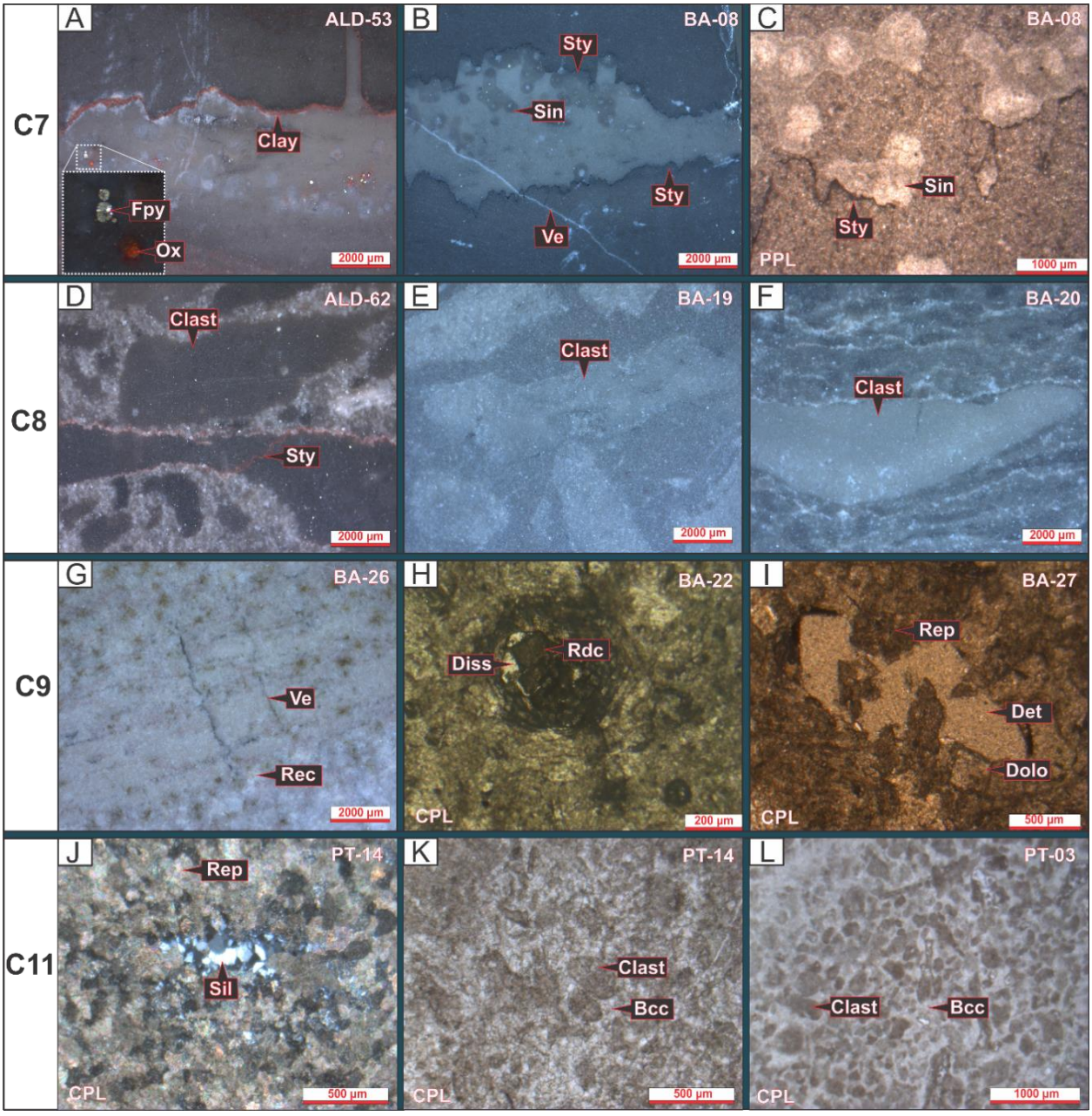

Figure 19. **(A–B)** polished slabs of dark-grey laminated peloidal calcimudstone with clay laminae (Clay), framboidal pyrite (Fpy), oxided sulfides (Ox), spherical micronodules of silica (Sil) associated with stylolites (Sty), late diagenetic calcite veinlet (Ve). **(C)** photomicrograph of laminated peloidal calcimudstones showing spherical radiating micronodules of silica (Sil) associated with stylolites (Sty) (**D–F)** polished slabs of intraclastic rudstone showing clasts (Clast) cutted by stylolite (Sty). **(G)** polished slab of intraclastic dolograinstone with recrystallization (Rec). **(H–I)** photomicrographs of intraclastic dolograinstone showing

dissolution (Diss) followed by precipitation of rhombic dolomite cement (Rdc), replacement of intraclastic detrital grain (Det) by calcite, crystals of euhedral dolomite (Dol). **(J–L)** photomicrographs of intraclastic grainstone showing silica cement (Sil), recrystallization (Rec), carbonate intraclasts (clast) and blocky calcite cement (Bcc). CPL: Cross-polarized light; PPL Plane-polarized light). Sample code at the upper right corner.

4.6 Discussion

4.6.1 Diagenetic history of the basal Bambuí Group

The diagenetic studies that were carried out on carbonates of the basal Bambuí Group at the Januária and Santa Maria da Vitória sections in the Januária High are based on the analysis of carbonate petrography and available geochemical and isotopic data. This allow the determination of the main diagenetic and post-depositional changes on different environments, such as syn-sedimentary marine processes, subaerial (meteoric and shallow phreatic) alteration, and burial diagenesis. A sequenting paragenesis of main diagenetic events and relative importance on carbonates of the Bambuí Group at the Januária High are presented in Fig. 20.

During the first stages of marine diagenesis of the Bambuí Group sediments, syn-sedimentary processes take place on a ramp-type platform development on the Januária paleohigh. This stage records the formation of aragonite sea-floor precipitates followed by sparry calcite cementation and blocky calcite cementation, the latter being presented in cavities associated with soluble material and second generation of calcite cement. The marine sediments of the Bambuí Group were progressively buried, giving rise to important characteristics such as overexpression of syntaxial overgrowth of calcite involving dissolution as well as crystal dislocation as a result of burial loading or tectonic deformation. Neomorphism also occurs at the burial diagenesis, associated with replacement and recrystallization processes, including the coarsening of crystal sizes in calcimudstones and bindstones (aggrading neomorphism) and the replacement of detrital clasts by calcite. Also, silica cementation is associated to pressure-dissolution structures (stylolites), dissolution seams and less important physical compaction evidenced by fractures (Fig. 20).

Silica cementation is one of the most important processes observed in the basal carbonates of the Bambuí Group. This autigenic silica is present in different ways: a) direct silica precipitation: it is occasionally observed in calcimudstones from facies C2 at the Januária section and intraclastic grainstones from facies C11 at the Santa Maria da Vitória section, indicating a silica cement precipitation in cavities in the forms of chalcedony, which is present in amorphous crystals with undulating extinctions. b) spherical radiating silica micro-nodules of 400–800 μm in diameter observed in bindstones and calcimudstone from facies C6 and C7 at the Januária section, and calcimudstones from facies C7 at the Santa Maria da Vitória section, presenting fibrous crystals with undulating extinctions, probably of chalcedony.

There are several sources of silica in diagenetic processes, considering them as the most common solutions in silica generated by pressure-solution of limestones, and biogenic silica, which can derive from the dissolution of organisms producing this element, such as radiolarian and diatom sponges (e. g. Boggs, 1992). According to previous observations in the petrographic analysis, it is assumed that the source of silica for these rocks in the diagenetic process corresponds to the silica-rich solution, generated from the siliciclastic levels found within the Bambuí Group. The silica cementation process of this unit is strongly related to compacting processes, evidenced by the association with stylolites, dissolution seams and fractures. For the foregoing, this interpretation suggests that silica cementation occurs in a diagenetic burial environment.

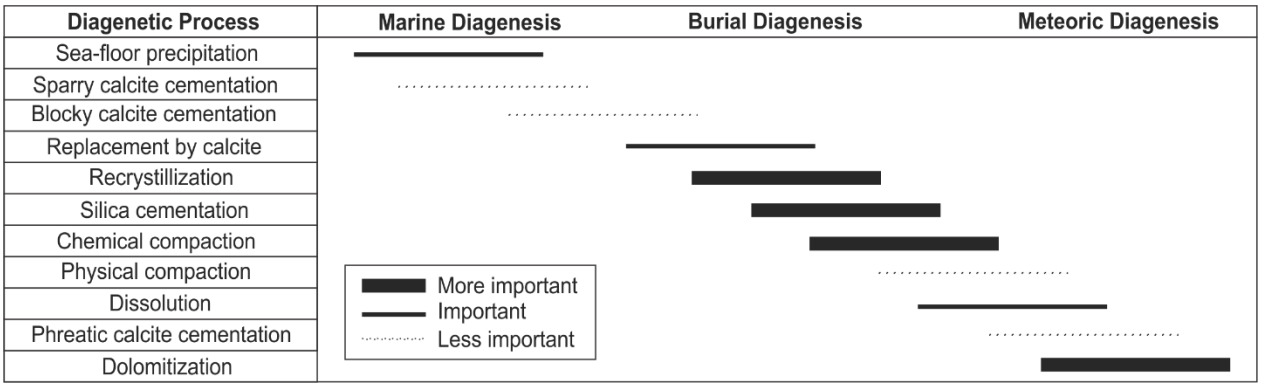

Figure 20. Paragenesis of the main diagenetic events and relative importance on carbonates of the Bambuí Group at the Januária High.

During meteoric diagenesis, tectono-eustatic variations controlled a strong fall in the relative sea level leading to the sub-aerial exposure of the carbonate platform, producing the entry of meteoric waters into the unit (i.e., Caetano-Filho et al. 2019). The interaction of meteoric water with marine carbonate produces the solution and neomorphism of components rigidly composed of calcite and aragonite. As the marine components dissolve, the water that crosses the intraclastic levels of the unit, turns the precipitation of phreatic calcite cement (Fig. 20). Dolomitization is associated with dissolution features, as vugular to moldic porosity, developed in intertidal shallow environments. Caxito et al. (2018) and Caetano-Filho et al., 2019 discussed the effects of sub-aerial exposure on both isotope and elemental chemistry in the lower Sete Lagoas Formation in Santa Maria da Vitoria this same region.

4.7 Conclusions

Different diagenetic environments are recognized in the basal Bambuí Group at the Januária and Santa Maria da Vitória sections on the Januária High. The main processes in the marine diagenesis are sea-floor precipitation, and less important are the sparry and blocky calcite cementation. During burial diagenesis, neomorphism, recrystallization, silica cementation and chemical compaction are the main diagenetic processes in this environment, probably leading to expulsion of interstitial fluids and decreasing of rate of chemical reactions (Boggs, 2009). Finally, dissolution and phreatic calcite precipitation and dolomitization comprises the main diagenetic processes associated to meteoric diagenetic environments (i. e., Caxito et al., 2018; Caetano-Filho et al. 2019).

4.8 References

Boggs, S., 1992. Petrology of sedimentary rocks. New York: Macmillan Publishing Company.

Caetano-Filho, S., Paula-Santos, G.M., Guacaneme, C., Babinski, M., Bedoya-Rueda, C., Peloso, M., Amorim, K., Afonso, J., Kuchenbecker, M., Reis, H.L.S., Trindade, R.I.F.,

2019. Sequence stratigraphy and chemostratigraphy of an Ediacaran-Cambrian foreland-related carbonate ramp (Bambuí Group, Brazil). Precambrian Research 331, 105365.

Caxito, F.A., Frei, R., Uhlein, G.J., Dias, T.G., Árting, T.B., Uhlein, A., 2018. Multiproxy geochemical and isotope stratigraphy records of a neoproterozoic oxygenation event in the Ediacaran Sete Lagoas cap carbonate, Bambuí Group, Brazil. Chemical Geology 481, 119–132.

Dunham, R. J., 1962. Classification of carbonate rocks according to their depositional texture, *in* W. E. Ham, ed., Classification of Carbonate Rocks—a symposium: Tulsa, OK, American Association of Petroleum Geologists Memoir 1, p. 108-121.

Embry, A. F., and J. E. Klovan, 1971. A Late Devonian reef tract on northeastern Banks Island, N.W.T.: Bulletin of Canadian Petroleum Geology, v. 19, p. 730-781.

Flügel, Erik (Ed.), 2004. Microfacies of Carbonate Rocks. Springer Berlin Heidelberg, Berlin, Heidelberg.

Folk, R. L., 1962. Spectral subdivision of limestone types, *in* W. E. Ham, ed., Classification of Carbonate Rocks—a symposium: Tulsa, OK, American Association of Petroleum Geologists Memoir 1, p. 62-84.

Iglesias-Martínez, M. 2007. Estratigrafia e Tectônica do Vale do Rio São Francisco no norte de Minas Gerais. MSc. Dissertation, IGC-UFMG

Martins, M., Lemos, V.B., 2007. Análise estratigráfica das sequências neoproterozoicas da Bacia do São Francisco. Revista Brasileira de Geociências 37 (4), 156–167.

Miranda, L.F., 2003. Bacia do São Francisco entre Santa Maria da Vitória e Iuiú, Bahía: geologia e potencialidade econômica. Companhia Baiana de Pesquisa Mineral - CBPM

Okubo, J., Muscente, A.D., Luvizotto, G.L., Uhlein, G.J., Warren, L.V., 2018. Phosphogenesis, aragonite fan formation and seafloor environments following the Marinoan glaciation. Precambr. Res. 311, 24–36.

Perrella Jr., P., Uhlein, A., Uhlein, G.J., Sial, A.N., Pedrosa-Soares, A.C., Lima, O.N.B., 2017. Facies analysis, sequence stratigraphy and chemostratigraphy of the Sete Lagoas Formation (Bambuí Group), northern Minas Gerais State, Brazil: evidence of a cap carbonate deposited on the Januária basement high. Braz. J. Geol. 47, 59–77.

Reis, H.L.S., Suss, J.F., 2016. Mixed carbonate-siliciclastic sedimentation in forebulge grabens: an example from the Ediacaran Bambuí Group, São Francisco Basin, Brazil. Sedimentary Geology 339, 83–103.

Scholle, P.A., Ulmer-Scholle, D.S. 2003. A Color Guide to the Petrography of Carbonate Rocks: Grains, textures, porosity, diagenesis. AAPG Memoir 77

Tucker, M. E., 2001. Sedimentary petrology: an introduction to the origin of sedimentary rocks. Blackwell Scientific Publications —3rd ed.

Tucker, M., Wright V.P. (1990). Carbonate sedimentology. Londres: Blackwell Scientific Publications.

Vieira, L.C., Almeida, R.P., Trindade, R.I.F., Nogueira, A.C.R., Janikian, L., 2007a. A Formação Sete Lagoas em sua área-tipo: fácies, estratigrafia e sistemas deposicionais. Revista Brasileira de Geociências, 37:1-14.

Vieira, L.C., Trindade, R.I.F, Nogueira, A.C.R., Ader, M., 2007b. Identification of a Sturtian cap carbonate in the Neoproterozoic Sete Lagoas carbonate plataform, Bambuí Group, Brazil. Comptes Rendus Geoscience, 339:240-258.

Vieira, L.C., Nedelec, A., Fabre, S., Trindade, R.I.F., de Almeida, R.P., 2015. Aragonite Crystal Fans In Neoproterozoic Cap Carbonates: A Case Study From Brazil and Implications For the Post-Snowball Earth Coastal Environment. Journal of Sedimentary Research 85, 285–300.

Wilkin, R.T., Barnes, H.L., 1997. Formation processes of framboidal pyrite. Geochim. Cosmochim. Acta 61, 323–339.

Wright, V.P., 1992. A revised classification of limestones. Sed. Geol. 76, 177–186.

Zalán, P.V., Romeiro-Silva, P.C., 2007. Bacia do São Francisco. Boletim de Geociências Petrobrás 15 (2), 561–571.

5 CHAPTER 5 – TECTONICALLY-INDUCED STRONTIUM ISOTOPES CHANGES IN RESTRICTED SEAS: THE CASE OF THE EDIACARAN-CAMBRIAN BAMBUÍ FORELAND BASIN SYSTEM, EAST BRAZIL

Authors

Cristian Guacaneme[a]*, Marly Babinski[a], Carolina Bedoya-Rueda[a], Gustavo M. Paula-Santos[b], Sergio Caetano-Filho[a], Matheus Kuchenbecker[c,d], Humberto L.S. Reis[e], Ricardo I.F. Trindade[f]

[a]Universidade de São Paulo, Instituto de Geociências, Rua do Lago, 562, São Paulo, Brazil – ZIP code 05508-080

[b]Universidade de Campinas, Instituto de Geociências, Rua Carlos Gomes 255, Campinas, Brazil – ZIP code 13083-855

[c]Universidade Federal dos Vales do Jequitinhonha e Mucuri, Instituto de Ciência e Tecnologia, Centro de Estudos em Geociências, Laboratório de Estudos Tectônicos, Rodovia MGT 367, Km 583 – Diamantina, Brazil – ZIP code 39100-000

[d]Universidade Federal de Minas Gerais, Centro de Pesquisas Professor Manoel Teixeira da Costa. Av. Antônio Carlos, 6627 – Belo Horizonte, Brazil - ZIP code 31270-901

[e]Universidade Federal de Ouro Preto, Departamento de Geologia-Escola de Minas, Laboratório de Modelagem Tectônica (LabMod), Campus Morro do Cruzeiro, Ouro Preto, Brazil – ZIP code 35400-000

[f]Universidade de São Paulo, Instituto de Astronomia, Geofísica e Ciências Atmosféricas, Rua do Matão, 1226 - São Paulo, Brazil – ZIP code 05508-090

5.1 Abstract

The Bambuí Group is a marine sedimentary record of an intracratonic foreland basin developed at the terminal Ediacaran and early Cambrian during the assembly of West Gondwana. Here we present a basin-scale high-resolution Sr isotope stratigraphy for the basal Bambuí Group, aiming to understand the spatial and temporal variations of the $^{87}Sr/^{86}Sr$ ratios and to explore the controls over the Sr isotope system in intracontinental marine environments. Assessment of the stratigraphic evolution of both Sr concentrations and Sr isotopes shows a major increase in Sr/Ca ratios (up to 0.004) and a decrease in the $^{87}Sr/^{86}Sr$ ratios from 0.7086 to 0.7076 in the high stand system tract of the basal 2nd-order sequence. These changes precede a large positive $\delta^{13}C$ excursion typically found across the basin in the middle Bambuí Group. The high variability of both $^{87}Sr/^{86}Sr$ and Sr/Ca ratios was not caused by globally uniform changes in isotopic compositions of seawater, but rather likely reflect marine restriction and paleogeographic changes of the depositional environments at basin scale. This would result from the tectonic uplift of Neoproterozoic orogenic belts around the São Francisco craton, which generated an isolated foreland marine basin. Compared to the global ocean, such a smaller intracontinental reservoir would be more sensitive to the Sr isotope composition from the different rock sources. We suggest that changes on the balance between carbonate production and accommodation associated with tectonically-related flexural subsidence progressively modified the continental drainage patterns, sedimentary sources and the chemical weathering regimes, altering the strontium influxes and isotopic compositions of the seawater in the early Bambuí basin cycle. Similar anomalies in the strontium isotope record are also recorded in coeval marine basins across West Gondwana and suggest that tectonics might have played an important role on seawater chemistry at the Neoproterozoic–Paleozoic transition.

Keywords: Ediacaran-Cambrian, São Francisco Basin, strontium isotopes, foreland basin

5.2 Introduction

The assumption that modern oceans are homogeneous with respect to $^{87}Sr/^{86}Sr$ ratios is based on the residence time of Sr (10^6 years) in this reservoir, which is far higher than its mixing time (10^3 years) and also in the efficient oceanic circulation patterns observed in the modern Earth's tectonic configuration. (Elderfield, 1986; Hodell et al., 1990; Veizer, 1989; Veizer et al., 1999; Krabbenhoft et al., 2010; McArthur et al., 2012). This fact has endorsed this isotopic proxy to be used to correlate marine sedimentary successions worldwide, especially in Precambrian sections where biostratigraphic data is scarce (Melezhik et al., 2001; Halverson et al., 2007, 2010; Krabbenhoft et al., 2010; McArthur et al., 2012; Kuznetsov et al., 2013). Moreover, considering the continental weathering regime and hydrothermal fluxes related to oceanic crust spreading as the main controls over this marine isotope system, the $^{87}Sr/^{86}Sr$ ratio is an essential tool for understanding the tectonic processes of the past and their impacts on marine ecosystems, habitats, biological diversity, and geochemical cycles (DePaolo and Ingram, 1985; Chaudhuri and Clauer, 1986; Palmer and Edmond, 1989; Zaky et al., 2019).

In modern epicontinental basins, however, variations in climate and sea-level changes can strongly influence the $^{87}Sr/^{86}Sr$ record, and continental water inputs can locally modify the Sr isotope compositions of the basins (i. e., Ingram and Sloan, 1992; Huang et al., 2011; Beck et al., 2013; Schildgen et al., 2014; Peucker-Ehrenbrink and Fiske, 2019). For instance, on longer time scales, low $^{87}Sr/^{86}Sr$ ratios in the Miocene record of the Mediterranean Sea adjacent to the uplifting Alps and Apennines mountains, are attributed to a high influx of Sr from non-radiogenic $^{87}Sr/^{86}Sr$ Mesozoic carbonates in the hinterland coupled with restricted exchange of water with the global oceans (Schildgen et al., 2014). Therefore, the continental flux of Sr into the oceans does not necessarily have to be radiogenic but rather depends on changes in spatial distribution and the age of the exoreic continental bedrock, climate and drainage patterns through geological time (i.e., Peucker-Ehrenbrink and Fiske, 2019).

The strontium isotope record of the Ediacaran-Cambrian marine carbonates from the Bambuí Group, in the São Francisco Basin, shows a potential link between major geochemical disturbances on the Sr budget and episodic restriction of the marine basin during Gondwana assembly (Paula-Santos et al., 2017). This sedimentary unit presents non-radiogenic $^{87}Sr/^{86}Sr$ ratios, mismatching those expected for the late Ediacaran and early Cambrian record (Melezhik et al., 2001; Halverson et al., 2010; Kuznetsov et al., 2013; Zaky et al. 2019). Additionally, a regional increase in Sr/Ca ratios is observed in the 2nd-order scale, preceding an extremely coupled positive $\delta^{13}C$ excursion (reaching values as high as +16‰ and −14‰, for $\delta^{13}C_{carb}$ and $\delta^{13}C_{org}$, respectively; Iyer et al., 1995; Caetano-Filho et al., 2020), suggesting that tectonics and/or climate induced changes in seawater chemistry, triggering biochemical responses (Caetano-Filho et al., 2019; 2021).

Here, we present a basin-scale high-resolution Sr isotope stratigraphy for the basal Bambuí Group, aiming to understand the spatial and temporal variations of the $^{87}Sr/^{86}Sr$ ratios and explore the controls over the Sr isotope system in ancient intracontinental marine environments. We also aim to better understand how tectonic and climate changes may have impacted the biogeochemical cycles of the basin. Major paleogeographic reconfigurations, orogeneses and strong climatic oscillations had occurred at the Ediacaran–Cambrian transition, which are apparently linked to geochemical disturbances and to profound ecological innovations in the marine ecosystems (Kaufman et al., 1997; Knoll et al., 2006; Canfield et al., 2007; Hoffman et al., 1998; Hoffman and Schrag, 2002; Campbell and Squire, 2010; Young, 2013; Reis and Suss, 2016).

5.3 Geological Setting

5.3.1 The São Francisco basin in West Gondwana

The São Francisco craton, together with the Congo craton, in western Africa, corresponds to the inner and most stable part of one of the continents involved in the assembly of West Gondwana supercontinent (Fig. 21B), during Neoproterozoic–Paleozoic transition (e.g. Alkmim et al., 2006; Heilbron et al., 2017). The

craton is surrounded by diachronic Neoproterozoic mobile belts, namely Brasília (west), Araçuaí (east), Rio Preto, Riacho do Pontal and Sergipano (north) each one presenting a singular tectonic and structural history (e.g. Alkmim et al., 2017; Caxito et al., 2017; Valeriano, 2017 and references therein).

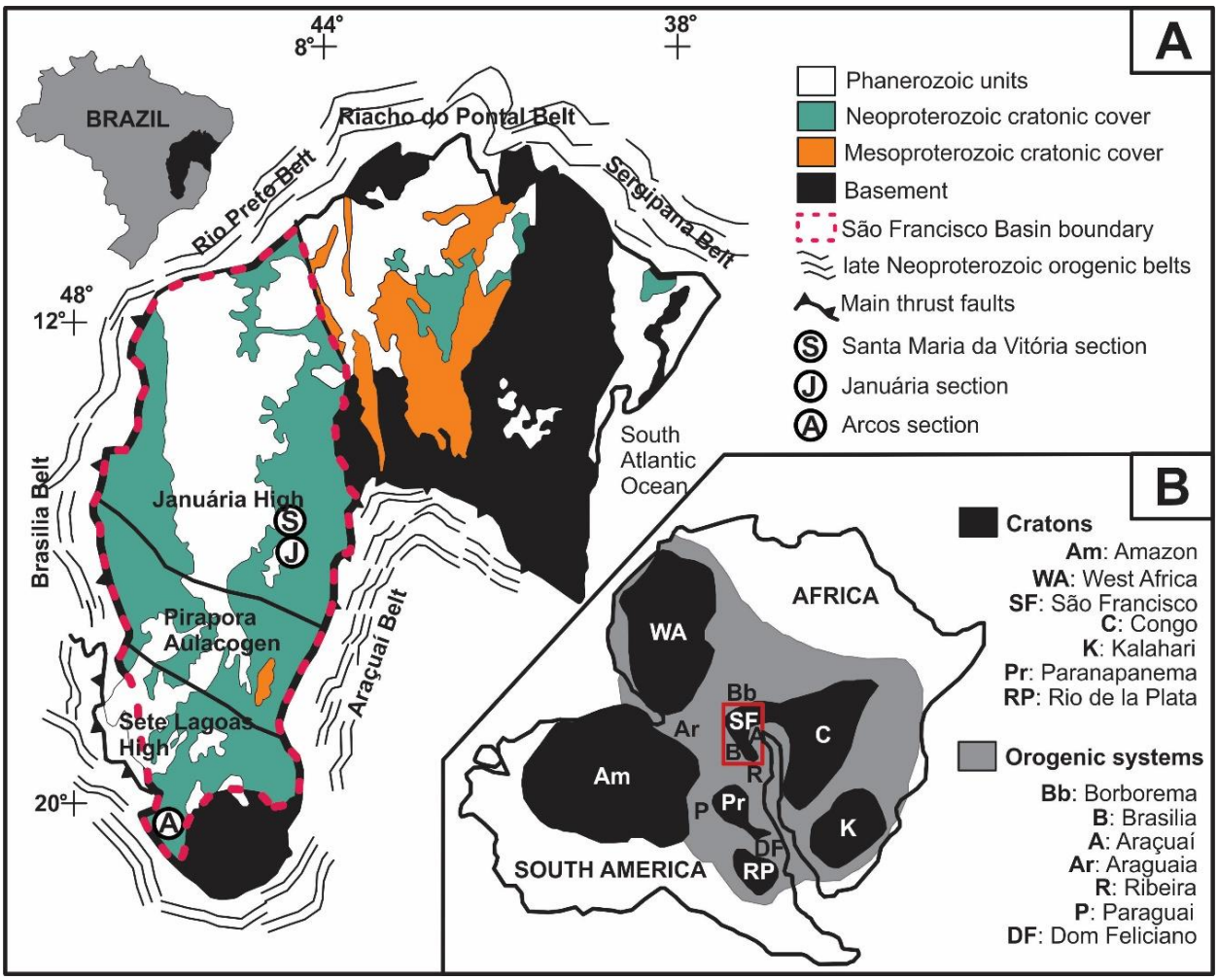

Figure 21. A. Geological map of the São Francisco Basin (east-central Brazil) with location of stratigraphic sections. (modified from Caetano-Filho et al., 2019) **B**. Paleogeographic reconstruction of the late Neoproterozoic West Gondwana (modified from Alkmim et al., 2006).

As consolidated in the literature, the São Francisco basin (Fig. 21A) encompasses the various sedimentary units that cover a large part of the homonymous craton, representing in fact, a set of superposed sedimentary basins (e.g. Alkmim and Martins Neto 2001; Reis et al., 2017). These sedimentary units unconformably overly the Archean

to Paleoproterozoic cratonic basement, and occur within three major structural domains: the Pirapora Aulacogen, a buried NW-trending graben at the central portion of the basin, and two basement highs, named Sete Lagoas and Januária, which bound this aulacogen to south and north, respectively (Fig. 21A).

At the end of the Neoproterozoic era, the São Francisco basin hosted the sediments of a complex foreland system developed on the São Francisco craton in response of the multiple loads exerted by the growth of the surrounding orogens (e.g. Martins-Neto, 2005, 2009; Alkmim et al. 2006; Alkmim and Martins-Neto, 2012; Reis et al., 2016, 2017; Pimentel et al., 1999; Santos et al., 2000; Alkmim and Martins-Neto, 2001; Reis and Suss, 2016; Kuchenbecker et al., 2020). The rocks encompassed in the Bambuí Group are the remaining records of a late stage of such foreland system (Kuchenbecker et al., 2020).

The Bambuí Group consists of mixed carbonate-siliciclastic succession that can reach up to 3km-thick in its main depocenter (Alkmim and Martins-Neto, 2012; Martins-Neto, 2009; Reis and Suss, 2016; Reis et al., 2017; Caetano-Filho et al., 2019). The lithostratigraphic array of the group (Costa and Branco, 1961; Dardenne, 1978) includes six basinwide formations (base to top): Carrancas (diamictite, pelite, dolomite), Sete Lagoas (limestone, dolomite, pelite), Serra de Santa Helena (pelite, limestone), Lagoa do Jacaré (limestone, pelite), Serra da Saudade (pelite, limestone) and Três Marias (sandstone, pelite). The Samburá (conglomerate) and Lagoa Formosa (conglomerate, pelite, dolomite) formations are restricted to the western border of the basin (Castro and Dardenne, 2000; Uhlein et al., 2011; Uhlein et al., 2017), while the Jaíba (limestone) and Gorutuba (conglomerate, sandstone) formations occur only in its eastern border (Chiavegatto et al., 2003; Kuchenbecker et al., 2016b).

The occurrences of the index fossil *Cloudina* sp (Warren et al., 2014; Perrella et al., 2017) and the presence of c. 550 Ma zircons (e.g. Paula-Santos et al. 2015; Kuchenbecker et al., 2020) in the Sete Lagoas Formation converge towards an Ediacaran-Early Cambrian age for the deposition of the Bambuí Group. This was reinforced by the dating of a tuff layer within Serra da Saudade Formation, which yielded the age of 520.2 ± 5.3 Ma (Moreira et al., 2020).

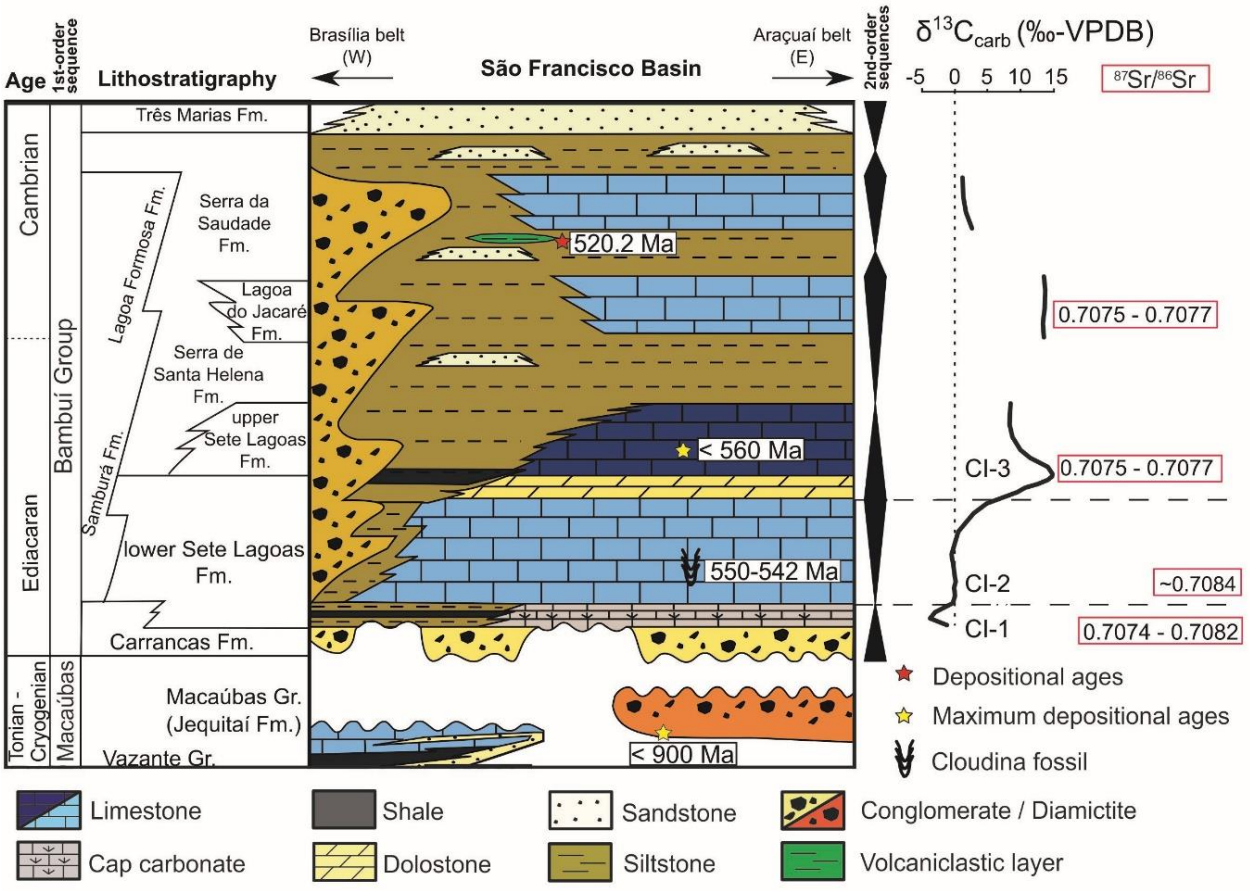

Figure 22. Lithostratigraphic chart of the 1st-order Bambuí Sequence and chemostratigraphic evolution in the São Francisco Basin (modified from Caetano-Filho et al., 2019). *Cloudina* sp. index fossil defines a late Ediacaran age (lower Sete Lagoas Formation - Warren et al., 2014). Maximum depositional ages are represented by the yellow stars (Macaúbas Group – Babinski et al., 2012; upper Sete Lagoas Formation – Paula-Santos et al., 2015), depositional age of volcaniclastic layer is represented by the red star (upper Serra da Saudade Formation - Moreira et al., 2020). Chemostratigraphic Intervals (CI) from Paula-Santos et al. (2017).

5.3.2 Sequence stratigraphy and chemostratigraphy of the basal Bambuí Group

In the last decades, many studies about the stratigraphic architecture and chemostratigraphic patterns of the Bambuí Group have been carried out to investigate the basin's evolution and paleoenvironmental conditions (e.g. Santos et al., 2000, 2004; Martins and Lemos 2007; Misi et al., 2007; Vieira et al., 2007; Babinski et al., 2007; Caxito et al., 2012, 2018; Reis and Suss, 2016; Alvarenga et al., 2014; Warren et al., 2014; Paula-Santos et al., 2015, 2017; Kuchenbecker et al., 2016a; Perrella et al., 2017;

Guacaneme et al., 2017; Uhlein et al., 2016, 2019; Hippertt et al., 2019; Caetano-Filho et al., 2019, 2020).

The Bambuí Group has been envisaged as an unconformity-bounded 1st-order sequence, which encompasses four retrogradational-progradational 2nd order sequences (e.g. Martins and Lemos 2007; Reis and Suss 2016; Caetano-Filho et al. 2019; Uhlein et al., 2019). The focus of this paper is the basal 2nd order sequence, which has been the most studied interval of the basin.

From a chemostratigraphic perspective, Paula-Santos et al., (2017) divided the basal Bambuí Group in three Chemostratigraphic Intervals (CIs) based on $\delta^{13}C$ values and $^{87}Sr/^{86}Sr$ ratios (Fig. 22), which are associated with three different stages of the basin. Integrating the previous contributions, Caetano-Filho et al. (2019) presented a basin-scale sequence stratigraphy framework for the basal 2nd-order sequence of the Bambuí Group coupled to the chemostratigraphy patterns described by Paula-Santos et al. (2017). This framework is briefly described below.

The lowermost Bambuí 2nd-order sequence is up to a few hundreds of meters-thick, and comprises a basal transgressive system tract (TST) and a highstand systems tract (HST). The TST is formed by the coarse-grained siliciclastics of the Carrancas Formation grading upward into the carbonates and pelites of Sete Lagoas Formation, in a retrogradational stacking pattern (Vieira et al., 2007a; Kuchenbecker et al., 2013, 2016a; Reis et al., 2016; Caetano-Filho et al., 2019). This interval is bounded in the top by a maximum flooding surface and encompasses the CI-1 of Paula-Santos et al. (2017), which records a sharp increase of the $^{87}Sr/^{86}Sr$ ratios from 0.7074 to 0.7082 (e.g., Babinski et al., 2007). The TST cap carbonates commonly present aragonite pseudomorph fans and negative to positive $\delta^{13}C$ excursions from –5 to c. 0‰ (Santos et al., 2000; Babinski et al., 2007; Vieira et al., 2007b, 2015; Caxito et al., 2012; 2018; Alvarenga et al., 2014; Kuchenbecker et al. 2016a, Paula-Santos et al., 2015, 2017), which are typical features of Neoproterozoic post-glacial deposits (Hoffman et al., 1998; Hoffman and Schrag, 2002). Sr contents of the TST carbonates are low (< 500 ppm), resulting in low average Sr/Ca ratio of 0.001 (Caetano-Filho et al., 2019).

The overlying highstand systems tract (HST) encompasses the carbonate-dominated successions of the basal to middle Sete Lagoas Formation (Reis and Suss,

2016; Caetano-Filho et al., 2019). Defining a progradational pattern, the HST evolves from outer to inner carbonate ramp deposits (Reis and Suss, 2016). This systems tract corresponds to most of the CI-2, which shows $\delta^{13}C$ values around 0‰ and $^{87}Sr/^{86}Sr$ ratios of ~0.7084 (Paula-Santos et al., 2017 – Fig. 22). Considering the occurrence of the index fossil *Cloudina* sp. within this interval (Warren et al., 2014; Perrella et al., 2017) and the overall tectono-stratigraphic architecture of the Ediacaran–Cambrian strata, it has been proposed that the Bambuí inner sea was connected to the global ocean, allowing the strontium isotope homogenization and animal migration. An important basin-wide geochemical change in the Sr content and Sr/Ca ratios is observed within this HST, allowing its subdivision into a basal early highstand systems tract (EHST) and an upper late highstand systems tract (LHST) (Caetano-Filho et al., 2019).

The EHST is represented by dark-gray calcimudstones to bindstones with very low terrigenous contents, displaying slightly positive $\delta^{13}C$ values between 0 and +1‰ right above the MFS, and a slight increase in the Sr content. Average Sr/Ca ratio remains similar to the lower TST around 0.001. This stratigraphic interval marks the stabilization of a marine carbonate ramp in the basal Bambuí sequence, with predominance of carbonate sedimentation (Caetano-Filho et al., 2019). The LHST presents mainly bindstones and peloidal calcimudstones deposited in mid- to inner ramp settings (Reis and Suss, 2016; Caetano-Filho et al., 2019), whose chemostratigraphic features record major paleoenvironmental changes in the basin, probably enhanced seawater alkalinity (Paula-Santos et al., 2020). In the LHST, a remarkable increase in Sr content is observed, reaching up to 3500 ppm, and Sr/Ca ratios with an average value of 0.004. Such increase is not followed by a change in the carbonate facies through regressive systems tract, neither by any major increase in carbonate content. This interval is correlative to the *Cloudina* fossil interval of Warren et al. (2014).

An erosional unconformity locally associated with dolomitic layers and subaerial exposure features bounds the upper 2^{nd}-order sequence boundary. This unconformity is overlain by the next retrogradational-progradational 2^{nd}-order sequence, represented by the deposits of the uppermost Sete Lagoas Formation and the Serra de Santa Helena and Lagoa do Jacaré formations (Reis and Suss, 2016; Caetano-Filho et al., 2019). The carbonate rocks of this sequence show an extreme positive $\delta^{13}C$ excursion that reach

values as high as +16‰ (i.e., Iyer et al., 1995), with these unusual heavy carbon isotope compositions persisting throughout the 2nd-order sequence (Middle Bambuí Isotope Excursion; Uhlein et al., 2019; Caetano-Filho et al., 2020 – Fig. 22). This interval corresponds to the CI-3 from Paula-Santos et al. (2017).

The $^{87}Sr/^{86}Sr$ ratios recorded in the CI-3 decrease to 0.7074–0.7076 (Caxito et al., 2012; Alvarenga et al., 2014; Paula-Santos et al., 2015, 2017) and deviate from the $^{87}Sr/^{86}Sr$ ratios around 0.7084 expected for late Ediacaran to early Cambrian carbonate successions (Melezhik et al., 2001; Halverson et al., 2010; Kuznetsov et al., 2013; Zaky et al. 2019). Thus, this interval might be interpreted as marking the increasingly restricted conditions of the Bambuí foreland system, caused by the continuous uplift of the surrounding orogenic belts. It would have culminated with a restricted or absent connection with global water reservoirs, limiting the water circulation and isotope system homogenization (Kuchenbecker et al. 2016a, Paula-Santos et al., 2017; Uhlein et al., 2019; Hippertt et al., 2019; Caetano-Filho et al., 2019).

5.4 Samples and Methods

5.4.1 Studied sections

In this study, three stratigraphic sections of the basal Bambuí Group were described and sampled from different portions the São Francisco Basin, corresponding to the Arcos, Januária and Santa Maria da Vitória sections (Fig. 21A). Description of sedimentary facies, sequence stratigraphy framework, chemostratigraphy and correlation of these sections were previously presented by Kuchenbecker et al. (2016a) and Caetano-Filho et al. (2019). They encompass the two lowermost 2nd-order sequences from the Bambuí Group, recording the typical $\delta^{13}C$ and Sr/Ca ratios evolution presented in section 2.2. The stratigraphic correlation was based on the identification of two major stratigraphic surfaces (a maximum flooding surface and an unconformity) and stratigraphic stacking patterns (Figs. 23–25).

The Arcos section is a 175 meters-thick continuous section obtained from drill-cores acquired at the southern portion of the basin (Figs. 21 and 23). It records the lowermost 2nd-order sequence from the Bambuí Group, represented by the Carrancas and Sete Lagoas formations unconformably overlying the Archean cratonic basement within the Sete Lagoas High. In this section, the TST is marked by a fining-upward pattern comprising basal diamictites that grade upward into intraclastic calcarenites and calcilutites, and then to marlstones and siltstones, which marks the MFS. These limestones present aragonite pseudomorph crystal fans and display negative δ^{13}C values of CI-1 (Kuchenbecker et al., 2016a; Paula-Santos et al., 2017; Caetano-Filho et al., 2019), which led to the interpretation of post-glacial cap carbonates formed under the influence of melted freshwaters (Kuchenbecker et al., 2016a). Upward, calcilutites grade into marlstones and siltstones that mark the MFS (Fig. 23). The EHST is defined by the transition of siltstones to intraclastic limestones that grade into a thick package of calcilutites with microbial lamination and interbedded shales, presenting a plateau of δ^{13}C values close to +1‰, matching the CI-2 (Kuchenbecker et al. 2016a; Paula-Santos et al., 2017; Caetano-Filho et al., 2019). Within the microbial calcilutites interval, an abrupt increase in Sr/Ca ratios defines the LHST, ending with thick beds of coarse-grained dolostones and oolitic dolostones (Caetano-Filho et al., 2019). Intraclastic carbonate breccia layers mark the upper sequence boundary (SB1) Kuchenbecker et al., 2016a; Reis and Suss, 2016; Caetano-Filho et al., 2019 – Fig. 23). The dolostones grade upward into dark stromatolitic limestones with a large positive δ^{13}C excursion up to +8‰ and low Sr/Ca ratios in the overlying sequence (Kuchenbecker et al. 2016a; Caetano-Filho et al., 2019).

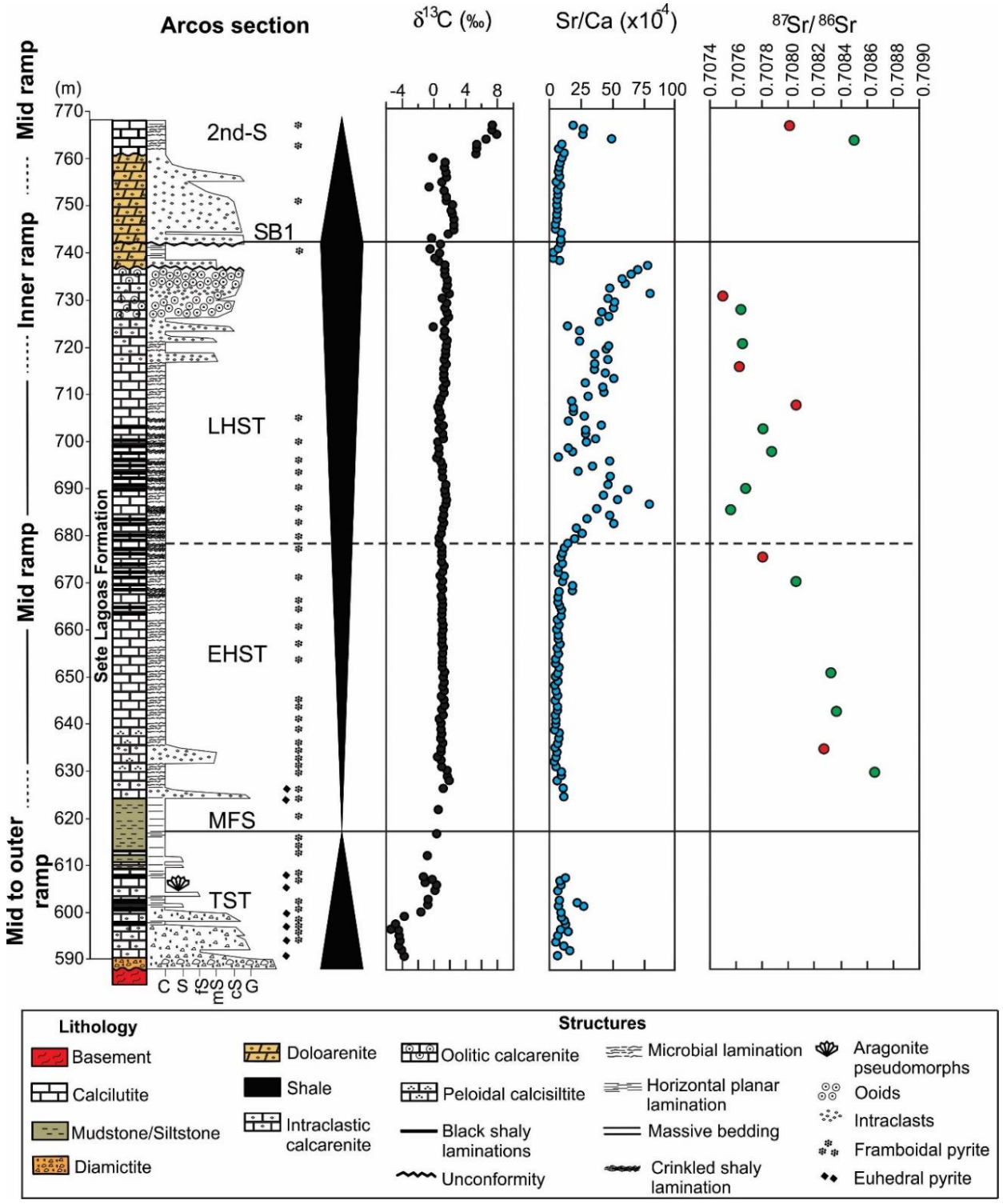

Figure 23. Arcos section − integrated sequence stratigraphy and chemostratigraphy of $\delta^{13}C$ and Sr/Ca presented by Caetano-Filho et al. (2019), and new $^{87}Sr/^{86}Sr$ ratios. TST – Transgressive System Tract; MFS – Maximum Flooding Surface; EHST – Early Highstand System Tract; LHST – Late Highstand System Tract; SB1 – Sequence Boundary. Red dots represent $^{87}Sr/^{86}Sr$ ratios presented previously by Kuchenbecker et al. (2016a).

The Januária section is a 140 m-thick composite section encompassing the mixed carbonate-siliciclastic strata of the Sete Lagoas, Serra de Santa Helena and Lagoa do Jacaré formations exposed in the Januária basement High (Figs. 21 and 24). The TST displays pinkish to reddish limestones with microbial lamination and aragonite pseudomorphs, which unconformably overlie Archean-Paleoproterozoic basement assemblages and are marked by a negative to positive $\delta^{13}C$ excursion within their basal 5 meters (CI-1; Paula-Santos et al., 2017; Caetano-Filho et al., 2019). An interval of reddish to light gray peloidal bindstones with more frequent pelite intercalations and $\delta^{13}C$ values around 1‰ marks the maximum flooding surface (Fig. 24).

Upward, the EHST comprises peloidal limestones with microbial laminations, hummocky cross-stratification and wavy bedding, displaying a slightly increase on $\delta^{13}C$ values from -1 to +1‰. In the LHST, peloidal calcilutites grade upward into intraclastic calcarenite layers and intraclastic carbonate breccia beds that are overlain by a intraclastic doloarenite marking the upper sequence boundary (Fig. 24). The $\delta^{13}C$ values remain stable and positive around +1‰ through the highstand systems tract (CI-2; Paula-Santos et al., 2017). Although no fossil remnants have been described, this interval is correlated to the Cl*oudina*-bearing interval described by Warren et al. (2014) and Perrella et al. (2017). The overlying 2nd-order sequence is represented by mudstones and siltstones with planar laminations of the Serra de Santa Helena Formation and shallow water carbonate facies of the Lagoa do Jacaré Formation (Caetano-Filho et al., 2019). Positive $\delta^{13}C$ values ranging between +8 and +12‰ support the correlation with the CI-3 of Paula-Santos et al. (2017).

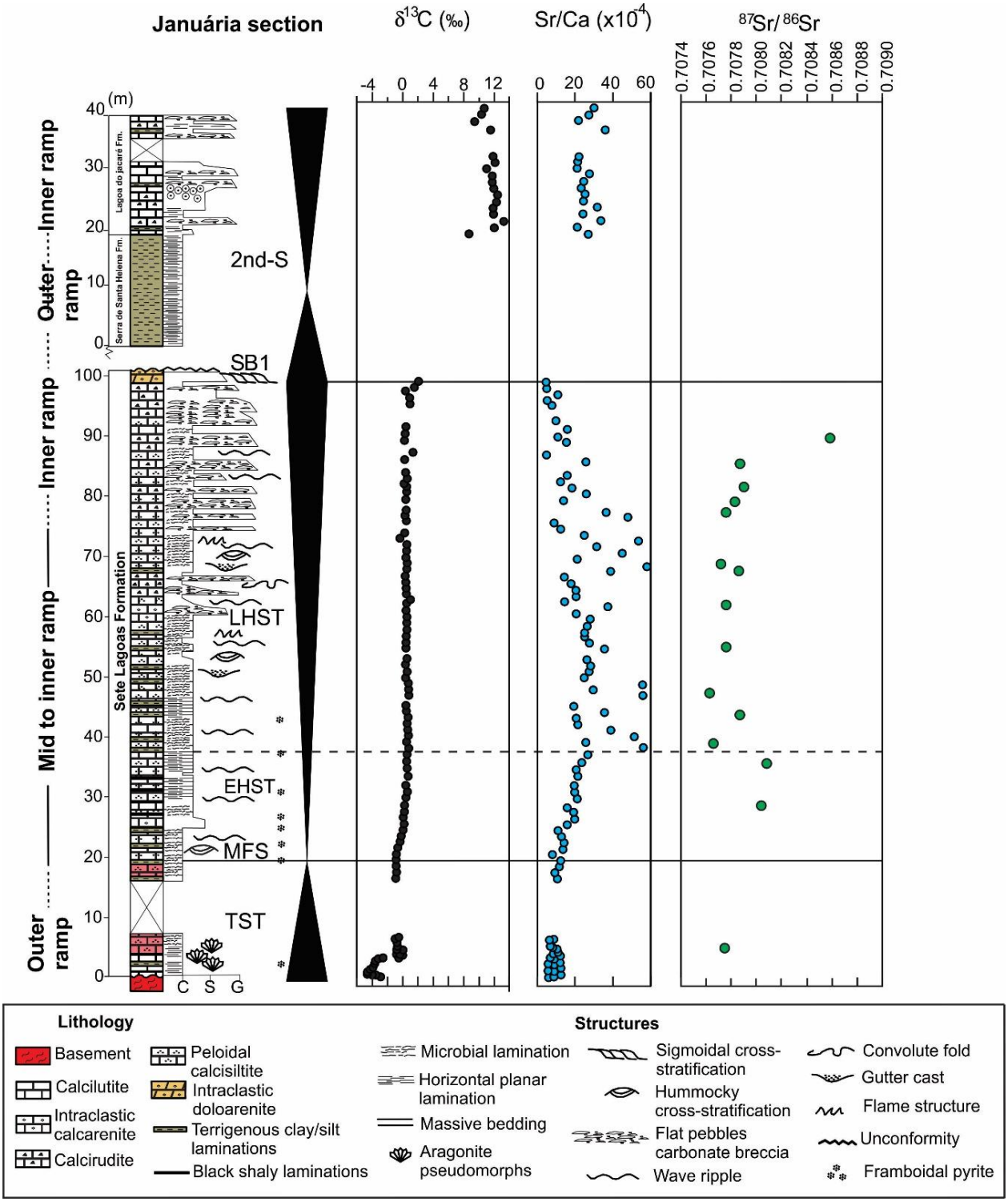

Figure 24. Januária section − integrated sequence stratigraphy and chemostratigraphy of $\delta^{13}C$ values and Sr/Ca presented by Caetano-Filho et al. (2019), and new $^{87}Sr/^{86}Sr$ ratios; TST – Transgressive System Tract; MFS – Maximum Flooding Surface; EHST – Early Highstand System Tract; LHST – Late Highstand System Tract; SB1 – Sequence Boundary.

The Santa Maria da Vitória section (SMV) is a composite section that comprises around a 150 m-thick carbonate-siliciclastic succession of the Sete Lagoas, Serra de Santa Helena and Lagoa do Jacaré formations overlying the cratonic basement on the northern Januária High (Figs. 21 and 25). In this section, the basal Bambuí transgressive systems tract is represented by 3 m-thick strata of white dolostones overlain by a thick succession of pinkish limestones with microbial lamination and sporadic occurrences of aragonite pseudomorphs. This interval displays in its basal 15 meters the negative $\delta^{13}C$ excursion typical of the CI-1 (Paula-Santos et al., 2017). Pelitic layers interbedded with microbial limestones mark the maximum flooding surface (Fig. 5).

The overlying EHST is composed of microbial pinkish limestones with slightly negative $\delta^{13}C$ values (–1 to 0‰) that grade into gray limestones with hummocky cross-stratification, wavy bedding and restricted carbonate breccias, presenting slightly positive $\delta^{13}C$ values around +1‰. Sr/Ca ratios notably increase within the gray limestone interval marking the LHST interval (Fig. 25). A possible paleosol layer marks the sequence boundary (SB1) accompanied by a discontinuity in the $\delta^{13}C$ profile. The overlaying 2nd-order sequence starts with dolostones presenting microbial laminations and tepee-like structures of the uppermost Sete Lagoas Formation succeeded by siltstones and interbedded oolitic limestone layers of the Serra de Santa Helena Formation (Fig. 25). A remarkable increase on $\delta^{13}C$ values from +2 to +14‰ is observed in these strata (CI-3, Paula-Santos et al., 2017).

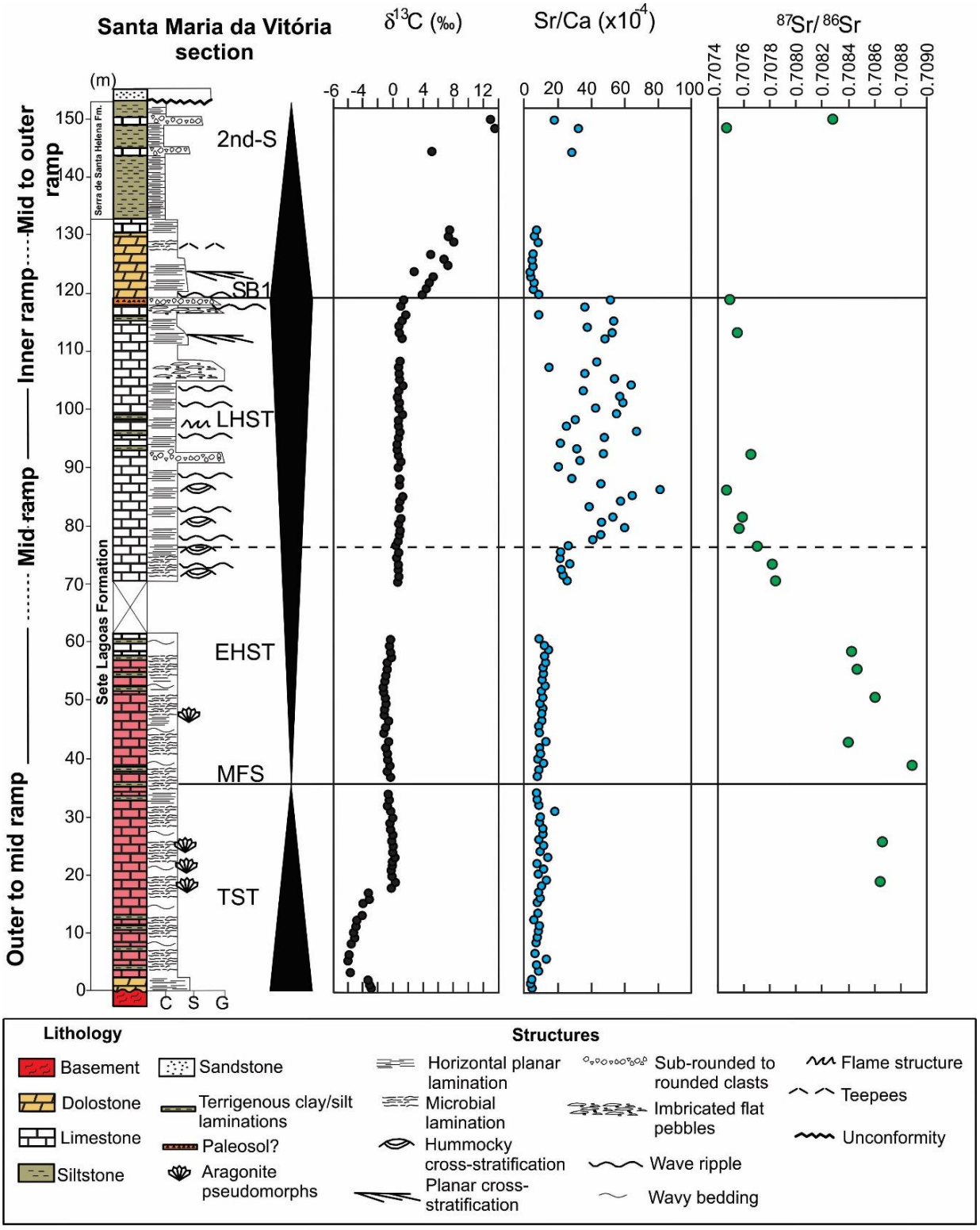

Figure 25. Santa Maria da Vitória section − integrated sequence stratigraphy and chemostratigraphy of $\delta^{13}C$ values and Sr/Ca presented by Caetano-Filho et al. (2019), and new $^{87}Sr/^{86}Sr$ ratios. TST – Transgressive System Tract; MFS – Maximum Flooding Surface; EHST – Early Highstand System Tract; LHST – Late Highstand System Tract; SB1 – Sequence Boundary.

5.4.2 Strontium isotope analyses

Sixty-three carbonate samples distributed along the three studied sections were selected for Sr isotope analyses (Table 1), based on previously bulk rock samples analyzed for Sr and Ca using X-ray fluorescence, as well as stratigraphic-chemostratigraphic framework and sedimentology (Caetano-Filho et al., 2019). Petrographic analyses were carried out to identify depositional fabrics and sedimentary structures, and select the more preserved areas to obtain carbonate powder. A sequential leaching method was applied to systematically isolate least-altered carbonate phases from detrital siliciclastic Sr contamination (e.g., Li et al. 2011; Paula-Santos et al. 2017; Bellefroid et al., 2018), increasing the reliability of the results as a representative proxy of seawater.

Strontium isotope compositions were analyzed through the reaction of 100 mg of carbonate powder with 2.0 mL of HCl 0.1 N for one hour. The supernatant was discarded, and the sample was centrifuged and washed three times with Milli-Q water, also discarding the supernatant from each wash. Subsequently, ~3.0 mL of HCl 0.1 N was added into the dried sample for reaction through one hour. Again, the sample was centrifuged for 15 minutes, the supernatant transferred to Savillex and washed three times with Milli-Q water. This solution is the second leachate (L2) that underwent Sr purification process by the ion exchange chromatography technique, using a Sr-spec resin and HNO_3 as eluant. The $^{87}Sr/^{86}Sr$ ratios were measured in the TRITON thermal ionization mass spectrometer (TIMS, Thermo Fisher, Germany) at the Geochronological Research Center (CPGeo) of the University of São Paulo, Brazil. The ratios were normalized to $^{86}Sr/^{88}Sr$ = 0.1194 in order to correct variable mass fractionation. The average value of the NBS-987 standard measured during analyses was 0.710250 ± 0.000018, (n=6), and the Sr analytical blanks were generally below 28 ng.

5.4.3 Elemental geochemistry

For major and trace element mass fraction measurements, small pieces of carbonate samples devoid of terrigenous laminae and post-depositional features were

carefully powdered in an agate mortar. The same leaching procedure used for Sr isotope analyses was performed and only the second leachate (L2) was analyzed. After drying L2 solution on a hot plate, the residue was converted into nitrates by adding 0.5 mL of concentrated HNO_3. This solution was evaporated and the residue was dissolved in 1% (v/v) HNO_3. Concentrations of Rb, Sr, Mn, Fe, Mg and Ca of carbonate fractions were measured by quadrupole inductively coupled plasma mass spectrometry (Q-ICP-S) using a X-Series (Thermo Fisher, Germany) mass spectrometer at the Laboratory of Isotope Geology of the Institute of Geosciences of the University of Campinas, Brazil.

5.5 Results

Strontium isotope compositions, element mass fractions and geochemical ratios of carbonates of the basal Bambuí Group are presented in Table 1, and primary $^{87}Sr/^{86}Sr$ ratios (selected in the item 5.1) are presented in Figs. 23, 24 and 25.

Carbonate samples from the Arcos section display very radiogenic $^{87}Sr/^{86}Sr$ ratios within the lowermost TST, between 0.7100 and 0.7177, and presents Sr content from 400 to 900 µg/g and Sr/Ca between 0.0018 and 0.0028 (Table 1). The $^{87}Sr/^{86}Sr$ ratios decrease progressively from 0.7087 to 0.7078 towards the top of EHST (Fig. 3), with Sr content varying from 300 to 600 µg/g and Sr/Ca ratios from 0.0008 to 0.0014 (Table 1). At the lower to middle LHST, $^{87}Sr/^{86}Sr$ ratios increase from 0.7075 to 0.7080, then decreasing to values around 0.7076 at the uppermost highstand systems tract (Fig. 3), accompanied by high strontium contents between 800 and 4,000 µg/g, and high Sr/Ca ratios from 0.0025 to 0.001 (Table 1). Dolomites from the top this interval show very radiogenic $^{87}Sr/^{86}Sr$ ratios (> 0.7121), with low Sr contents and Sr/Ca ratios below 270 µg/g and 0.0016, respectively (Table 1). Carbonates from the basal portion of the overlying 2nd-order sequence show $^{87}Sr/^{86}Sr$ ratios between 0.7080 and 0.7085 (Fig. 3), with Sr contents varying from 600 to 2,000 µg/g and Sr/Ca ratios of 0.0078 (Table 1). Geochemical contents recorded in this section show Rb/Sr ratios between 0.00005 and 0.00100, Mn/Sr between 0.001 and 1.500, Fe/Sr ranging from 0.01 to 24.98, and Mg/Ca ratios between 0.003 and 0.500 (Table 1).

In the Januária section, the $^{87}Sr/^{86}Sr$ ratios are also very radiogenic at the lowermost TST, with values up to 0.7117, and Sr contents and Sr/Ca ratios varying from 360 to 500 µg/g and 0.0005 to 0.0014, respectively (Table 1). However, one sample at the base of the Januária section (CM-03f) shows very low $^{87}Sr/^{86}Sr$ ratio of 0.7077, which is associated with high Sr mass fraction (3,920 µg/g) and aragonite pseudomorph crystal fans (Table 1, Fig. 24). Carbonate rocks of the EHST show $^{87}Sr/^{86}Sr$ ratios around 0.7080 (Fig. 4), and an upward progressive increase in Sr contents and Sr/Ca ratios from 500 to 1,100, and from 0.0017 to 0.0032, respectively (Table 1). $^{87}Sr/^{86}Sr$ ratios from the LHST vary between 0.7076 and 0.7078, and increase to 0.7085 at the topmost portion (Fig. 24), presenting Sr contents from 430 to 2,800 µg/g, and Sr/Ca ratios between 0.0012 to 0.0077 (Table 1). The carbonate successions of the Januária section show Rb/Sr ratios ranging from 0.00002 to 0.00300, Mn/Sr between 0.002 and 4.100, Fe/Sr varying from 0.02 to 2.66, and Mg/Ca ratios between 0.003 to 0.470 (Table 1).

Limestones of the Santa Maria da Vitória section display very radiogenic $^{87}Sr/^{86}Sr$ ratios at the lower TST between 0.7091 and 0.7134 (Fig. 25), associated to low Sr contents between 100 and 500 µg/g, and low Sr/Ca ratios from 0.0005 to 0.0010 (Table 1). Also, two samples of this interval (COR-18 and COR-25) show $^{87}Sr/^{86}Sr$ ratios around 0.7086 and present aragonite pseudomorphs (Table 1, Fig. 25). In the EHST, the $^{87}Sr/^{86}Sr$ ratios decrease upward, from 0.7088 to 0.7077 (Fig. 25), coupled to an increase in the Sr content from 400 to 1,200 µg/g, and Sr/Ca ratios from 0.0009 to 0.0027 (Table 1). At the LHST, $^{87}Sr/^{86}Sr$ ratios are dominantly around 0.7075 (Fig. 25), and associated with high Sr contents between 2,000 and 4,000 µg/g, and high Sr/Ca ratios from 0.0040 to 0.0090 (Table 1). At the basal portion of the LHST, the $^{87}Sr/^{86}Sr$ and Sr/Ca ratios seem to define-untithetical trends, with non-radiogenic ratios associated with high Sr/Ca ratios (Fig. 25). Carbonates from the second 2^{nd}-order sequence show $^{87}Sr/^{86}Sr$ ratios between 0.7074 and 0.7087 (Fig. 25), with Sr contents from 700 to 1,400 µg/g, and Sr/Ca ratios from 0.0017 to 0.0024 (Table 1). Dolomites from this interval exhibit very radiogenic $^{87}Sr/^{86}Sr$ ratios between 0.7094 and 0.7121, with low Sr contents and Sr/Ca ratios less 300 µg/g and 0.0011, respectively (Table 1). This section shows Rb/Sr ratios between 0.00003 and 0.00360, Mn/Sr between 0.001 and 2.800, Fe/Sr ranging from 0.002 to 23.100, and Mg/Ca ratios between 0.003 and 0.550 (Table 1).

Table 1. Sr contents, geochemical ratios and $^{87}Sr/^{86}Sr$ ratios of carbonate samples from the basal Bambuí Group at the Arcos, Januária and Santa Maria da Vitória sections.

Section	Sample	(m)	Tract	Lithology	Sr (µg/g)	Rb/Sr	Mn/Sr	Fe/Sr	Mg/Ca	Sr/Ca	$^{87}Sr/^{86}Sr$	erro (2σ)
Arcos	M-4	592.0	TST	Calcarenite	402	0.00158	1.235	24.978	0.367	0.0018	0.717756	0.000020
	M-12	599.3	TST	Calcarenite	890	0.00078	0.559	0.874	0.012	0.0028	0.711227	0.000016
	M-18*	604.8	TST	Calcarenite	174	0.06322	n.a.	n.a.	n.a.	n.a.	0.715348	0.000048
	M-20*	606.5	TST	Calcilutite	292	0.04795	n.a.	n.a.	n.a.	n.a.	0.709992	0.000008
	k-24a	613.0	TST	Calcilutite	760	0.00103	0.450	4.829	0.050	0.0021	0.710085	0.000017
	M-28	631.2	EHST	Calcisiltite	365	0.00050	0.087	0.464	0.033	0.0014	0.708663	0.000016
	M-29*	636.0	EHST	Calcisiltite	304	0.02303	0.329	2.531	0.013	0.0008	0.708271	0.000042
	K-30c	644.0	EHST	Calcilutite	308	0.00038	0.053	0.228	0.012	0.0010	0.708368	0.000020
	K-32a	652.0	EHST	Calcilutite	370	0.00025	0.035	0.661	0.025	0.0012	0.708326	0.000017
	M-36*	671.4	EHST	Calcilutite	598	0.00061	0.029	0.374	0.010	0.0012	0.708057	0.000020
	M-37*	676.4	EHST	Calcilutite	414	0.00725	0.242	0.725	0.014	0.0011	0.707804	0.000022
	M-39	686.7	LHST	Calcilutite	3950	0.00005	0.001	0.030	0.005	0.0108	0.707551	0.000019
	M-40*	690.9	LHST	Calcilutite	2538	0.00012	0.002	0.037	0.003	0.0051	0.707683	0.000072
	K-41b	698.7	LHST	Calcilutite	816	0.00014	0.005	0.060	0.005	0.0025	0.707872	0.000018
	K-42b	703.4	LHST	Calcilutite	1132	0.00007	0.002	0.050	0.003	0.0032	0.707799	0.000019
	M-45*	716.4	LHST	Calcilutite	1817	0.00055	0.055	0.154	0.003	0.0046	0.707622	0.000040
	M-46*	721.4	LHST	Calcilutite	1957	0.00051	0.051	0.358	0.003	0.0050	0.707648	0.000023
	K-43b	708.4	LHST	Calcilutite	863	0.00008	0.006	0.059	0.003	0.0030	0.708055	0.000018
	K-47b	728.4	LHST	Calcarenite	2643	0.00003	0.006	0.011	0.003	0.0089	0.707628	0.000017
	M-48*	731.4	LHST	Calcarenite	3304	0.00009	0.030	0.085	0.002	0.0083	0.707493	0.000020
	K-49c	738.9	LHST	Doloarenite	97	0.00050	1.436	6.235	0.524	0.0006	0.712481	0.000016
	K-52b	754.2	LHST	Doloarenite	268	0.00125	0.149	0.825	0.372	0.0016	0.712144	0.000020
	M-54	762.2	LHST	Doloarenite	188	0.00219	0.488	2.876	0.467	0.0008	0.713115	0.000019
	M-D6	764.2	2nd-S	Calcilutite	2094	0.00022	0.019	0.090	0.042	0.0078	0.708507	0.000018
	M-55*	767.2	2nd-S	Calcilutite	678	0.03687	n.a.	n.a.	n.a.	n.a.	0.708009	0.000022
Januária	CM-02	1.2	TST	Calcilutite	361	0.00186	1.097	1.770	0.008	0.0010	0.709710	0.000020
	CM-03	2.2	TST	Calcilutite	234	0.00383	4.088	2.656	0.007	0.0005	0.711768	0.000018
	CM-03f	3.2	TST	Calcilutite	3917	0.00011	0.162	0.072	0.006	0.0104	0.707740	0.000018
	CM-03h	3.9	TST	Calcilutite	380	0.00203	0.409	1.081	0.016	0.0010	0.709170	0.000021
	CM-06a	6.3	TST	Calcisiltite	353	0.00196	0.497	2.312	0.047	0.0009	0.710316	0.000019
	CM-09	18.5	TST	Calcisiltite	450	0.00119	0.182	1.482	0.031	0.0011	n.a.	n.a.
	CM-10	19.5	TST	Calcisiltite	467	0.00139	0.149	1.653	0.027	0.0014	0.709797	0.000019
	CM-14	23.5	EHST	Calcisiltite	562	0.00074	0.137	1.236	0.042	0.0017	n.a.	n.a.
	CM-18	27.5	EHST	Calcisiltite	822	0.00011	0.009	0.125	0.017	0.0027	0.708020	0.000016
	CM-22	31.9	EHST	Calcisiltite	1092	0.00018	0.008	0.154	0.019	0.0029	n.a.	n.a.
	CM-24	34.7	EHST	Calcisiltite	952	0.00013	0.006	0.131	0.029	0.0032	0.708055	0.000019
	CM-27	38.1	LHST	Calcisiltite	2878	0.00002	0.002	0.016	0.004	0.0068	0.707644	0.000020

	CM-32	43.1	LHST	Calcisiltite	1056	0.00010	0.008	0.100	0.010	0.0027	0.707855	0.000021
	CM-35	46.8	LHST	Calcisiltite	2558	0.00003	0.002	0.027	0.005	0.0077	0.707622	0.000020
	CM-42	54.5	LHST	Calcisiltite	1446	0.00003	0.004	0.039	0.005	0.0040	0.707741	0.000018
	BAR-12	61.7	LHST	Calcisiltite	1724	0.00016	0.015	0.103	0.003	0.0031	0.707740	0.000019
	BAR-18	67.5	LHST	Calcarenite	1832	0.00006	0.012	0.075	0.005	0.0039	0.707845	0.000017
	BAR-19	68.5	LHST	Calcarenite	2637	0.00008	0.006	0.059	0.004	0.0070	0.707701	0.000017
	BAR-28	77.3	LHST	Calcarenite	2224	0.00010	0.015	0.050	0.004	0.0046	0.707742	0.000018
	BAR-29	79.1	LHST	Calcarenite	778	0.00011	0.028	0.115	0.013	0.0018	0.707814	0.000018
	BAR-32	81.7	LHST	Calcarenite	872	0.00004	0.019	0.049	0.013	0.0022	0.707883	0.000017
	BAR-35	85.7	LHST	Calcarenite	1080	0.00009	0.023	0.095	0.018	0.0029	0.707851	0.000017
	BAR-38	89.9	LHST	Calcarenite	438	0.00003	0.049	0.112	0.014	0.0012	0.708538	0.000018
	BAR-42	95.9	LHST	Calcarenite	n.a.	n.a.	n.a.	n.a.	n.a.	n.a.	0.709604	0.000016
Santa Maria da Vitória	COR-02	1.5	TST	Dolostone	103	0.00322	2.827	23.143	0.508	0.0005	0.710511	0,000020
	COR-05	4.5	TST	Calcilutite	234	0.00366	1.669	2.652	0.027	0.0006	0.713400	0,000018
	COR-07	6.5	TST	Calcilutite	181	0.00228	1.168	0.721	0.009	0.0005	0.709219	0.000021
	COR-11	11.3	TST	Calcilutite	252	0.00197	1.716	0.779	0.009	0.0007	0.709148	0.000019
	COR-15	16.0	TST	Calcilutite	282	0.00101	1.099	4.498	0.105	0.0011	0.709093	0.000016
	COR-18	19.0	TST	Calcilutite	456	0.00067	0.411	1.587	0.075	0.0011	0.708572	0.000016
	COR-25	26.0	TST	Calcilutite	293	0.00091	0.339	0.349	0.007	0.0008	0.708589	0.000018
	ALD-06	39.0	EHST	Calcilutite	408	0.00065	0.280	1.138	0.027	0.0009	0.708801	0.000019
	ALD-10	43.0	EHST	Calcilutite	446	0.00075	0.310	1.044	0.025	0.0009	0.708346	0.000017
	ALD-17	50.6	EHST	Calcilutite	552	0.00058	0.131	1.202	0.032	0.0012	0.708531	0.000018
	ALD-22	55.6	EHST	Calcilutite	396	0.00065	0.199	2.904	0.080	0.0013	0.708408	0.000016
	ALD-25	58.6	EHST	Calcilutite	469	0.00055	0.181	1.152	0.022	0.0012	0.708364	0.000016
	ALD-28	70.6	EHST	Calcilutite	1087	0.00007	0.013	0.059	0.008	0.0022	0.707816	0.000021
	ALD-31	73.6	EHST	Calcilutite	1209	0.00010	0.011	0.063	0.007	0.0027	0.707791	0.000019
	ALD-34	76.6	EHST	Calcilutite	1176	0.00010	0.016	0.076	0.005	0.0025	0.707687	0.000017
	ALD-37	79.6	LHST	Calcilutite	3947	0.00003	0.001	0.011	0.004	0.0081	0.707559	0.000016
	ALD-39	81.6	LHST	Calcilutite	2297	0.00003	0.005	0.022	0.005	0.0048	0.707576	0.000018
	ALD-43	86.3	LHST	Calcilutite	4099	0.00004	0.001	0.018	0.003	0.0084	0.707465	0.000019
	ALD-48	92.3	LHST	Calcilutite	1997	0.00002	0.005	0.019	0.005	0.0041	0.707640	0.000016
	BA-16	113.3	LHST	Calcilutite	2070	0.00002	0.001	0.010	0.004	0.0040	0.707539	0.000018
	BA-21	118.8	LHST	Calcilutite	2835	0.00001	0.001	0.002	0.003	0.0059	0.707486	0.000019
	BA-22	119.8	2nd-S	Dolostone	199	0.00039	0.236	1.229	0.528	0.0008	0.710041	0.000019
	BA-27	124.8	2nd-S	Dolostone	87	0.00018	2.541	3.827	0.527	0.0004	0.709446	0.000017
	BA-30	128.8	2nd-S	Dolostone	311	0.00068	0.513	6.288	0.409	0.0011	0.711044	0.000016
	BA-32	130.8	2nd-S	Dolostone	164	0.00230	1.414	19.577	0.548	0.0007	0.710846	0.000017
	BA-33	144.3	2nd-S	Calcisiltite	701	0.00098	1.290	1.139	0.267	0.0024	0.708736	0.000017
	BA-34	148.3	2nd-S	Calcisiltite	1367	0.00005	0.010	0.038	0.005	0.0024	0.707465	0.000019
	BA-35	149.8	2nd-S	Calcisiltite	705	0.00013	0.025	0.047	0.004	0.0017	0.708225	0.000018

Notes: *sample data from Kuchenbecker et al. (2016a); n.a. – not analyzed.

5.6 Discussion

5.6.1 Assessing post-depositional alteration and carbonate diagenesis

During post-depositional rock/fluid interaction such as meteoric-water diagenesis and dolomitization, carbonate minerals usually incorporate more Mn and Fe, accompanied by a decrease in the $\delta^{18}O$ values and in Sr concentrations, as well as an increase in $^{87}Sr/^{86}Sr$ ratios (Brand and Veizer 1980, 1981; Veizer et al., 1983; Banner and Hanson, 1990; Jacobsen and Kaufman, 1999; Melezhik et al., 2001; Brand, 2004; Halverson et al., 2007; Derry, 2010). Based on these observations, several studies have proposed systematic geochemical screenings based on elemental and isotope proxies to evaluate the original seawater signature and the post-depositional alteration on $^{87}Sr/^{86}Sr$ ratios of marine carbonates (i. e., Banner and Hanson, 1990; Derry et al., 1992; Montañez et al., 1996, 2000; Jacobsen and Kaufman, 1999; Melezhik et al., 2001; Fölling and Frimmel, 2002; Halverson et al., 2007, 2010; Kuznetsov et al., 2013; Zaky et al., 2019). $^{87}Sr/^{86}Sr$ *vs*. Mn/Sr and Fe/Sr diagrams, as well as Mg/Ca ratios are often deployed to such task.

These works attempted to define “cut-off” values for these elements and geochemical ratios in order to determine the reliability of a given isotope dataset to record a primary marine signal of the Neoproterozoic seawater (i. e., Asmeron et al., 1991; Kaufman et al., 1993; Kaufman and Knoll, 1995; Kuznetsov et al., 1997; Jacobsen and Kaufman, 1999; Folling and Frimmel et al., 2002; Kuznetsov et al., 2013). However, such works relied on limited number of samples, usually from a single stratigraphic unit or from sedimentary units that share similar geologic histories. This resulted in very discrepant cut-off values, which means they may not be suitable for all ancient carbonate successions deposited under different environmental conditions (i.e., Paula-Santos et al., 2017; Zaky et al., 2019).

Additionally, the identification of stratigraphic levels with high Sr concentrations on the Bambuí Group can introduce a bias in the geochemical analysis of post-depositional processes. Paula-Santos et al. (2017) show that most of the considered pristine $^{87}Sr/^{86}Sr$ ratios were selected from these Sr-rich carbonates, with the more radiogenic ratios from the EHST and TST being discarded, though some of them were in accordance with ratios

expected for the late Ediacaran. Caetano-Filho et al. (2019) argued the basin-wide increase in Sr mass fractions and Sr/Ca ratios are non-facies dependent feature, which might indicate a paleoenvironmental change in the basin resulting in increased incorporation of Sr in the carbonate lattice. This shows that the difference in Sr mass fractions across the basal 2nd-order sequence of the Bambuí Group are probably environmental driven, rather than a post-depositional artifact.

To avoid misuse of pre-established cut-off values and introduction of such bias, instead of fixed numerical values, we carefully evaluate Sr isotope ratios from each stratigraphic interval from the Bambuí Group, we follow Paula-Santos et al. (2017) who suggest that these values should be dynamic and determined according to regional chemostratigraphy.

For the lowermost TST, the dominant very radiogenic $^{87}Sr/^{86}Sr$ ratios from 0.7090 to 0.7177 are associated with high geochemical ratios of Rb/Sr, Mn/Sr, Fe/Sr and Mg/Ca for most of carbonate samples of this interval. In contrast, some carbonate samples display lower Sr ratios between 0.7075 to 0.7077, which are associated to lower geochemical ratios, as well as to aragonite pseudomorphs and higher Sr contents (Fig. 6). Sample COR-25 from SMV section also has a lower $^{87}Sr/^{86}Sr$ ratios of 0.7086 coupled to lower elemental ratios (Table 1). These ratios between 0.7075 and 0.7086 are consistent with those reported by Paula-Santos et al. (2017) for the basal cap carbonates and we also considered them as the most representative of seawater composition for the TST. The more radiogenic ratios are considered altered.

Carbonates with $^{87}Sr/^{86}Sr$ ratios > 0.7090 from the TST could record a mixing between less radiogenic seawater and radiogenic freshwater, which diminished as transgression progressed increasing the relative proportion of the geochemical marine patterns. This is supported by flat rare earth element patterns that suggest a large input of freshwater/meltwater mixed to seawater during transgression, and is consistent with a post-glacial scenario for the TST (i. e., Shields, 2005; Liu et al., 2014; Kuchenbecker et al., 2016a; Wei et al., 2019; Paula-Santos, 2018; 2020). In any case, they are not considered in our geological discussion.

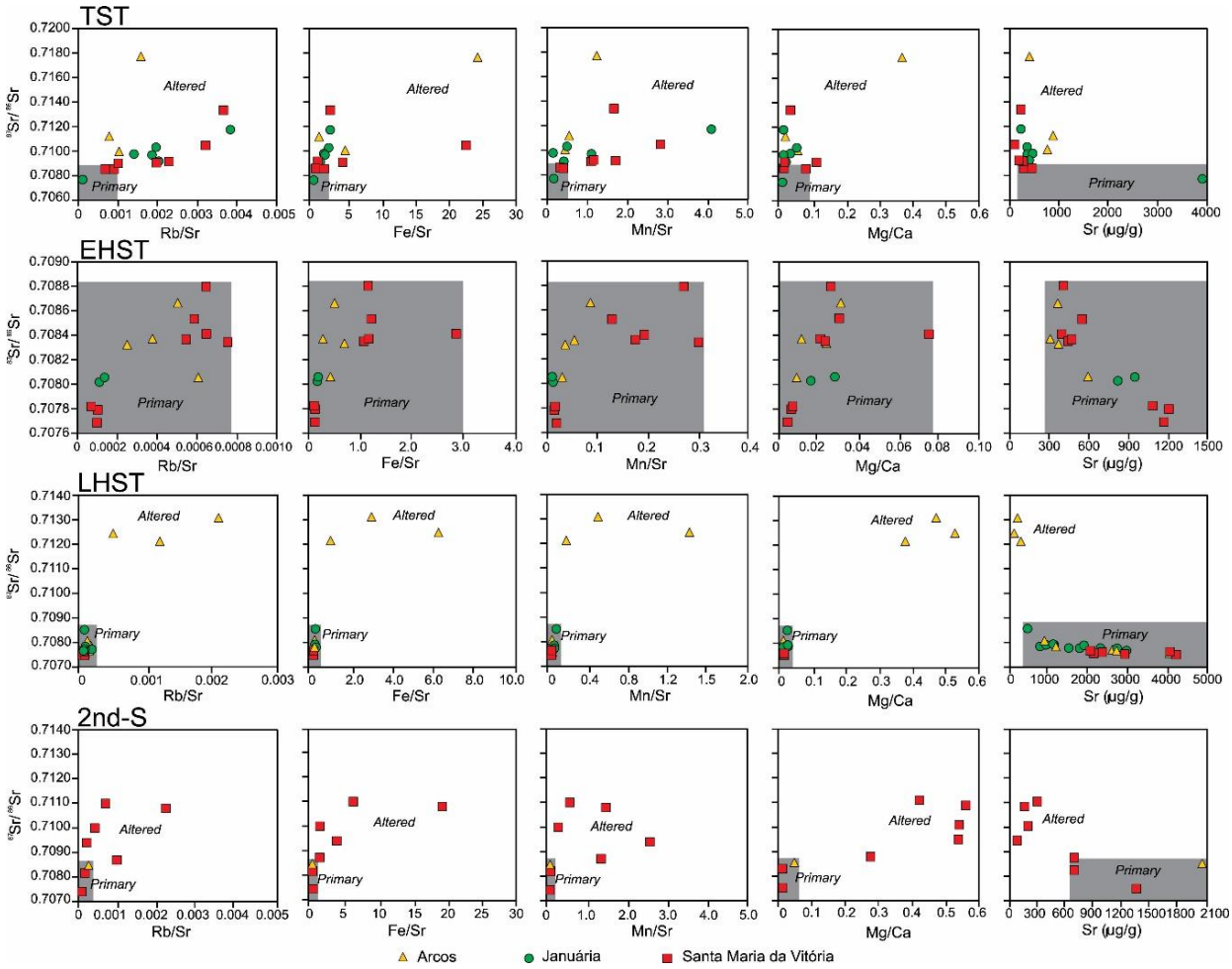

Figure 26. Cross-plot diagrams of $^{87}Sr/^{86}Sr$ ratios *vs*. geochemical ratios of Rb/Sr, Fe/Sr, Mn/Sr, Mg/Ca and Sr contents for the systems tracts (TST, EHST, LHST and 2nd-S) of the basal Bambuí Sequence. Primary $^{87}Sr/^{86}Sr$ ratios are inside the grey square.

Strontium isotope ratios for the EHST range from 0.7077 to 0.7088 and show a positive correlation with geochemical ratios of Rb/Sr, Mn/Sr, Fe/Sr and Mg/Ca (Fig. 26), which would suggest a diagenetic trend towards the higher $^{87}Sr/^{86}Sr$ ratios (Banner and Hanson, 1990; Jacobsen and Kaufman, 1999; Fölling and Frimmel, 2002; Halverson et al., 2007; Alvarenga et al., 2014; Kuchenbecker et al., 2016a; Paula-Santos et al., 2017). However, we note that an upward decreasing trend of the ratios is observed in all studied sections, preceding the increase in the Sr/Ca at the LHST. If such recurrent feature basin-wide were to be a post-depositional feature it would require a diagenetic overprint of basinal scale that we find unlikely due the lack of petrographical evidence. Also, since this drop down in the Sr isotope ratios precedes a very well describe major environmental change in the

basin, we find it more reasonable that they are the record of a progressive change in seawater chemistry, rather than any diagenetic overprint. In addition, geochemical ratios are extremely low (Rb/Sr < 0.008, Mn/Sr < 0.3 and Fe/Sr < 3) for this interval in all the sections (Table 1) and there is no significant variation in Rb, Mn, and Fe mass fractions of the EHST samples. At the light of these evidences we argue that these Sr isotope ratios are pristine and that the decrease in these isotope ratios reflects basin-scale paleoenvironmental changes, rather than pointing to basin wide diagenetic processes restricted to the EHST strata.

For the LHST, the $^{87}Sr/^{86}Sr$ ratios vary between 0.7074 to 0.7131 (Fig. 26) and, in dolomites, presents a systematic correlation with Rb/Sr, Mn/Sr, Fe/Sr and Mg/Ca ratios, indicating posst-depositional alteration of the more radiogenic isotope ratios higher than 0.7085 (i.e., Banner and Hanson, 1990; Jacobsen and Kaufman, 1999; Fölling and Frimmel, 2002; Halverson et al., 2007; Alvarenga et al., 2014; Kuchenbecker et al., 2016a; Paula-Santos et al., 2017). The $^{87}Sr/^{86}Sr$ ratios range between 0.7074 and 0.7085 display no correlations with the elemental ratios and are considered pristine and to record seawater chemistry. These samples are Sr-rich carbonates, with very low Rb/Sr ratios < 0.00014, Fe/Sr ratios < 0.1, Mn/Sr ratios < 0.05, Mg/Ca ratios < 0.018, high Sr contents (Fig. 26), and a high consistency between neighboring samples within each studied section.

Geochemical cross-plot diagrams for the upper 2nd-order sequence display $^{87}Sr/^{86}Sr$ between 0.7074 and 0.7110, showing positive correlations with Rb/Sr, Mn/Sr, Fe/Sr and Mg/Ca ratios (Fig. 26). It indicates post-depositional alteration of the more radiogenic ratios (> 0.7087; Banner and Hanson, 1990; Jacobsen and Kaufman, 1999; Fölling and Frimmel, 2002; Halverson et al., 2007; Alvarenga et al., 2014; Kuchenbecker et al., 2016a; Paula-Santos et al., 2017). Samples with low ratios of Rb/Sr < 0.0002, Mn/Sr < 0.1, Fe/Sr < 1.0 and Mg/Ca < 0.1 coupled with Sr contents higher than 700 µg/g exhibit $^{87}Sr/^{86}Sr$ radiogenic ratios between 0.7074 to 0.7085, which are considered records of the primary marine geochemistry during the deposition of the lowermost portion of the upper 2nd-order sequence (Fig. 26).

The regional assessment of post-depositional alteration and diagenesis for each stratigraphic interval demonstrates that fixed values Mn/Sr and Fe/Sr ratios may not be suitable screeners for detecting or deciding between alteration/preservation in carbonates given heterogeneous geochemical signatures that characterize each stage in the basin evolution. Instead flexible ratios and trends are more useful to assess the degree of preservation of carbonates in order to provide a representative Sr isotope chemostratigraphy (Brand et al., 2011; Paula-Santos et al., 2017; Zaky et al., 2019).

5.6.2 Implications for the marine Sr isotope budget in West Gondwana

Non-radiogenic $^{87}Sr/^{86}Sr$ ratios between 0.7074 and 0.7077 have been interpreted as the representative of the basal Bambuí Group (Misi et al., 2007; Babinski et al., 2007; Kuchenbecker, 2011, 2016a; Alvarenga et al., 2012, 2014; Caxito et al., 2012, 2018; Paula-Santos et al., 2015). Some authors considered these unradiogenic ratios for global correlation, assigning them to early Ediacaran seawater composition (e.g. Caxito et al., 2012, 2018), while others interpreted them as indicative of restrict marine conditions during the late Ediacaran (Paula-Santos et al., 2017). On the other hand, $^{87}Sr/^{86}Sr$ ratios of 0.7080–0.7084 were initially discarded due to a bias on the post-depositional assessment caused by Sr-enriched carbonates and the lack of basin wide studies to investigate the spatio-temporal significance of these ratios. However, this study attests that primary ratios between 0.7080 and 0.7088 are common in the lower Sete Lagoas Formation (EHST; Fig. 27), succeeding deposition of cap carbonates and preceding the basin wide increase in Sr/Ca ratios. This is in accordance with late Ediacaran fossils and global Sr isotope seawater curves (CI-2 from Paula-Santos et al., 2017). The primary $^{87}Sr/^{86}Sr$ ratios presented here, as well as previous Sr-isotope data reassessed from Arcos section (Kuchenbecker et al., 2016a; Bedoya-Rueda, 2019), together with $\delta^{13}C$ values and Sr/Ca ratios, allow a further step in the interpretation of the paleoenvironmental and sedimentary evolution of the Ediacaran-Cambrian Bambuí foreland basin system.

A new feature for the Sr isotope stratigraphy of the Bambuí Group revealed by this study is the relatively rapid fall on the $^{87}Sr/^{86}Sr$ ratios from 0.7086 to 0.7076 through the

progradational stage of the lowermost Bambuí 2nd-order sequence (i.e., lower to middle Sete Lagoas Formation) (Fig. 27). This decreasing trend is well observed in Arcos and SMV sections (Figs. 3 and 5). In the Januária section, only two samples showed $^{87}Sr/^{86}Sr$ ratios around 0.7080, and are recorded at the end of the EHST (Fig. 24). This $^{87}Sr/^{86}Sr$ drawdown precedes the $\delta^{13}C$ positive excursion of the basal Bambuí sequence and occurs stratigraphically below than previously suggested by Paula-Santos et al. (2017), which associated this isotope feature with the CI-2/CI-3 boundary (i. e., close to the sequence boundary and associated with the $\delta^{13}C$ positive excursion). This Sr isotope signal can be explained in two hypotheses: 1) stratified water column for $^{87}Sr/^{86}Sr$ ratios and 2) temporal variation of Sr isotopes at basin scale.

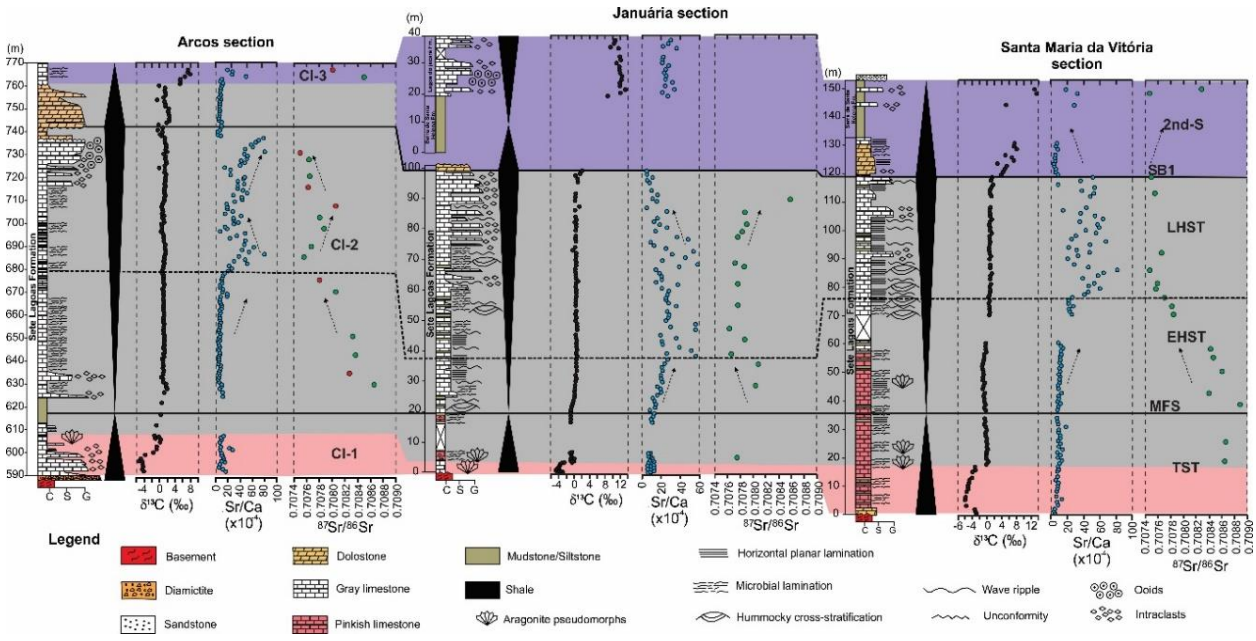

Figure 27. Stratigraphic-chemostratigraphic correlations for the basal Bambuí Sequence between Arcos, Januária and Santa Maria da Vitória sections. $\delta^{13}C$ and Sr/Ca data presented by Caetano-Filho et al. (2019). TST: Transgressive System Tract; MFS: Maximum Flooding Surface; EHST: Early Highstand System Tract; LHST: Late Highstand System Tract; SB1: Sequence Boundary.

The progressive decrease of $^{87}Sr/^{86}Sr$ ratios from 0.7086 to 0.7076 could be a reflect of stratified seawater, according to the facies bathymetry, leading to Sr isotopic gradients with depth (i.e., Shields et al., 1997, Shields, 2005; Liu et al. 2014), and the $^{87}Sr/^{86}Sr$ ratios ought to be significantly lower in the shallower environments and higher at greater depths. However, this hypothesis does not seem plausible due to several reasons; a) Sr isotopic

heterogeneities produced in stratified oceans have not been well constrained (i.e., Banner, 2004); b) stratified seawater models are proposed to explain the formation of cap dolostones in a Snowball Earth context (i.e., Liu et al. 2014); c) are global oceanic models, and d) are short-term duration models (~8 Ky) with rapid carbonate deposition.

The second hypothesis seems to be more consistent, considering the high residence time of Sr (~10^6 years) in the oceans, and the long-term geological history of the Bambuí foreland basin system during several million years at the Ediacaran and Cambrian times (i.e., Kuchenbecker et al., 2020), and therefore, the mechanisms for the progressive fall of $^{87}Sr/^{86}Sr$ ratios in the basal Bambuí Group are better explained by temporal changes of the seawater composition due to paleogeographic changes.

Another implication is that the $^{87}Sr/^{86}Sr$ ratios of ca. 0.7076 seem to match the interval of rare *Cloudina* fossil occurrences in the basin, based on stratigraphic-chemostratigraphic correlations in the Januária city area (in the LHST; Caetano-Filho et al., 2019). This means that late Ediacaran strata in the Bambuí Group present $^{87}Sr/^{86}Sr$ ratios that mismatch the expected ones for coeval open marine basins, if considered global Sr isotope curves (i.e., Halverson et al., 2007; Zaky et al., 2019). Such fall in $^{87}Sr/^{86}Sr$ ratios through EHST to LHST does not seem to be associated with global changes in the oceanic Sr reservoir at the late Ediacaran and early Cambrian, as they are far below than the expected ratios for this time period (> 0.7080; i.e., Montañez et al. 1996, 2000; Zaky et al., 2019), and it is associated with other geochemical anomalies, such as basin wide increases in Sr/Ca ratios and succeeded by coupled positive $\delta^{13}C$ excursions reaching superheavy values (Caetano-Filho et al., 2019; 2021). Furthermore, some occurrences of more radiogenic $^{87}Sr/^{86}Sr$ ratios as high as ~0.7085 within Sr-rich interval (LHST of the lowermost 2nd-order sequence and in the overlying 2nd-order sequence; Fig. 27) demonstrates large and sharp $^{87}Sr/^{86}Sr$ variations in the Bambuí sea, which challenge the assumptions based on modern oceanographic Sr system (residence time >>> mixing of ocean waters). Depending on the depositional rates, this sharp transition would represent a rapid geochemical change on seawater, as expected for restricted seas and smaller reservoirs. Therefore, local processes controlling Bambuí Sr isotope chemostratigraphy might have prevailed over global ones.

Similar Sr isotope disturbance is also observed in other late Ediacaran West Gondwana basins bearing *Cloudina* occurrences (i.e., Kawashita, 1998; Gaucher et al., 2005; Goméz-Peral et al., 2007). Non-radiogenic $^{87}Sr/^{86}Sr$ ratios are reported in the Rio de la Plata Craton (Arroyo del Soldado Group, Uruguay), with ratios as low as 0.7073 (Gaucher et al., 2005, 2009), and for the Sierras Bayas Group (Argentina), $^{87}Sr/^{86}Sr$ ratios from 0.7070 to 0.7075 (Kawashita, 1998; Goméz-Peral et al., 2007), also mismatching the $^{87}Sr/^{86}Sr$ ratios proposed for the Ediacaran and early Cambrian oceans (Paula-Santos et al., 2017). Carbonates deposited in basins formed directly over the basement cratons, such as Rio de la Plata and São Francisco cratons, should record strontium isotope signatures reflecting regional inputs (source areas, aquifers), deviating from the contemporary oceanic water. If the drainage patterns of intracontinental basins were composed of a significant volume of juvenile magmatic rocks or older carbonate rocks, the Sr input on the restricted basins could have had unradiogenic $^{87}Sr/^{86}Sr$ ratios, and thus the calcium carbonate forming in these settings. Therefore, the amalgamation of West Gondwana and related orogenies could have been one of the factors responsible by this regional decrease in Sr ratios recorded in several intracontinental marine basins.

This would not be a singular event in geological time, since other significant temporal $^{87}Sr/^{86}Sr$ variations of seawater have been identified. They were correlated with periods of glaciations, mountain building, major volcanic eruptions or periods of enhanced submarine hydrothermal activity and ocean crust alteration, as well as changes in submarine groundwater discharge and total land area on continents (Peucker-Ehrenbrink and Fiske, 2019). These authors argue that the temporal variation in the $^{87}Sr/^{86}Sr$ of seawater is not primarily caused by variations in the balance between radiogenic continental and hydrothermal-related unradiogenic submarine Sr sources. Rather, $^{87}Sr/^{86}Sr$ temporal variations primarily reflect the changing on composition of continental exorheic runoff that is determined by the changing spatial distributions and age of the continental masses, as well as climate and drainage patterns through geological time. In a regional scale, variations in climate and sea-level changes can influence the $^{87}Sr/^{86}Sr$ record of marginal seas such as the Mediterranean, and continental freshwater inputs can locally modify the $^{87}Sr/^{86}Sr$ of coastal waters (i.e., Huang et al., 2011; Beck et al., 2013; Schildgen et al., 2014). In shorter time scales, unradiogenic $^{87}Sr/^{86}Sr$ patterns in Miocene

marine basins adjacent to the uplifted Alps and Apennines were attributed to a high influx of Sr from Mesozoic carbonates bearing low $^{87}Sr/^{86}Sr$ exposed in the hinterland, coupled to restricted exchange of water between these basins and the global oceans (Schildgen et al., 2014).

The factors mentioned above could explain the upward decreasing on Sr isotope contents of carbonates from the EHST to the LHST throughout the basin. Changes on the balance between accommodation and carbonate production/sedimentary supply could have changed the spatial distribution of the exorheic continental rivers, increasing geochemical input from dissolved carbonates exposed in catchment areas along the regression, as recorded by the studied highstand systems tract. The increasing tectonic uplift of source areas during the West Gondwana assembly might have also increased the contribution of ancient carbonate rocks to runoff waters (Paula-Santos et al., 2017), as well as the Bambuí carbonate ramp itself recycled by the orogenic activity surrounding the basin. Thus, mountain uplift and chemical weathering of rocks with unradiogenic Sr isotope ratios at regional scale can reasonably explain the homogenization in second order successions and the decrease in the $^{87}Sr/^{86}Sr$ ratios observed from EHST to LHST in the basal Bambuí Group.

Based on this, we suggest that ca. 550 million years ago (i.e., Kuchenbecker et al. 2020), changes on the balance between carbonate production and accommodation associated with tectonically-related flexural subsidence marked by the LHST progressively modified the continental drainage patterns, sedimentary sources and the chemical weathering regimes, altering the strontium influxes and isotopic compositions of the seawater in the early Bambuí basin cycle (Fig. 28). Variations on the contribution from the continents and changes on oceanic water connection due to the drop of the relative sea-level, combined with increased dissolution of ancient hinterland carbonate rocks may be responsible for the drastic decrease in $^{87}Sr/^{86}Sr$ ratios low to ~0.7076 (Fig. 28). This interpretation is supported by coupled basin-wide stratigraphic cycles and geochemical patterns ($^{87}Sr/^{86}Sr$ and Sr/Ca ratios, carbonate REE/PAAS patterns), suggesting these geochemical systems were controlled by the same forcing (e.g., Reis and Suss, 2016; Reis et al., 2017; Caetano-Filho et al., 2019; Paula-Santos et al., 2020). It is possible that

these mechanisms acted in other coeval West Gondwana basins bearing similar Sr isotope disturbances.

Also, continental inputs into seawater are not restricted to river discharge (Peucker-Ehrenbrink and Fiske, 2019). Submarine groundwater discharge (SGD) along the coasts and reactions in estuarine salinity gradients have a potential impact on the marine $^{87}Sr/^{86}Sr$ record (Chaudhuri and Clauer, 1986; Basu et al., 2001; Allègre et al., 2010; Beck et al., 2013; Trezzi et al., 2016; Guacaneme et al., 2017, Chakrabarti et al., 2018). This also would have led to great lateral and stratigraphic Sr isotope variability due to regional hydrologic controls on epicontinental seas (McArthur et al., 2001; Doebbert et al., 2014; Pietzsch et al., 2018; Peucker-Ehrenbrink and Fiske, 2019).

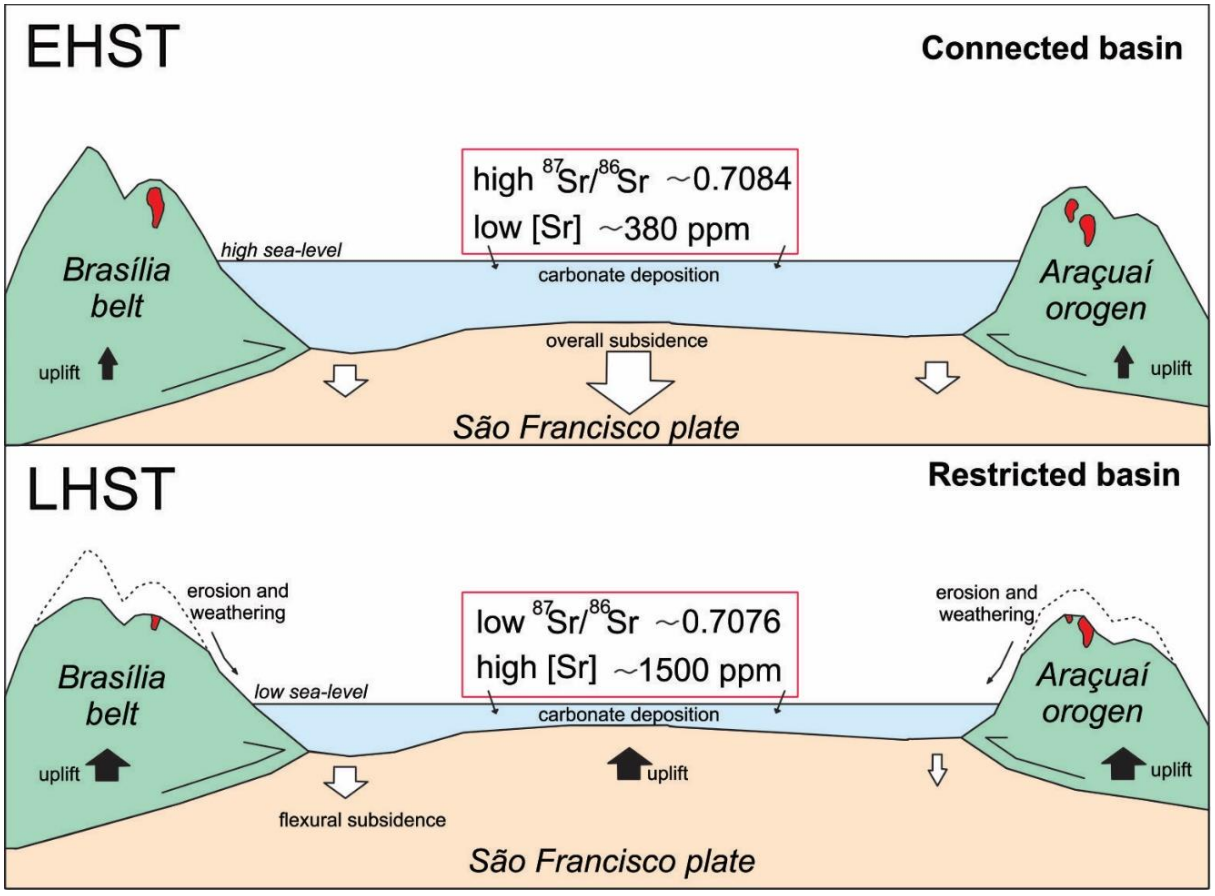

Figure 28. Sketch illustrating the Bambuí basin and the adjoining orogens at ca. 550 Ma (modified from Kuchenbecker et al., 2020). EHST: connected basin with high relative sea-level associated to overall subsidence; LHST: restricted basin with low relative sea-level associated to flexural subsidence and uplift of marginal orogens.

High Sr contents and Sr/Ca ratios, and pristine but variable radiogenic $^{87}Sr/^{86}Sr$ ratios persist through the basal portion of the upper 2nd-order sequence addressed in this work (Fig. 27; except the dolomite-rich intervals). These observations suggest that the Sr budget on the Bambuí seawater was more sensitive to paleoenvironmental changes, probably related to the progressive basin restriction driven by the forelandward advance of the marginal orogenic fronts (Paula-Santos et al., 2017; Uhlein et al., 2019; Caetano-Filho et al. 2019; Kuchenbecker et al. 2020). This is coherent with isotopic and elemental geochemistry that suggest a connected to restricted evolution of the Bambuí foreland basin system, leading to major changes in the seawater patterns, recording an increase in alkalinity, driving fractionation between LREY and HREY, which might have played an important role for biomineralization (Paula-Santos et al., 2020).

The new Sr isotope stratigraphy interpretation proposed here demonstrates that the strontium isotope system recorded the first steps on environmental restriction of the Bambuí foreland basin system, preceding the well-known carbon isotope disturbances to extreme values ($\delta^{13}C_{carb}$ and $\delta^{13}C_{org}$ as high as +16‰ and –14‰, respectively; Iyer et al., 1995; Caetano-Filho et al., 2020), which have been often associated with the plate reorganizations and environmental changes during the Gondwana assembly (e.g., carbon burial, methanogenesis, increased in $\delta^{13}C$ inputs; Paula-Santos et al., 2017; Uhlein et al., 2019; Caetano-Filho et al., 2020). The high Sr-content and unradiogenic Sr interval observed in the LHST studied here was likely associated with more alkaline and/or hypersaline conditions (Caetano-Filho et al., 2019; Paula-Santos et al., 2020), marking the first tectonically-driven isotope disturbance in the Ediacaran-Cambrian Bambuí basin cycle.

5.7 Conclusions

Temporal variations of $^{87}Sr/^{86}Sr$ ratios of marine carbonates of the basal Bambuí Group suggest that the Bambuí foreland basin system has evolved from a connected seaway to a restricted sea during the late Ediacaran and early Cambrian, in the context of West Gondwana assembly. A major decrease in the Sr isotope ratios from 0.7086 to 0.7076 is observed coupled to the sequence stratigraphic framework, preceding the positive carbon isotope excursion observed upwards and extending through the middle to

upper Bambuí Sequence. Such large variations were not caused by worldwide uniform changes in isotopic compositions of the global Ediacaran–Cambrian seawater reservoir. Instead, these anomalies may have resulted from marine isolation and paleogeographic changes induced by the evolving marginal orogenic systems. Changes in the chemical weathering regime within surrounding uplifted source areas and variations on the balance between accommodation and carbonate production/sedimentary supply might have been associated with increasingly inputs of unradiogenic $^{87}Sr/^{86}Sr$ by continental waters such as riverine freshwater and groundwater, limited marine dissolution of carbonates, which constitute strong local controls over the Sr isotope compositions of restricted seas. This culminated with a significant change in seawater chemistry and Sr budget and may have contributed to cause large $^{87}Sr/^{86}Sr$ variations coupled to the studied 2nd-order cycles. Similar anomalies in the strontium budget are also recorded in other marine basins of the West Gondwana, suggesting that these mechanisms may have played an important role in continental-scale throughout the late Ediacaran and early Cambrian times.

5.8 Acknowledgments

This study was funded by the São Paulo Research Foundation (FAPESP) thematic project grant #2016/06114-6, and was also supported by CNPq grant #400764/2016-4. CAPES for the fellowship provided to the first author. Sergio Caetano-Filho holds a FAPESP scholarship grant #2016/11496-5. Gustavo Paula-Santos holds a FAPESP post□doc grant #2017/00399-1. Marly Babinski, Ricardo Trindade and Matheus Kuchenbecker are fellows of the Brazilian Research Council (#307563/2013-8, #206997/2014-0 and #309106/2017-6, respectively). Technical support by Liliane Aparecida Petronilho, which provided the Sr isotope analyses at the CPGeo-USP and Margareth Sugano Navarro for elemental geochemistry at the Laboratory of Isotope Geology-UNICAMP. We would like to thank Jhon Afonso, Kamilla Amorim, Marilia Peloso and Sara dos Santos for field and lab work support and discussions. We are also grateful to Prof. Ian D. Somerville and an anonymous GR reviewer, whose suggestions greatly improved this manuscript.

5.9 References

Allègre, C.J., Louvat, P., Gaillardet, J., Meynadier, L., Rad, S., Capmas, F., 2010. The fundamental role of island arc weathering in the oceanic Sr isotope budget. Earth and Planetary Science Letters, 292: 51–56. doi:10.1016/j.epsl.2010.01.019.

Alkmim, F.F., Martins-Neto, M.A., 2001. A bacia intracratônica do São Francisco: Arcabouço estrutural e cenários evolutivos. In: Pinto, C.P., Martins-Neto, M. (Eds.). A Bacia do São Francisco: geologia e recursos naturais. SBG, Belo Horizonte, pp. 9–30.

Alkmim, F.F., Marshak, S., Pedrosa-Soares, A.C., Peres, G.G., Cruz, S., Whittington, A. 2006. Kinematic evolution of the Araçuaí-West Congo orogen in Brazil and Africa: nutcracker tectonics during the neoproterozoic assembly of Gondwana. Precambrian Research 149, 43-64.

Alkmim, F.F., Martins-Neto, M.A., 2012. Proterozoic first-order sedimentary sequences of the São Francisco craton, eastern Brazil. Marine and Petroleum Geology33:127-139.

Alkmim, F.F., Kuchenbecker, M., Reis, H.L., Pedrosa-Soares, A.C., 2017. The Araçuaí belt. In: Heilbron, M., Cordani, U.G., Alkmim, F.F. (Eds.), Sao Francisco Craton, Eastern Brazil. Tectonic Genealogy of a Miniature Continent. Springer, New York, pp. 255–276.

Almeida, F.F., Hasui, Y., Brito Neves, B.B., 1976. The Upper Precambrian of South America. Boletim do Instituto de Geociências, Universidade de São Paulo, 7: 45-80

Alvarenga, C.J.S., Dardenne M.A., Vieira L.C., Martinho C.T., Guimarães E.M., Santos R.V., Santana R.O., 2012. Estratigrafia da borda ocidental da Bacia do São Francisco. Boletim de Geociências da Petrobras 20, 145-164.

Alvarenga, C.J.S., Santos, R.V., Vieira, L.C., Lima, B.A.F., Mancini, L.H., 2014. Meso□Neoproterozoic isotope stratigraphy on carbonates platforms in the Brasília Belt of Brazil. Precambrian Research 251, 164–180.

Babinski, M., Vieira, L.C., Trindade, R.I.F., 2007. Direct dating of Sete Lagoas cap carbonate (Bambuí Group, Brazil) and implications for the Neoproterozoic glacial events. Terra Nova 19, 401-406.

Bailey, T., McArthur, J., Prince, H., Thirlwall, M., 2000. Dissolution methods for strontium isotope stratigraphy: whole rock. Chemical Geology, 167: 313–319. doi:10.1016/S0009 2541(99)00235-1.

Banner, J.L., Hanson, G.N., Meyer, W.J., 1988. Rare earth element and Nd isotopic variations in regionally extensive dolomites from the Burlington-Keokuk Formation (Mississippian): implications for REE mobility during carbonate diagenesis. Journal of Sedimentary Petrology, 58: 415–432. doi:10.1306/212F8DAA-2B24-11D7-8648000102C1865D.

Banner, J.L., Hanson, G.N., 1990. Calculation of simultaneous isotopic and trace element variations during water-rock interaction with application to carbonate diagenesis. Geochimica et Cosmochimica Acta 54, 3123–3137.

Banner, J.L. (2004). Radiogenic isotopes: systematics and applications to earth surface processes and chemical stratigraphy. Earth-Science Reviews 65, 141–194.

Barbosa, J.S.F., Barbosa, R.G., 2017. The paleoproterozoic eastern Bahia orogenic domain, 2017. In: Heilbron, M., Cordani, U.G., Alkmim, F.F. (Eds.), Sao Francisco Craton: Tectonic Genealogy of a Miniature Continent. Regional Geology Reviews. Springer, pp. 57–70.

Basu, A.R., Jacobsen, S.B., Poreda, R.J., Dowling, C.B., and Aggarwal, P.K. 2001. Large groundwater strontium flux to the oceans from the Bengal Basin and the marine strontium isotope record. Science, **293**: 1470–1473. doi:10.1126/science.1060524.

Bedoya-Rueda, C., 2019. Quimiostratigrafia isotópica (C, O, Sr) de alta resolução dos carbonatos da Formação Sete Lagoas, Grupo Bambuí, na região sudoeste da Bacia do São Francisco. Master Thesis, Instituto de Geociências, University of São Paulo, Brazil.

Beck, A.J., Charette, M.A., Cochran, J.K., Gonneea, M.E., Peucker-Ehrenbrink, B., 2013. Dissolved strontium in the subterranean estuary – Implications for the marine strontium isotope budget. Geochimica et Cosmochimica Acta 117, 33–52.

Bellefroid, E.J., Planavsky, N.J., Miller, N.R., Brand, U., Wang, C., 2018. Case study on the utility of sequential carbonate leaching for radiogenic strontium isotope analysis. Chemical Geology, 497: 88–99.

Brand, U., 2004. Carbon, oxygen and strontium isotopes in Paleozoic carbonate components: an evaluation of original seawater–chemistry proxies. Chemical Geology, **204**: 23–44. doi:10.1016/j.chemgeo.2003.10.013.

Brand, U., Veizer, J., 1980. Chemical diagenesis of a multicomponent carbonate system; 1, Trace elements. Journal of Sedimentary Research, 50: 1219–1236. doi:10.1306/212F7BB7-2B24-11D7-8648000102C1865D.

Brand, U., Veizer, J., 1981. Chemical diagenesis of a multicomponent carbonate system; 2, Stable isotopes. Journal of Sedimentary Research, 51: 987–997.doi:10.1306/212F7DF6-2B24-11D7-8648000102C1865D.

Brand, U., Logan, A., Bitner, M.A., Griesshaber, E., Azmy, K., Buhl, D., 2011. What is the ideal proxy of Palaeozoic seawater chemistry? Memoirs of the Association of Australasian Palaeontologists, 41: 9–24.

Caetano-Filho, S., Paula-Santos, G.M., Guacaneme, C., Babinski, M., Bedoya-Rueda, C., Peloso, M., Amorim, K., Afonso, J., Kuchenbecker, M., Reis, H.L.S., Trindade, R.I.F., 2019. Sequence stratigraphy and chemostratigraphy of an Ediacaran-Cambrian foreland-related carbonate ramp (Bambuí Group, Brazil). Precambrian Research 331, 105365.

Caetano-Filho, S., Sansjofre, P., Ader, M., Paula-Santos. G.M., Guacaneme, C., Babinski, M., Bedoya-Rueda, C., Kuchenbecker, M. Reis, H., Trindade, R.I.F., 2020. A large epeiric methanogenic Bambuí sea in the core of Gondwana Supercontinent. Geoscience Frontiers.

Campbell, I.H., Squire, R.J., 2010. The mountains that triggered the Late Neoproterozoic increase in oxygen: the second great oxidation event. Geochimica et Cosmochimica Acta, 74 (15), 4187–4206.

Canfield, D.E., Poulton, S.W., Narbonne, G.M., 2007. Late-Neoproterozoic deep□ocean oxygenation and the rise of animal life. Science 315 (5808), 92–95.

Castro, P.T.A., Dardenne, M.A. 2000. The sedimentology, stratigraphy and tectonic context of the São Francisco Supergroup at the southwestern domain of the São Francisco craton, Brazil. Revista Brasileira de Geociências 30, 439-441.

Caxito, F.A., Halverson, G.P., Uhlein, A., Stevensson, R., Dias, T.G., Uhlein, G.J., 2012. Marinoan glaciation in east central Brazil. Precambrian Research 200, 203:38-58.

Caxito, F.A., Uhlein, A., Dantas, E., Stevenson, R., Egydio-Silva, M., Salgado, S.S. 2017. The Rio Preto and Riacho do Pontal Belts, in M. Heilbron et al. (eds.), São Francisco Craton, Eastern Brazil, Regional Geology Reviews, DOI 10.1007/978-3-319-01715-0_12

Caxito, F.A., Frei, R., Uhlein, G.J., Dias, T.G., Árting, T.B., Uhlein, A., 2018. Multiproxy geochemical and isotope stratigraphy records of a neoproterozoic oxygenation event in the Ediacaran Sete Lagoas cap carbonate, Bambuí Group, Brazil. Chemical Geology 481, 119–132.

Chakrabarti, R., Mondal, S., Shankar, S., Sree, J., Sengupta, D., 2018. Submarine groundwater discharge derived strontium from the Bengal Basin traced in Bay of Bengal water samples Nature 8, 43-83.

Chaudhuri, S., Clauer, N., 1986. Fluctuations of isotopic composition of strontium in seawater during the Phanerozoic Eon. Chemical Geology 59, 293–303.

Chaudhuri, S., Clauer, N., 1993. Strontium isotopic compositions and potassium and rubidium contents of formation waters in sedimentary basins: clues to the origin of the solutes. Geochimica et Cosmochimica Acta 57, 429–437.

Chiavegatto, J.R.S., Gomes, N.S., Dardenne, M.A., Delgado, C.E.R., 2003. Estratigrafia do Grupo Bambuí nas regiões do norte de Minas Gerais: Uma nova unidade estratigráafic em um contexto de inversão de bacia. In: SBG, Siimpsio de Geologia de Minas Gerais, vol. 12. Ouro Preto, Anais, p. 24.

Costa, M.T., Branco, J.R., 1961. Roteiro para a excursão Belo Horizonte-Brasília. In Congresso Brasileiro de Geologia 14, UFMG, Inst. Pesq. Radioat., Publ. 15, 25p., Belo Horizonte.

Dardenne, M.A., 1978. Síntese sobre a estratigrafia do Grupo Bambuí no Brasil Central. In: Congresso Brasileiro de Geologia, 30, Recife, Anais, SBG, v. 2, p. 597-610.

DePaolo, D.J., and Ingram, B.L. 1985. High-resolution stratigraphy with strontium isotopes. Science, **227**: 938–942. doi:10.1126/science.227.4689.938.

Derry, L.A., 2010. A burial diagenesis origin for the Ediacaran Shuram–Wonoka carbon isotope anomaly. Earth and Planetary Science Letters 294, 152–162.

Derry, L.A., Kaufman, A.J., Jacobsen, S.B., 1992. Sedimentary cycling and environmental changes in the Late Proterozoic: Evidence from stable and radiogenic isotopes. Geochimica et Cosmochimica Acta, 56:1317-1329.

Doebert, A.C., Johnson, C.M., Carroll, A.R., Beard, B.L., Pietras, J.T., Carson, M.R., Norsted, B., Throckmorton, L.A., 2014. Controls on Sr isotopic evolution in lacustrine systems: Eocene Green River Formation, Wyoming. Chemical Geology 380, 172–189.

Drever, J.I., 1988. The geochemistry of natural waters. Vol. 437. Prentice Hall, Englewood Cliffs, NJ.

Elderfield, H., 1986. Strontium isotope stratigraphy. Palaeogeography, Palaeoclimatology, Palaeoecology 57, 71–90.

Fölling, P.G., Frimmel, H.E., 2002. Chemostratigraphic correlation of carbonate successions in the Gariep and Saldania Belts, Namibia and South Africa. Basin Research14; 69□88.

Gaucher, C., Poiré, D.G., Peral, L.G., Chiglino, L., 2005. Litoestratigrafia, bioestratigrafia y correlaciones de las sucesiones sedimentarias Neoproterozoico–Cambrico del Craton del Rio de la Plata (Uruguay y Argentina). Latin American Journal of Sedimentology and Basin Analysis 12 (2), 145–160.

Gaucher, C., Sial, A.N., Poiré, D.G., Gomes-Peral, L., Ferreira, V.P., Pimentel, M.M., 2009. Chemostratigraphy, Neoproterozoic-Cambrian evolution of the Río de la Plata paleocontinent. In: Gaucher, C., Sial, A.N., Halverson, G.P., Frimmel, H.E. (Eds.), Neoproterozoic-Cambrian Tectonics, Global Change and Evolution: A Focus on Southwestern Gondwana Developments in Precambrian Geology. Elsevier, Amsterdam, pp. 115–122.

Goméz-Peral, L.E., Poiré, D.G., Strauss, H., Zimmermann, U., 2007. Chemostratigraphy and diagenetic constraints on Neoproterozoic carbonate successions from the Sierras Bayas Group, Tandilia System, Argentina. Chemical Geology 237 (1), 109–128.

Guacaneme, C., Babinski, M., Paula-Santos, G.M.D., Pedrosa-Soares, A.C., 2017. C, O, and Sr isotopic variations in Neoproterozoic-Cambrian carbonate rocks from Sete Lagoas Formation (Bambuí Group), in the Southern São Francisco Basin, Brazil. Brazilian Journal of Geology 47, 521–543.

Halverson, G.P., Dudás, F.O., Maloof, A.C., Bowring, S.A., 2007. Evolution of the $^{87}Sr/^{86}Sr$ composition of Neoproterozoic seawater. Palaeogeography, Palaeoclimatology, Palaeoecology, 256 (3-4): 103-129.

Halverson, G.P., Wade, B.P., Hurtgen, M.T., Barovich, K.M., 2010. Neoproterozoic chemostratigraphy. Precambrian Research, 182:337□350.

Heilbron, M., Cordani, U.G., Alkmim, F.F. 2017. The São Francisco Craton and Its Margins, in M. Heilbron et al. (eds.), São Francisco Craton, Eastern Brazil, Regional Geology Reviews, DOI 10.1007/978-3-319-01715-0_1.

Higgins, J.A., Blättler, C.L., Lundstrom, E.A., Santiago-Ramos, D.P., Akhtar, A.A., Crüger Ahm, A.S., Bialik, O., Holmden, C., Bradbury, H., Murray, S.T., Swart, P.K., 2018. Mineralogy, early marine diagenesis, and the chemistry of shallow-water carbonate sediments. Geochimica et Cosmochimica Acta 220, 512–534.

Hippertt, J.P., Caxito, F.A., Uhlein, G.J., Nalini, H.A., Sial, A.N., Abreu, A.T., Nogueira, L.B., 2019. The fate of a Neoproterozoic intracratonic marine basin: Trace elements, TOC and IRON speciation geochemistry of the Bambuí Basin, Brazil. Precambrian Research, 330: 101-120

Hood, A.V.S., Wallace, M.W., 2018. Neoproterozoic marine carbonates and their paleoceanographic significance. Glob. Planet. Change160, 28–45.

Hoffman, P.F., Kaufman, A.J., Halverson, G.P., Schrag, D.P., 1998. A Neoproterozoic Snowball Earth. Science, 281: 1342-1346.

Hoffman, P.F., Schrag, D.P., 2002. The Snowball Earth hypothesis: testing the limits of global change. Terra Nova, 14:129-155.

Huang, K.-F., You, C.-F., Chung, C.-H., Lin, I.-T., 2011. Nonhomogeneous seawater Sr isotopic composition in the coastal oceans: a novel tool for tracing water masses and submarine groundwater discharge. Geochemistry, Geophysics, Geosystems 12 (5), Q05002. https://doi.org/10.1029/2010GC003372.

Hodell, D.A., Mead, G.A., Mueller, P.A., 1990. Variation in the strontium isotopic composition of seawater (8 Ma to present): Implications for chemical weathering rates and dissolved fluxes to the oceans. Chemical Geology 80, 291–307. doi: 10.1016/0168-9622(90)90011-Z

Ingram, B.L., Sloan, D., 1992. Strontium isotopic composition of estuarine sediments as paleosalinity□paleoclimate indicator. Science 255, 68–72.

Iyer, S.S., Babinski, M., Krouse, H.L., Chemale, F., 1995. Highly ^{13}C-enriched carbonate and organic matter in the Neoproterozoic sediments of the Bambuí Group, Brazil. Precambrian Research, 73: 271-282.

Jacobsen, S.B., Kaufman, A.J., 1999. The Sr, C and O isotopic evolution of Neoproterozoic seawater. Chemical Geology, 161:37-57.

Kaufman, A.J., Knoll, A.H., Narbonne, G.M., 1997. Isotopes, ice ages, and terminal Proterozoic Earth history. National Academy Sciences Proceedings, 94:600□605.

Kawashita, K., 1998. Rochas carbonáticas neoproterozoicas da América do Sul: idades e inferências quimioestratigráficas. (Livre Docência Thesis). University of São Paulo, Brazil.

Knoll, A.H., Walter, M.R., Narbonne, G.M. Christie-Blick, N., 2006. The Ediacaran Period: a new addition to the geologic time scale. Lethaia, 39, 13–30.

Krabbenhoft, A., Eisenhauer, A., Bohm, F., Vollstaedt, H., Fietzke, J., Liebetrau, V., 2010. Constraining the marine strontium budget with natural strontium isotope fractionations ($^{87}Sr/^{86}Sr$, $\delta^{88}/^{86}Sr$) of carbonates, hydrothermal solutions and river waters. Geochimica et Cosmochimica Acta,74: 4097–4109.

Kuchenbecker, M., 2011. Quimioestratigrafia e proveniência sedimentar da porção basal do Grupo Bambuí em Arcos (MG). Master Thesis, Universidade Federal de Minas Gerais, Belo Horizonte, p. 91.

Kuchenbecker, M., Babinski, M., Pedrosa-Soares, A. C., Costa, R. D., Lopes-Silva. L., Pimenta, F., 2013. Proveniência e análise sedimentar da porção basal do Grupo Bambuí em Arcos (MG). Geologia USP 13(4): 49–61.

Kuchenbecker, M., Babinski, M., Pedrosa-Soares, A.C., Lopes-Silva, L., Pimenta, F., 2016a. Chemostratigraphy of the lower Bambuí Group, southwestern São Francisco Craton, Brazil: insights on Gondwana paleoenvironments. Brazilian Journal of Geology 46, 145–162.

Kuchenbecker, M., Atman, D., Costa, R.D., Pedrosa-Soares, A.C., Babinski, M., 2016b. A formação Gorutuba: sedimentação litorânea a continental na margem leste da Bacia Bambuí (MG). Geologia USP Série Científica 16 (2), 67–81.

Kuchenbecker, M., Pedrosa-Soares, A.C., Babinski, M., Reis, H.L.S., Atman, D., Costa, R.D. 2020. Towards an integrated tectonic model for the interaction between the Bambuí basin and the adjoining orogenic belts: Evidences from the detrital zircon record of syn-orogenic units. Journal of South American Earth Sciences, 104-102831

Kuznetsov, A.B., Ovchinnikova, G.V., Gorokhov, I.M., Letnikova, E.F., Kaurova, O.K., Konstantinova, G.V., 2013. Age constraints on the Neoproterozoic Baikal Group from combined Sr isotopes and Pb-Pb dating of carbonates from the Baikal type section, southeastern Siberia. Journal of Asian Earth Sciences 62, 51–66.

Li, D., Shields□Zhou, G.A., Ling, H.-F., Thirlwall, M., 2011. Dissolution methods for strontium isotope stratigraphy: guidelines for the use of bulk carbonate and phosphorite rocks. Chemical Geology, 290: 133–144. doi:10.1016/j.chemgeo.2011.09.004.

Liu, C., Wang, Z., Raub, T.D., 2013. Geochemical constraints on the origin of Marinoan cap dolostones from Nuccaleena Formation, South Australia. Chemical Geology, 395: 95–104. doi:10.1016/j.chemgeo.2013.05.012.

Liu, C., Wang, Z., Raub, T.D., Macdonald, F.A., Evans, D.A.D., 2014. Neoproterozoic cap-dolostone deposition in stratified glacial meltwater plume. Earth Planetary Science Letters, 404, 22–32.

Martins-Neto, M.A., Pedrosa-Soares, A.C., Lima, S.A.A., 2001. Tectono-sedimentary evolution of sedimentary basis from Late Paleoproterozoic to Late Neoproterozoic in the São Francisco craton and Araçuaí fold belt, eastern Brazil. Sedimentary Geology, 142:343-370.

Martins-Neto, M.A., 2005. A Bacia do São Francisco: arcabouços estratigráfico e estrutural com base na integração de dados de superfície e subsuperfície. In Simpósio sobre o Cráton do São Francisco, III, Salvador/BA, 2005, Anais, pp. 283-286.

Martins-Neto, M.A. 2009. Sequence stratigraphic framework of Proterozoic successions in eastern Brazil. Marine and Petroleum Geology, 26:163-176.

McArthur, J.M., Howarth, R.J., Bailey, T.R., 2001. Strontium isotope stratigraphy: LOWESS version 3: best fit to the marine Sr-isotope curve for 0–509 Ma and accompanying look-up table for deriving numerical age. The Journal of Geology, **109**: 155–170. doi:10.1086/319243.

McArthur, J.M., Howarth, R.J., Shields, G.A., 2012. Chapter 7 – Strontium isotope stratigraphy. The Geologic Time Scale, **1**: 127–144. doi:10.1016/B978-0-444-59425-9.00007-X.

Melezhik, V.A., Gorokhov, I.M., Kuznetsov, A.B., Fallick, A.E., 2001. Chemostratigraphy of Neoproterozoic carbonates: implications for “blind dating”. Terra Nova, 13: 1-11.

Misi, A., Kaufman, A.J., Veizer, J., Powis, K., Azmy, K., Boggiani, P.C., Gaucher, C., Teixeira J.B.G., Sanchez, A.L., Iyer, S.S.S., 2007. Chemostratigraphic correlation of Neoproterozoic successions in South America. Chemical Geology, 237: 143□167.

Montañez, I.P., Banner, J., Osleger D.A., Borg, L.E., Bosserman, P.J. 1996. Integrated Sr isotope variations and sea-level history of Middle to Upper Cambrian platform carbonates: Implications for the evolution of Cambrian seawater $^{87}Sr/^{86}Sr$. Geology, v. 24-10, p. 917-920.

Montañez, I.P., Osleger, D.A., Banner, J.L., Mack, L.E., Musgrove, M. 2000. Evolution of the Sr and C Isotope Composition of Cambrian Oceans. GSA today, v. 10-5

Moreira, D.S., Uhlein, A., Dussin, I.A., Uhlein, G.J., Misuzaki, A.M., 2020. A Cambrian age for the upper Bambuí Group, Brazil, supported by the first U-Pb dating of volcaniclastic bed, Journal of South American Earth Sciences, https://doi.org/10.1016/j.jsames.2020.102503.

Palmer M.R. and Edmond J.M. 1989. The strontium isotope budget of the modem ocean. Earth Planetary Science Letters. 92, 11-26.

Paula-Santos, G.M., Babinski, M., Kuchenbecker, M., Caetano-Filho, S., Trindade, R.I., Pedrosa-Soares, A.C., 2015. New evidence of an Ediacaran age for the Bambuí Group in southern São Francisco craton (eastern Brazil) from zircon U-Pb data and isotope chemostratigraphy. Gondwana Research 28, 702-720.

Paula-Santos, G.M., Caetano-Filho, S., Babinski, M., Trindade, R.I., Guacaneme, C., 2017. Tracking connection and restriction of West Gondwana São Francisco Basin through isotope chemostratigraphy. Gondwana Research 42, 280-305.

Paula-Santos, G.M., Caetano-Filho, S., Babinski, M., Enzweiler, J., 2018. Rare earth elements of carbonate rocks from the Bambuí Group, southern São Francisco Basin, Brazil, and their significance as paleoenvironmental proxies. Precambrian Research 305, 327-340.

Paula-Santos, G.M., Caetano-Filho, S., Enzweiler, J., Navarro, M.S., Babinski, M., Guacaneme, C., Kuchenbecker, M., Reis, H., Trindade, R.I.F., 2020. Rare earth elements in the terminal Ediacaran Bambuí Group carbonate rocks (Brazil): evidence for high seawater alkalinity during rise of early animals. Precambrian Research 336, 105506.

Perrella, P., Uhlein, A., Uhlein, G.J., Sial, A.N., Pedrosa-Soares, A.C., Lima, O.N.B., 2017. Facies analysis, sequence stratigraphy and chemostratigraphy of the Sete Lagoas Formation (Bambuí Group), northern Minas Gerais State, Brazil: evidence of a cap carbonate deposited on the Januária basement high. Brazilian Journal of Geology 47, 59−77.

Peucker-Ehrenbrink, B., Fiske, G.J., 2019. A continental perspective of the seawater $^{87}Sr/^{86}Sr$ record: A review. Chemical Geology 510, 140–165.

Pietzsch, R., Oliveira, D.M., Tedeschi, L.R., Queiroz Neto, J.V., Figueiredo, M.F., Vazquez, J.C., Souza, R.S. 2018. Palaeohydrology of the Lower Cretaceous pre-salt lacustrine system, from rift to post-rift phase, Santos Basin, Brazil. Palaeogeography, Palaeoclimatology, Palaeoecology 507, 60–80

Pimentel, M.M., Fuck, R.A., Botelho, N.F. 1999. Granites and the geodynamic history of the Neoproterozoic Brasilia belt, Central Brazil: a review. Lithos 46 (3), 463–483.

Reis, H.L.S., Suss, J.F., 2016. Mixed carbonate-siliciclastic sedimentation in forebulge grabens: an example from the Ediacaran Bambuí Group, São Francisco basin, Brazil. Sedimetary Geology, 339, 83–103.

Reis, H.L.S., Alkmim, F.F., Fonseca, R.C.S., Nascimento, T.C., Suss, J.F., Prevatti, L.D., 2016. The São Francisco Basin. In: Heilbron, M., Cordani, U.G., Alkmim, F.F. (Eds.), São Francisco Craton, Eastern Brazil, Regional Geology Reviews. Springer, Switzerland, pp. 117–143.

Reis, H.L.S., Suss, J.F., Fonseca, R.C.S., Alkmim, F.F., 2017. Ediacaran forebulge grabens of the southern São Francisco basin, SE Brazil: Craton interior dynamics during West Gondwana assembly. Precambrian Research 302, 150–170.

Rocha-Campos A.C., Brito-Neves B.B., Babinski M., Santos P.R., Oliveira S.M.B., Romano A. 2011. Moema Laminites: a newly recognized Neoproterozoic (?) glaciogenic unit, São Francisco Basin, Brazil. Geological Society London Memoirs, 36:535-540.

Romano, A.W. 2007. Geologia da Folha Pará de Minas (SE.23-Z-C-IV), escala 1:100.000: nota explicativa. UFMG/CPRM-Serviço Geológico do Brasil, Belo Horizonte

Santos, R.V., Alvarenga, C.J.S., Dardenne, M.A., Sial, A.N., Ferreira, V.P., 2000. Carbon and oxygen isotope profiles across Meso□Neoproterozoic limestones from central Brazil: Bambuí and Paranoá Groups. Precambrian Research 104, 107–122.

Santos, R.V., Alvarenga, C.J.S., Babinski, M., Ramos, M.L.S, Cukrov, N., Fonseca, M.A., Sial, A.N., Dardenne, M.A., Noce, C.M., 2004. Carbon isotopes of Mesoproterozoic–Neoproterozoic sequences from Southern São Francisco craton and Araçuaí Belt, Brazil: Paleogeographic implications. Journal of South American Earth Sciences, 18: 27-39.

Schildgen, T.F., Cosentino, D., Frijia, G., Castorina, F., Dudas, O., Iadanza, A., Sampalmieri, G., Cipollari, P., Caruso, A., Bowring, S.A., Strecker, M.R., 2014. Sea level and climate forcing of the Sr isotope composition of late Miocene Mediterranean marine basins. Geochemistry, Geophysics, Geosystems 15, 2964–2983. https://doi.org/10.1002/2014GC005332.

Shields, G.A., Stille, P., Brasier, M.D., Atudorei, N. 1997. Stratified oceans and oxygenation of the late Precambrian environment: a post glacial geochemical record from the Neoproterozoic of W. Mongolia. Terra Nova, 9, 218-222.

Shields, G.A., 2005. Neoproterozoic cap carbonates: a critical appraisal of existing models and the plumeworld hypothesis. Terra Nova, 17 (4), 299–310.

Teixeira, W., Sabaté, P., Barbosa, J., Noce, C.M., Carneiro, M.A., 2000. Archean and Paleoproterozoic tectonic evolution of the São Francisco craton, Brazil. In: Cordani, U.G., Milani, E.J., Thomaz-Filho, A., Campos, D.A. (eds.). Tectonic Evolution of South America. 31st International Geology Congress, Rio de Janeiro, p. 101-137.

Teixeira, W., Oliveira, E.P., Marques, L.S., 2017. Nature and evolution of the archean crust of the São Francisco craton, 2017. In: Heilbron, M., Cordani, U.G., Alkmim, F.F. (Eds.), São Francisco Craton: Tectonic Genealogy of a Miniature Continent. Regional Geology Reviews. Springer, pp. 29–56.

Trezzi, G., Garcia-Orellana, J., Rodellas, V., Masque, P., Garcia-Solsona, E., Andersson, P.S., 2016. Assessing the role of submarine groundwater discharge as a source of Sr to the Mediterranean Sea. Geochimica et Cosmochimica Acta, GCA10057. https://doi.org/10.1016/j.gca.2016.12.005.

Uhlein, A., Baptista, M.C., Seer, H.J., Caxito, F.A., Uhlein, G.J., Dardenne, M.A., 2011. A Formação Lagoa Formosa, Grupo Bambuí (MG): Sistema deposicional de leque submarino em bacia de antepaís. Geonomos 19(2): 163–172.

Uhlein, G.J., Uhlein, A., Stevenson, R., Halverson, G.P., Caxito, F.A., Cox, G.M., 2017. Early to late Ediacaran conglomeratic wedges from a complete foreland basin cycle in the southwest São Francisco Craton, Bambuí Group, Brazil. Precambrian Research 299, 101–116.

Uhlein, G.J., Uhlein, A., Pereira, E., Caxito, F.A., Okubo, J., Warren, L.V., Sial, A.N., 2019. Ediacaran paleoenvironmental changes recorded in the mixed carbonate siliciclastic Bambuí Basin, Brazil. Palaeogeography, Palaeoclimatology, Palaeoecology, 517, 39–51.

Valeriano, C.M., 2017. The southern Brasília belt. In: Heilbron, M., Cordani, U.G., Alkmim, F.F. (Eds.), São Francisco Craton, Eastern Brazil: Tectonic Genealogy of a Miniature Continent. Springer International Publishing, Switzerland, pp. 189–204.

Veizer, J., Compston, W., Clauer, N., Schidlowski, M., 1983. $^{87}Sr/^{86}Sr$ in Late Proterozoic carbonates: evidence for a mantle event at 900 Ma ago. Geochimica et Cosmochimica Acta 47, 295–302.

Veizer, J., Ala, D., Azmy, K., Brukschen, P., Buhl, D., Bruhn, F., Carden, G.A.F., Diener, A., Ebneth, S., Godderis, Y., Jasper, T., Korte, C., Pawellek, F., Podlaha, O.G., Strauss, H., 1999. $^{87}Sr/^{86}Sr$, $\delta^{13}C$ and $\delta^{18}O$ evolution of Phanerozoic seawater. Chemical Geology, 161:59–88.

Veizer, J., Hoefs, J., Ridler, R.H., Jensen, L.S., Lowe, D.R., 1989. Geochemistry of Precambrian carbonates: I. Archean hydrothermal systems. Geochimica et Cosmochimica Acta, 53:845–857.

Vieira, L.C., Almeida, R.P., Trindade, R.I.F., Nogueira, A.C.R., Janikian, L., 2007a. Formação Sete Lagoas em sua área-tipo: fácies, estratigrafia e sistemas deposicionais. Revista Brasileira de Geociências, 37:1–4.

Vieira, L.C., Trindade, R.I.F, Nogueira, A.C.R., Ader, M., 2007b. Identification of a Sturtian cap carbonate in the Neoproterozoic Sete Lagoas carbonate plataform, Bambuí Group, Brazil. Comptes Rendus Geoscience, 339:240–258.

Warren, L.V., Quaglio, F., Riccomini, C., Simões, M.G., Poiré, D.G., Strikis, N.M., Anelli, L.E. Strikis, P.C., 2014. The puzzle assembled: Ediacaran guide fossil Cloudina reveals an old proto□Gondwana seaway. Geology, 42 (5): 391–394.

Wei, G., Hood, A.V.S., Chen, Xi., Li, D., Wei, W., Wen, B., Gong, Z., Yang, T., Zhang, Z., Ling, H., 2019. Ca and Sr isotope constraints on the formation of the Marinoan cap dolostones. Earth and Planetary Science Letters, 511 202–212

Young, G.M., 2013. Evolution of Earth's climatic system: Evidence from ice ages, isotopes, and impacts. GSA Today, v. 23, no. 10.

Zaky, A.M., Brand, U., Buhl, D., Blamey, N.M., Bitner, A., Logan, A., Gaspard, D., Popov, A., 2019. Strontium isotope geochemistry of modern and ancient archives: tracer of secular change in ocean chemistry. Canadian Journal of Earth Sciences. 56: 245–264.

6 CHAPTER 6 – PALEOENVIRONMENTAL REDOX EVOLUTION OF A LATE EDIACARAN–EARLY CAMBRIAN RESTRICTED SEA: INSIGHTS FROM TRACE–METAL ENRICHMENT PATTERNS OF CARBONATES OF THE BASAL BAMBUÍ GROUP, EAST BRAZIL

Cristian Guacaneme[1]*, Sergio Caetano-Filho[1], Gustavo M. Paula-Santos[2], Marly Babinski[1], Paula L. Fraga-Ferreira[1], Carolina Bedoya-Rueda[1], Matheus Kuchenbecker[3,4], Humberto L.S. Reis[5], Ricardo I.F. Trindade[6]

[1]*Universidade de São Paulo, Instituto de Geociências, Rua do Lago, 562, São Paulo, Brazil - ZIP code 05508-080*

[2]*University of Bremen, Faculty of Geosciences and MARUM-Center for Marine Environmental Sciences, Leobener Strasse 8, 28359, Bremen, Germany*

[3]*Universidade Federal dos Vales do Jequitinhonha e Mucuri, Instituto de Ciência e Tecnologia, Centro de Estudos em Geociências, Laboratório de Estudos Tectônicos, Rodovia MGT 367, Km 583 – Diamantina, Brazil - ZIP code 39100-000*

[3]*Universidade Federal de Minas Gerais, Centro de Pesquisas Professor Manoel Teixeira da Costa. Av. Antônio Carlos, 6627 - Belo Horizonte, Brazil - ZIP code 31270-901*

[5]*Universidade Federal de Ouro Preto, Departamento de Geologia-Escola de Minas, Laboratório de Modelagem Tectônica (LabMod), Campus Morro do Cruzeiro, Ouro Preto, Brazil - ZIP code 35400-000*

[6]*Universidade de São Paulo, Instituto de Astronomia, Geofísica e Ciências Atmosféricas, Rua do Matão, 1226 - São Paulo, Brazil - ZIP code 05508-090*

6.1 Abstract

The sedimentary evolution of the Bambuí marine basin in the interior of West Gondwana is marked by periods of connection and isolation from the global ocean at the late Neoproterozoic and early Paleozoic. In order to understand the link between these periods and seawater redox conditions, we present an integrated study of trace-metal geochemistry and stratigraphy of carbonates from the Bambuí Group in east Brazil. At the basal 2nd-order sequence, trace-metal normalized data show a progressive increase of the enrichment factor (EF) relative to PAAS for Cd, Cu, and Zn in the order of 1–100 times, and for Mo and U in the order of 10–1000 times, concomitant with a decrease in Al contents and Mo/TOC ratios. These changes in sedimentary trace-metal patterns provide evidence for the chemical evolution of basinal deep-waters, whose conditions changed progressively from suboxic-anoxic to anoxic-euxinic at the basal transgressive-regressive sequence. We suggest that probably the Bambuí paleomarine system has evolved as an intracontinental silled basin recording changes in seawater chemistry associated with redox variations and restricted hydrographic conditions. Sedimentary trace-metal patters indicate that Bambuí epeiric sea was communication with open ocean followed by the marine restriction during the transgressive and regressive cycles, respectively. This results in long deepwater residence time and chemical evolution of deep watermass as a response to tectonic pulses and consequent sea-level variations at the restricted stage. Under anoxic-euxinic conditions of seawater, trace metals scarcity and micronutrient fixation limitation would have impacted nitrate bioavailability, preventing the evolution of early benthic metazoans in the Bambuí paleomarine system during the late Ediacaran and early Cambrian.

Keywords: Ediacaran-Cambrian transition, trace-metal enrichment patterns, restricted sea, Bambuí Group

6.2 Introduction

The Ediacaran-Cambrian transition can be considered as some of the most important time intervals in the Earth System evolution, when striking changes in the planet dynamics, extreme climate events and the appearance of the first complex animals occurred (Kaufman et al., 1997; Knoll et al., 2006; Canfield et al., 2007; Campbell and Squire, 2010; Liyuan et al. 2021). These changes are preserved in the record of sedimentary basins worldwide, whose sedimentary, geochemical and paleontological registers have been interpreted under the view of a global interconnected ocean-climate system (Shen et al., 1998; Marshall, 2006; Li et al., 2013).

Although this scenario has been consistently described in sedimentary successions throughout the world, recent advances in the study of the stratigraphic, geochemical and paleontological record of the Ediacaran-Cambrian Bambuí Group, exposed on the São Francisco craton (east Brazil), have showed contrasting paleoenvironmental conditions. Allowing a significant step forward in understanding the ancient conditions under which the early metazoans started to inhabit benthic environments, the available data have pointed that much of the Bambuí strata was deposited in a restricted foreland marine basin surrounded by Brasiliano/Pan-African orogens in the core of West Gondwana (i. e., Paula-Santos et al., 2017; Uhlein et al., 2017, 2019; Hippertt et al., 2019; Caetano-Filho et al., 2019, 2021; Kuchenbecker et al., 2020; Guacaneme et al., 2021, Fraga-Ferreira et al., 2021; Caxito et al. 2021c). This foreland basin system would have experienced intermittent periods of connection with contemporary seas (Paula-Santos et al., 2017; Kuchenbecker et al., 2020; Uhlein et al., 2019; Hippertt et al., 2019; Caetano-Filho et al., 2019, 2021, Guacaneme et al. 2021; Caxito et al. 2021c), which allowed the episodic spread of cosmopolitan organisms (e.g., *Cloudina* sp.) through an epicontinental seaway (Warren et al., 2014; Perrella et al., 2017). Conversely, the tectonically-related confinement of the basin triggered the disconnection with global oceans and major geochemical changes of seawater after a glacial episode (Paula-Santos et al., 2017, 2018; Uhlein et al., 2019; Hippertt et al., 2019; Caetano-Filho et al., 2019, 2021, Guacaneme et al., 2021; Caxito et al. 2021c).

Significant redox changes in seawater chemistry are recorded in the basal strata of the Bambuí Group, which has been interpreted as the consequence of its unusual

restricted paleoenvironmental conditions. It has been suggested that the lack of oceanic connection prevented the re-supply of sulfate, trace metals, micronutrients, and ultimately dissolved O_2, leading to a decrease in the biological activity and preventing the animal evolution of typical Cambrian benthic ecosystems (Hippertt et al., 2019; Caetano-Filho et al., 2021, Caxito et al. 2021c). However, basin-wide detailed approaches on these subjects are still scarce. It is specially the case of trace metal-based studies, which have been proved excellent proxies to understand the redox evolution of seawater and hydrographic changes in ancient paleomarine systems, and comprise chemical elements essential for the metabolic paths of organisms, including metazoans (e.g., Anbar and Knoll, 2002; Tribovillard et al., 2006; Algeo and Tribovillard, 2009; Algeo et al., 2012; Algeo and Rowe, 2012).

This study presents a detailed trace metal investigation in a high-resolution sampling of carbonates of the Ediacaran-Cambrian Bambuí Group. Combined to the available sequence stratigraphy framework, chemostratigraphic and paleotectonic reconstructions (e.g., Reis and Suss, 2016; Caetano-Filho et al., 2019, 2021; Uhlein et al., 2019; Paula-Santos et al., 2020; Kuchenbecker et al., 2020, Guacaneme et al., 2021; Fraga-Ferreira et al., 2021), it provides invaluable information for reconstructing the paleoenvironmental conditions that reigned during the unusual evolution of the Bambuí basin and also might offer insights to understanding other similar systems.

6.3 Background on marine trace-metal geochemistry

Reconstructions of paleomarine systems have been improved in recent years with significant contribution of the application of trace-metal geochemistry in sedimentary rocks, which allows to assess the redox state and chemical evolution of seawater, productivity/preservation of organic matter, and the degree of hydrographic restriction in anoxic marine basins and deepwater residence time (Lyons et al., 2009, 2014; Algeo and Maynard, 2004, 2008; Brumsack, 2006; McManus et al., 2006; Tribovillard et al., 2006; Algeo and Tribovillard, 2009; Algeo et al., 2012; Algeo and Rowe, 2012; Sweere et al., 2016).

Trace metals (Cd, Co, Cr, Cu, Mo, Ni, U, V, Zn) in seawater are less soluble under reducing conditions, which may result in their overall authigenic enrichment of sedimentary successions deposited in oxygen-poor settings (Brumsack, 2006; Tribovillard et al., 2006; Algeo et al., 2012; Algeo and Rowe, 2012; Sansjofre et al., 2014). For example, since the Mo and U are more easily scavenged or diffusively trapped across the sediment-water interface, they are often adsorbed in previously formed deposits or concentrated in minerals formed during the early diagenesis of sediments deposited under anoxic conditions (Brumsack, 2006; Tribovillard et al., 2006; Algeo and Tribovillard, 2009; Algeo and Rowe, 2012).

Mo and U are incorporated into anoxic sediments via different processes (Algeo and Maynard, 2004; Sansjofre et al., 2014). In the modern seawater, part of dissolved U^{6+} diffuses into the sediment and when it reaches the ferruginous redoxcline (where Fe^{3+} reduces to Fe^{2+}), U^{6+} is reduced to U^{4+} and then fixed into the sediments by adsorption or precipitation (Canfield and Thamdrup, 2009). This accumulation is partly mediated by bacterial sulfate reduction, which lead to uranium authigenic enrichment in marine sediments with free H_2S (Tribovillard et al., 2006; Sansjofre et al., 2014). In contrast, dissolved Mo varies little with depth, reflecting its more conservative behavior in an oxygenated water column. The reduction of Mn-oxyhydroxides liberates adsorbed Mo into pore waters through the formation of thiomolybdate (MoO_4^{2-}), which is fixed in Fe-sulfide and/or organic matter molecules and allows the Mo sediment-enrichment in shallow burial conditions. Since thiomolybdate requires free H_2S to form, Mo accumulation in the sediment occurs dominantly under euxinic (sulfidic) conditions (Zheng et al., 2000; Tribovillard et al., 2006).

The mechanisms of Mo and U accumulation into sediments in euxinic and anoxic waters are particularly well understood, which, in combination with their low detrital abundance, makes them powerful redox proxies (Algeo and Lyons, 2006; Algeo and Tribovillard, 2009; Scott and Lyons, 2012; Algeo and Rowe, 2012). U-Mo covariation patterns in marine sedimentary successions also have been strongly applied to paleogeographic reconstructions (Algeo and Tribovillard, 2009), with the use of Mo/TOC

ratios to constrain both the degree of watermass restriction and the approximate time of deepwater renewal in restricted anoxic marine basins (Algeo and Rowe, 2012).

Some trace metals are important components of enzymes and can be concentrated in modern phytoplankton (p. e., Cd, Cu, Ni and Zn). When organic matter degrades, these metals are delivered to the sedimentary environments and are retained within organic-rich sedimentary facies (e.g., associated to pyrite formation), favoring their use as a reliable proxy for organic carbon sinking flux (Tribovillard et al., 2006; Sansjofre et al. 2014). Other trace-elements, such as Co and Cr, are also reduced under anoxic conditions, and they can be complexed with humic/fulvic acids. However, these elements tend to be less incorporated into authigenic sulfides and their concentration in sediments is also associated with the abundance of clastic material, which limits their use as reliable redox proxies (Brumsack, 2006; Tribovillard et al., 2006).

6.4 Geological Setting

The Ediacaran-Cambrian Bambuí Group consists of an up to 3000 m-thick successions of carbonate and siliciclastic rocks that covers most of the western São Francisco craton (Fig. 29A). As one of the main basin-fill units of the intracratonic São Francisco basin, it unconformably overlies Meso to Neoproterozoic sedimentary successions and Archean-Paleoproterozoic basement assemblages and is deformed within the foreland fold and thrust belts of the Brasiliano/Pan-African Brasília and Araçuaí orogens (Fig. 29B). The Bambuí Group has been interpreted as recording the late stages of a foreland system (i. e., 1st-order sedimentary sequence) developed in response to the multiple overloads imposed on the São Francisco paleoplate by diachronic Neoproterozoic-early Paleozoic Brasiliano/Pan-African orogens (e. g., Martins-Neto, 2009; Alkmim et al., 2006; Alkmim and Martins-Neto, 2001, 2012; Heilbron et al., 2017; Reis et al., 2016, 2017; Santos et al., 2000; Reis and Suss, 2016; Caxito et al., 2017, 2021c; Kuchenbecker et al., 2020).

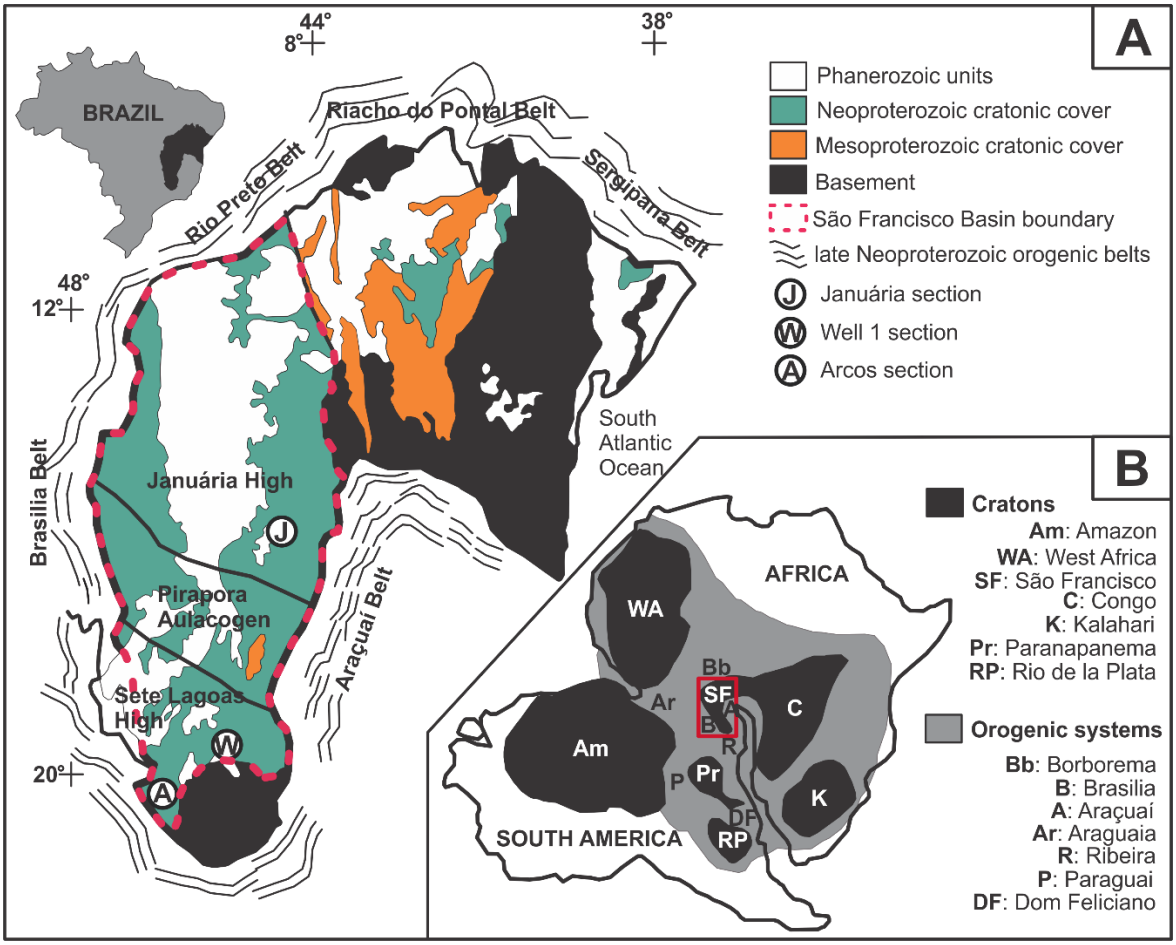

Figure 29. (**A**) Geologic map of the São Francisco craton in east Brazil and locations of the stratigraphic sections in the São Francisco basin (**B**) paleogeographic reconstruction of the late Neoproterozoic West Gondwana (modified from Alkmim et al., 2006).

From the base to the top, the Bambuí Group includes eight formations represented (main lithology) by diamictites of the Carrancas Formation, limestones of the Sete Lagoas Formation, pelites of the Serra de Santa Helena Formation, limestones of the Lagoa do Jacaré Formation, pelites of the Serra da Saudade Formation and sandstones of the Três Marias Formation (i.e., Costa and Branco, 1961; Dardenne, 1978; Uhlein et al.; 2016). Conglomerates of the Samburá and Lagoa Formosa formations occur in the western border of the basin (Castro and Dardenne, 2000; Uhlein et al., 2011; Uhlein et al., 2017), while the conglomerates and sandstones of the Gorutuba Formation and limestones of the Jaíba Formation are exclusive from the eastern border (Chiavegatto 2003, Kuchenbecker et al., 2016b, 2020; Uhlein et al., 2020).

The Bambuí basin record two major depocenters, whose evolution were mostly controlled by the Brasília orogenic system (Martins-Neto, 2009; Alkmim and Martins-Neto, 2012; Reis and Suss, 2016; Reis et al., 2017): i) a forebulge filled with mixed carbonate-siliciclastic strata in the east; and ii) a foredeep filled with fan deltaic fine- to coarse-grained siliciclastics and minor chemical sedimentary rocks to the west. A younger and superimposed foredeep depocenter is recorded in the easternmost São Francisco basin by continental to transitional fine- to coarse-grained clastic successions. This younger depocenter is related to flexural subsidence imposed dominantly by the Araçuaí orogen to the east (Chiavegatto et al., 2003; Kuchenbecker et al., 2016b, 2020; Rossi et al., 2020).

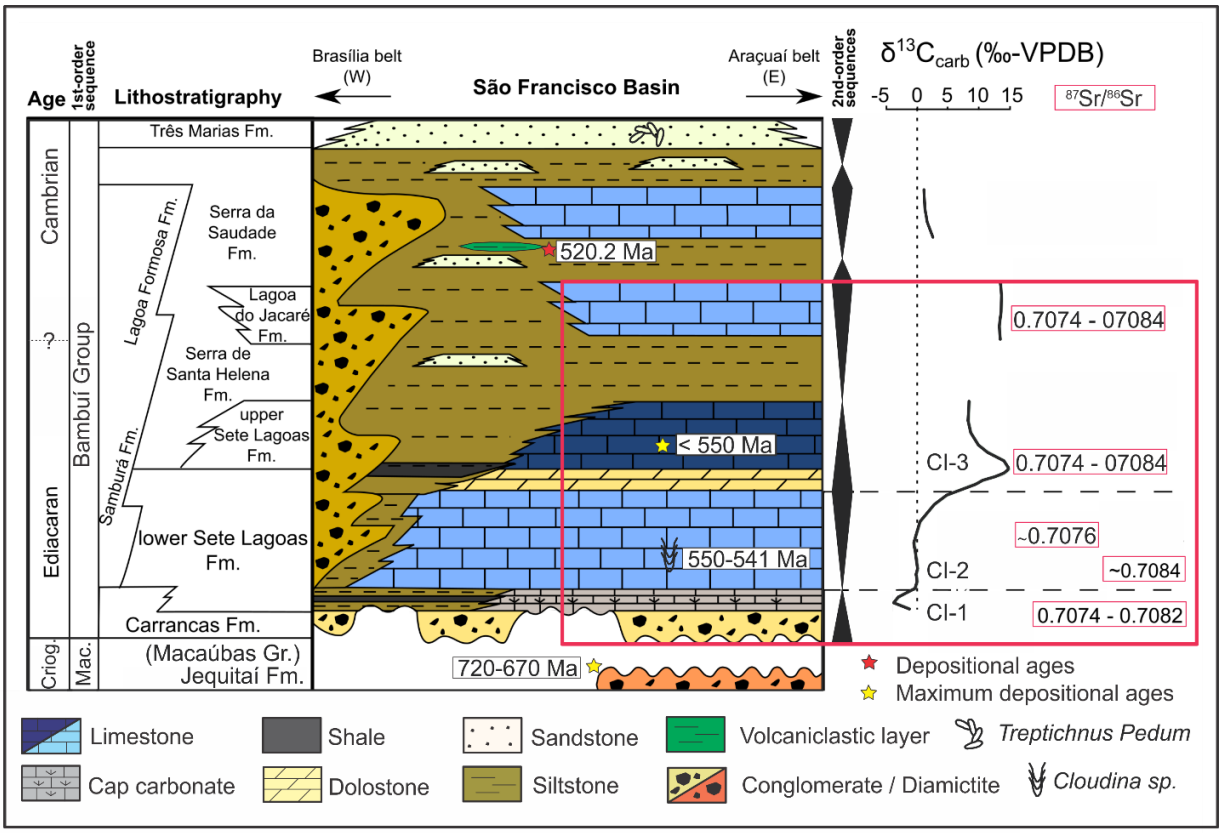

Figure 30. Lithostratigraphic chart of the Bambuí 1st-order sequence and chemostratigraphic evolution (modified from Caetano-Filho et al. 2019). Index fossil of *Cloudina* sp. defines a late Ediacaran age (lower Sete Lagoas Formation; Warren et al., 2014). Maximum depositional age is represented by the yellow star (upper Sete Lagoas Formation – Paula-Santos et al., 2015), depositional age of volcaniclastic layer is represented by the red star (upper Serra da Saudade Formation; Moreira et al., 2020). Index ichnofossil *Treptichnus Pedum* in the Tres Marias Formation define the Ediacaran-Cambrian transition within the Bambuí Group (Sanchez et al., 2021). Chemostratigraphic Intervals (CI) are from Paula-Santos et al. (2017).

Occurrences of the index fossil *Cloudina* sp. (Warren et al., 2014; Perrella et al., 2017) and c. 550 Ma detrital zircons (e.g., Paula-Santos et al. 2015, Kuchenbecker et al., 2020) in the Sete Lagoas Formation constrain a late Ediacaran maximum depositional age for the Bambuí Group. A tuff layer yielding the age of 520.2 ± 5.3 Ma within the Serra da Saudade Formation (Moreira et al., 2020), the recent discovery of the *Treptichnus Pedum* ichnofossil (Sanchez et al., 2021), and detrital zircons yielding a maximum depositional age of 527± 5.3 Ma (Tavares et al., 2020) in the Três Marias Formation indicate that the deposition spanned through the Cambrian period (Fig. 30).

In terms of sequence stratigraphy, the Bambuí Group encompasses four transgressive-regressive 2nd-order sequences (e.g., Reis and Suss, 2016; Reis et al., 2017a, b). This work focuses in the two basal 2nd-order sequences, which might be tracked throughout most of the basin (Fig. 30). The obtained data is integrated with the previous contributions of Caetano-Filho et al. (2019) that present a basin-scale $\delta^{13}C$ and Sr/Ca data coupled to the sequence stratigraphic framework and the chemostratigraphic zoning described by Paula-Santos et al. (2017) and Guacaneme et al. (2021), revealing the marine connection and restriction stages of the Bambuí foreland basin. Stratigraphic-chemostratigraphic intervals of main importance for this work are summarized below:

(i) The lowermost 2nd-order sequence shows a basal transgressive system tract (TST) composed of glacial-related coarse-grained siliciclastics of the Carrancas Formation that grade upward into carbonate rocks and pelites of the Sete Lagoas Formation, defining a retrogradational stacking pattern (Vieira et al., 2007a; Kuchenbecker et al., 2013, 2016a; Reis et al., 2017a; Caetano-Filho et al., 2019). Bounded by a basal erosional surface and an upper maximum flooding surface, this interval displays a low average Sr/Ca ratio of 0.001, negative to positive $\delta^{13}C$ excursions from -5 to c. 0‰, an increase of $^{87}Sr/^{86}Sr$ ratios from 0.7074 to 0.7084, and some layers with aragonite pseudomorph fans, associated to Neoproterozoic cap carbonates (Caetano-Filho et al., 2019; Guacaneme et al., 2021).

(ii) This lowermost TST is overlain by a highstand systems tract (HST) that encompasses the mixed carbonate-siliciclastic successions passing upward into mid to inner carbonate ramp deposits of the Sete Lagoas Formation (Reis and Suss, 2016; Caetano-Filho et al., 2019). Presenting a progradational stacking pattern, these strata are bounded at the top by an erosional unconformity surface. This whole interval displays slightly positive $\delta^{13}C$ values between 0 and +1‰ and shows a low average Sr/Ca ratio around 0.002. However, a basin-wide geochemical change in the Sr content and Sr/Ca ratios within the HST led to Caetano-Filho et al. (2019) to subdivide it into a basal (EHST) early highstand systems tract and an upper (LHST) late highstand systems tract. The latter records a decrease on the $^{87}Sr/^{86}Sr$ ratios to ~0.7076 and an increase on the Sr/Ca ratios around 0.004, reflecting marine restriction and major basin-scale paleogeographic changes (Guacaneme et al., 2021) and probably enhanced seawater alkalinity (Paula-Santos et al., 2020).

(iii) The overlying 2nd-order sequence is represented by a basal TST, consisting of carbonates of the uppermost Sete Lagoas Formation and siltstones of the basal Serra de Santa Helena, which define a retrogradational stacking pattern. Bounded at the top by another maximum flooding surface, these strata are overlain by a HST that presents siliciclastics that grade upward into the carbonate-dominated successions of the Lagoa do Jacaré Formation (Reis and Suss, 2016, Caetano-Filho et al., 2019). This interval displays an extreme positive $\delta^{13}C$ excursion that reaches values as high as +16‰ (i.e., Iyer et al., 1995; Uhlein et al., 2019; Caetano-Filho et al., 2021), an average Sr/Ca ratio of 0.002 and variable $^{87}Sr/^{86}Sr$ ratios between 0.7074 and 0.7084 (Caetano-Filho et al., 2019; Guacaneme et al., 2021). Some paleoenvironmental interpretations based on Sr isotope ratios and REY patterns suggest a significant change in the weathering regime on the marginal orogenic belts of the São Francisco craton with a preferential contribution from carbonates during the restricted stage of the basin (Paula-Santos et al., 2017, 2018; Guacaneme et al., 2021). The highly positive $\delta^{13}C$ excursion, named as the Middle Bambuí Excursion

(MIBE), have been interpreted as short-lived changes in total carbon input to the basin, higher burial rates, higher carbonate authigenesis (Uhlein et al., 2019), and biogeochemical turnover from predominantly sulfate-reducing to methanogenic conditions (Caetano-Filho et al., 2021) after sulfate-distillation through the basal sequence. The lack of oceanic connection would have prevented the re-supply of marine sulfate, trace elements, nutrients, and ultimately dissolved O_2, thus leading to a decrease in the biological activity and prevented the animal evolution of a typical Cambrian ecosystem (Hippertt et al., 2019, Caetano-Filho et al., 2021).

6.5 Methods

6.5.1 Studied sections

Three stratigraphic sections from the basal Bambuí Group were studied: Januária, Arcos and Well 1 sections (Figs. 31–33). The Januária section is a composite stratigraphic section of ~140 m-thick that is based on surface information and includes the sedimentary strata of the Sete Lagoas, Serra de Santa Helena and Lagoa do Jacaré formations, overlying basement assemblages in the Januária High (Fig. 31; Caetano-Filho et al., 2019). It encompasses almost complete successions of the two lower 2nd order sequences of the Bambuí basin.

In the Sete Lagoas High, the Arcos and Well 1 sections were constructed based on the interpretation of two drill cores previously studied by Kuchenbecker et al. (2016a) and Reis and Suss (2016), respectively. The Arcos section displays a c. 175 m-thick succession that includes the Carrancas and Sete Lagoas formations, which unconformably overlie the Archean cratonic basement and represent the lowermost 2nd-order sequence and part of the following one (Fig. 32; Kuchenbecker et al., 2013, 2016a; Caetano-Filho et al., 2019; Bedoya-Rueda, 2019).

Well 1 section represents a ~430 m-thick and continuous succession including the Carrancas, Sete Lagoas and the basal Serra de Santa Helena formations. Comprising the

lowermost 2nd-order sequence and part of the overlying succession, these units were deposited within a forebulge graben developed in the eastern foreland basin depocenter, through the reactivation of preexisting Archean-Proterozoic basement structures in the Sete Lagoas High (Fig. 33; Reis and Suss, 2016; Reis et al., 2017a).

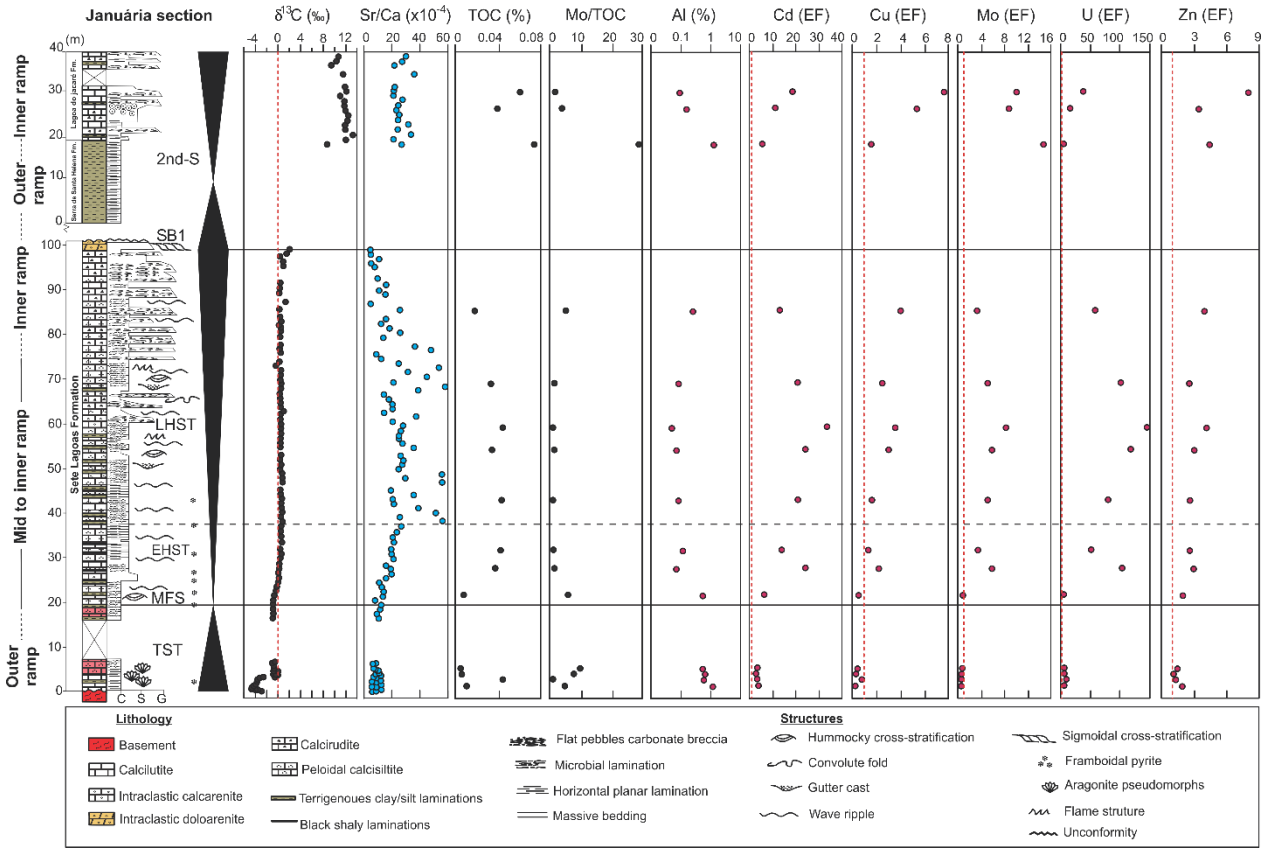

Figure 31. Januária section showing integrated sequence and chemostratigraphy of $\delta^{13}C$ values and Sr/Ca presented by Caetano-Filho et al. (2019), and TOC values from Caetano-Filho et al. (2021), Mo/TOC ratios, Al contents and enrichment factors of trace-metal (modified from Caetano-Filho et al. 2019). Red dotted lines represent EF = 1. TST – Transgressive System Tract; MFS – Maximum Flooding Surface; EHST – Early Highstand System Tract; LHST – Late Highstand System Tract; SB1 – Sequence Boundary; 2nd-S – Upper Second Order Sequence.

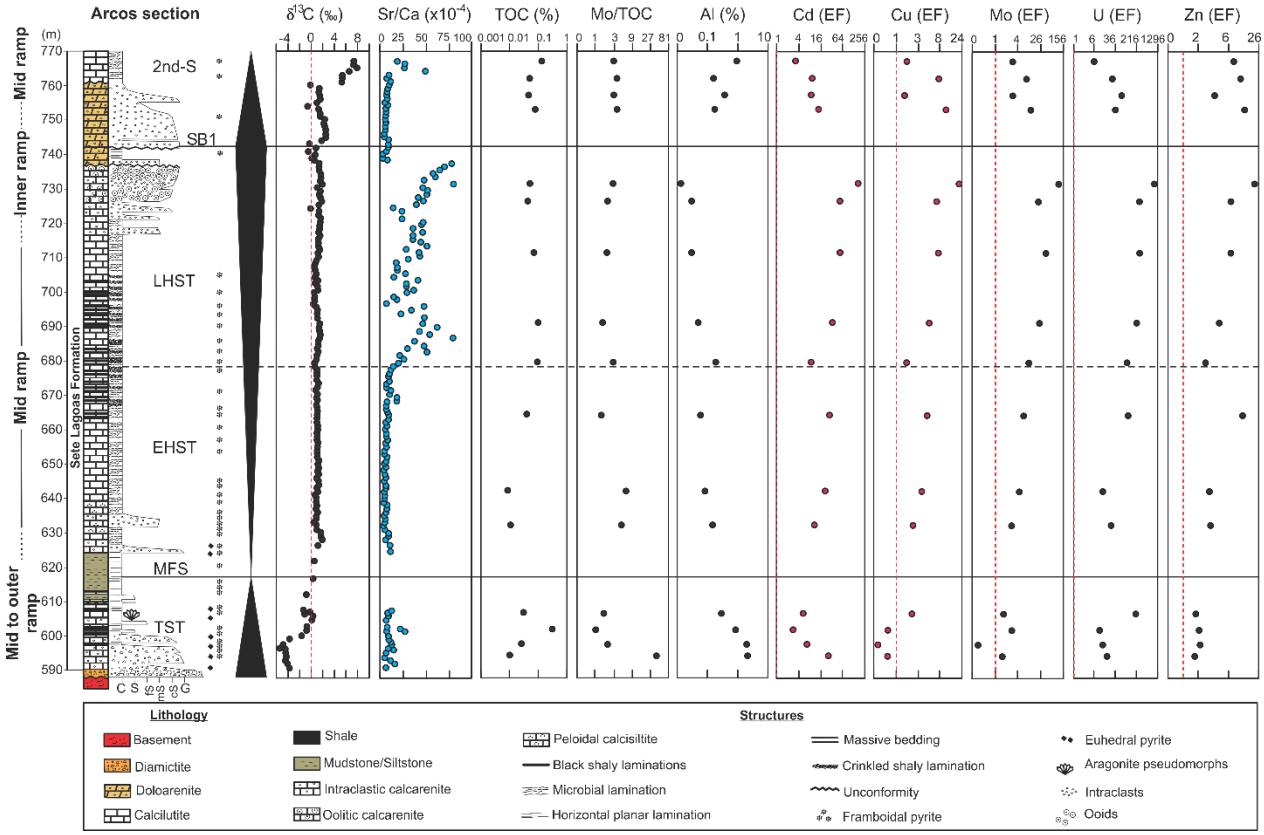

Figure 32. Arcos section showing integrated sequence and chemostratigraphy of $\delta^{13}C$ values and Sr/Ca presented by Caetano-Filho et al. (2019), and TOC values from Caetano-Filho et al. (2021), Mo/TOC ratios, Al contents and enrichment factors of trace-metal (modified from Caetano-Filho et al. 2019). Red dotted lines represent EF = 1. TST – Transgressive System Tract; MFS – Maximum Flooding Surface; EHST – Early Highstand System Tract; LHST – Late Highstand System Tract; SB1 – Sequence Boundary; 2^{nd}-S – Upper Second Order Sequence.

Detailed sedimentary facies description, sequence stratigraphy framework, and regional $\delta^{13}C$ and Sr/Ca chemostratigraphy of the three studied sections were presented by Kuchenbecker et al. (2016a), Reis and Suss (2016), and Caetano-Filho et al. (2019). Organic carbon content (TOC) from these sections were presented by Caetano-Filho et al. (2021). Part of the chemostratigraphic and TOC data presented by Caetano-Filho et al. (2019; 2021) are reproduced in Figs. 31 to 33.

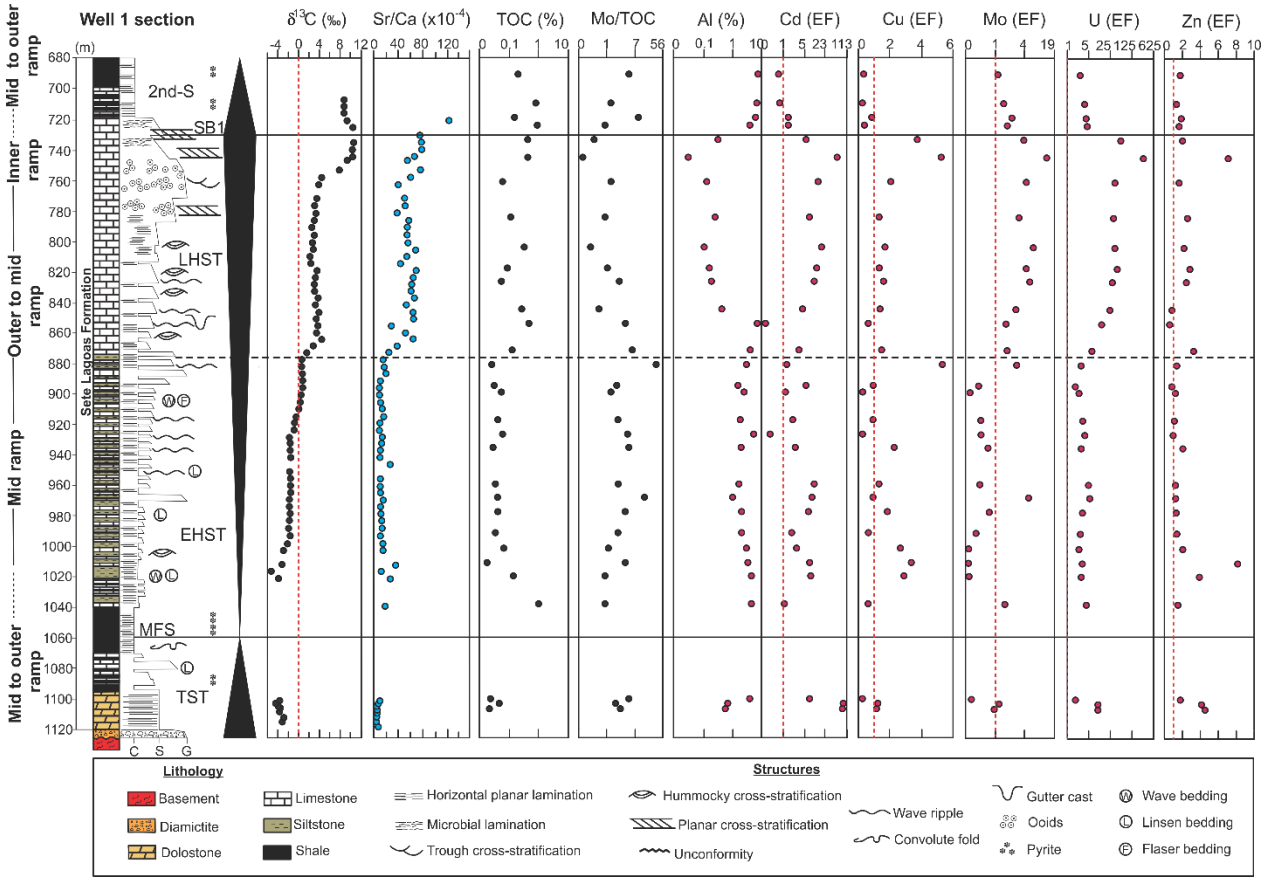

Figure 33. Well 1 section showing integrated sequence and chemostratigraphy of $\delta^{13}C$ values and Sr/Ca presented by Caetano-Filho et al. (2019), and TOC values from Caetano-Filho et al. (2021), Mo/TOC ratios, Al contents and enrichment factors of trace-metal (modified from Caetano-Filho et al. 2019). Red dotted lines represent EF = 1. TST – Transgressive System Tract; MFS – Maximum Flooding Surface; EHST – Early Highstand System Tract; LHST – Late Highstand System Tract; SB1 – Sequence Boundary; 2^{nd}-S – Upper Second Order Sequence.

6.5.2 Trace-metal geochemistry

Sixty-two rock samples from the sections Januária (n=15), Arcos (n=16), and Well 1 (n=31) were analyzed for trace metal contents. They were chosen based on previously rock samples analyzed for TOC data, as well as the stratigraphic and chemostratigraphic framework (Caetano-Filho et al., 2019, 2021). Macroscopic observations and petrographic analyses were carried out to select the more preserved areas on rock samples, which were then crushed and pulverized using an agate mortar. The samples were analyzed

using the ME-MS61 method, which comprises a four-step acid digestion with ICP instrumentation at the ALS Global laboratories, Brazil.

Each prepared sample (0.25 g) was digested with perchloric, nitric and hydrofluoric acids. The residue was leached with dilute hydrochloric acid and diluted to volume. The final solution was analysed by the inductively coupled plasma- mass spectrometry (ICP-MS) for trace elements and inductively coupled plasma- atomic emission spectrometry (ICP-AES) for major elements. Results were corrected for spectral inter-element interferences. Analytical precision based on replicate analyses was better than 2% for all elements. Procedural blanks for Al and Fe were <0.01%, Mn <5 ppm, Zn <2 ppm, Cr and V <1 ppm, Cu and Ni <0.2 ppm, Co and U <0.1 ppm, Mo <0.05 ppm and Cd <0.02 ppm. The reliability of analytical results was monitored by the analysis of the standard reference materials MRGeo08, OREAS 905, GBM908-10 and EMOG-17.

6.5.3 Normalization of trace element data

For paleoenvironmental analysis, an assessment of whether trace-metals are relatively enriched or depleted is mandatory. The degree of enrichment or depletion of a given trace element in a sample might be evaluated by comparing its concentration relative to a reference value that represents the average crustal composition or the PAAS (Post-Archean Australian Shale – Taylor and McLennan, 1985). To compare trace-element proportions in sedimentary rocks with variable proportions of mineral phases, trace-metal concentrations are normalized against Al content (e.g., Tribovillard et al., 2006, 2012). To make the results of the normalization procedure easier to interpret, it is common to use Enrichment Factor (EF) of a given element (X) (Eq. a). The advantage of using EF is that any value larger than 1 indicates the trace metals that are enriched relative to the PAAS. Conversely, if EF < 1, it means that the given element X is depleted (Tribovillard et al., 2006).

(Eq. a) $EF = (X/Al)_{sample}/(X/Al)_{PAAS}$

Also, normalization of Mo concentrations to TOC values allows the comparison of levels of sedimentary enrichment among restricted marine systems containing variable amounts of organic matter, acting as a substrate for Mo uptake by the sediment (Algeo and Lyons, 2006; Algeo and Rowe, 2012). A method for estimating water mass restriction from both trace metals and TOC concentrations was proposed by Algeo and Lyons, (2006), based on the observation that the amount of Mo incorporated in sediments ($[Mo]_{sed}$) in anoxic marine systems depends on both source-ion availability of aqueous Mo concentration ($[Mo]_{aq}$) and the host-phase availability of sedimentary organic matter ($[TOC]_{sed}$). This can be represented by the equations b:

(Eq. b) $[Mo]_{sed} = [TOC]_{sed} * [Mo]_{aq}$ or $[Mo]_{sed}/[TOC]_{sed} = [Mo]_{aq}$

These equations indicate that the ratio of Mo to TOC in the sediment should be proportional to the concentration of aqueous Mo in the deep watermass. Where $[Mo]_{aq}$ is high due to strong deepwater renewal, $[Mo/TOC]_{sed}$ ratios will be high. Conversely, where $[Mo]_{aq}$ concentrations are low due to limited deepwater renewal, $[Mo/TOC]_{sed}$ ratios will be low.

6.6 Results

6.6.1 Major and trace elements

Trace-metal (ppm), major elements (%), and TOC (%) contents of carbonate rocks from the studied sections are presented in Table 1 – Supplementary Material. Al contents vary from 0.01 to 9.01%, showing a progressive decrease at the basal regressive sequence of all studied sections (Figs. 31, 32 and 33). Fe and Mn concentrations vary from 0.01 to 6.25%, and from 5 to 31000 ppm, respectively; and also show a progressive decrease at the regressive stage (Table 2 – Supplementary Material). Trace-metal PAAS-normalized data and Mo/TOC ratios are presented in Table 3 – Supplementary Material. Trace metals less affected by detrital influence, such as Cd, Cu, Mo, U and Zn (selected in section 6.1) are plotted aside the Januária, Arcos and Well 1 sections (Figs. 31, 32 and 33, respectively).

[Cd] ranges from 0.02 to 0.84 ppm, with some samples below the detection limit of 0.02ppm; [Co] varies between 0.4 and 32.6 ppm; Cr contents range from 1.0 to 144 ppm with some samples presenting [Cr] <1.0; Cu contents vary between 1 and 138 ppm; Mo concentrations range from 0.07 and 2.22 ppm with some samples of Januária section displaying [Mo] <0.05 ppm; [Ni] varies between 0.2 and 67.4 ppm; [U] ranges from 0.1 to 13.1 ppm, V contents vary between 1.0 and 105.0 ppm, and some samples present [V] <1.0 ppm; Zn contents vary from 2.0 to 249 ppm, with some samples displaying [Zn] <2.0 ppm (Table 2 – Supplementary Material).

6.6.2 Mo/TOC ratios and Enrichment Factors

6.6.2.1 Januária section

The TST samples from the Januária section present TOC contents varying between 0.01 to 0.04%, and yield Mo/TOC ratios that fluctuate between 1.1 and 9.8. Trace-metal normalized data show that Cd and U are moderately enriched relative to PAAS, ranging from 2.7 to 3.7 and from 4.3 to 9.7, respectively. Co and Zn present enrichment factors around 1.0; whereas Cr, Cu, Mo, Ni and V are depleted, showing EFs < 1.0 (Fig. 31; Table 3 – Supplementary Material).

The EHST carbonates show an increase of TOC content from 0.01 to 0.04% with a concomitant decrease of Mo/TOC ratios from 6.0 to 1.1. Cd, Co, Cu, Mo, U, and Zn are enriched relative to PAAS and present similar trends. Cd-EF ranges between 6.5 to 24.0, Co-EF slightly varies from 1.2 to 2.4, Cu-EF ranges between 0.5 and 2.2, Mo-EF varies between 0.8 to 6.0, U-EF fluctuates from 3.5 to 105. 5, and Zn-EF slightly varies between 2.0 to 3.0. Cr-EF slightly increases from 0.6 to 1.4; whereas V and Ni are depleted relative to PAAS with EFs < 0.9 (Fig. 31; Table 3 – Supplementary Material).

The LHST samples display a decrease of TOC values from 0.05 to 0.02% and a progressive increase of Mo/TOC from 0.1 to 5.4. Trace-metal normalized data of this interval reveals an overall increase of enrichment factors relative to PAAS. Cd-EFs ranges between 12.9 and 33.6, Co-EFs slightly vary from 2.1 and 3.4, Cr-EF ranges between 0.7

and 2.1, Cu-EFs varies between 1.8 to 4.0, Mo-EFs fluctuates 3.2 to 8.4, U-EF strongly varies between 60.3 and 147.7, and Zn slightly varies between 2.6 and 4.2. V is depleted relative to PAAS, with one sample reaching up to 1.8 at the top of this interval (Fig. 31; Table 3).

Carbonates from the overlying 2nd-sequence display relatively high TOC values ranging from 0.04 to 0.07%, and Mo/TOC ratios decreasing upward from 29.9 to 4.0. Trace-metal patterns display slight enrichments relative to PAAS for Cd, Co, Cu, Mo, U and Zn, and show increasing trends at this stage. Cd-EFs rises from 5.3 to 18.6, Co-EFs increases from 1.2 to 4.2, Cu-EFs rises from 1.6 to 7.6, Mo-EFs increases from 8.9 to 14.9, U-EFs increases from 7.3 to 41.0, and Zn-EFs rises from 3.5 to 8.1. Cr, Ni, and V presents EFs closer to PAAS composition varying between 0.7 and 1.6 (Fig. 31; Table 3 – Supplementary Material).

6.6.2.2 Arcos section

The TST carbonates from the Arcos section show TOC contents rising from 0.01 to 0.30%, and Mo/TOC ratios progressively decreasing from 32.3 to 0.9. Cd, Co, Cr, Ni, and U are enriched relative to PAAS and present fluctuating trends. Cd-EF varies between 2.8 and 26.4, Co-EF slightly ranges from 1.0 to 3.2, Cr-EFs fluctuates between 0.6 and 3.5, Ni-EF varies from 0.9 to 3.9, and U-EF varies from 9.2 to 190.1. Cu-EF and Mo-EF vary from 0.2 to 2.7, and Zn presents EFs factors around 1.4 (Fig. 32; Table 3 – Supplementary Material).

The samples from the EHST show an increase of TOC contents from 0.01 to 0.10%, whereas Mo/TOC ratios exhibit an upward decrease from 4.5 to 1.4. Trace-metal patterns indicate that Cd, Co, Cu, Mo, U, and Zn are enriched relative to PAAS: from the base to top, Cd-EF, Co-EF, Cu-EF, Mo-EF, U-EF and Zn-EF vary between 8.8 and 28.0, 1.6 and 2.8, 1.6 and 4.3, 2.8 and 11.1, 11.5 and 107.7, and 2.2 and 12.2, respectively. Enrichment factors for Cr and Ni are around 1.0, while for V-EF is <1.0 (Fig. 32; Table 3 – Supplementary Material).

The LHST carbonates display TOC values varying between 0.04 and 0.10% and Mo/TOC increasing from 1.45 to 2.67. Normalized data show an overall enrichment of trace metal relative to PAAS and similar increasing upward trends in the section. Cd-EF increase from 33.6 to 168.0, Co-EF rises from 4.2 to 21.0, Cr-EF increases from 1.7 to 8.4, Cu-EFs rises from 4.7 to 20.1, Mo-EF increases from 25.2 to 109.2, Ni-EF slightly increases from 1.1 to 2.8, U-EF rises exponentially from 221.5 to 1200, V-EF rises from 1.2 to 6.0 and Zn-EF increases from 4.2 to 21.0 (Fig. 32; Table 3 – Supplementary Material).

The samples from the overlying 2nd-order sequence show, in the basal transgressive systems tract, high TOC values ranging from 0.40 to 0.13%, and Mo/TOC ratios ranging between 2.8 and 3.6. Trace-metal patterns display that Cd, Co, Cu, and V are enriched relative to PAAS and present decreasing upward trends. Cd-EF falls from 14.0 to 3.4, Co-EF decreases from 2.8 to 0.9, Cu-EF falls from 11.1 to 1.4, Mo-EF varies between 2.9 and 12.1 and U-EF between 5.6 and 62.3. Although similar, the Zn values show slightly upward decreasing patterns ranging between 3.4 and 13.4. Cr-EF is around 1.0, Ni-EF varies between 0.6 to 2.3, and V-EF ranges from 0.8 to 2.1 (Fig. 32; Table 3 – Supplementary Material).

6.6.2.3 Well 1 section

The samples from the TST of the Well 1 section show low TOC contents ranging from 0.02 to 0.04%, and Mo/TOC ratios varying between 1.8 and 4.5. Trace-metal patterns show that Cd, U, and Zn are enriched relative to PAAS and present overall upward decreasing trends: Cd-EF vary from 108.5 to 6.4, U-EF decreases from 10.4 to 1.9 and Zn-EFs changes from 4.6 to 1.7. Co, Cu, Ni and Mo displays enrichment factors around 1.0, recording some depletions for Cu and Mo toward the top of the TST. Cr and V are depleted relative to PAAS with EFs <1.0, showing a weak increasing trend for V (Fig. 33; Table 3 – Supplementary Material).

The EHST records upward decreasing TOC contents that vary from 0.97 to 0.02% and remain around 0.04%, whereas Mo/TOC ratios increase upward from 0.7 to 35.0. Cd-

EF ranges between 0.3 and 9.6, Cu-EF varies from 0.1 to 5.3, Mo-EF fluctuates between 0.2 and 5.0, and U-EF varies from 1.9 to 5.7. Co, Ni and Zn share similar increasing-decreasing trends, Co-EF varies between 0.8 and 5.2, Ni-EF ranges from 0.4 to 2.9 and Zn-EF varies between 1.1 and 8.1. Cr and V are depleted relative to PAAS with EFs <1.0, and display similar slightly decreasing trends (Fig. 33; Table 3 – Supplementary Material).

The LHST samples display TOC values ranging from 0.06 to 0.45% and Mo/TOC decreasing from 5.8 to 0.1. Trace-metal patterns show that Cd, Cu, Mo, U, and Zn are enriched relative to PAAS and present progressively increasing trends, Cd-EF rises from 2.9 to 56.0, Cu-EF increases from 0.5 to 5.2, Mo rises from 1.4 to 14.0 at, U-EF increases from 6.6 to 307.7 and Zn-EF rises from 0.5 to 7.0. On the other hand, Co and Ni are slightly enriched relative to PAAS, with enrichment factors varying from 1.0 to 7.0 and from 0.6 to 1.9, respectively. Cr and V are depleted, except for one sample at the top of this interval that reaches EFs up to 2.8 and 2.0, respectively (Fig. 33; Table 3 – Supplementary Material).

The basal portion of the overlying 2nd-order sequence shows high TOC contents varying between 0.9 and 0.2, and Mo/TOC ratios ranging between 0.8 and 9.1. Normalized data at this interval reveals a thorough depletion of trace metals relative to PAAS. Mo and U are weakly enriched and presents similar decreasing trends from 2.0 to 0.9 and from 4.5 to 2.7, respectively. Zn-EFs are slightly enriched around 1.6. Cd and Co present enrichment factor around 1.0; and Cr, Cu, Ni and V are depleted relative to PAAS with EFs < 1.0 (Fig. 33; Table 3 – Supplementary Material).

6.7 Discussion

6.7.1 Detrital influence on trace-metal composition

Trace-metal content in marine sedimentary rocks is usually of both detrital and authigenic origin. The detrital influence on the trace-metal compositions in carbonate samples can be tracked by petrography and also by mass fractions of Al, since it is a

common element of detrital origin and is immobile during diagenesis (Brumsack, 2006, 2006; Tribovillard et al., 2006). When rock samples with trace-metal mass fractions do not deviate greatly from the PAAS concentration (i.e., Taylor and McLennan, 1985), and present positive correlations with the detrital monitors, it can be inferred that their composition is mainly of detrital origin and, thus, they cannot be used as redox proxies for paleoenvironmental reconstructions.

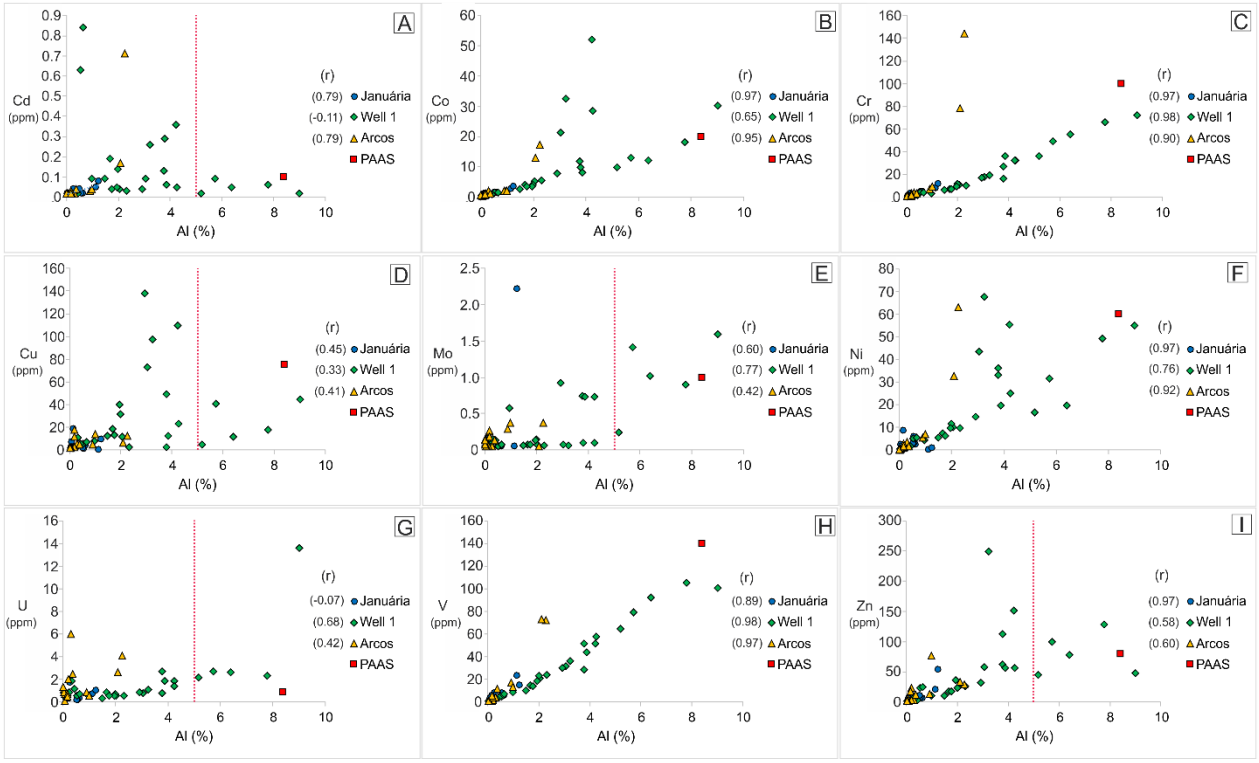

Figure 34. Cross-plot diagrams of trace metals contents *vs*. Al concentrations of samples from the Arcos, Well 1, and Januária sections. PAAS values from Taylor and McLennan (1985) are plotted for comparison. Red dotted line indicates a cut-off value of [Al] < 5% for less or not affected rock samples by detrital contamination.

In fact, the detrital signals exposed above are identified in the sedimentary rocks from the basal Bambuí Group in the Januária, Arcos and Well sections. The sections are composed mainly by limestones (80-90%) that present a low proportion of detrital siliciclastic sediments observed in petrography (quartz and feldspar grains, and some clay laminae), and by siltstones and shales (10-20%) that are mostly composed of fine-grained detrital components and organic matter. These rocks exhibit variable concentrations of Al

up to 10%, and display positive correlations with trace-metal contents in cross-plot diagrams (Fig. 34A–I).

Strong positive correlations ($r \geq 0.76$; $p(\alpha) < 0.01$) are observed between the concentrations of Al against Cr (Fig. 34C), Ni and V in all sections (Figs. 34F and 34H), Cd and Co in Januária and Arcos sections (Figs. 34A and 34B), and Zn and Mo in Januária and Well 1 sections (Figs. 34 and 34E), indicating a high detrital effect on these elements. Positive correlations ($r = 0.58–0.68$; $p(\alpha) < 0.01$) are yielded for Al versus Co, U and Zn contents in Well 1 (Figs. 34B, 34G and 34I), and for Mo and Zn in Januária and Arcos sections (Figs. 34E and 34I), respectively; suggesting some degree of detrital influence. Low positive correlations ($r = 0.33–0.45$; $p(\alpha) < 0.01$) of Al against Cu in all sections, and Mo in Arcos section indicate a low detrital composition effect (Figs. 34D and 34E). Nevertheless, no correlations are observed between the concentrations of Al versus Cd in Well 1 section ($r = –0.11$; $p(\alpha) > 0.01$), and U in Januária section ($r = –0.07$; $p(\alpha) > 0.01$), suggesting negligible detrital effect on these elements (Figs. 34A and 34G).

The detrital monitoring by [Al] exhibit that the concentrations of Co, Cr, Ni and V points to PAAS composition (Figs. 34B, 34C, 34F and 34H), supporting that these trace metals are mainly of detrital provenance in the sediments of the Bambuí Group and cannot be used for paleoenvironmental analysis. This is often the case for Cr and Co, but rarely for V and Ni (i. e, Jones and Manning, 1994; Tribovillard et al. 2006).

Moreover, Cd and Zn are suspected to be of mixed origin (detrital and authigenic) in the sediments of the Bambuí Group, mainly at Januária and Arcos sections (Figs. 34A and 34I). In these elements, the authigenic fraction can be estimated as the part in excess of the PAAS (i. e., Tribovillard et al. 2006). Despite that Mo presents positive correlations with [Al] in Well 1 and Januária sections, this element, together with Cd, Cu, U and Zn (Figs. 34A, 34D, 34E, 34G and 34I), are the less affected trace metals by detrital sources of sediments of the Bambuí Group, as evidenced by samples with Al mass fractions below 5% and compositions strongly deviated from the PAAS, suggesting authentic enrichments. Therefore, we applied [Al] < 5% as a cut-off value to select samples that record enrichment or depletion in these trace-metals.

The assessment by Al monitoring shows that the trace metals present a variable degree of detrital influence, which varies laterally through the Bambuí sequences, likely

as a result of detrital influx from different crustal source areas (i.e., Januária and Sete Lagoas Highs, Brasília and Araçuaí orogens). Integrating these proxies, it can be concluded that Co, Cr, Ni, and V mass fractions are strongly affected by detrital influence, and these elements should not be used herein as reliable redox proxies. Nevertheless, Cd, Cu, Mo, U, and Zn mass fractions seem to be less or not affected by detrital influence. Thus, considering the cut-off values of Aluminium content defined above, these trace metals can be used as reliable redox proxies for the paleoenvironmental analysis of the studied Bambuí strata.

6.7.2 Controls on trace-metal accumulation in the epeiric Bambuí sea

As showed in this study, sedimentary rocks of the basal Bambuí Group consist of 80-90% of carbonates and 10-20% of shales. This means that there is a wide range of lithologic variation in the studied succession, which often leads to elemental compositions that reflect strong positive covariance with major elements, such as Al, Fe and Mn. Generally, in studies of sedimentary trace-metal composition, carbonate-rich samples are excluded and focused on shale-rich samples (i. e., Algeo and Maynard, 2004). However, there are several reasons to make this approach viable in carbonate rocks. First, this study shows that authigenic fractions recorded for Cd, Cu, Mo, U and Zn are associated with low Al content and presenting mass fractions above the PAAS concentrations. Second, other proxies applied to these rocks, such as Sr/Ca and $^{87}Sr/^{86}Sr$ ratios, REY and $\delta^{15}N$ data support chemical disturbances at the basal regressive stage, instead of lithologic variation (Caetano-Filho et al. 2019; Paula-Santos et al. 2020; Guacaneme et al. 2021; Fraga-Ferreira et al. 2021). Third, recent research in the Bambuí Group support major mayor paleoenvironmental changes in epeiric seawater on the core of Gondwana at the late Ediacaran (Uhlein et al., 2019; Caxito et al. 2021c). Fourth, carbonates rocks have been successfully used to constraints redox environments in the Ediacaran-Cambrian transition (i. e., Liyuan et al., 2021). Based on this, we consider that trace-metal enrichment patters recorded in the basal Bambuí Group are indicative of environmental conditions of epicontinental seawater, and other mechanisms can be suggested for explain these particular trace-metal stratigraphic trends.

Controls on the trace-metal removal from seawater to the sediment has been categorized in three main classes, based on differences in authigenic Mo–U covariation patterns of modern and ancient low-oxygen marine systems: i) benthic redox conditions, ii) operation of particulate shuttles and iii) changes in seawater chemistry (Algeo and Tribovillard, 2009). Deep-water mass restriction can be estimated from Mo/TOC ratios (Algeo and Lyons, 2006; Lyons et al., 2009; Algeo and Rowe, 2012), and also, Cd/Mo ratios > 0.1 allow the distinction between hydrographically restricted basins and upwelling-associated settings (Sweere et al., 2016). Using the contrasting stratigraphic behavior in the studied Bambuí strata, it is possible to recognize the main factors controlling the trace-metal enrichment patterns for each 2nd-order systems tract. Coevally, it is proposed that the Bambuí paleomarine system has evolved as an intracratonic enclosed basin in the interior of West Gondwana limited by shallow sills and orogens that hinders deep-water circulation and the exchange with oxygenated waters from the open ocean (i. e., modern anoxic silled basins, Algeo and Rowe, 2012).

Trace-metal patterns from the lowermost TST are indicative of suboxic conditions of seawater controlled by benthic redox variations. Cross-plot of enrichment factors of Mo vs U (Fig. 35A) shows trends of an open marine setting during this interval in which rates of aqueous U uptake exceeds those of aqueous Mo, resulting in sediment Mo/U ratios that range between 0.3 and 0.1x SW as EFs increases (Algeo and Tribovillard, 2009). This interval presents low Mo contents (mean = 0.11 ppm) and low TOC contents varying between 0.01 to 0.30% (mean = 0.05%). Mo and TOC contents exhibit a weak positive correlation ($r = 0.50$; $p(\alpha) > 0.01$) and yield relatively high Mo/TOC ratios varying between 1.1 and 32.3 (mean = 6.84). These patterns suggest that aqueous Mo concentrations were relatively high in seawater (i. e., Algeo and Rowe, 2012) within a weakly restricted basin or open marine system that experienced watermass exchange with coeval oceans (Fig. 35B), allowing the deepwater renewal of aqueous Mo (Algeo and Lyons, 2006; Tribovillard et al., 2006; Algeo and Rowe, 2012). High Cd/Mo ratios showing no correlation with TOC also indicate a connection with open marine systems (Sweere et al. 2016; Fig. 35C).

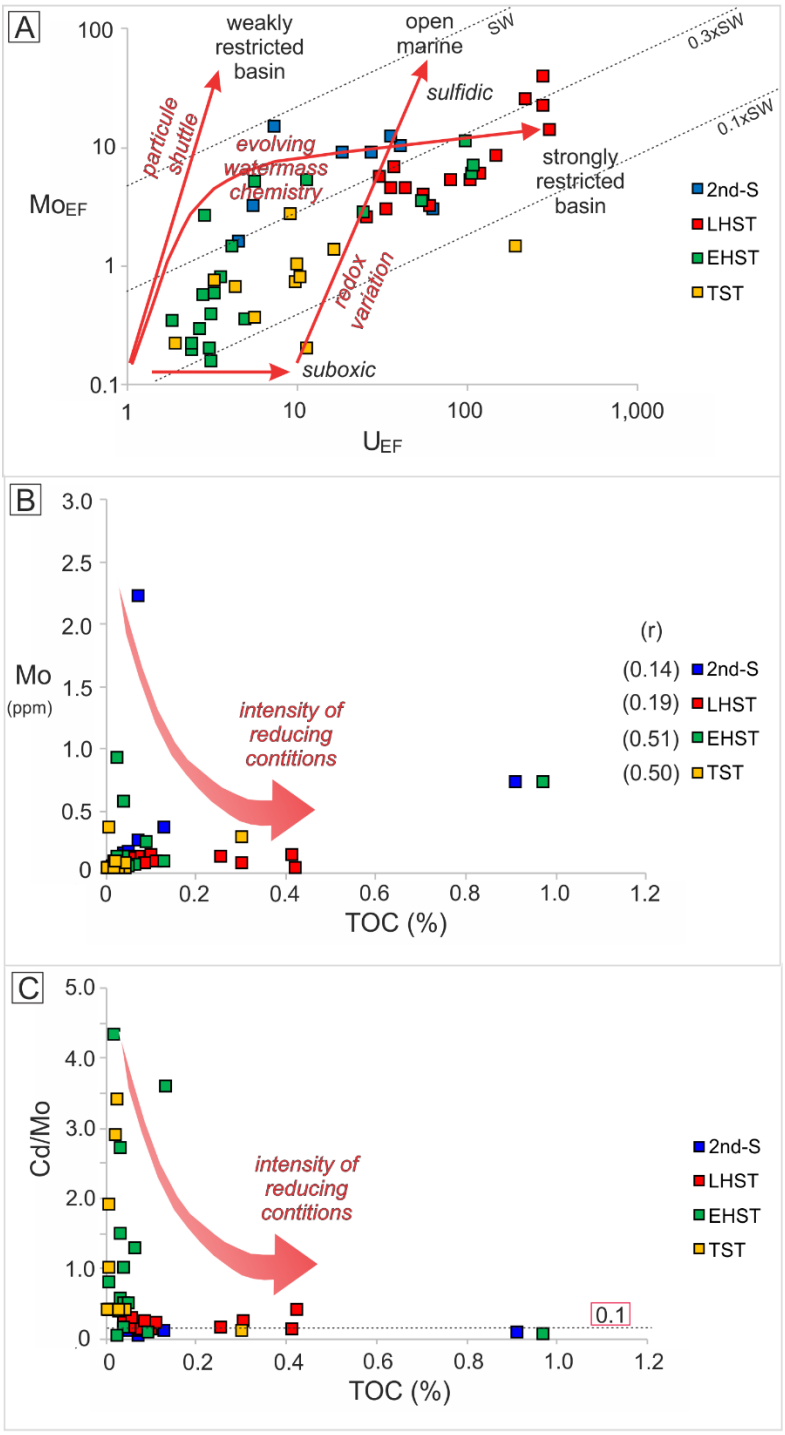

Figure 35. Trace-metals patterns of the basal Bambuí 2nd-order sequence. **(A)** Mo-EF versus U-EF. The diagonal lines represent the aqueous Mo/U ratio of the present-day seawater (SW) that ranges between ~7.5 and 7.9 (1×SW), and fractions thereof (0.3×SW and 0.1×SW as proposed by Algeo and Tribovillard (2009). **(B)** Mo versus TOC contents. **(C)** Cd/Mo ratios versus TOC content. TST – Transgressive System Tract; MFS – Maximum Flooding Surface; EHST – Early Highstand System Tract; LHST – Late Highstand System Tract; SB1 – Sequence Boundary; 2nd-S – Upper Second Order Sequence.

The basal transgressive sequence presents relatively high Mn and Fe concentrations around 0.06 and 0.93%, respectively (Table 2), suggesting a low downward diffusion of Mn^{2+} and Fe^{2+} and leading to their precipitation with $CaCO_3$ (i. e., Brumsack, 2006). It thus reflects suboxic and possibly sulfidic conditions controlled by benthic redox variations of seawater. At this stage, renovation of oxygenated water column could have been a result of enhanced nutrient supply to the Bambuí seawater through the upwelling of deep ocean waters and renewal of Mo (Fig. 36A). This inference is consistent with strong but temporally variable watermass exchange across the TST and the subsequent HST of the lowermost 2nd-order sequence, in which low Sr/Ca ratios (Caetano-Filho et al., 2019), and relatively radiogenic $^{87}Sr/^{86}Sr$ ratios of ~0.7084, match the Sr-isotope composition of the ocean reservoir during the late Ediacaran and early Cambrian (Guacaneme et al., 2021). The high-frequency variations of the relative sea level can be of great amplitude and higher than the long-term variations.

Mo-EF vs U-EF plot of the basal regressive sequence (EHST) show patterns of a weakly restricted basin with a strong enrichment of Mo relative to U, probably due to the operation of a particulate shuttle linked to Mn–Fe redox cycling within the water column, enhancing the transfer of Mo to the seafloor, as in the modern Cariaco Basin (Algeo and Tribovillard, 2009). These conditions result in high rates of Mo uptake that substantially exceed those of U, resulting in a large variability of sediment Mo/U ratios that range from ~0.1×SW to ~1×SW as EFs increase (Fig. 36A). This stratigraphic interval displays high Mo contents that vary between 0.05 and 0.92 ppm (mean = 0.18 ppm) and low TOC contents (mean = 0.03%), except for one sample at the base of the EHST in Well 1 section that presents the highest TOC content of 0.97% (Fig. 33). These data show a positive correlation between Mo and TOC contents ($r = 0.51$; $p(\alpha) < 0.01$) (Fig. 36B), yielding relatively high Mo/TOC ratios between 0.75 and 35.05 (mean = 4.75), suggesting high aqueous Mo concentrations in the watermass due to deepwater renewal (e.g.., Algeo and Lyons, 2006; Tribovillard et al., 2006; Algeo and Rowe, 2012). High Cd/Mo ratios exhibiting no correlation with TOC support slightly reducing conditions for this interval (Sweere et al., 2016; Fig. 36C).

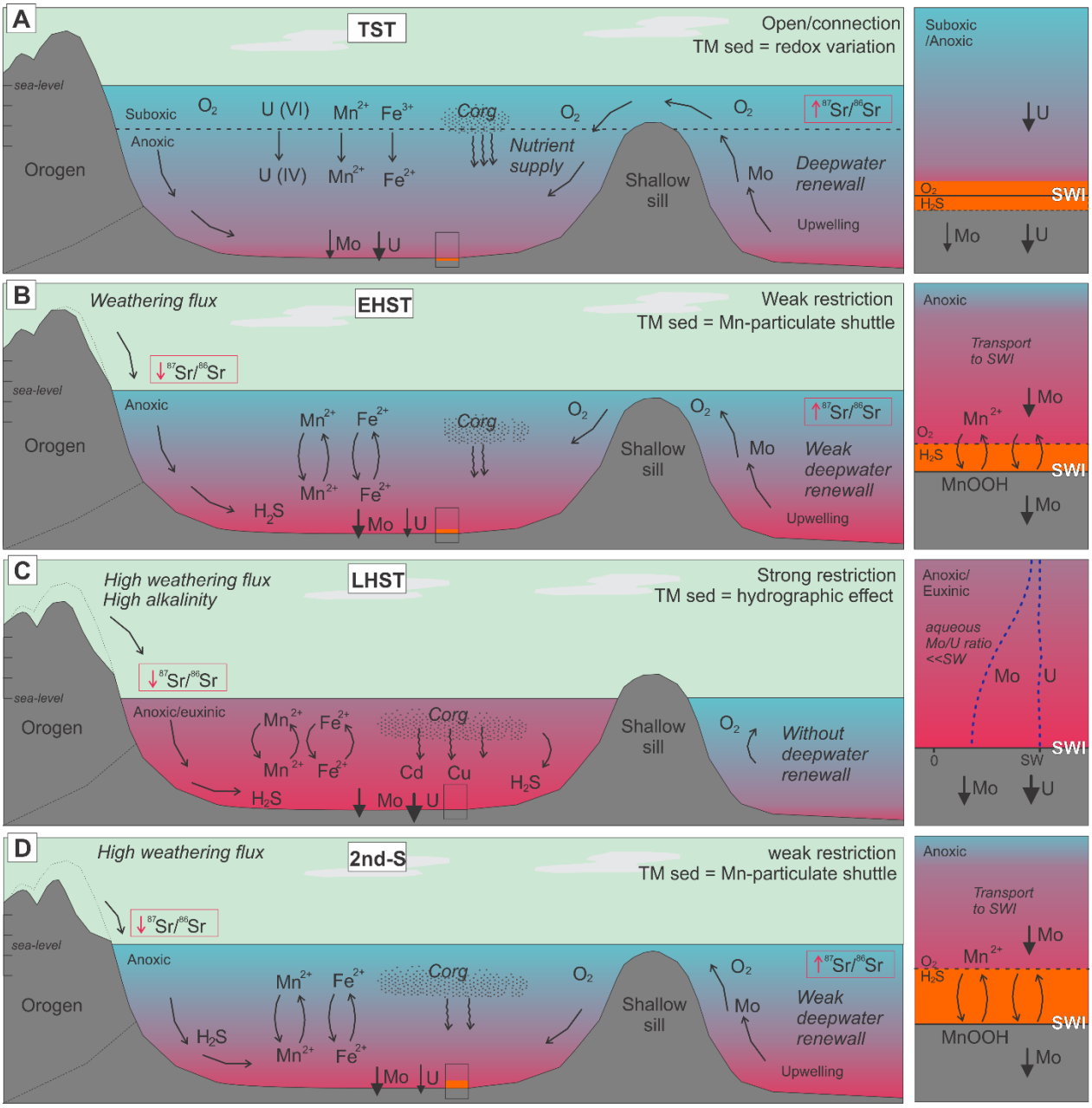

Figure 36. Models of influences on trace-metal accumulation in different stages of the basal Bambuí 2nd-order sequence in a context of a silled basin. (**A**) suboxic-anoxic basin dominated by benthic redox controls, connected with open ocean and deepwater renewal by upwelling and continuous resupply of trace metals; (**B**) anoxic basin with weak restricted circulation dominated by Mn-particulate shuttles, (**C**) anoxic-euxinic basin with limited resupply of trace metals dominated by hydrographic control and (**D**) anoxic basin with weak restricted circulation dominated by Mn-particulate shuttles.

The effectiveness of a particulate shuttle in promoting Mo accumulation in the EHST may be enhanced by variations in water-column redox conditions at intermediate

timescales and implies that seawater in this stage starts to experience frequent redox fluctuations between suboxic, anoxic, and moderately sulfidic conditions (i. e., Algeo and Tribovillard, 2009). A weakly restricted basin scenario during the EHST is coherent with the start of a progressive decrease of the $^{87}Sr/^{86}Sr$ ratios due to poor watermass exchange (Fig. 36B), which caused the Bambuí watermass to change progressively and differ from the Sr-isotope compositions of the ocean reservoir (Guacaneme et al., 2021). Also, stratigraphic changes in trace-metal patterns and Mo/TOC ratios are likely to be controlled by abrupt changes in the redox state of depositional environment or major changes in lithology (i.e., Algeo and Rowe, 2012).

In the case of the LHST, trace-metal patterns of Mo-EF and U-EF indicate deposition over anoxic-euxinic conditions in the water column within a strongly restricted basin, resulting in low aqueous Mo/U ratios, around 0.3 times lower than seawater as EFs increases (Fig. 35A). The relationship between this trend and the seawater molar ratio line is unambiguously different from that of the underlying TST and partially from the one of the overlying EHST, showing authigenic Mo–U covariation patterns similar to the modern Black Sea (e.g., Algeo and Tribovillard, 2009).

These strata display very low Mo concentrations (mean = 0.09 ppm) and relatively high TOC contents varying between 0.02 to 0.42% (mean = 0.13%) that are poorly correlated ($r = 0.19$; $p(\alpha) > 0.01$). They yield low Mo/TOC ratios varying between 0.12 and 5.42 (mean = 1.47). These patterns show a significant drawdown of aqueous Mo concentrations in the deep watermass owing to a strong restriction (Fig. 35B), in which substantially less dissolved Mo is available for uptake by sediments compared with the underlying TST and EHST. Low Cd/Mo ratios present negligent correlation with TOC (Fig. 35C), which indicates an increase in the intensity of reducing conditions in this interval (Sweere et al. 2016).

Anoxic-euxinic conditions at this interval suggests that the Bambuí seawater was highly reducing, presenting the lowest Mn and Fe contents, with average value of 0.005 and 0.08%, respectively (Table 2). Such environmental conditions lead to the upward diffusion of these elements since they escape to the water column due to the higher solubilization, resulting in Mn-Fe-depleted sediments (i. e., Algeo and Maynard, 2004;

Tribovillard et al., 2006). These conditions result in strong U and Mo enrichments and weak correlations with TOC, because these elements reside mainly in authigenic mineral phases rather than organic phases, contrarily to Ni and Cu that reside in organic phases and may be incorporated into pyrite.

An authigenic trace-metal enrichment through the LHST is associated with anoxic-euxinic conditions developed in a confined water mass, leading to insufficient circulation, which prevented O_2 renewal (Fig. 36C). Also, intense organic matter degradation would have consumed O_2 faster than it is replenished (i.e., Tribovillard et al., 2006; Algeo et al., 2012). These successions display non-radiogenic $^{87}Sr/^{86}Sr$ ratios of ~0.7076 (Guacaneme et al., 2021), associated with congruent weathering and high alkalinity (Paula-Santos et al., 2020). These isotopic signals precede a large positive $\delta^{13}C$ excursion typical of the upper 2nd-order sequence in the middle Bambuí Group (i.e., Paula-Santos et al., 2017, Uhlein et al., 2019; Hippertt et al., 2019, Caetano-Filho et al. 2019, 2020, Cui et al. 2020b).

In the anoxic-euxinic restrict stage recorded by the LHST, organic-rich sediment deposition probably occurred in depths below the chemocline, where Cd and Cu are delivered to the sediments in association with organic matter decay (organometallic complexes), and trapped under intense sulfate-reducing conditions (Fig. 36C). Limited circulation patterns could have impacted the primary productivity rates due to controls on the basinal nutrient budget (i.e., Sweere et al., 2016, Caxito et al., 2021c).

The upper 2nd-order sequence displays trace metals patterns of weakly restricted basins controlled by several factors. Enrichments of Mo relative to U is probably due to the operation of Mn–Fe particulate shuttle that enhanced the transfer of Mo to deepwater, resulting in sediment Mo/U ratios very close to that of seawater (~1×SW) with no apparent relationship to variation in EFs (Fig. 35A). This implies that the Bambuí seawater at this stage was affected by some degree of redox variations in the reduced water-column (i. e., Algeo and Tribovillard, 2009). This interval show an increase in Mo contents varying from 0.11 to 2.22 ppm (mean = 0.52 ppm) and variable TOC contents ranging from 0.04 to 0.91%, the correlation between Mo and TOC is low ($r = 0.14$; $p(\alpha) > 0.01$), and Mo/TOC ratios fluctuates between 0.80 and 29.95 (mean = 6.17). Although its significance is uncertain (Fig. 35B), this relationship may reflect weak restriction (and, hence, higher

aqueous Mo concentrations) of the deep watermass within the 2nd-order sequence (i.e., Algeo and Lyons, 2006; Tribovillard et al., 2006; Algeo and Rowe, 2012). However, low Cd/Mo ratios suggest that intense reducing conditions prevailed during the deposition of this interval (Fig. 35C; Sweere et al., 2016).

We argue that anoxic and possibly euxinic conditions prevailed during the deposition of the overlying 2nd-order sequence (e.g., Caetano-Filho et al., 2021), in which sediments were intensely reduced as shown by low Mn and Fe concentrations (Table 2), due to continuous upward diffusion of Mn and Fe that escaped to the water column, resulting in Mn-Fe-depleted sediments with little fixation in carbonates (i. e., Algeo and Maynard, 2004; Tribovillard et al., 2006). Renewal of aqueous Mo and oxygenated waters from upwelling could have affected the chemical composition of sulfidic seawater during this basin stage (Fig. 36D); however, sulfate depletion could also have accelerated the transfer of trace metals into the sediments. The sedimentary rocks from the HST of the second sequence displays extremely positive $\delta^{13}C$ values up to +14%, variable high Sr/Ca ratios (Caetano-Filho et al. 2019), and variable radiogenic $^{87}Sr/^{86}Sr$ ratios (Guacaneme et al., 2021). Such features are associated with major disturbances on the carbon cycle and major paleoenvironmental changes in the middle Bambuí Group which could have evolved in a predominantly sulfate limited and methanogenic environment (Cui et al. 2020b; Caetano-Filho et al., 2021).

A model of silled basin, analogous to modern anoxic silled basins (i. e., the Black Sea; Algeo and Rowe, 2012), is coherent with the stratigraphic evolution of the basal Bambuí Group, indicating that tectonically-related changes on the balance between sedimentary supply and accommodation might have been accompanied by changes on seawater circulation and connection with the global reservoir (e.g., Reis et al., 2017; Caetano-Filho et al., 2019; Guacaneme et al., 2021). Based on above, an apparent connection was active during the deposition of the lowermost TST/EHST and partially during the deposition of the overlying 2nd-order sequence. The mechanisms controlling these changes also resulted in strong restriction of the Bambuí sea, the consequent long deepwater residence time and progressively exhaustion of oxidants (i.e., Kuchenbecker et al., 2020; Caetano-Filho et al., 2019, 2021; Paula-Santos et al., 2020; Guacaneme et al., 2021). Examination of covariation patterns between trace-metal/TOC ratios and DOP

(degree-of-pyritization) could assist in determining the relative importance of hydrographic versus redox influences on trace-metal sedimentary accumulation in the Bambuí Group rocks (i.e., Algeo and Rowe, 2012).

6.7.3 Implications for the marine biota at the Bambuí restricted stage

The understanding of temporal changes in the trace-metal inventory on the Bambuí paleomarine system is crucial, since trace metals play essential roles on biogeochemical processes (e.g., Mo and/or V in nitrogenase, an enzyme used by nitrogen-fixing bacteria), and Cu and Zn in many other enzymes and proteins (i.e., Algeo and Rowe, 2012). Also, comparison between trace-metal data and stable isotope proxies (i.e., $\delta^{13}C$, $\delta^{34}S$, $\delta^{15}N$) is fundamental to understand the geochemical evolution and redox state of seawater in the Ediacaran-Cambrian Bambuí paleomarine system.

The discussion is focused on the *Cloudina*-bearing LHST (Warren et al., 2014; Perrella et al., 2017), which is marked by intense anoxic-euxinic conditions that are able to affect the availability of redox-sensitive bio-essential metals. In particular, Fe and Mo (important for biological N_2 fixation and NO_3^- assimilation) are removed from solution in H_2S-bearing waters, which are directly couple to N bioavailability (i.e., Anbar and Knoll, 2002). The energy-intensive process of N_2 fixation, a capability limited to some bacteria and archaea, are catalyzed by nitrogenase metalloenzyme, which requires Fe and Mo as part of Fe_7MoS_9 clusters (Anbar and Knoll, 2002).

An abrupt decrease in Mo/TOC ratios occurs at the LHST and suggests a significant drawdown of bioavailable aqueous [Mo] in the deep watermass owing to strong restriction. The LHST may thus be the only interval in the Bambuí Group that records a seawater composition in which Fe and Mo were simultaneously scarce. If so, the consequences for biology would have been profound. This is also consistent with N stress and with the scarcity of other micronutrients, such as Zn and Cd. Rates of N_2 fixation could have presumably changed the N budget during the deposition of the LHST due to the scarcity of Fe, particularly if the use of the more efficient MoFe-nitrogenase is limited by Mo scarcity. Relevant N isotope data display increasing upward $\delta^{15}N$ values ranging from +2

to +4‰ within the lowermost HST, reflecting anoxic conditions associated with the reduction of nitrate assimilation in the favor of N_2 fixation (Fraga-Ferreira et al., 2021).

Also, sedimentary pyrites in the basal Bambuí Group are progressively ^{34}S-enriched towards the LHST, suggesting that bacterial sulfate reduction strongly depleted the SO_4^{2-} reservoir in a close deep-water system of the Bambuí sea (Caetano-Filho et al., in prep.). Basin isolation led to anoxic and sulfate limited conditions, and probably resulted in a biological turnover from a sulfate-reducing to methanogenic-dominated environment through sulfate consumption by intense activity of bacterial sulfate reduction (BSR) during the regressive cycle of the basal sequence (Caetano-Filho et al., 2021; Caetano-Filho et al., in prep.), As a consequence, marine DIC would be influenced by ^{13}C-enriched methanogenic CO_2, in the absence of sufficient amounts of methane oxidants and its loss to the atmosphere, resulting in the extreme $\delta^{13}C$ excursions in the overlying 2nd-order sequence. The lack of iron in the detrital-lean during the deposition of the LHST prevented pyrite precipitation and resulted in H_2S accumulation in benthic environments, sustained by trace metal data presented here, turning the marine environment into toxic and unfavorable conditions for colonization of benthic metazoans.

Under conditions of micro-nutrient fixation limitation during the above-mentioned cycle, the late Ediacaran eukaryotic algae would likely have fared best in coastal and estuarine habitats where proximity to riverine metal sources minimized the effects of metal limitation, and where upwelling of NH_4^+-bearing deep waters could have provided an adequate source of bioavailable N (i.e., Anbar and Knoll, 2002). Greatly enhanced weathering associated with the extensive Brasiliano/Pan-African orogeny at the late Ediacaran may have increased the supply of metals to seawater (Caxito et al., 2021c) and could have promoted N limitation, facilitating limited eukaryotic diversification (Campbell and Squire, 2010). However, we argue that strong restriction and ultimately paleohydrographic factors likely prevented Mo renewal from deep waters by upwelling, leading to anoxic and sulfate limited conditions predominating over this marine environment at the Ediacaran-Cambrian transition. As upwelling is key for the formation of a nitrate pool, the lack of this phenomena might have diminished the NO_3- reservoir, consequently, eukaryotic life and benthic metazoan would not thrive in such epicontinental setting.

6.8 Conclusions

Changes in sedimentary trace-metal patterns of the basal Bambuí Group rocks provide evidence of the chemical evolution of basinal deep-waters, varying progressively from oxidant to reducing conditions as a response to differential rates of trace-metal removal to the sediment linked to the relative sea-level variation. A model of anoxic silled basin in the core of West Gondwana is here proposed for the Bambuí paleomarine system during the late Ediacaran and early Cambrian. Based on the chemical evolution of seawater we envisage a basin with episodic connection with open ocean controlled by the sea level variation. Connected periods were detected mainly across the TST/EHST transition of the basal 2nd order sequence (lower Sete Lagoas Formation) and partially at the TST of the overlying 2nd order sequence (upper Sete Lagoas Formation/Serra de Santa Helena Formation/Lagoa do Jacaré Formation), in which renewal of oxygenated waters and renewal of Mo from upwelling setting would have been increased. On the other hand, marine restriction at the apex of sea-level fall between the two 2nd order sequences result in extremely anoxic-euxinic conditions with long deepwater residence time and chemical evolution of deep watermass in response to tectono-eustasy. This is a possible mechanism that challenged colonization of interior seas by the early benthic metazoans at the late Ediacaran and early Cambrian. Little is known of the impacts of Mo and other trace metals on the N cycle in the past, and it is necessary to deepen knowledge in their impact on biogeochemical processes in ancient oceans.

6.9 Acknowledgments

Thanks to Petra and Lhoist companies for supplying the Well 1 samples. This study was funded by the São Paulo Research Foundation (FAPESP) thematic project grant #2016/06114-6, and was also supported by CNPq grant #400764/2016□4. CAPES provided the Ph.D. fellowship to the first author. Gustavo Paula-Santos held a FAPESP post-doc grant #2017/00399-1 during this work. Sergio Caetano-Filho also held a FAPESP scholarship grant #2016/11496-5. Paula Luiza Fraga Ferreira holds a FAPESP scholarship grant #2019/13228-6. Marly Babinski, Ricardo Trindade, and Matheus

Kuchenbecker are fellows of the Brazilian Research Council (#307563/2013-8, #206997/2014-0, and #309106/2017-6, respectively).

6.10 References

Anbar, A.D., Knoll, A.H., 2002. Proterozoic ocean chemistry and evolution: A bioinorganic bridge? Science 297, 1137–1142

Algeo, T.J., Lyons, T.W., 2006. Mo-total organic carbon covariation in modern anoxic marine environments: implication for analysis of paleoredox and –hydrographic conditions. Paleoceanography 21, PA1016 23 pp

Algeo, T.J., Maynard, J.B., 2004. Trace-element behavior and redox facies in core shales of Upper Pennsylvanian Kansas-type cyclothems. Chemical Geology 206, 289–318.

Algeo, T.J., Maynard, J.B., 2008. Trace metal covariation as a guide to water-mass conditions in ancient anoxic marine environments. Geosphere 4 (5), 872–887.

Algeo, T.J., Rowe, H., 2012. Paleoceanographic applications of trace-metal concentration data. Chemical Geology 324-325, 6–18

Algeo, T.J., Morford, J., Cruse, A., 2012. New applications of trace metals as proxies in marine paleoenvironments. Chemical Geology 306–307, 160–164.

Algeo, T.J., Tribovillard, N., 2009. Environmental analysis of paleoceanographic systems based on molybdenum–uranium covariation. Chemical Geology 268, 211–225

Alkmim, F.F., Martins-Neto, M.A., 2001. A bacia intracratônica do São Francisco: Arcabouço estrutural e cenários evolutivos. In: Pinto, C.P., Martins□Neto, M. (Eds.). A Bacia do São Francisco: geologia e recursos naturais. SBG, Belo Horizonte, pp. 9–30

Alkmim, F.F., Marshak, S., Pedrosa-Soares, A.C., Peres, G.G., Cruz, S., Whittington, A. 2006. Kinematic evolution of the Araçuaí-West Congo orogen in Brazil and Africa: nutcracker tectonics during the Neoproterozoic assembly of Gondwana. Precambrian Research 149, 43–64

Alkmim, F.F., Martins-Neto, M.A., 2012. Proterozoic first-order sedimentary sequences of the São Francisco craton, eastern Brazil. Marine and Petroleum Geology 33, 127–139

Bedoya-Rueda, C., 2019. Quimiostratigrafia isotópica (C, O, Sr) de alta resolução dos carbonatos da Formação Sete Lagoas, Grupo Bambuí, na região sudoeste da Bacia do São Francisco. Master Thesis, Instituto de Geociências, University of São Paulo, Brazil.

Brumsack, H.J., 2006. The trace metal content of recent organic carbon-rich sediments: implications for Cretaceous black shale formation. Palaeogeography Palaeoclimatology Palaeoecology 232, 344–361.

Caetano-Filho, S., Paula-Santos, G.M., Guacaneme, C., Babinski, M., Bedoya-Rueda, C., Peloso, M., Amorim, K., Afonso, J., Kuchenbecker, M., Reis, H.L.S., Trindade, R.I.F., 2019. Sequence stratigraphy and chemostratigraphy of an Ediacaran-Cambrian foreland-related carbonate ramp (Bambuí Group, Brazil). Precambrian Research 331, 105365.

Caetano-Filho, S., Paula-Santos, G., Sansjofre, P., Ader, M., Cartigny, P., Guacaneme, C., Babinski, M., Kuchenbecker, M., Reis, H., Trindade, R.I.F., 2020. Eustatic control on superheavy pyrite trends from late Ediacaran-early Cambrian carbonate successions of the West Gondwana: sulfate distillation cycles in shallow water platforms? In Goldschmidt virtual 2020.

Caetano-Filho, S., Sansjofre, P., Ader, M., Paula-Santos. G.M., Guacaneme, C., Babinski, M., Bedoya-Rueda, C., Kuchenbecker, M. Reis, H., Trindade, R.I.F., 2021. A large epeiric methanogenic Bambuí sea in the core of Gondwana Supercontinent. Geoscience Frontiers 12, 203–218.

Caetano-Filho, S., Sansjofre, P., Paula-Santos, G.M., Cartigny, P., Ader, M., Guacaneme, C., Babinski, M., Kuchenbecker, M., Reis, H.L.S., Trindade, R.I.F. Multiple sulfur isotope constraints and stratigraphic relationships on ^{34}S enrichments in pyrites of the late Ediacaran-Cambrian record: a product of supercontinent assembly and restricted seas (in press.)

Campbell, I.H., Squire, R.J., 2010. The mountains that triggered the Late Neoproterozoic increase in oxygen: the second great oxidation event. Geochimica et Cosmochimica Acta 74 (15), 4187–4206.

Canfield, D.E., Poulton, S.W., Narbonne, G.M., 2007. Late-Neoproterozoic deep-ocean oxygenation and the rise of animal life. Science 315 (5808), 92–95.

Canfield, D.E., Thamdrup, B., 2009. Towards a consistent classification scheme for geochemical environments, or, why we wish the term 'suboxic' would go away. Geobiology 7 (4), 385–392.

Castro, P.T.A., Dardenne, M.A. 2000. The sedimentology, stratigraphy and tectonic context of the São Francisco Supergroup at the southwestern domain of the São Francisco craton, Brazil. Revista Brasileira de Geociências 30, 439–441.

Caxito, F.A., Uhlein, A., Dantas, E., Stevenson, R., Egydio-Silva, M., Salgado, S.S. 2017. The Rio Preto and Riacho do Pontal Belts, in M. Heilbron et al. (eds.), São Francisco Craton, Eastern Brazil, Regional Geology Reviews, DOI 10.1007/978-3-319-01715-0_12

Caxito, F., Lana, C., Frei, R., Uhlein, G., Sial, A., Dantas, E., Pinto, A.G., Campos, F.C., Galvão, P., Warren, L., Okubo, J., Ganade, C., 2021c. Goldilocks at the dawn of complex life: mountains might have damage Ediacaran-Cambrian ecosystems and prompted an early Cambrian greenhouse world. Scientific Reports 11, 20010

Chiavegatto, J.R.S., Gomes, N.S., Dardenne, M.A., Delgado, C.E.R., 2003. Estratigrafia do Grupo Bambuí nas regiões do norte de Minas Gerais: Uma nova unidade estratigráfica em um contexto de inversão de bacia. In: SBG, Simpósio de Geologia de Minas Gerais, vol. 12. Ouro Preto, Anais, p. 24.

Costa, M.T., Branco, J.R., 1961. Roteiro para a excursão Belo Horizonte-Brasília. In Congresso Brasileiro de Geologia 14, UFMG, Inst. Pesq. Radioat., Publ. 15, 25p., Belo Horizonte.

Cui, H., Warren, L.V., Uhlein, G.J., Okubo, J., Liu, X.M., Plummer, R.E., Baele, J.M., Goderis, S., Claeys, P., Li, F., 2020b. Global or regional? Constraining the origins of the middle Bambui carbon cycle anomaly in Brazil. Precambrian Research 348, 105861

Dardenne, M.A., 1978. Síntese sobre a estratigrafia do Grupo Bambuí no Brasil Central. In: Congresso Brasileiro de Geologia, 30, Recife, Anais, SBG, v. 2, p. 597–610.

Fraga-Ferreira, P.L., Ader, M., Caetano-Filho, S., Sansjofre, P., Paula-Santos, G.M., Babinski, M., Guacaneme, C., Bedoya-Rueda, C., Rojas, V., Reis, H.L.S., Kuchenbecker, M., Trindade, R.I.F., 2021. The Nitrogen Cycle in an Epeiric Sea in the Core of Gondwana Supercontinent: A Study on the Ediacaran-Cambrian Bambuí Group, East-central Brazil. Front. Earth Sci. 9:692895. doi: 10.3389/feart.2021.692895

Guacaneme, C., Babinski, M., Bedoya-Rueda, C., Paula-Santos, G.M., Caetano-Filho, S., Kuchenbecker, M., Reis, H.L.S., Trindade, R.I.F., 2021. Tectonically-induced strontium isotope changes in ancient restricted seas: The case of the Ediacaran-Cambrian Bambuí foreland basin system, east Brazil. Gondwana Research 93, 275–290

Heilbron, M., Cordani, U.G., Alkmim, F.F., 2017. São Francisco craton: tectonic genealogy of a miniature continent. Regional Geology Reviews. Springer, p. 326.

Hippertt, J.P., Caxito, F.A., Uhlein, G.J., Nalini, H.A., Sial, A.N., Abreu, A.T., Nogueira, L.B., 2019. The fate of a Neoproterozoic intracratonic marine basin: Trace elements, TOC and IRON speciation geochemistry of the Bambuí Basin, Brazil. Precambrian Research 330, 101–120

Iyer, S.S., Babinski, M., Krouse, H.L., Chemale, F., 1995. Highly ^{13}C-enriched carbonate and organic matter in the Neoproterozoic sediments of the Bambuí Group, Brazil. Precambrian Research, 73: 271–282.

Jones, B., Manning, D.A.C., 1994. Comparison of geochemical indices used for the interpretation of paleoredox conditions in ancient mudstones. Chem. Geol. 114, 111–129.

Kaufman, A.J., Knoll, A.H., Narbonne, G.M., 1997. Isotopes, ice ages, and terminal Proterozoic Earth history. National Academy Sciences Proceedings, 94:600-605.

Knoll, A.H., Walter, M.R., Narbonne, G.M. Christie-Blick, N., 2006. The Ediacaran Period: a new addition to the geologic time scale. Lethaia 39, 13–30.

Kuchenbecker, M., Babinski, M., Pedrosa-Soares, A.C., Costa, R.D., Lopes-Silva. L., Pimenta, F., 2013. Proveniência e análise sedimentar da porção basal do Grupo Bambuí em Arcos (MG). Geologia USP 13(4): 49–61.

Kuchenbecker, M., Babinski, M., Pedrosa-Soares, A.C., Lopes-Silva, L., Pimenta, F., 2016a. Chemostratigraphy of the lower Bambuí Group, southwestern São Francisco Craton, Brazil: insights on Gondwana paleoenvironments. Brazilian Journal of Geology 46, 145–162.

Kuchenbecker, M., Atman, D., Costa, R.D., Pedrosa-Soares, A.C., Babinski, M., 2016b. A formação Gorutuba: sedimentação litorânea a continental na margem leste da Bacia Bambuí (MG). Geologia USP Série Científica 16 (2), 67–81.

Kuchenbecker, M., Pedrosa-Soares, A.C., Babinski, M., Reis, H.L.S., Atman, D., Costa, R.D. 2020. Towards an integrated tectonic model for the interaction between the Bambuí basin and the adjoining orogenic belts: Evidences from the detrital zircon record of syn-orogenic units. Journal of South American Earth Sciences 104-102831

Li, D., Ling, H.F., Shields-Zhou, G.A., Chen, X., Cremonese, L., Och, L., Manning, C.J., 2013. Carbon and strontium isotope evolution of seawater across the Ediacaran-Cambrian transition: evidence from the Xiaotan section, NE Yunnan, South China. Precambrian Research 225, 128–147.

Liyuan, W., Qingjun; G., Changqiu, Z., Rongfei., W., Yinan, D., Xiaokun, H., Liyan, T., Jing, K., Xi, Y., 2021. Trace and rare earth elements geochemistry of sedimentary rocks in the Ediacaran-Cambrian transition from the Tarim Basin, Northwest China: Constrains for redox environments. Precambrian Research 352, 105942.

Lyons, T.W., Anbar, A.D., Severmann, S., Scott, C., Gill, B., 2009. Tracking euxinia in the ancient ocean: A multiproxy perspective and Proterozoic case study. Annual Review of Earth and Planetary Sciences 37, 507–34.

Lyons, T.W., Reinhard, C., Planavsky, N., 2014. The rise of oxygen in Earth's early ocean and atmosphere. Nature 506, 309.

Marshall, C.R., 2006. Explaining the Cambrian ''explosion" of animals. Annual Review Earth Planetary Science, 34, 355–384.

Martins-Neto, M.A. 2009. Sequence stratigraphic framework of Proterozoic successions in eastern Brazil. Marine and Petroleum Geology 26, 163–176.

Moreira, D.S., Uhlein, A., Dussin, I.A., Uhlein, G.J., Misuzaki, A.M., 2020. A Cambrian age for the upper Bambuí Group, Brazil, supported by the first U–Pb dating of volcaniclastic bed. Journal of South American Earth Sciences 99, 102503

Paula-Santos, G.M., Babinski, M., Kuchenbecker, M., Caetano-Filho, S., Trindade, R.I., Pedrosa-Soares, A.C., 2015. New evidence of an Ediacaran age for the Bambuí Group in southern São Francisco craton (eastern Brazil) from zircon U-Pb data and isotope chemostratigraphy. Gondwana Research 28, 702–720.

Paula-Santos, G.M., Caetano-Filho, S., Babinski, M., Trindade, R.I., Guacaneme, C., 2017. Tracking connection and restriction of West Gondwana São Francisco Basin through isotope chemostratigraphy. Gondwana Research 42, 280–305.

Paula-Santos, G.M., Caetano-Filho, S., Babinski, M., Enzweiler, J., 2018. Rare earth elements of carbonate rocks from the Bambuí Group, southern São Francisco Basin, Brazil, and their significance as paleoenvironmental proxies. Precambrian Research 305, 327–340.

Paula-Santos, G.M., Caetano-Filho, S., Enzweiler, J., Navarro, M.S., Babinski, M., Guacaneme, C., Kuchenbecker, M., Reis, H., Trindade, R.I.F., 2020. Rare earth elements in the terminal Ediacaran Bambuí Group carbonate rocks (Brazil): evidence for high seawater alkalinity during rise of early animals. Precambrian Research 336, 105506.

Perrella, P., Uhlein, A., Uhlein, G.J., Sial, A.N., Pedrosa-Soares, A.C., Lima, O.N.B., 2017. Facies analysis, sequence stratigraphy and chemostratigraphy of the Sete Lagoas Formation (Bambuí Group), northern Minas Gerais State, Brazil: evidence of a cap carbonate deposited on the Januária basement high. Brazilian Journal of Geology 47, 59−77.

Reis, H.L.S., Suss, J.F., 2016. Mixed carbonate-siliciclastic sedimentation in forebulge grabens: an example from the Ediacaran Bambuí Group, São Francisco basin, Brazil. Sedimentary Geology 339, 83–103.

Reis, H.L.S., Suss, J.F., Fonseca, R.C.S., Alkmim, F.F., 2017a. Ediacaran forebulge grabens of the southern São Francisco basin, SE Brazil: Craton interior dynamics during West Gondwana assembly. Precambrian Research 302, 150–170.

Reis, H.L.S., Alkmim, F.F., Fonseca, R.C.S., Nascimento, T.C., Suss, J.F., Prevatti, L.D., 2017b. The São Francisco Basin. In: Heilbron, M., Cordani, U.G., Alkmim, F.F. (Eds.), São Francisco Craton, Eastern Brazil, Regional Geology Reviews. Springer, Switzerland, pp. 117–143.

Rossi, A.V.A., Danderfer Filho, A., Bersan, S.M., Kelmer, L.R., Tavares, T.D., Lana, C.C., 2020. Stratigraphic, isotopic, and geochronological record of a superposed pro-foreland basin in the eastern São Francisco craton during west Gondwana amalgamation. Journal of South American Earth Science 97, 102406.

Sanchez, E.A.M., Uhlein, A. Fairchild, T.R. 2021. Treptichnus Pedum in the Três Marias Formation, south-central Brazil, and its implications for the Ediacaran-Cambrian transition in South America. Journal of South American Earth Sciences 105, 102983

Sansjofre, P., Trindade, R.I.F., Ader, M., Soares, J.L., Nogueira, A.C.R., Tribovillard, N., 2014. Paleoenvironmental reconstruction of the Ediacaran Araras platform (Western Brazil) from the sedimentary and trace metals record. Precambrian Research 241, 185–202.

Santos, R.V., Alvarenga, C.J.S., Dardenne, M.A., Sial, A.N., Ferreira, V.P., 2000. Carbon and oxygen isotope profiles across Meso-Neoproterozoic limestones from central Brazil: Bambuí and Paranoá Groups. Precambrian Research 104, 107–122.

Scott, C., Lyons, T.W., 2012. Contrasting molybdenum cycling and isotopic properties in euxinic versus non-euxinic sediments and sedimentary rocks: refining the paleoproxies. Chemical Geology 324, 19–27.

Shen, Y., Zhao, R., Chu, X., Lei, J., 1998. The carbon and sulfur isotope signatures in the Precambrian-Cambrian transition series of the Yangtze Platform. Precambrian Research 89, 77–86.

Sweere, T., van den Boorn, S., Dickson A.J., Reichart, G.J., 2016. Definition of new trace-metal proxies for the controls on organic matter enrichment in marine sediments based on Mn, Co, Mo and Cd concentrations. Chemical Geology 441, 235–245

Tavares, T.D., Martins, M.S., Alkmim, F.F., Lana, C., 2020. Detrital zircons from the Upper Três Marias Formation, São Francisco basin, SE Brazil: Record of foreland deposition during the Cambrian? Journal of South American Earth Sciences 97, 102395

Taylor, S.R., McLennan, S.M., 1985. The continental crust: its composition and evolution. Blackwell, Oxford. 312 pp.

Tribovillard, N., Algeo, T.J., Lyons, T., Riboulleau, A., 2006. Trace metals as paleoredox and paleoproductivity proxies: an update. Chemical Geology 232, 12–32.

Tribovillard, N., Algeo, T.J., Baudin, F., Riboulleau, A. 2012. Analysis of marine environmental conditions based on molybdenum–uranium covariation—Applications to Mesozoic paleoceanography. Chemical Geology 324-325, 46–58

Uhlein, A., Baptista, M.C., Seer, H.J., Caxito, F.A., Uhlein, G.J., Dardenne, M.A., 2011. A Formação Lagoa Formosa, Grupo Bambuí (MG): Sistema deposicional de leque submarino em bacia de antepaís. Geonomos 19(2): 163–172.

Uhlein, G.J., Uhlein, A., Stevenson, R., Halverson, G.P., Caxito, F.A., Cox, G.M., 2017. Early to late Ediacaran conglomeratic wedges from a complete foreland basin cycle in the southwest São Francisco Craton, Bambuí Group, Brazil. Precambrian Research 299, 101–116.

Uhlein, G.J., Uhlein, A., Pereira, E., Caxito, F.A., Okubo, J., Warren, L.V., Sial, A.N., 2019. Ediacaran paleoenvironmental changes recorded in the mixed carbonate siliciclastic Bambuí Basin, Brazil. Palaeogeography, Palaeoclimatology, Palaeoecology 517, 39–51.

Valeriano, C.M., 2017. The southern Brasília belt. In: Heilbron, M., Cordani, U.G., Alkmim, F.F. (Eds.), São Francisco Craton, Eastern Brazil: Tectonic Genealogy of a Miniature Continent. Springer International Publishing, Switzerland, pp. 189–204.

Vieira, L.C., Trindade, R.I.F, Nogueira, A.C.R., Ader, M., 2007b. Identification of a Sturtian cap carbonate in the Neoproterozoic Sete Lagoas carbonate plataform, Bambuí Group, Brazil. Comptes Rendus Geoscience, 339:240–258.

Warren, L.V., Quaglio, F., Riccomini, C., Simões, M.G., Poiré, D.G., Strikis, N.M., Anelli, L.E. Strikis, P.C., 2014. The puzzle assembled: Ediacaran guide fossil Cloudina reveals an old proto-Gondwana seaway. Geology 42 (5): 391–394.

Zheng, Y., Anderson, R.F., van Geen, A., Kuwabara, J.S., 2000. Authigenic molybdenum formation in marine sediments: a linkage to pore water sulfide in the Santa Barbara Basin. Geochimica et Cosmochimica Acta 64, 4165–4178.

6.11 Suplementary material

Section	Sample	m	Stage	C (%)	TOC (%)	Al (%)	Fe (%)	Mn	Th	Zr
Januária	CM-02	1,15	TST	0,12	0,01	1,14	0,66	577	1,68	19,6
	CM-03c	2,75		0,92	0,04	0,57	0,28	641	1	12,7
	CM-03h	3,87		0,09	0,01	0,64	0,35	237	1,01	12,6
	CM-04c	4,67		0,06	0,01	0,56	0,33	220	1,03	11
	CM-12	21,5	EHST	0,06	0,01	0,52	0,3	204	0,9	10,6
	CM-18	27,5		1,59	0,04	0,07	0,04	16	0,11	1,4
	CM-22	31,9		2,03	0,04	0,12	0,06	16	0,15	2
	CM-32	43,1	LHST	2,94	0,04	0,08	0,04	15	0,09	1,3
	CM-42	54,5		3,79	0,03	0,07	0,04	12	0,1	1,2
	BAR-10	59,50		4,38	0,05	0,05	0,03	17	0,07	1,1
	BAR-20	69,50		1,85	0,03	0,08	0,06	12	0,11	1,4
	BAR-35	85,70		1,73	0,02	0,26	0,17	34	0,51	5
	JL-01	150	2nd-S	0,42	0,07	1,25	1,04	2590	3,64	33,8
	JL-09	158		0,85	0,04	0,15	0,43	94	0,34	3,2
	JL-13	162		2,62	0,06	0,09	0,1	94	0,18	1,6
Arcos	M6	594,02	TST	0,08	0,01	2,26	1,68	423	0,61	7,9
	M10	597,54		0,08	0,02	2,09	2,75	723	0,97	13
	M15	601,72		1,62	0,30	0,9	0,89	934	3,15	15,2
	M20	606,52		0,35	0,03	0,29	0,22	1100	12,95	5,3
	K28a	632,17	EHST	0,24	0,01	0,15	0,09	33	0,3	3
	K30a	642,02		0,58	0,01	0,08	0,06	27	0,1	1,6
	K34c	664,17		2,44	0,04	0,06	0,03	16	0,07	1,1
	K37c	679,36		3,38	0,09	0,19	0,12	13	0,4	4,6
	M40	690,9	LHST	12,38	0,10	0,05	0,03	<5	0,1	1
	M44	711,41		14,89	0,07	0,03	0,02	10	0,07	0,6
	M47	726,41		18,52	0,04	0,03	0,01	28	0,08	0,6
	M48	731,41		13,45	0,05	0,01	0,01	16	0,15	0,6
	K52a	753,16	2nd-S/dolo	4,61	0,08	0,18	0,25	211	1,13	3,6
	M53	757,16		2,01	0,04	0,37	0,2	62	0,73	7,5
	M54	762,16		0,61	0,05	0,17	0,14	121	0,31	2,8
	M55	767,16	2nd-S	0,84	0,13	0,99	0,65	159	2,55	22,4
Well 1	WS-02b	1112,34	TST	0,41	0,02	0,53	0,28	145	1,02	10,4
	WS-03b	1108,66		0,62	0,04	0,65	0,23	205	1,14	10,9
	WS-04a	1105,51		0,07	0,02	3,79	2,58	1520	4,25	59,4
	WS-18	1043,1	EHST	1,35	0,97	4,25	3,16	31000	6,65	75,3
	WS-22	1025,1		0,17	0,13	4,23	6,25	7690	6,06	70,6

	WS-24	1015,84		0,08	0,02	3,24	5	13800	4,19	47,3
	WS-26	1006,63		0,22	0,07	3,05	2,53	10100	3,76	44,3
	WS-28	996,77		0,18	0,03	2,04	1,41	2740	3,05	33,4
	WS-31	982,43		0,31	0,04	1,99	1,19	2510	3,38	33
	WS-33	973,34		0,09	0,04	0,97	0,52	9210	1,44	14,1
	WS-35	964,3		0,05	0,03	1,67	0,79	4850	2,55	26
	WS-40	940,81		0,08	0,03	1,95	1,37	2080	3,2	29,7
	WS-42	932,21		0,12	0,06	5,19	2,66	1100	9,28	92,9
	WS-44	922,85		0,09	0,04	1,75	0,86	3020	2,67	25,8
	WS-48	904,28		0,07	0,05	2,31	1,2	1070	3,24	32,7
	WS-49	899,7		0,06	0,03	1,48	0,5	1140	2,18	20,2
	WS-52	886,04		0,05	0,03	2,92	1,69	1100	4,89	48,2
	WS-54	876,74	LHST	0,97	0,13	3,77	1,56	3770	10,65	81,5
	WS-58	859,12		0,85	0,45	9,01	4,44	108	17,6	193,5
	WS-60	850,11		1,71	0,26	0,43	0,16	55	0,56	4,8
	WS-64	832,03		3,77	0,06	0,18	0,15	74	0,27	2
	WS-66	822,75		5,18	0,09	0,15	0,11	52	0,33	2,7
	WS-69	809,01		1,78	0,30	0,1	0,08	65	0,13	1,5
	WS-73	789,86		2,00	0,11	0,25	0,22	123	0,4	2,9
	WS-78	766,36		0,27	0,06	0,13	0,1	127	0,15	2
	WS-81	750,45		41,27	0,42	0,03	0,05	84	0,05	0,6
	WS-84	738,61		10,28	0,41	0,32	0,18	66	0,62	6,5
	WS-86	729,14	2nd-S	2,07	0,91	3,87	2,32	780	5,32	77,2
	WS-87	724,45		1,40	0,16	5,73	3,19	448	8,62	122
	WS-89	715		1,14	0,81	6,39	3,27	572	9,26	131,5
	WS-93	695,68		0,25	0,20	7,78	4,46	824	9,56	141

Section	Sample	m	Stage	Mo	U	V	Zn	Cd	Co	Cr	Cu
Januária	CM-02	1,15	TST	<0.05	0,7	23	20	0,05	2,7	8	1,5
	CM-03c	2,75		<0.05	0,6	8	7	0,02	1,4	5	3,9
	CM-03h	3,87		<0.05	0,3	6	7	<0.02	1,5	5	1
	CM-04c	4,67		<0.05	0,2	5	8	0,02	1,4	5	2
	CM-12	21,5	EHST	<0.05	0,2	5	10	0,04	1,5	4	2,5
	CM-18	27,5		<0.05	0,8	<1	2	<0.02	0,4	1	1,4
	CM-22	31,9		<0.05	0,7	1	3	<0.02	0,5	2	1,4
	CM-32	43,1	LHST	<0.05	0,7	1	<2	<0.02	0,4	1	1,3
	CM-42	54,5		<0.05	0,9	<1	<2	<0.02	0,4	1	1,9
	BAR-10	59,5		<0.05	0,8	<1	<2	<0.02	0,4	1	1,6
	BAR-20	69,5		<0.05	0,9	1	2	<0.02	0,5	2	1,8
	BAR-35	85,7		0,1	1,7	8	10	0,04	1	2	9,3

	JL-01	150	2nd-S	2,22	1	15	54	0,08	3,4	12	18,4
	JL-09	158		0,16	0,3	6	5	0,02	1,2	3	7,2
	JL-13	162		0,11	0,4	3	7	<0.02	0,9	1	6,1
Arcos	M6	594,02	TST	0,37	4,1	72	30	0,71	17,3	144	12,4
	M10	597,54		<0.05	2,6	73	34	0,17	13,1	78	6,2
	M15	601,72		0,29	0,9	17	14	0,03	2,2	7	4,9
	M20	606,52		<0.05	6	4	4	<0.02	2,2	4	5,3
	K28a	632,17	EHST	<0.05	0,4	1	4	<0.02	0,6	2	2,8
	K30a	642,02		<0.05	<0.1	1	2	<0.02	0,6	1	2,3
	K34c	664,17		<0.05	0,7	<1	7	<0.02	0,4	1	2,3
	K37c	679,36		0,25	2	2	4	<0.02	0,9	1	2,7
	M40	690,9	LHST	0,15	1,2	<1	<2	0,02	0,5	<1	2,1
	M44	711,41		0,14	0,9	<1	<2	<0.02	0,5	<1	2
	M47	726,41		0,08	0,9	<1	<2	<0.02	0,5	<1	1,8
	M48	731,41		0,13	1,3	<1	<2	<0.02	0,5	<1	1,8
	K52a	753,16	2nd-S/dolo	0,26	0,7	4	23	0,03	1,2	3	17,8
	M53	757,16		0,13	2,5	12	12	0,04	1,1	3	4,7
	M54	762,16		0,18	0,5	6	18	<0.02	1	2	11,4
	M55	767,16	2nd-S	0,37	0,6	13	77	0,04	2,1	9	13,9
Well 1	WS-02b	1112,34	TST	0,05	0,6	5	23	0,63	1,4	4	5,4
	WS-03b	1108,66		0,08	0,7	7	25	0,84	1,4	4	6,9
	WS-04a	1105,51		0,1	0,8	52	62	0,29	9,9	27	2,4
	WS-18	1043,1	EHST	0,73	1,9	58	57	0,05	28,5	32	23
	WS-22	1025,1		0,1	1,4	52	152	0,36	52	32	110
	WS-24	1015,84		0,06	1,1	36	249	0,26	32,6	19	97,1
	WS-26	1006,63		0,07	0,8	32	58	0,09	21,4	18	73
	WS-28	996,77		0,07	0,6	21	25	0,04	5,2	11	11,5
	WS-31	982,43		0,14	0,7	23	24	0,14	4	12	31,9
	WS-33	973,34		0,58	0,6	9	11	0,09	2	3	8
	WS-35	964,3		0,07	0,9	15	18	0,19	4	7	18,8
	WS-40	940,81		0,13	0,6	19	36	0,05	3,6	9	39,7
	WS-42	932,21		0,24	2,2	65	45	<0.02	9,7	36	4,9
	WS-44	922,85		0,08	0,6	14	18	0,04	3,4	7	13,5
	WS-48	904,28		0,06	0,6	24	26	0,03	5,5	10	2,5
	WS-49	899,7		0,06	0,3	10	11	0,09	2,6	6	12,2
	WS-52	886,04		0,92	0,9	30	32	0,04	7,9	17	138
	WS-54	876,74	LHST	0,74	2,7	29	113	0,13	11,9	16	48,8
	WS-58	859,12		1,59	13,6	101	48	0,02	30,3	72	44,9
	WS-60	850,11		0,13	1,2	4	3	0,02	1	2	5,2
	WS-64	832,03		0,12	0,6	2	4	0,02	0,8	1	2,5
	WS-66	822,75		0,08	0,7	1	4	<0.02	0,7	1	1,7

	WS-69	809,01		0,08	0,4	1	<2	<0.02	0,6	<1	1,5
	WS-73	789,86		0,09	0,9	2	6	<0.02	0,8	<1	2,8
	WS-78	766,36		0,07	0,5	1	2	<0.02	0,7	<1	2,4
	WS-81	750,45		<0.05	1	<1	2	<0.02	0,5	<1	1,4
	WS-84	738,61		0,15	1,9	3	6	<0.02	1,1	2	10,6
	WS-86	729,14	2nd-S	0,73	1,9	44	56	0,06	8,1	36	12,7
	WS-87	724,45		1,42	2,7	79	100	0,09	12,9	49	40,5
	WS-89	715		1,02	2,6	92	78	0,05	12,2	55	11,3
	WS-93	695,68		0,9	2,3	105	128	0,06	18,1	66	18,1

Section	Sample	Stage	Lithology	Cd	Co	Cr	Cu	Mn	Mo	Ni	U	V	Zn	Mo/TOC
Januária	CM-02	TST	Calcilutite	3,7	1,0	0,6	0,1	3,0	0,4	0,7	5,7	1,2	1,8	5,08
	CM-03c		Calcilutite	2,9	1,0	0,7	0,8	6,7	0,7	0,6	9,7	0,8	1,3	1,11
	CM-03h		Calcisiltite	2,6	1,0	0,7	0,2	2,2	0,7	0,6	4,3	0,6	1,1	7,72
	CM-04c		Calcisiltite	3,0	1,1	0,8	0,4	2,4	0,8	0,7	3,3	0,5	1,5	9,78
	CM-12	EHST	Calcisiltite	6,5	1,2	0,6	0,5	2,4	0,8	0,7	3,6	0,6	2,0	6,00
	CM-18		Calcisiltite	24,0	2,4	1,2	2,2	1,4	6,0	0,6	105,5	0,9	3,0	1,32
	CM-22		Calcisiltite	14,0	1,8	1,4	1,3	0,8	3,5	0,5	53,8	0,5	2,6	1,17
	CM-32	LHST	Calcisiltite	21,0	2,1	1,1	1,8	1,1	5,3	0,5	80,8	0,8	2,6	1,14
	CM-42		Calcisiltite	24,0	2,4	1,2	3,0	1,0	6,0	0,8	118,7	0,9	3,0	1,46
	BAR-10		Calcisiltite	33,6	3,4	1,7	3,6	2,0	8,4	0,6	147,7	1,2	4,2	1,11
	BAR-20		Calcarenite	21,0	2,6	2,1	2,5	0,9	5,3	0,7	103,8	0,8	2,6	1,47
	BAR-35		Calcarenite	12,9	1,6	0,6	4,0	0,8	3,2	0,4	60,4	1,8	4,0	5,42
	JL-01	2nd-S	Calcarenite	5,4	1,1	0,8	1,6	12,4	14,9	1,0	7,4	0,7	4,5	29,95
	JL-09		Calcarenite	11,2	3,4	1,7	5,4	3,8	9,0	1,4	18,5	2,4	3,5	4,05
	JL-13		Calcisiltite	18,7	4,2	0,9	7,6	6,3	10,3	1,2	41,0	2,0	8,2	1,80
Arcos	M6	TST	Calcarenite	26,4	3,2	5,4	0,6	1,1	1,4	3,9	16,7	1,9	1,4	38,23
	M10		Calcarenite	6,8	2,6	3,1	0,3	2,1	0,2	2,2	11,5	2,1	1,7	2,01
	M15		Shale	2,8	1,0	0,7	0,6	6,2	2,7	0,9	9,2	1,1	1,6	0,96
	M20		Calcarenite	5,8	3,2	1,2	2,0	22,8	1,4	1,7	191,0	0,8	1,4	1,59
	K28a	EHST	Calcarenite	11,2	1,7	1,1	2,1	1,3	2,8	1,0	24,6	0,4	2,8	4,48
	K30a		Calcarenite	21,0	3,2	1,1	3,2	2,0	5,3	0,9	11,5	0,8	2,6	5,93
	K34c		Calcarenite	28,0	2,8	1,4	4,3	1,6	7,0	0,9	107,7	1,0	12,3	1,33
	K37c		Calcisiltite	8,8	2,0	0,4	1,6	0,4	11,1	1,0	97,2	0,6	2,2	2,70
	M40	LHST	Calcisiltite	33,6	4,2	1,7	4,7	0,6	25,2	1,1	221,5	1,2	4,2	1,45
	M44		Calcisiltite	56,0	7,0	2,8	7,5	2,0	39,2	1,4	276,9	2,0	7,0	1,93
	M47		Calcarenite	56,0	7,0	2,8	6,7	5,6	22,4	1,4	276,9	2,0	7,0	1,96
	M48		Calcarenite	168,0	21,0	8,4	20,2	9,6	109,2	2,8	1200,0	6,0	21,0	2,67
	K52a	2nd-S/dolo	Doloarenite	14,0	2,8	1,4	11,1	7,0	12,1	2,3	35,9	1,3	13,4	3,46
	M53		Doloarenite	9,1	1,2	0,7	1,4	1,0	3,0	0,6	62,4	1,9	3,4	2,90

	M54		Doloarenite	9,9	2,5	1,0	7,5	4,3	8,9	1,3	27,1	2,1	11,1	3,54
	M55	2nd-S	Calcilutite	3,4	0,9	0,8	1,6	1,0	3,1	1,0	5,6	0,8	8,2	2,85
Well 1	WS-02b	TST	Dolostone	99,8	1,1	0,6	1,1	1,6	0,8	1,3	10,4	0,6	4,6	2,46
	WS-03b		Dolostone	108,6	0,9	0,5	1,2	1,9	1,0	1,2	9,9	0,6	4,0	1,80
	WS-04a		Dolostone	6,4	1,1	0,6	0,1	2,4	0,2	1,2	1,9	0,8	1,7	4,46
	WS-18	EHST	Shale	1,0	2,8	0,6	0,6	43,8	1,4	0,8	4,1	0,8	1,4	0,75
	WS-22		Lime/Siltstone	7,1	5,2	0,6	2,9	10,9	0,2	1,8	3,1	0,7	3,8	0,75
	WS-24		Lime/Siltstone	6,7	4,2	0,5	3,4	25,6	0,2	2,9	3,1	0,7	8,1	3,46
	WS-26		Lime/Siltstone	2,5	2,9	0,5	2,7	19,9	0,2	2,0	2,4	0,6	2,0	1,04
	WS-28		Lime/Siltstone	1,6	1,1	0,5	0,6	8,1	0,3	0,7	2,7	0,6	1,3	2,02
	WS-31		Lime/Siltstone	5,9	0,8	0,5	1,8	7,6	0,6	0,8	3,2	0,7	1,3	3,36
	WS-33		Lime/Siltstone	7,8	0,9	0,3	0,9	57,0	5,0	0,6	5,7	0,6	1,2	13,95
	WS-35		Lime/Siltstone	9,6	1,0	0,4	1,3	17,4	0,4	0,6	5,0	0,5	1,1	2,09
	WS-40		Lime/Siltstone	2,2	0,8	0,4	2,3	6,4	0,6	0,7	2,8	0,6	1,9	4,55
	WS-42		Lime/Siltstone	0,3	0,8	0,6	0,1	1,3	0,4	0,4	3,9	0,8	0,9	4,11
	WS-44		Lime/Siltstone	1,9	0,8	0,3	0,9	10,4	0,4	0,5	3,2	0,5	1,1	2,01
	WS-48		Lime/Siltstone	1,1	1,0	0,4	0,1	2,8	0,2	0,6	2,4	0,6	1,2	1,17
	WS-49		Lime/Siltstone	5,1	0,7	0,3	0,9	4,6	0,3	0,5	1,9	0,4	0,8	1,90
	WS-52		Lime/Siltstone	1,2	1,1	0,5	5,3	2,3	2,6	0,7	2,8	0,6	1,2	35,05
	WS-54	LHST	Limestone	2,9	1,3	0,4	1,4	6,0	1,6	1,3	6,6	0,5	3,1	5,85
	WS-58		Limestone	0,2	1,4	0,7	0,6	0,1	1,5	0,9	13,9	0,7	0,6	3,57
	WS-60		Limestone	3,9	1,0	0,4	1,4	0,8	2,5	0,6	25,8	0,6	0,7	0,51
	WS-64		Limestone	9,3	1,9	0,5	1,6	2,5	5,6	0,9	30,8	0,7	2,3	2,16
	WS-66		Limestone	11,2	2,0	0,6	1,3	2,1	4,5	0,7	43,1	0,4	2,8	0,93
	WS-69		Limestone	16,8	2,5	0,8	1,7	3,9	6,7	0,7	36,9	0,6	2,1	0,26
	WS-73		Limestone	6,7	1,3	0,3	1,3	3,0	3,0	0,7	33,2	0,5	2,5	0,79
	WS-78		Limestone	12,9	2,3	0,6	2,1	5,9	4,5	0,9	35,5	0,5	1,6	1,18
	WS-81		Limestone	56,0	7,0	2,8	5,2	16,8	14,0	1,9	307,7	2,0	7,0	0,12
	WS-84		Limestone	5,3	1,4	0,5	3,7	1,2	3,9	0,8	54,8	0,6	2,0	0,36
	WS-86	2nd-S	Limestone	1,3	0,9	0,8	0,4	1,2	1,6	0,7	4,5	0,7	1,5	0,80
	WS-87		Shale	1,3	0,9	0,7	0,8	0,5	2,1	0,8	4,3	0,8	1,8	9,08
	WS-89		Shale	0,7	0,8	0,7	0,2	0,5	1,3	0,4	3,8	0,9	1,3	1,27
	WS-93		Shale	0,6	1,0	0,7	0,3	0,6	1,0	0,9	2,7	0,8	1,7	4,60

7 CHAPTER 7 – INTEGRATED DISCUSSIONS AND CONCLUSIONS

This work provides new aspects on the diagenetic, isotope and chemical evolution of the sedimentary rocks from the basal Bambuí Group based on petrography, high-resolution sampling on Sr-isotope stratigraphy and detailed trace-metal geochemistry that potentially record important paleoenvironmental changes in the context of a foreland marine basin developed in the Gondwana assembly. Identification of the controls on Sr-isotope composition and trace-metal enrichment patterns are essential tools in the understanding of the paleoenvironmental evolution associated with redox cycles and biogeochemical characteristics of the epicontinental seawater at the late Ediacaran and early Cambrian times, and explores how they may have affected the benthic life in this connected/isolated foreland marine basin. This occurrs through the analysis of previously chemostratigraphic data and the acquisition of new data, together with petrographic and geochemical analysis of carbonates from the basal Bambuí Group.

A number of criteria have been established for unraveling the effects of diagenesis on altering original marine Sr isotope signatures. These include petrography, stratigraphic assessment, trace-element measurements, and other isotopic measurements (i.e., Jacobsen and Kaufman 1999; Banner, 2004, Halverson et al. 2007). During diagenesis and post-depositional alteration, carbonate minerals of some specific stratigraphic levels of the Bambuí Group incorporate more Mn and Fe, accompanied by a decrease in Sr concentrations, as well as an increase in $^{87}Sr/^{86}Sr$ ratios, indicated by positive correlations between these geochemical parameters. As discussed in the Chapter 5, the identification of stratigraphic levels of carbonates with high Sr concentrations on the Bambuí Group can introduce a bias in the geochemical analysis of post-depositional processes. The increase in Sr mass fractions and Sr/Ca ratios are non-facies dependent feature, which indicate a paleoenvironmental change in the basin resulting in increased incorporation of Sr in the carbonate lattice (Caetano-Filho et al., 2019), and suggest that the difference in Sr mass fractions across the basal 2nd-order sequence of the Bambuí Group are environmentally driven, rather than a post-depositional artifact. Based on this, Guacaneme et al. (2021) carefully evaluated the primary $^{87}Sr/^{86}Sr$ ratios from each stratigraphic interval of the basal

Bambuí Group, and also followed suggestions from Paula-Santos et al. (2017) on the assessment of altered Sr-isotope signatures according to regional chemostratigraphy.

For the basal transgressive sequence (TST), the dominant very radiogenic $^{87}Sr/^{86}Sr$ ratios from 0.7090 to 0.7177 are associated with facies C1 that present white to beige dolomitic limestone layers that display intense recrystallization and vugs filled with sparry calcite, reaching $^{87}Sr/^{86}Sr$ ratios as high as 0.7134 in the Januária High (Januária and Santa Maria da Vitoria sections), and 0.7177 in the Sete Lagoas High (Arcos section). Moreover, altered signatures of marine $^{87}Sr/^{86}Sr$ ratios remain pervasive on samples represented by light grey calcimudstone, red bindstone and light bindstone related to facies C2, C3 and C4, respectively, with$^{87}Sr/^{86}Sr$ ratios up to 0.7134.

It is mentioned that $^{87}Sr/^{86}Sr$ ratios >0.7090 from the TST could record a mixing between less radiogenic seawater and radiogenic freshwater, which diminished as transgression progressed increasing the relative proportion of the geochemical marine signals. This is supported by flat rare earth element patterns that suggest a large input of freshwater/meltwater mixed to seawater during transgression, and is consistent with a post-glacial scenario for the TST (i.e., Shields, 2005; Liu et al., 2014; Kuchenbecker et al., 2016a; Wei et al., 2019; Paula-Santos et al., 2018, 2020). However, another explanation for $^{87}Sr/^{86}Sr$ ratios > 0.7090 could be an alteration by radiogenic fluids during meteoric and burial diagenesis as the cause of the high Sr-isotope values in the lowermost TST leading to secondary dolomitization (i. e., Caxito et al., 2018). This is coherent with petrographic observations that indicate replacement and recristallization as the main post-depositional processes in these diagenetic environments, leading to low temperature reactions by which radiogenic ^{87}Sr is added to the carbonates through dolomitic solutions, and coherent with field criteria such as mudcracks in the tidal flat carbonates of the Correntina region (Caxito et al., 2018).

In contrast, some carbonate samples from facies C2 at the Januária section and facies C3 display lower Sr ratios around 0.7076, which are associated to lower geochemical Mn/Sr, Fe/Sr and Mg/Ca ratios, as well as to aragonite pseudomorphs and higher Sr contents. Carbonate samples from SMV section also have marine $^{87}Sr/^{86}Sr$ ratios of 0.7086 coupled to lower elemental ratios (Guacaneme et al., 2021). These ratios between 0.7076 and 0.7086 are consistent with those reported by Paula-Santos et al.

(2017) for the basal carbonates and are considered as the most representative of seawater composition for the TST.

Strontium isotope ratios for the basal part of the regressive sequence (EHST) range from 0.7077 to 0.7088 and show a positive correlation with geochemical ratios of Rb/Sr, Mn/Sr, Fe/Sr and Mg/Ca, which would suggest a diagenetic trend towards the higher $^{87}Sr/^{86}Sr$ ratios (Guacaneme et al., 2021). However, it is noted that an upward decreasing trend of the ratios is observed in all studied sections, preceding the increase in the Sr/Ca at the LHST. If such recurrent feature basin-wide were to be a post-depositional feature it would require a diagenetic overprint of basinal scale that it is find unlikely due to the lack of petrographical evidence. Facies association from this interval display light bindstone, dark gray calcimudstone and dark-grey bindstone with microbial lamination, frequent intercalations of brown to green argillaceous laminae and nodular fabrics developed by differential mechanical compaction. Despite the fact that these facies present some clay layers, stylolites and radiating silica micronodules within a carbonate matrix, these structures are avoided in the microdrilling process, which confirms the reliability of the carbonate extraction method for the analysis of primary signals of marine $^{87}Sr/^{86}Sr$. Also, since this drop down in the Sr isotope ratios precedes a very well described major environmental change in the basin, is more reasonable that they are the record of a progressive change in seawater chemistry, rather than any diagenetic overprint.

For the upper part of the regressive sequence (LHST), the $^{87}Sr/^{86}Sr$ ratios vary between 0.7074 and 0.7131, and the dolomites from the Arcos section present a systematic correlation with Rb/Sr, Mn/Sr, Fe/Sr and Mg/Ca ratios, indicating post-depositional alteration of the more radiogenic isotope ratios, higher than 0.7085 (Guacaneme et al., 2021). The $^{87}Sr/^{86}Sr$ ratios range between 0.7074 and 0.7085, display no correlations with the elemental ratios, and are considered pristine and to record seawater chemistry. This is coherent with petrographic analysis that display fine-grained laminated peloidal calcimudstone from facies C7 with well-preserved horizontal planar-lamination and rudstones with micritic intraclasts from facies C8 presenting preserved depositional fabrics. Despite some diagenetic structures such as silica micro-nodules, stylolites, dissolution cavities and calcite cements are observed in these facies, the microdrilling extraction of carbonate in polished slabs erases or helps minimazing the

impact of these diagenetic structures on the isotopic signatures of marine Sr, suggesting that the extraction process is as fundamental as the petrographic and stratigraphic analysis of the carbonate samples. Also, these samples are Sr-rich carbonates and chemically, with very low Rb/Sr, Fe/Sr, Mn/Sr and Mg/Ca ratios, with high consistency between neighboring samples within each studied section.

Geochemical data from the upper 2nd-order sequence display $^{87}Sr/^{86}Sr$ ratios between 0.7074 and 0.7110, showing positive correlations with Rb/Sr, Mn/Sr, Fe/Sr and Mg/Ca ratios, mainly for samples of Santa Maria da Vitória section, indicating post-depositional alteration of the more radiogenic ratios. The high radiogenic values are related to white to beige intraclastic dolograinstone from facies C9 that show detrital grains, dissolution features such as vugular porosity, precipitation of phreatic calcite cement and rhombic dolomite cement, strong recrystalization and replacement of extraclastic detrital grain by calcite and dolomite. The identification of a series of diagenetic structures by means of detailed petrography allows to establish important dolomitization processes related to meteoric diagenesis and that also leads to define the sequence boundary and marks the beginning of a new marine transgression. However, a few carbonate samples with low ratios of Rb/Sr, Mn/Sr, Fe/Sr and Mg/Ca coupled with Sr contents higher than 700 µg/g exhibit $^{87}Sr/^{86}Sr$ radiogenic ratios between 0.7074 and 0.7085, which are considered records of the primary marine geochemistry during the deposition of the lowermost portion of the upper 2nd-order sequence.

The regional assessment of post-depositional alteration and diagenesis for each stratigraphic interval of the Bambuí Group demonstrates that fixed geochemical parameters to define “cut-off” values for these elements and even petrography may not be suitable screeners for detecting or deciding between alteration/preservation in carbonates given heterogeneous geochemical signatures that characterize each stage in the basin evolution. Instead of flexible ratios, detailed petrographic criteria and isotopic stratigraphic trends are more useful to assess the degree of preservation of carbonates in order to provide a representative Sr isotope chemostratigraphy, and it is always recommended to use the carbonate microdrilling technique or LA-ICPMS (i. e., Caxito et al., 2021), as a guarantee of chemical and isotopic signatures of seawater.

By determining the marine Sr isotope composition of carbonates from the basal Bambuí Group, it is possible to conclude that variations of $^{87}Sr/^{86}Sr$ ratios respond to the sedimentary evolution of a foreland basin system developed in the West Gondwana assembly, changing from a connected seaway to a restricted sea during the late Ediacaran and early Cambrian. A major decrease in the Sr isotope ratios from 0.7086 to 0.7076 is coupled to the sequence stratigraphic framework, preceding the positive carbon isotope excursion observed upwards and extending through the middle to upper Bambuí Sequence. These large variations were not caused by worldwide uniform changes in isotopic compositions of the global Ediacaran–Cambrian seawater reservoir. Instead, these anomalies may have resulted from marine isolation and paleogeographic changes induced by the evolving marginal orogenic systems. Changes in the chemical weathering regime within surrounding uplifted source areas and variations on the balance between accommodation and carbonate production/sedimentary supply might have been associated with increasingly inputs of non-radiogenic $^{87}Sr/^{86}Sr$ by continental waters such as riverine freshwater and groundwater, limited marine dissolution of carbonates, which constitute strong local controls over the Sr isotope compositions of restricted seas. This culminated with a significant change in seawater chemistry and Sr budget and may have contributed to cause large $^{87}Sr/^{86}Sr$ variations coupled to the studied 2nd-order cycles.

Also, temporal changes in the sedimentary trace-metal patterns of the basal 2nd-order sequence provide evidence for the chemical evolution of basinal deep-waters, whose conditions changed progressively from suboxic-anoxic to anoxic-euxinic. Changes in seawater chemistry are associated with redox variation, Mn-particulate shuttle, and hydrographic factors. Based on the chemical evolution of seawater, it is envisaged a basin with episodic connection with open ocean controlled by the sea level variation. Connected periods were detected mainly across the TST/EHST transition of the basal 2nd order sequence and partially at the TST of the overlying 2nd order sequence, in which renewal of oxygenated waters as well as renewal of Mo from upwelling setting would have been increased. On the other hand, marine restriction at the apex of sea-level fall between the two 2nd-order sequences results in extremely anoxic-euxinic conditions with long deepwater residence times for trace metals and chemical evolution of deep watermass in response to tectonoeustasy. Under sulfidic conditions, trace metals scarcity and

micronutrient fixation limitation would have hindered N bioavailability (Fraga-Ferreira et al., 2021), preventing the evolution of early metazoans in the Bambuí paleomarine system during the late Ediacaran and early Cambrian.

8 REFERENCES

Ader, M., Sansjofre, P., Halverson, G. P., Busigny, V., Trindade, R. I. F., Kunzmann, M., Nogueira, A. C.R. 2014. Ocean redox structure across the Late Neoproterozoic oxygenation event: a nitrogen isotope perspective. Earth Planetary Science Letters 396, 1–13.

Algeo, T. J. & Maynard, J. B. 2004. Trace–element behavior and redox facies in coreshales of Upper Pennsylvanian Kansas-type cyclothems. Chemical Geology 206(3–4), 289–318.

Algeo, T. J. & Morford, J., Cruse, A., 2012. New applications of trace metals as proxiesin marine paleoenvironments. Chemical Geology 306–307, 160–164.

Algeo, T.J. & Rowe, H. 2012. Paleoceanographic applications of trace-metal concentration data. Chemical Geology 324–325, 6–18.

Algeo, T. J. & Tribovillard, N., 2009. Environmental analysis of paleoceanographic systems based on molybdenum–uranium covariation. Chemical Geology 268 (3–4), 211–225.

Alkmim, F. F. & Marshak, S., 1998. Transamazonian Orogeny in the southern São Francisco Cráton region in Minas Gerais, Brazil: evidence for Paleoproterozoic collision and collapse in the Quadrilátero Ferrífero. Precambrian Research 90, 29–58.

Alkmim, F. F., Chemale Jr., F., Endo, I., 1996. A deformação das coberturas proterozoicas do Craton do São Francisco e o seu significado tectônico. Revista da Escola de Minas 49, 22–38.

Alkmim, F. F. & Martins-Neto, M.A., 2001. A bacia intracratônica do São Francisco: Arcabouço estrutural e cenários evolutivos. In: Pinto, C.P., Martins-Neto, M. (Eds.). A Bacia do São Francisco geologia e recursos naturais. SBG, Belo Horizonte, pp. 9–30.

Alkmin, F. F. & Martins-Neto, M.A., 2012. Proterozoic first-order sedimentary sequences of the São Francisco craton, eastern Brazil. Marine and Petroleum Geology, 33:127-139.

Alkmim, F. F., Marshak, S., Fonseca, M.A., 2001. Assembling West Gondwana in the Neoproterozoic: clues from the São Francisco craton region, Brazil. Geology 29, 319–322.

Almeida, F.F.M., 1977. O Cráton do São Francisco. Revista Brasileira de Geociências, 7:349–364.

Almeida, F. F.M., Hasui, Y., Brito Neves, B.B., 1976. The Upper Precambrian of South America. Boletim do Instituto de Geociências, Universidade de São Paulo, 7: 45–80

Almeida, F. F.M., Brito Neves, B.B., Carneiro, C.D.R., 2000. Origin and evolution of the South American Platform. Earth-Science Reviews 50, 77–111.

Alvarenga C. J. S., Dardenne M. A., Vieira L. C., Martinho C. T., Guimarães E. M., Santos R. V., Santana R. O. 2012. Estratigrafia da borda ocidental da Bacia do São Francisco. Boletim de Geociências da Petrobras 20, 145–164.

Alvarenga, C. J. S., Santos, R.V., Vieira, L.C., Lima, B.A.F., Mancini, L.H., 2014. Meso–Neoproterozoic isotope stratigraphy on carbonates platforms in the Brasília Belt of Brazil. Precambrian Research 251, 164–180.

Asmerom, Y., Jacobsen, S., Knoll, A.H., Butterfield, N.J., Swett, K., 1991. Strontium isotope variations of Neoproterozoic seawater: implications for crustal evolution. Geochimica et Cosmochimica Acta, 55, 2883-2894.

Azmy, K., Kaufman, A.J., Misi, A., Oliveira, T.F., 2006. Isotope stratigraphy of the Lapa Formation, São Francisco Basin, Brazil: implications for Late Neoproterozoic glacial events in South America. Precambrian Research, 149:231–248.

Azmy, K., Kendall, B., Creaser, R.A., Heaman, L., Oliveira, T.F., 2008. Global correlation of the Vazante Group, São Francisco Basin, Brazil: Re–Os and U–Pb radiometric age constraints. Precambrian Research, 164:160–172.

Babinski, M., Van Schmus, W.R., Chemale, F. 1999. Pb–Pb dating and Pb isotope geochemistry of Neoproterozoic carbonate rocks from the São Francisco basin, Brazil: implications for the mobility of Pb isotopes during tectonism and metamorphism. Chemical Geology, 160:175–199.

Babinski, M., Trindade, R.I.F., Alvarenga, C.J.S., Boggiani, P.C., Liu, D., Santos, R.V., Brito Neves, B.B., 2006. Chronology of Neoproterozoic ice ages in central Brazil. In: South American Symposium on Isotope Geology, 6, Punta del Este, Uruguay.

Babinski, M., Vieira, L.C., Trindade, R.I.F., 2007. Direct dating of Sete Lagoas cap carbonate (Bambuí Group, Brazil) and implications for the Neoproterozoic glacial events. Terra Nova, 19:401-406.

Babinski, M., Pedrosa-Soares, A.C., Trindade, R.I.F., Martins, M., Noce, C.M., Liu, D., 2012. Neoproterozoic glacial deposits from the Araçuaí orogen, Brazil: Age, provenance and correlations with the São Francisco craton and West Congo belt. Gondwana Research, 21:451-465.

Babinski, M. Paula-Santos, G.M., Freitas, B.T., Kuchenbecker, M., Pedrosa-Soares, A.C., 2013. Geocronologia U-Pb do embasamento do Grupo Bambuí na região de Sete Lagoas, MG: Implicação para a proveniência sedimentar da Bacia do São Francisco. In: Simpósio de Geologia do Sudeste, Juiz de Fora, MG. Abstracts, CD-ROM.

Babinski, M., Paula–Santos, G. M. Guacaneme, C., Leme, J. M., Amorim, K., Trindade, R., Caetano–Filho. 2018. Only getting younger: New geochronological constraints on the Bambuí Group, Brazil. In South American Symposium on Isotope Geology – SSAGI, Cochabamba, Bolivia, Abstracts.

Banner, J.L. & Hanson, G.N., 1990. Calculation of simultaneous isotopic and trace element variations during water-rock interaction with application to carbonate diagenesis. Geochimica et Cosmochimica Acta, 54: 3123–3137.

Barbosa, O., Braun, O. P. G., Dyer. R.C., Cunha, C. A. B. R. 1970. Geologia do Triângulo Mineiro, Boletim 136. DNPM/DFPM, Rio de Janeiro.

Baptista M.C. 2004. Estratigrafia e evolução geológica da região de Lagoa Formosa (MG). Master Dissertation, Universidade Federal de Minas Gerais (UFMG).

Bau, M. & Dulski, P., 1996. Distribution of yttrium and rare–earth elements in the Penge and Kuruman Iron-Formations, Transvaal Supergroup, South Africa. Precambrian Research, 79:37–55.

Bau, M., Koschinsky, A., Dulski, P., Hein, J.R., 1996. Comparison of the partitioning behaviours of yttrium, rare earth elements, and titanium between hydrogenetic marine

ferromanganese crusts and seawater. Geochimica et Cosmochimica Acta, 60:1709–1725.

Basu A. R., Jacobsen S. B., Poreda R. J., Dowling C. B., Aggarwal P. K. 2001. Large groundwater strontium flux to the oceans from the Bengal Basin and the marine strontium isotope record. Science 293, 1470–1473.

Beck, A. J., Charette, M. A., Cochran, J. K., Gonneea, M. E. & Peucker–Ehrenbrink, B. 2013. Dissolved strontium in the subterranean estuary – Implications for the marine strontium isotope budget. Geochimica et Cosmochimica Acta 117, 33–52.

Bekker, A., Holland, H. D., Wang, P.-L., Rumble III, D., Stein, H. J., Hannah, J. L., Coetzee, L. L. & Beukes, N. J. 2004. Dating the rise of atmospheric oxygen. Nature 427, 117–120.

Boggs, S. 1992. Petrology of Sedimentary Rocks. McMillan Publish Company, New York, 707 p.

Bolhar, R., Van Kranendonk, M.J., 2007. A non-marine depositional setting for the northern Fortescue Group, Pilbara Craton, inferred from trace element geochemistry of stromatolitic carbonates. Precambrian Research 155, 229–250.

Brand, U., Veizer, J., 1980. Chemical diagenesis of a multicomponent carbonate system:1. Trace elements. J. Sediment. Petrol. 50, 1219–1236.

Brito Neves, B.B.D., da Costa Campos Neto, M., Fuck, R.A., 1999. From Rodinia to western Gondwana; an approach to the Brasiliano-Pan African cycle and orogenic collage. Episodes 22, 155–166.

Brumsack, H.-J., 2006. The trace metal content of recent organic carbon-rich sediments: implications for Cretaceous black shale formation. Palaeogeography,Palaeoclimatology, Palaeoecology 232 (2–4), 344–361.

Buick, R., Des Marais, D.J., Knoll, A.H., 1995. Stable isotope compositions from the Mesoproterozoic Bangemall Group, northwestern Australia. Chemical Geology, 123:153-171.

Buchwaldt, R., Toulkeridis, T., Babinski, M., Santos, R., Noce, C.M., Martins-Neto, M.A., Hercos, C.M. 1999. Age determination and age-related provenance analysis of the

Proterozoic glaciation event in central-eastern Brazil. *In*: South American Symposium on Isotope Geology, 2, Cordoba, Argentina, *Actas*, p. 387-390.

Calvert, S.E., Pedersen, T.F., 1993. Geochemistry of recent oxic and anoxic sediments: implications for the geological record. Marine Geology, 113, 67–88.

Calvert, S.E., Pedersen, T.F., 1996. Sedimentary geochemistry of manganese: implications for the environment of formation of manganiferous black shales. Economic Geology. 91, 36–47.

Campbell, I. H. & Squire, R. J. 2010. The mountains that triggered the Late Neoproterozoic increase in oxygen: the second great oxidation event. Geochim. Cosmochim. Acta, 74, 4187–4206.

Canfield, D.E., Poulton, S.W., Narbonne, G.M., 2007. Late–Neoproterozoic deep–ocean oxygenation and the rise of animal life. Science 315 (5808), 92–95.

Canfield, D.E., Poulton, S.W., Knoll, A.H., Narbonne, G.M., Ross, G., Goldberg, T., Strauss, H. (2008) Ferruginous conditions dominated later Neoproterozoic deep-water chemistry. Science, 321, 949–952.

Castro, P.T.A. & Dardenne, M.A., 2000. The sedimentology, stratigraphy and tectonic context of the São Francisco Supergroup at the southwestern domain of the São Francisco craton, Brazil. Revista Brasileira de Geociências, 30: 439-441.

Castro, M.P., Queiroga, G., Martins, M., Alkmim, F., Pedrosa-Soares, A.C., Dussin, I., Souza, M.E., 2019. An Early Tonian rifting event affecting the São Francisco-Congo paleocontinent recorded by the Lower Macaúbas Group, Araçuaí Orogen, SE Brazil. Precambrian Research 331, 105351

Castro, M.P., Queiroga, G.N., Martins, M., Pedrosa-Soares, A.C., Dias, L., Lana, C., Babinski, M., Alkmim, A.R., Silva, M.A., 2020. Provenance shift through time in superposed basins: From Early Cryogenian glaciomarine to Late Ediacaran orogenic sedimentations (Araçuaí Orogen, SE Brazil) Gondwana Research 87, 41–66

Caxito, F. A., Dantas E.L., Stevenson, R., Uhlein, A. 2014. Detrital zircon (U-Pb) and Sm-Nd isotope studies of the provenance and tectonic setting of basins related to collisional orogens: The case of the Rio Preto fold belt on the northwest São Francisco Craton margin, NE Brazil. Gondwana Research 26: 741–754.

Caxito, F.A., Uhlein, A., Dantas, E., Stevenson, R., Egydio-Silva, M., Salgado, S.S., 2017. The Rio Preto and Riacho do Pontal Belts. In: Heilbron, M., Cordani, U.G., Alkmim, F.F. (Eds.), São Francisco Craton, Eastern Brazil, Regional Geology Reviews. Springer, Switzerland, pp. 117–143.

Caxito, F.A., Halverson, G.P., Uhlein, A., Stevensson, R., Dias, T.G., Uhlein, G.J., 2012. Marinoan glaciation in east Central Brazil. Precambrian Research, 200-203:38-58.

Caxito, F.A., Frei, R., Uhlein, G.J., Dias, T.G., Árting, T.B., Uhlein, A., 2018. Multiproxy geochemical and isotope stratigraphy records of a neoproterozoic oxygenation event in the Ediacaran Sete Lagoas cap carbonate, Bambuí Group, Brazil. Chemical Geololy, 481, 119–132.

Chaillou, G., Anschutz, P., Lavaux, G., Schäfer, J., Blanc, G. (2002). The distribution of Mo, U, and Cd in relation to major redox species in muddy sediments of the Bayof Biscay. Marine Chemistry 80, 41–59.

Chang, H. K., Miranda, F.P., Magalhães, L., Alkmim, F. F. 1988. Considerações sobre a evolução tectônica da bacia do São Francisco. In: Proceedings of the 35th Congresso Brasileiro de Geologia, Sociedade Brasileira de Geologia (SBG), Belém, vol 5, pp 2076–2090.

Chaves, M.L.S.C., Silva, M.C.R., Scholz, R., Babinski, M., 2013. Grenvillian age magmatism in the Southern Espinhaço Range (Minas Gerais): evidence from U-Pb zircon ages. Brazilian Journal of Geology, 43(3): 477-486.

Chakrabarti1, R., Mondal, S., Shankar, S., Sree, J., Sengupta, D., 2018. Submarine groundwater discharge derived strontium from the Bengal Basin traced in Bay of Bengal water samples Nature8, 43–83.

Chemale, F., Alkmim, F.F., Endo, I., 1993. Late Proterozoic tectonism in the interior of the São Francisco craton. In: Findlay, R.H., et al. (Eds.), Gondwana Eight- Assembly, Evolution and Dispersal. Balkema, pp. 29–42.

Chemale Jr. F., Dussin I. A., Alkmim F. F., Martins M. S., Queiroga G., Armstrong, R., Santos, M. N. 2012. Unravelling a Proterozoic basin history through detrital zircon geochronology: the case of the Espinhaço Supergroup, Minas Gerais, Brazil. Gondwana Research 22, 200–206.

Cherniak, D.J. & Watson, E.B., 2000. Pb diffusion in zircon. Chemical Geology, 172: 5-24.

Chiavegatto, J.R.S. 1992. Análise estratigráfica das sequências tempestíticas da Formação Três Marias (Proterozoico Superior), na porção meridional da Bacia do São Francisco. Dissertation, Universidade Federal de Ouro Preto (UFOP).

Cloud, P., Dardenne, M. A., 1973. Proterozoic age of the Bambuí Group in Brazil. Geological Society of America bulletin 84 (5), 1673–1676.

Coelho, J.C.C., Martins-Neto, M.A., Marinho, M., 2008. Estilos estruturais e evolução tectônica da porção mineira da bacia proterozoica do São Francisco. Revista Brasileira de Geociências, 38:149-165.

Costa, M.T. & Branco, J.R., 1961. Roteiro para a excursão Belo Horizonte-Brasília. In Congresso Brasileiro de Geologia 14, UFMG, Inst. Pesq. Radioat., Publ. 15, 25p., Belo Horizonte.

Danderfer, A., De Waele, B., Pedreira, A. J., Nalini, H. A. 2009. New geochronological constraints on the geological evolution of Espinhaço basin within the São Francisco Craton – Brazil. Precambrian Research, 170: 116–128.

Dardenne, M.A., 1978. Síntese sobre a estratigrafia do Grupo Bambuí no Brasil Central. In: Congresso Brasileiro de Geologia, 30, Recife, Anais, SBG, v. 2, p. 597-610.

Dardenne, M. A. 1981. Os grupos Paranoá e Bambuí na Faixa Dobrada Brasília. In: Proceedings of the 1st Simpósio sobre o Cráton do São Francisco, Sociedade Brasileira de Geologia (SBG) - Núcleo BA, Salvador, pp 140–157.

Dardenne, M.A., 2000. The Brasília fold belt. In: Cordani, U.G., Milani, E.J., Thomaz Filho, A., Campos, D.A. (Eds.), Tectonic Evolution of South America. 31st International Geological Congress, Rio de Janeiro, pp. 231- 263.

Dardenne, M.A., Pimentel, M.M., Alvarenga, C.J.S., 2003. Provenance of conglomerates of the Bambuí, Jequitaí, Vazante and Ibiá groups: Implications for the evolution of The Brasília Belt. In: Boletim de Resumos of the 9th Simpósio Nacional de Estudos Tectônicos, pp 47–49.

Derry, L.A., Kaufman, A.J., Jacobsen, S.B., 1992. Sedimentary cycling and environmental changes in the Late Proterozoic: Evidence from stable and radiogenic isotopes. Geochimica et Cosmochimica Acta, 56:1317-1329.

Derry, L.A., 2010. A burial diagenesis origin for the Ediacaran Shuram-Wonoka carbon isotope anomaly. Earth and Planetary Science Letters, 294:152-162.

Dias, P. H. A., Noce, C. M., Pedrosa–Soares, A. C., Seer, H. J., Dussin. I. A., Valeriano, C., Kuchenbecker, M. 2011. O Grupo Ibiá (Faixa Brasília Meridional): evidências isotópicas Sm–Nd e U–Pb de bacia colisional do tipo flysch. Geonomos 19(2): 90–99.

Dickson, J.A.D. 1990. Carbonate mineralogy and geochemistry. Carbonate Sedimentology, Eds. Tucker, M. & Wright, P. Blackwell Science

Doebert, A.C., Johnson, C.M., Carroll, A.R., Beard, B.L., Pietras, J.T., Carson, M.R., Norsted, B., Throckmorton, L.A., 2014. Controls on Sr isotopic evolution in lacustrine systems: Eocene Green River Formation, Wyoming. Chemical Geology 380, 172–189.

Dowling C. B., Poreda R. J. and Basu A. R. (2003) The groundwater geochemistry of the Bengal Basin: Weathering, chemsorption, and trace metal flux to the oceans. Geochimica et Cosmochimica Acta 67(12), 2117–2136.

Dunham, R.J., 1962. Classification of carbonate rocks according to depositional texture. In: Ham W.E (Ed.), Classification of Carbonate Rocks. American Association of Petroleum Geology, Tulsa, p. 108–121.

Eyles, N. & Januszczak, N. 2004. `Zipper–rift´: a tectonic model for Neoproterozoic glaciations during the breakup of Rodinia after 750 Ma. Earth-Science Reviews, 65:1–73.

Faure, G. & Mensing, T.M. 2005. Isotopes: Principles and Applications. 3rd edition, New Jersey, John Wiley & Sons, 897 p.

Fike, D.A., Grotzinger, J.P., Pratt, L.M., Summons, R.E., 2006. Oxidation of the Ediacaran Ocean. Nature 444 (7120), 744–747.

Fike, D.A., Finke, N., Zha, J., Blake, G., Hoehler, T.M., Orphan, V.J., 2009. The effect of sulfate concentration on (sub) millimeter–scale sulfide $\delta^{34}S$ in hypersaline cyanobacterial mats over the diurnal cycle. Geochimica et Cosmochimica Acta 73, 6187–6204.

Fölling, P.G. & Frimmel, H.E., 2002. Chemostratigraphic correlation of carbonate successions in the Gariep and Saldania Belts, Namibia and South Africa. Basin Research, 14:69-88.

Fraga-Ferreira P.L., Ader, M., Caetano-Filho, S., Sansjofre, P., Paula-Santos, G.M., Babinski, M., Guacaneme, C., Bedoya-Rueda, C., Rojas, V., Reis, H.L.S., Kuchenbecker, M., and Trindade, R.I.F., 2021. The Nitrogen Cycle in an Epeiric Sea in the Core of Gondwana Supercontinent: A Study on the Ediacaran-Cambrian Bambuí Group, East-central Brazil. Frontiers in Earth Science 9:692895. doi: 10.3389/feart.2021.692895

Fragoso, D.G.C., 2011. Geologia da região de Presidente Olegário e evolução tectono-sedimentar do Grupo Areado, Eocretácio da Bacia Sanfranciscana, Minas Gerais. Master Dissertation, Universidade Federal de Minas Gerais (UFMG).

Friedrich, O., Norris, R.D., Erbacher, J., 2012. Evolution of middle to Late Cretaceous oceans—a 55 m.y. record of Earth's temperature and carbon cycle. Geology 40, 107–110.

Frei, R., Gaucher, C., Døssing, L.N., Sial, A.N., 2011. Chromium isotopes in carbonates — a tracer for climate change and for reconstructing the redox state of ancient seawater. Earth and Planetary Science Letters 236, 28–40.

Frimmel, H.E., Tack, L., Basei, M.S., Nutman, A.P., 2006. Provenance and chemostratigraphy of the Neoproterozoic West Congolian Group in the Democratic Republic of Congo. Journal of African Earth Sciences, 46:221–239.

Frimmel, H.E., 2009. Trace element distribution in Neoproterozoic carbonates as palaeoenvironmental indicator. Chemical Geology, 258:338-353.

Frimmel, H.E., 2010. On the reliability of stable carbon isotopes for Neoproterozoic chemostratigraphic correlation. Precambrian Research, 182(4):239-253.

García, M.G., Lecomte, K.L., Pasquini, A.I., Formica, S.M., Depetris, P.J., 2007. Sources of dissolved REE in mountainous streams draining granitic rocks, Sierras Pampeanas (Córdoba, Argentina). Geochimica et Cosmochimica Acta 71, 5355–5368.

Gaucher, C., Sial, A.N., Ferreira, V.P., Pimentel, T.M., Chiglino, M., Sprechmann, P., 2007. Chemostratigraphy of the Cerro Victoria Formation (Lower Cambrian, Uruguay): evidence for progressive climate stabilization across the Precambrian–Cambrian boundary. Chemical Geololy 237, 28–46.

Goldstein, S.J. & Jacobsen, S.B., 1988. Rare-earth elements in river waters. Earth and Planetary Science Letters 89, 35–47.

Grabau, A. W., 1913. Principles of stratigraphy. New York e Dover: v. 2, p. 582-1185 (Re-impression 1960).

Grotzinger, J. P.,Watters, W. A., Knoll, A. H. 2000. Calcified metazoans in thrombolite–stromatolite reefs of the terminal Proterozoic Nama Group, Namibia. Paleobiology **26**, 334–59.

Guacaneme, C., Babinski, M., Paula–Santos, G.M.D., Pedrosa–Soares, A.C., 2017. C, O, and Sr isotopic variations in Neoproterozoic–Cambrian carbonate rocks from Sete Lagoas Formation (Bambuí Group), in the Southern São Francisco Basin, Brazil. Brazilian Journal of Geology, 47, 521–543.

Guacaneme, C., Babinski, M., Paula–Santos, G. M., Caetano–Filho, S. Bedoya–Rueda, C., Trindade, R. I. F., 2018. On the realibility of Sr isotope chemostratigraphy of late Ediacaran carbonates from the Bambuí Group. In: Goldschmidt conference, Boston, MA, Abstracts

Guadagnin, F. & Chemale, F., 2015. Detrital zircon record of the Paleoproterozoic to Mesoproterozoic cratonic basins in the São Francisco Craton. Journal of South American Earth Sciences 60, 104-116.

Halverson, G.P., Hoffman, P.F., Schrag, D.P., Maloof, A.C., Rice, A.H., 2005. Toward a Neoproterozoic composite carbon-isotope record. Geological Society of American Bulletin, 117: 1181-1207.

Halverson, G.P., Dudás, F.O., Maloof, A.C., Bowring, S.A., 2007. Evolution of the $^{87}Sr/^{86}Sr$ composition of Neoproterozoic seawater. Palaeogeography, Palaeoclimatology, Palaeoecology, 256 (3-4): 103-129.

Halverson, G.P., Wade, B.P., Hurtgen, M.T., Barovich, K.M., 2010. Neoproterozoic chemostratigraphy. Precambrian Research, 182:337-350.

Harley, S.L. & Kelly, N.M., 2007. Zircon tiny but timely. Elements, Vol. 3, pp. 13 -18.

Hercos CM (2008) Arcabouço estrutural da Bacia do São Francisco nos arredores da Serra da Água Fria e da Onça, porção centro-norte do estado de Minas Gerais. Dissertation, Universidade Federal de Ouro Preto (UFOP).

Hoffman, P.F., Kaufman, A.J., Halverson, G.P., Schrag, D.P. 1998. A Neoproterozoic Snowball Earth. Science, 281: 1342-1346.

Hoffman, P.F. & Schrag, D.P., 2002. The Snowball Earth hypothesis: testing the limits of global change. Terra Nova, 14:129-155.

Holland, H.D., 2006. The oxygenation of the atmosphere and oceans. Philos. Trans. R. Soc. B-Biol. Sci. 361 (1470), 903–915.

Houghton, R.A., 2005. The contemporary carbon cycle. In: Schlesinger, W.H. (Ed.), Biogeochemistry. Treatise on Geochemistry, vol. 8. Elsevier–Pergamon, Oxford, p. 473–513.

Iglesias, M. & Uhlein, A., 2009. Estratigrafia do Grupo Bambuí e coberturas fanerozoicas no vale do rio São Francisco, norte de Minas Gerais. Revista Brasileira de Geociências, 39 (2):256-266.

Isotta, C.A.L., Rocha-Campos, A.C., Yoshida, R., 1969. Striated pavement of the Upper Precambrian glaciation in Brazil. Nature, 222:466–468.

Iyer, S.S., Babinski, M., Krouse, H.L., Chemale, F., 1995. Highly ^{13}C-enriched carbonate and organic matter in the Neoproterozoic sediments of the Bambuí Group, Brazil. Precambrian Research, 73: 271-282.

Jacobsen, S.B. & Kaufman, A.J., 1999. The Sr, C and O isotopic evolution of Neoproterozoic seawater. Chemical Geology, 161:37-57.

Jones, C.E. & Jenkyns, H.C., 2001. Seawater strontium isotopes, oceanic anoxic events, and seafloor hydrothermal activity in the Jurassic and Cretaceous. American Journal of Science, 301:112-149.

Kah L. C. (2000) Depositional d18O signatures in Proterozoic dolostones: constraints on seawater chemistry and early diagenesis. Spec. Publ. SEPM 67, 345–360.

Kamber, B.S., Greig, A., Collerson, K.D., 2005. A new estimate for the composition of weathered young upper continental crust from alluvial sediments, Queensland, Australia. Geochimica et Cosmochimica Acta, 69:1041-1058.

Karfunkel, J. & Hoppe, A.1988. Late Proterozoic Glaciation in Central-Eastern Brazil: synthesis and model. Paleogeography, Paleoclimatology, Paleoecology, 65: 1–21.

Kaufman, A.J., Hayes, J.M., Knoll, A.H., Germs, G.J.B., 1991. Isotopic composition of carbonates and organic carbon from upper Proterozoic successions in Namibia:

stratigraphic variation and the effects of diagenesis and metamorphism. Precambrian Research, 49: 301-327.

Kaufman, A.J., Jacobsen, S.B., Knoll, A.H., 1993. The Vendian record of Sr and C isotopic variations in seawater: Implications for tectonics and paleoclimate. Earth Planetary Science Letters, 120:409-430.

Kaufman, A.J. & Knoll, A.H., 1995. Neoproterozoic variations in the C–isotopic composition of seawater: stratigraphic and biogeochemical implications. Precambrian Research, 73:27-49.

Kaufman, A.J., Knoll, A.H., Narbonne, G.M., 1997. Isotopes, ice ages, and terminal Proterozoic Earth history. National Academy Sciences Proceedings, 94:600-605.

Kaufman, A.J., Sial, A.N., Frimmel, H.E., Misi, A., 2009. Neoproterozoic to Cambrian Palaeoclimatic events in Southwestern Gondwana. In: Gaucher, C., Sial, A.N., Halverson, G.P., Frimmel, H. (Eds.), Neoproterozoic-Cambrian Tectonics, Global Change and Evolution: a focus on southwestern Gondwana. Developments in Precambrian Geology. vol. 16. Elsevier, Amsterdam, pp. 369–388.

Kennedy, M.J., 1996. Stratigraphy, sedimentology, and isotope geochemistry of Australian Neoproterozoic postglacial cap dolostones: deglaciation, $\delta^{13}C$ excursions, and carbonate precipitation. Journal of Sedimentology Research, 66:1050-1064.

Kirschvink, J.L., 1992. Late Proterozoic low latitude glaciations: the snowball Earth. In: Schopf J.W. & Klein C, (eds.) The Proterozoic Biosphere: A Multidisciplinary Study. Cambridge, Cambridge University Press, p. 51-52.

Knoll, A.H. & Walter, M.R., 1992. Latest Proterozoic stratigraphy and Earth history, Nature, 356:673-678.

Knoll, A.H., Walter, M.R., Narbonne, G.M. and Christie- Blick, N. 2006a. The Ediacaran Period: a new addition to the geologic time scale. Lethaia, 39, 13–30.

Kryc, K.A., Murray, R.W., Murray, D.W. 2003. Al–to–oxide and Ti–to–organic linkages in biogenic sediment: relationships to paleo–export production and bulk Al/Ti. Earth and Planetary Science Letters 211, 125–141.

Kuchenbecker, M., 2011. Quimioestratigrafia e proveniência sedimentar da porção basal do Grupo Bambuí em Arcos (MG) (Msc thesis) Universidade Federal de Minas Gerais, Belo Horizonte, p. 91.

Kuchenbecker, M., Babinski, M., Pedrosa–Soares, A. C., Costa, R. D., Lopes–Silva. L., Pimenta, F. 2013. Proveniência e análise sedimentar da porção basal do Grupo Bambuí em Arcos (MG). Geologia USP 13(4): 49–61.

Kuchenbecker, M., Reis, H.L.S., Silva, L.C. da, Costa, R.D. da, Fragoso, D.G.C., Knauer, L.G., Pedrosa-Soares, A.C., Dussin, I. 2014. Age constraints for deposition and sedimentary provenance of the Espinhaço Supergroup and Bambuí Group in eastern São Francisco craton. Geonomos 23(2), 14–28.

Kuznetsov, A.B., Gorokhov, I.M., Semikhatov, M.A., Melnikov, N.N. and Kozlov, V.I., 1997. Strontium isotopic composition from the Inzer Formation limestones, the Upper Riphean type section in southern Urals. Trans. Russian Academy of Science, Earth Sciences Sections, 353, 319–324.

Kuznetsov, A.B., Ovchinnikova, G.V., Gorokhov, I.M., Letnikova, E.F., Kaurova, O.K., Konstantinova, G.V., 2013. Age constraints on the Neoproterozoic Baikal Group from combined Sr isotopes and Pb-Pb dating of carbonates from the Baikal type section, southeastern Siberia. Journal of Asian Earth Sciences 62, 51–66.

Lana, C., Alkmim, F.F., Armstrong, R., Scholz, R., Romano, R., Nalini Jr., H.A., 2013. The ancestry and magmatic evolution of Archean TTG rocks of the Quadrilátero Ferrífero province, southeast Brazil. Precambrian Research, 231:157-173.

Lawrence, M.G., Greig, A., Collerson, K.D., Kamber, B.S., 2006. Rare earth element and yttrium variability in South East Queensland waterways. Aquatic Geochemistry, 12:39-72.

Lima, S. A., Martins–Neto, M. A., Pedrosa–Soares, A.C., Cordani, U. G., Nutman, A. 2002. A Formação Salinas na área–tipo, NE de Minas Gerais: Uma proposta de revisão da estratigrafia da Faixa Araçuaí com base em evidências sedimentares, metamórficas e idades U–Pb SHRIMP. Revista Brasileira de Geociências 32(4): 491–500.

Ling, H.-F., Chen, X., Li, D., Wang, D., Shields-Zhou, G.A., Zhu, M., 2011. Cerium anomaly variations in Ediacaran–earliest Cambrian carbonates from the Yangtze Gorges area, South China: Implications for oxygenation of coeval shallow seawater. Precambrian Research, 10:10-16.

Lyons, T.W., Werne, J.P., Hollander, D.J., Murray, R.W., 2003. Contrasting sulfur geochemistry and Fe/Al and Mo/Al ratios across the last oxic-to-anoxic transitionin the Cariaco Basin, Venezuela. Chemical Geology 195 (1–4), 131–157.

Lyons T. W., Reinhard C. T., Planavsky, N. J. 2014. The rise of oxygen in Earth's early ocean and atmosphere. Nature 506, 307–315.

Lopes, T.C., 2012. O Supergrupo Espinhaço na Serra do Cabral, MinasGerais: contribuição ao estudo de proveniência sedimentar. Universidade Federal de Minas Gerais, Brazil. Master Dissertation. www.bibliotecadigital.ufmg.br

McLennan, S. M. (1989). Rare earth elements in sedimentary rocks: influence of provenance and sedimentary processes. Reviews in Mineralogy and Geochemistry 21, 169–200.

McManus, J., Berelson, W.M., Severmann, S., Poulson, R.L., Hammond, D.E., Klinkhammer, G.P., Holm, C., 2006. Molybdenum and uranium geochemistryin continental margin sediments: paleoproxy potential. Geochimica et Cosmochimica Acta 70 (18), 4643–4662.

Magalhães, P.M., 1989. Análise estrutural das rochas do Grupo Bambuí, na porção sudoeste da Bacia do São Francisco. Dissertação de Mestrado, UFOP, Ouro Preto, 100 p.

Marshak, S. & Alkmim, F.F., 1989. Proterozoic contraction/extension tectonics of the southern São Francisco region, Minas Gerais, Brazil. Tectonics, 8(3):555-571.

Martínez, I.M., 2007. Estratigrafia e tectônica do Grupo Bambuí no norte do estado de Minas Gerais. Dissertação de Mestrado, Instituto de Geociências, Universidade Federal de Minas Gerais, 147 p.

Martins–Neto, M. A. & Alkmim, F. F., 2001. Estratigrafia e evolução tectônica das bacias neoproterozoicas do paleocontinente São Francisco e suas margens: registro da quebra de Rodínia e colagem de Gondwana. In: Pinto C.P., Martins-Neto M.A. (Eds.), Bacia do São Francisco: Geologia e Recursos Naturais, SBG/MG, pp. 9–30.

Martins–Neto, M. A. & Hercos, C. M. 2002. Sedimentation and tectonic setting of Early Neoproterozoic glacial deposits in southern Brazil. Precambrian Sedimentary Environments: A Modern Approach to Ancient Depositional Systems, Altermann W, Corcoran PL (eds). Special Publication of the International Association of Sedimentologists, 33.

Martins–Neto, M.A., Pedrosa–Soares, A.C., Lima, S.A.A., 2001. Tectono–sedimentary evolution of sedimentary basis from Late Paleoproterozoic to Late Neoproterozoic in the São Francisco craton and Araçuaí fold belt, eastern Brazil. Sedimentary Geology, 142:343–370.

Martins-Neto, M.A., 2005. A Bacia do São Francisco: arcabouços estratigráfico e estrutural com base na integração de dados de superfície e subsuperfície. In Simpósio sobre o Cráton do São Francisco, III, Salvador/BA, 2005, Anais, pp. 283-286.

Martins-Neto, M.A. 2009. Sequence stratigraphic framework of Proterozoic successions in eastern Brazil. Marine and Petroleum Geology, 26:163-176.

McArthur, J.M., 1994. Recent trends in strontium isotope stratigraphy. Terra Nova 6, 331 358.

Melezhik, V.A., Gorokhov, I.M., Kuznetsov, A.B., Fallick, A.E., 2001. Chemostratigraphy of Neoproterozoic carbonates: implications for “blind dating”. Terra Nova, 13: 1-11.

Melezhik, V.A., Pokrovsky, B.G., Fallick, A.E., Kuznetsov, A.B., Bujakaite, M.I., 2009. Constrain on $^{87}Sr/^{86}Sr$ of Late Ediacaran seawater: insight from high-Sr Siberian limestones. Journal of the Geological Society, London 166, 183–191.

Misi, A. 2001. Estratigrafia isotópica das sequencias do Supergrupo São Francisco, coberturas neoproterozoicas do Cráton do São Francisco: idade e correlações. In: Pinto CP, Martins–Neto MA (eds). Bacia do São Francisco: Geologia e Recursos Naturais. Sociedade Brasileira de Geologia-Núcleo MG, Belo Horizonte.

Misi, A. & Veizer, J. 1998. Neoproterozoic carbonate sequences of the Una Group, Irecê Basin: chemostratigraphy, age and correlations. Precambrian Research 89: 87–100.

Misi, A., Kaufman, A.J., Veizer, J., Powis, K., Azmy, K., Boggiani, P.C., Gaucher, C., Teixeira J.B.G., Sanchez, A.L., Iyer, S.S.S., 2007. Chemostratigraphic correlation of Neoproterozoic successions in South America. Chemical Geology, 237: 143-167.

Narbonne, G.M., Xiao, S. and Shields, G.A. 2012. The Ediacaran Period. In: The Geologic Time Scale 2012 (Eds F.M. Gradstein, J.G. Ogg, M. Schmitz and G. Ogg), pp. 413–435. Elsevier, Amsterdam.

Nobre-Lopes J (1995) Faciologia e gênese dos carbonatos do Grupo Bambuí na região de Arcos, estado de Minas Gerais. Dissertation, Universidade de São Paulo (USP).

Noce, C.M., Zucchetti, M., Baltazar, O.F., Armstrong, R., Dantas, E.L., Renger, F.E., Lobato, L.M., 2005. Age of felsic volcanism and the role of ancient continental crust in the evolution of the Neoarchean Rio das Velhas greeenstone belt (Quadrilátero Ferrífero, Brazil): U–Pb zircon dating of volcaniclastic graywackes. Precambrian Research, 141:67–82.

Nothdurft, L.D., Webb, G.E., Kamber, B.S., 2004. Rare earth element geochemistry of Late Devonian reefal carbonates, Canning Basin Western Australia: confirmation of a seawater REE proxy in ancient limestones. Geochimica et Cosmochimica Acta 68, 263–283.

Och, L.M., Shields-Zhou, G.A., 2012. The Neoproterozoic oxygenation event: environmental perturbations and biogeochemical cycling. Earth Sciences Review 110 (1–4), 26–57.

Palmer M. R. & Edmond J. M. 1989. The strontium isotope budget of the modem ocean. Earth Planetary Science Letters. 92, 11–26.

Paula–Santos, G.M., Babinski, M., Kuchenbecker, M., Caetano–Filho, S., Trindade, R.I., Pedrosa–Soares, A.C., 2015. New evidence of an Ediacaran age for the Bambuí Group in southern São Francisco craton (eastern Brazil) from zircon U-Pb data and isotope chemostratigraphy. Gondwana Research 28, 702–720.

Paula–Santos, G.M., Caetano–Filho, S., Babinski, M., Trindade, R.I., Guacaneme, C., 2017. Tracking connection and restriction of West Gondwana São Francisco Basin through isotope chemostratigraphy. Gondwana Research 42, 280-305.

Paula–Santos, G.M., Caetano–Filho, S., Babinski, M., Enzweiler, J., 2018. Rare earth elements of carbonate rocks from the Bambuí Group, southern São Francisco Basin, Brazil, and their significance as paleoenvironmental proxies. Precambrian Research 305, 327-340.

Paula–Santos, G.M. & Babinski, M. 2018. Sedimentary provenance in the southern sector of the São Francisco Basin, SE Brazil. Brazilian Journal of Geology 48(1), 51−74.

Perrella Jr., P., Uhlein, A., Uhlein, G.J., Sial, A.N., Pedrosa-Soares, A.C., Lima, O.N.B., 2017. Facies analysis, sequence stratigraphy and chemostratigraphy of the Sete Lagoas Formation (Bambuí Group), northern Minas Gerais State, Brazil: evidence of a cap

carbonate deposited on the Januária basement high. Brazilian Journal of Geology 47, 59−77.

Pedrosa−Soares, A.C., Cordani, U.G., Nutman, A., 2000. Constraining the age of Neoproterozoic glaciation in Eastern Brazil: first U−Pb (SHRIMP) data for detrital zircons. Revista Brasileira de Geociências, 30:58-61.

Pedrosa−Soares A.C., Noce C.M., Alkmim F.F., Silva L.C., Babinski M., Cordani U.G., Castañeda C. 2007. Orógeno Araçuaí: síntese do conhecimento 30 anos após Almeida 1977. Geonomos 15(1): 1–16.

Pedrosa−Soares, A.C., Alkmim, F.F., Tack, L., Noce, C.M., Babinski, M., Silva, L.C., Martins−Neto, M., 2008. Similarities and differences between the Brazilian and African counterparts of the Neoproterozoic Araçuaí-West Congo Orogen. In: Pankhurst, J.R., Trouw, R.A.J., Brito-Neves, B.B., De Wit, M.J. (Eds.) West Gondwana: Pre-Cenozoic Correlations across the South Atlantic Region. Geological Society of London Special Publications, 294:153-172.

Pedrosa−Soares, A.C., Campos, C.P., Noce, C., Silva, L.C., Novo, T., Roncato, J., Medeiros, S., Castañeda, C., Queiroga, G., Dantas, E., Dussin, I., Alkmim, F.F., 2011. Late Neoproterozoic-Cambrian granitic magmatism in the Araçuaí orogen (Brazil), the Eastern Brazilian Pegmatite Province and related mineral resources. Geological Society of London Special Publications, 350:25-51.

Pedrosa−Soares, A.C., Babinski, M., Noce, C., Martins, M., Queiroga, G., Vilela, F., 2011a. The Neoproterozoic Macaúbas Group (Araçuaí orogen, SE Brazil). In: Arnaud, E., Halverson, G.P., Shields-Zhou, G. (Eds.), The Geological Record of Neoproterozoic Glaciations. Geological Society, London, Memoirs. 36, pp. 523–534.

Pereira, L., Dardenne, M.A., Rosière, C.A., Pedrosa-Soares, A.C., 1994. Evolução geológica dos grupos Canastra e Ibiá na região entre Coromandel e Guarda-Mor, MG. Geonomos, 2:22–32.

Pimentel, M. M., Fuck, R. A., Botelho, N.F. 1999. Granites and the geodynamic history of the Neoproterozoic Brasilia belt, Central Brazil: A review. Lithos, 46 (3): 463−483.

Pimentel, M. M., Dardenne, M. A., Fuck, R. A., Viana, M. G., Junges, S.L., Fischel, D. P., Seer, H. J., Dantas, E. L. 2001. Nd isotopes and the provenance of detrital sediments of the Neoproterozoic Brasília Belt, central Brazil. Journal of South American Earth Sciences 14: 571–585.

Pimentel, M.M., Rodrigues, J.B., Della Giustina, M.E.S., Junges, S., Matteini, M., Armstrong, R., 2011. The tectonic evolution of the Neoproterozoic Brasília Belt, central Brazil, based on SHRIMP and LA-ICPMS U-Pb sedimentary provenance data: a review. Journal of South America Earth Sciences, 31:345–357.

Planavsky, N.J, Tarhan, L.G., Bellefroid, E.J. Evans, D.A.D., Reinhard C.T., Love G.D., Lyons, T.W., 2015. Late Proterozoic transitions in climate, oxygen, and tectonics, and the rise of complex life In: Earth-Life Transitions: Paleobiology in the Context of Earth System Evolution. The Paleontological Society Papers, Volume 21, P. David Polly, Jason J. Head, and David L. Fox (eds.). The Paleontological Society Short Course, October 31, 2015. The Paleontological Society.

Rahaman, W. & Singh, S. K. 2012. Sr and $^{87}Sr/^{86}Sr$ in estuaries of western India: Impact of submarine groundwater discharge. Geochimica et Cosmochimica Acta, 85, 275–288.

Reis, H. L. S., Alkmim, F. F., Silva, L. C. 2012. O Cinturão neoproterozoico de antepaís da Faixa Brasília, Bacia do São Francisco (Brasil) – Características e principais traços tectônicos. In: Proceedings of the 46th Congresso Brasileiro de Geologia, Sociedade Brasileira de Geologia (SBG), Santos.

Reis, H.L.S. & Suss, J.F., 2016. Mixed carbonate–siliciclastic sedimentation in forebulge grabens: an example from the Ediacaran Bambuí Group, São Francisco basin, Brazil. Sedimetary Geology, 339, 83–103.

Reis, H.L.S., Alkmim, F.F., Fonseca, R.C.S., Nascimento, T.C., Suss, J.F., Prevatti, L.D., 2017a. The São Francisco Basin. In: Heilbron, M., Cordani, U.G., Alkmim, F.F. (Eds.), São Francisco Craton, Eastern Brazil, Regional Geology Reviews. Springer, Switzerland, pp. 117–143.

Rocha–Campos, A C. & Hasui, Y., 1981. Tillites of the Macaúbas Group (Proterozoic) in central Minas Gerais and southern Bahia, Brazil. In: Hambrey, M. J., Harland, W. B. (Eds) Earth's pre-Pleistocene Glacial Record. Cambridge University Press, p. 933-939.

Rocha-Campos, A.C., Brito Neves, B.B., Babinski, M., Santos, P.R., Romano, A.W. 2011. Moema laminites: a newly recognized Neoproterozoic (?) glaciogenic unit São Francisco Basin, Brazil. In: Arnaud, E., Halverson, G. P. & Shields-Zhou, G. (eds) The Geological Record of Neoproterozoic Glaciations. Geological Society, London, Memoirs, 36, 535–540.

Ribeiro, J.H., Tuller, M.P., Danferder, A., 2003. Mapeamento Geológico região Sete Lagoas, Pedro Leopoldo, Matozinhos, Lagoa Santa, Vespasiano, Capim Branco,

Prudente de Morais, Confins e Funilândia. Estado de Minas Gerais. Escala 1:50000 Texto explicativo PROJETO VIDA, Serviço Geológico do Brasil.

Ribeiro, J.H., Tuller, M.P., Pinho, J.M.M., Signorelli, N., Féboli, W.L., 2008. A fácies diamictito da Formação Carrancas, Grupo Bambuí, na região sudoeste da bacia do São Francisco, Minas Gerais. In: Congresso Brasileiro de Geologia, 44, Curitiba (PR), Anais, p 913.

Romano AW (2007) Geologia da Folha Pará de Minas (SE.23-Z-C-IV), escala 1:100.000: nota explicativa. UFMG/CPRM-Serviço Geológico do Brasil, Belo Horizonte

Rodrigues, J.B., 2008. Proveniência de sedimentos dos grupos Canastra, Ibiá, Vazante e Bambuí – um estudo de zircões detríticos e idades modelo Sm-Nd. Tese de Doutoramento, Instituto de Geociências, Universidade de Brasília, Brasília, 128p.

Rodrigues, J. B., Pimentel, M. M., Dardenne, M. A., Armstrong, R. A. 2010. Age, provenance and tectonic setting of the Canastra and Ibiá, Groups (Brasília Belt, Brazil): Implications for the age of a Neoproterozoic glacial event in central Brazil. Journal of South American Earth Sciences 29: 512–521.

Rodrigues J.B., Pimentel M.M., Buhn B., Matteini M., Dardenne M.A., Alvarenga C.J.S., Armstrong R.A. 2012. Provenance of the Vazante Group: New U-Pb, Sm-Nd, Lu-Hf isotopic data and implications for the tectonic evolution of the Neoproterozoic Brasília Belt. Gondwana Research 21: 439–450.

Sansjofre, P., Trindade, R.I.F., Ader, M., Soares, J.L., Nogueira, A.C.R., Tribovillard, N., 2014. Paleoenvironmental reconstruction of the Ediacaran Araras platform (Western Brazil) from the sedimentary and trace metals record. Precambrian Research 241, 185–202.

Santos, R.V., Alvarenga, C.J.S., Babinski, M., Ramos, M.L.S, Cukrov, N., Fonseca, M.A., Sial, A.N., Dardenne, M.A., Noce, C.M., 2004. Carbon isotopes of Mesoproterozoic–Neoproterozoic sequences from Southern São Francisco craton and Araçuaí Belt, Brazil: Paleogeographic implications. Journal of South American Earth Sciences, 18: 27-39.

Santos, R. F., Alkmim, F. F., Pedrosa–Soares, A. C. 2009. A Formação Salinas, Orógeno Araçuaí (MG): história deformacional e significado tectônico. Revista Brasileira de Geociências 39(1): 81–100.

Schobbenhaus, C. 1996. As tafrogêneses superpostas Espinhaço e Santo Onofre, estado da Bahia: revisão e novas propostas. Revista Brasileira de Geociências 26(4): 265–276.

Schöll, W.U., 1976. Sedimentologia e geoquímica do Grupo Bambuí na parte sudeste da Bacia do São Francisco. In: Congresso Brasileiro de Geologia, 29, Ouro Preto, Anais, p. 207-231.

Schrag, D., Higgins, J., Macdonald, F., Johnston, D., 2013. Authigenic Carbonate and the History of the Global Carbon Cycle. Science 339, 540.

Schrag, D., Higgins, J., Macdonald, F., Johnston, D., 2014. Authigenic carbonate and the history of the global carbon cycle: Why diagenesis matters even more. Goldschmidt Abstracts 2223.

Semikhatov, M.A., Gorokhov, I.M., Kuznetsov, A.B. et al., 1998. The strontium isotopic composition in early Late Riphean seawater: Limestones of the Lakhanda Group, the Uchur-Maya region, Siberia. Trans. (Dokl.) Russian Academy of Science. Earth Sciences Sections, 360, 488–492.

Shields, G.A., 2007. A normalised seawater strontium isotope curve: possible implications for Neoproterozoic–Cambrian weathering rates and the further oxygenation of the Earth. eEarth 2 (2), 35–42.

Sial, A.N., Dardenne, M.A., Misi, A., Pedreira, A.J., Gaucher, C., Ferreira, V.P., Silva Filho, M.A., Uhlein, A., Pedrosa-Soares, A.C., Santos, R.V., Egydio-Silva, M., Babinski, M., Alvarenga, C.J.S., Fairchild, T.R., Pimentel, M.M., 2009. The São Francisco Palaeocontinent. In: Gaucher, C., Sial, A.N., Halverson, G.P., Frimmel, H.E. (Eds): Neoproterozoic-Cambrian Tectonics, Global Change and Evolution: a focus on southwestern Gondwana. Developments in Precambrian Geology, 16, pp. 31–69.

Sial, A. N., Gaucher, G., Ferreira, V. P., Pereira, N. S., Cezario, W. S., Chiglino, L., Monteiro, H. (2015b). Isotope and Elemental Chemostratigraphy. M. Ramkumar (editor): Chemostratigraphy, Concepts, Techniques and Applications, Elsevier, 23–64.

Silva, L. C., Pedrosa–Soares, A. C., Teixeira, L.R., Armstrong, R. 2008. Tonian rift–related, A–type continental plutonism in the Araçuaí Orogen, eastern Brazil: New evidence for the breakup stage of the São Fransico–Congo Paleocontinent. Gondwana Research 13(4): 527–537.

Souza, S. L., Brito, P. C. R., Silva, R. W. S. 1993. Estratigrafia, Sedimentologia e Recursos Minerais da Formação Salitre na Bacia de Irecê, Bahia (Série Arquivos Abertos 2). Companhia Baiana de Pesquisa Mineral (CBPM), Salvador.

Tahata, M., Ueno, Y., Ishikawa, T., Sawaki, Y., Murakami, K., Han, J., Shu, D., Li, Y., Guo, J. Yoshida, N., Komiya, T. 2013. Carbon and oxygen isotope chemostratigraphies of the Yangtze platform, South China: decoding temperature and environmental changes through the Ediacaran. Gondwana Res. 23, 333–353.

Taylor, S.R. & McLennan, S.M. 1985. The Continental Crust: Its Composition and Evolution. Blackwell, Oxford, 312 p.

Teixeira, W., Sabaté, P., Barbosa, J., Noce, C.M., Carneiro, M.A., 2000. Archean and Paleoproterozoic tectonic evolution of the São Francisco craton, Brazil. In: Cordani, U.G., Milani, E.J., Thomaz-Filho, A., Campos, D.A. (eds.) Tectonic Evolution of South America. 31st International Geology Congress, Rio de Janeiro, p. 101-137.

Tribovillard, N., Algeo, T.J., Baudin, F., Riboulleau, A., 2012. Analysis of marine environmental conditions based on molybdenum–uranium covariation – applications to Mesozoic paleoceanography. Chemical Geology 324–325, 46–58.

Tribovillard, N., Algeo, T.J., Lyons, T., Riboulleau, A., 2006. Trace metals as paleoredox and paleoproductivity proxies: an update. Chemical Geology 232 (1–2), 12–32.

Tuller, M.P., 2009. Folha Sete Lagoas 1:100.000. Programa Geologia do Brasil, GEOBANK. http://geobank.sa.cprm.gov.br.

Tuller, M.P., Ribeiro, J.H., Signorelli, N., Feboli, W.L., Pinho, J.M.M., 2009. Projeto Sete Lagoas-Abaeté, Estado de Minas Gerais: texto explicativo, Belo Horizonte: CPRM.

Uhlein, A., Trompette, R.R., Alvarenga, C.J.S., 1999. Neoproterozoic glacial and gravitational sedimentation on a continental rifted margin: the Jequitaí-Macaúbas sequence (Minas Gerais, Brazil). Journal of South American Earth Sciences 12, 435–451.

Uhlein, A., Alvarenga, C.J.S., Trompette, R.R., Dupont, H.S.J.B., Egydio-Silva, M., Cukrov, N., Lima, O.N.B., 2004. Glaciação neoproterozoica sobre o cráton do São Francisco e faixas dobradas adjacentes. In: Mantesso-Neto V., Bartorelli A., Carneiro C.D.R., Brito-Neves B.B. (orgs.) Geologia do Continente Sul-Americano: evolucão da obra de Fernando Flávio Marques de Almeida, Beca, São Paulo, pp. 539–553.

Uhlein, A., Baptista, M. C., Seer, H. J., Caxito, F. A., Uhlein, G. J., Dardenne, M. A. 2011. A Formação Lagoa Formosa, Grupo Bambuí (MG): Sistema deposicional de leque submarino em bacia de antepais. Geonomos 19(2): 163–172.

Uhlein, A., Perrella, P., Uhlein, G.J., Caxito, F. A., Neiva, G. S., Souza, R.D., Mendes, T.A. A. 2014. Folha Januária SD-23-Z-C-II. Mapa geológico em escala 1:100.000. CODEMIG-UFMG.

Uhlein, G.J., Carvalho, J.F.M.G., Uhlein, A., Caxito, F.A., Halverson, G.P., Sial, A.N., 2012. Estratigrafia e sedimentologia da Formação Carrancas, Grupo Bambuí, nas regiões de Belo Horizonte e Pitangui, MG. Geonomos 20 (2), 79–97.

Uhlein, G.J., Uhlein, A., Halverson, G.P., Stevenson, R., Caxito, F.A., Cox, G.M., Carvalho, J.F.M.G., 2016. The Carrancas Formation, Bambuí Group: a record of pre-Marinoan sedimentation on the southern São Francisco craton, Brazil. J. S. Am. Earth Sci. 71, 1–16.

Uhlein, G.J., Uhlein, A., Stevenson, R., Halverson, G.P., Caxito, F.A., Cox, G.M., 2017. Early to late Ediacaran conglomeratic wedges from a complete foreland basin cycle in the southwest São Francisco Craton, Bambuí Group, Brazil. Precambrian Res. 299, 101–116.

Uhlein, G.J., Uhlein, A., Pereira, E., Caxito, F.A., Okubo, J., Warren, L.V., Sial, A.N., 2019. Ediacaran paleoenvironmental changes recorded in the mixed carbonatesiliciclastic Bambuí Basin, Brazil. Palaeogeography, Palaeoclimatology, Palaeoecology, 517, 39–51.

Uhlein, G.J., Caxito, F.A, Frei, R., Uhlein, A., Sial, A., Dantas, E.L., 2021. Microbially induced chromium isotope fractionation and trace elements behavior in lower Cambrian microbialites from the Jaíba Member, Bambuí Basin, Brazil. Geobiology, 19 (2), 125-146.

Valeriano, C.M., Machado, N., Simonetti, A., Valadares, C.S., Seer, H.J., Simões, L.S.A., 2004. U–Pb geochronology of the southern Brasília belt (SE-Brazil): sedimentary provenance, Neoproterozoic orogeny and assembly of West Gondwana. Precambrian Research, 130:27–55.

Veizer, J., 1983. Chemical diagenesis of carbonates: theory and application of trace element technique. In: Arthur, M.A., Anderson, T.F., Kaplan, I.R., Veizer, J., Land, L.S. (Eds.), Stable Isotopes in Sedimentary Geology. SEPM Short Course Notes 10, pp. 3.1–3.100.

Veizer, J., Hoefs, J., Ridler, R.H., Jensen, L.S., Lowe, D.R., 1989. Geochemistry of Precambrian carbonates: I. Archean hydrothermal systems. Geochimica et Cosmochimica Acta, 53:845–857.

Veizer, J., Ala, D., Azmy, K., Brukschen, P., Buhl, D., Bruhn, F., Carden, G.A.F., Diener, A., Ebneth, S., Godderis, Y., Jasper, T., Korte, C., Pawellek, F., Podlaha, O.G., Strauss,

H., 1999. $^{87}Sr/^{86}Sr$, $\delta^{13}C$ and $\delta^{18}O$ evolution of Phanerozoic seawater. Chemical Geology, 161:59-88.

Vieira, L.C., Almeida, R.P., Trindade, R.I.F., Nogueira, A.C.R., Janikian, L., 2007a. Formação Sete Lagoas em sua área-tipo: fácies, estratigrafia e sistemas deposicionais. Revista Brasileira de Geociências, 37:1-14.

Vieira, L.C., Trindade, R.I.F, Nogueira, A.C.R., Ader, M., 2007b. Identification of a Sturtian cap carbonate in the Neoproterozoic Sete Lagoas carbonate plataform, Bambuí Group, Brazil. Comptes Rendus Geoscience, 339:240-258.

Viveiros, J.F.M. & Walde, D., 1976. Geologia da Serra do Cabral, Minas Gerais, Brasil. Münsterische Forschungshefte Geologie und Palaeontologie 38/39, 15–27.

Webb, G.E., Kamber, B.S., 2000. Rare earth elements in Holocene reefal microbialites: a new shallow seawater proxy. Geochimica et Cosmochimica Acta 64, 1557–1565.

Webb, G.E., Nothdurft, L.D., Kamber, B.S., Kloprogge, J.T., Zhao, J.-X., 2009. Rare earth element geochemistry of scleractinian coral skeleton during meteoric diagenesis: a sequence through neomorphism of aragonite to calcite. Sedimentology, 56:1433-1463.

Warren, L.V., Quaglio, F., Riccomini, C., Simões, M.G., Poiré, D.G., Strikis, N.M., Anelli, L.E. Strikis, P.C., 2014. The puzzle assembled: Ediacaran guide fossil Cloudina reveals an old proto–Gondwana seaway. Geology, 42 (5): 391–394.

Young, G.M., 2013. Evolution of Earth's climatic system: Evidence from ice ages, isotopes, and impacts. GSA Today, v. 23, no. 10.

Zhang, J., & Nozaki, Y., 1996. Rare earth elements and yttrium in seawater: ICP-MS determinations in the East Caroline, Coral Sea, and South Fiji basins of the western South Pacific Ocean. Geochimica et Cosmochimica Acta, 60:4631–4644.

Zhao, Y., Zheng, Y., Chen, F., 2009. Trace element and strontium isotope on sedimentary environment of Ediacaran carbonates in southern Anhui, South China. Chemical Geology, 265:345–362.